UNIVERSITY OF CAPE TOWN
IYUNIVESITHI YASEKAPA • UNIVERSITEIT VAN KAAPSTAD

Department of Civil Engineering

Polar Engineering Research Group

Computational modelling of ice floe dynamics in the Antarctic marginal ice zone

A research thesis in fulfilment of the requirements for a Doctoral degree in the field of Civil Engineering

Prepared for: University of Cape Town

Author:
Mr. Rutger Marquart

Supervisors:
Prof. Sebastian Skatulla
Dr. Alfred Bogaers
Dr. Keith MacHutchon

September 10, 2022

Plagiarism Declaration

- I know that plagiarism is wrong. Plagiarism is to use another's work and to pretend that it is one's own.
- Each significant contribution to and quotation in this document from the work or works of other people has been attributed and has been cited and referenced.
- This thesis is my own work.
- I have not allowed and will not allow anyone to copy my work with the intention of passing it as his or her own work.

Name	Student No	Date	Signature
Rutger Marquart	MRQRUT001	September 10, 2022	

Preface

This report is part of the fulfilment of a doctoral degree in the field of Civil Engineering at the University of Cape Town (UCT) and is the result of four years of research under the supervision of Prof. Sebastian Skatulla, Dr. Alfred Bogaers and Dr. Keith MacHutchon.

First, I would like to express my deepest appreciation to Sebastian Skatulla for inviting me to South Africa as a research assistant at UCT in 2017, and for giving me the opportunity to start my PhD in 2018. I sincerely thank both Sebastian and Alfred Bogaers for supervising me during my PhD project. They have provided me with feedback regularly, allowing me to develop myself as a researcher in the field of Civil Engineering. Many thanks to Dr. Keith MacHutchon and all my fellow students in the Polar Engineering Research Group (PERG), who were always ready to lend a helping hand. They created a great working atmosphere at UCT.

I would like to thank the National Research Foundation (NRF) and the Marine and Antarctic Research Centre for Innovation and Sustainability (MARIS) for giving me financial support during the four years of my project. Computations were performed using facilities provided by the UCT's ICTS High Performance Computing team: hpc.uct.ac.za.

A special thanks to external researchers: Dr. Alberto Alberello (University of East Anglia), A/Prof. Alessandro Toffoli (University of Melbourne), Prof. Marcello Vichi (UCT) and Dr. Carina Schwarz (University of Duisburg-Essen) who have provided me with research data and feedback on my published paper 'A Computational Fluid Dynamics Model for the Small-Scale Dynamics of Wave, Ice Floe and Interstitial Grease Ice Interaction'. I enjoyed working with them and look forward to doing so again in the near future.

I would also like to thank the captain, crew and fellow researchers on the SA Agulhas II to the Antarctic marginal ice zone (MIZ) during the winter cruise in 2017 and both the SCALE winter and spring cruises in 2019. These research expeditions yielded productive data as input for my numerical model and have each been a once-in-a-life-time experience, which I will always cherish.

I am beyond grateful to my brother, Wijnand Marquart, and my friends, in particular Regardt Hennop, for making me feel at home in Cape Town during my PhD.

Last, words cannot express my deepest gratitude to my parents for giving me the opportunity to study in Cape Town and for their unconditional love and support.

R. Marquart
Cape Town, September 10, 2022

Table of Contents

List of Figures

List of Tables

List of Symbols

Parameter	Definition	Unit
a	wave amplitude	m
a_i	wave amplitude with $i = x, y$ in the x- and y-direction	m
ak	wave steepness	-
A_f	ice floe concentration	-
A_{floe}	ice floe area	m^2
b	time index	-
c	wave speed	ms^{-1}
C_a	air drag coefficient	-
C_{a_λ}	air drag multiplication factor	-
$C_{w_{f,g}}$	water drag coefficient for ice floes and grease ice	-
C_{10}	air drag coefficient at 10m from mean sea level	-
d_w	water depth	m
D	solution domain	m^2
D_d	diameter of idealised disk-shaped ice floe	m
$D_{i,m}$	median of the ice floe caliper diameter with $i = x, y$ in the x- and y-direction	m
e_Y	yield surface axes ratio	-
E_Y	Young's modulus	Nm^{-1}
g	gravitational acceleration	ms^{-2}
h	sea ice thickness	m
$h_{f,g}$	ice floe and grease ice thickness	m
h_w	submerged ice floe thickness	m
H	wave height	m
H_s	significant wave height	m
i	time step indicator	-
$\boldsymbol{I}$	identity matrix	-

$\boldsymbol{k}$	unit vector normal to the ice surface	-
k	wave number	m^{-1}
k_i	wave number with $i = 1, 2$ in the x- and y-direction	m^{-1}
l_i	actual observations time series	PDU
$\hat{l}_i$	estimated time series	PDU
m	sea ice mass	kgm^{-2}
$\boldsymbol{n}$	unit normal vector	-
n_f	number of ice floes	-
N_i	number of data points	-
p_{wi}	wave-induced pressure	Nm^{-2}
P_g	grease ice strength parameter	Nm^{-1}
P_g^*	constant grease ice strength parameter	Nm^{-2}
q_i	25^{th} and 75^{th} percentile of a box plot with $i = 1, 3$	PDU
$RMSE_i$	root mean square error with $i = x, y$ in the x- and y-direction	PDU
SD_i	standard deviation with $i = x, y$ in the x- and y-direction	m
t	time	s
T	wave period	s
$\boldsymbol{U}$	sea ice velocity vector	ms^{-1}
$U_{x,y}$	sea ice velocity in the x- and y-direction	ms^{-1}
$\boldsymbol{U}_a$	wind velocity vector	ms^{-1}
$U_{a_{x,y}}$	wind velocity in the x- and y-direction	ms^{-1}
U_{in}	initial velocity in the x-direction	ms^{-1}
U_{mag}	velocity magnitude	ms^{-1}
$\boldsymbol{U}_o$	ocean current velocity vector	ms^{-1}
$U_{o_{x,y}}$	ocean current velocity in the x- and y-direction	ms^{-1}
$U_{o,0}$	ocean current velocity at the mean sea level	ms^{-1}
$\boldsymbol{U}_w$	orbital wave velocity vector	ms^{-1}
$U_{w_{x,y,z}}$	orbital wave velocity in the x-, y- and z-direction	ms^{-1}
$\boldsymbol{U}^*$	friction velocity vector	ms^{-1}
$U^*_{x,y}$	friction velocity in the x- and y-direction	ms^{-1}
$\boldsymbol{U}_{10}$	wind velocity vector at 10m from mean sea level	ms^{-1}
w	multiplier whisker of a box plot	-
x	x-coordinate	m

y	y-coordinate	m
z	z-coordinate	m
z_0	sea surface roughness length	m
z_c	height of critical layer	m
α	non-dimensional phase fraction parameter	-
α_C	Charnock constant	-
Δ	effective deformation rate	s^{-1}
Δh	initial vertical distance in the y-direction between two ice floes	m
Δ_{min}	lower limit of the effective deformation rate	s^{-1}
$\boldsymbol{\epsilon}$	strain tensor	-
$\dot{\boldsymbol{\epsilon}}$	strain rate tensor	s^{-1}
$\dot{\epsilon}_{ij}$	Cartesian component of the symmetric strain rate tensor with $i = 1, 2, 3$ and $j = 1, 2, 3$	s^{-1}
$\dot{\epsilon}_{mag}$	strain rate magnitude	s^{-1}
ζ	bulk viscosity	kgs^{-1}
ζ_c	vertical curvilinear coordinate	m
η	shear viscosity	kgs^{-1}
$\eta(x, t)$	wave elevation	m
$\theta_{a,w}$	air and water turning angle	rad
θ_{wa}	wave direction angle	rad
θ_{wi}	true wind direction	rad
κ	von Kármán constant	-
λ	first Lamé parameter	Nm^{-1}
Λ	wave length	m
μ	second Lamé parameter	Nm^{-1}
ν	Poisson's ratio	-
ν_k	kinematic viscosity	m^2s^{-1}
ρ	sea ice density	kgm^{-3}
$\rho_{a,w}$	air and sea water density	kgm^{-3}
$\rho_{f,g}$	ice floe and grease ice density	kgm^{-3}
$\boldsymbol{\sigma}$	stress tensor	kgs^{-2}

$\dot{\boldsymbol{\sigma}}$	stress rate tensor	$\mathrm{kgs}^{-2}\mathrm{s}^{-1}$
σ_{col}	collision stress intensity	kgs^{-2}
σ_{col}^{avg}	time-averaged collision stress intensity	kgs^{-2}
σ_{col}^{peak}	peak collision stress intensity	kgs^{-2}
σ_{col}^{thres}	collision stress intensity threshold	kgs^{-2}
$\boldsymbol{\sigma}_{f,g}$	ice floe and grease ice stress tensor	kgs^{-2}
σ_{ij}	Cartesian component of the symmetric stress tensor with $i = 1, 2, 3$ and $j = 1, 2, 3$	kgs^{-2}
σ_{mag}	stress magnitude	kgs^{-2}
σ_{min}	minimum principal stress	kgs^{-2}
$\boldsymbol{\tau}$	total wind shear stress vector	Nm^{-2}
$\boldsymbol{\tau}_a$	atmospheric surface traction vector	$\mathrm{m}^2\mathrm{s}^{-2}$
$\boldsymbol{\tau}_{fk}$	Froude-Krylov stress vector	$\mathrm{m}^2\mathrm{s}^{-2}$
$\boldsymbol{\tau}_o$	ocean current drag vector	$\mathrm{m}^2\mathrm{s}^{-2}$
$\boldsymbol{\tau}_{sd}$	current-dependent skin drag vector	$\mathrm{m}^2\mathrm{s}^{-2}$
$\boldsymbol{\tau}_t$	oceanic surface traction vector	$\mathrm{m}^2\mathrm{s}^{-2}$
$\boldsymbol{\tau}_w$	wave traction vector	$\mathrm{m}^2\mathrm{s}^{-2}$
ϕ	velocity potential	$\mathrm{m}^2\mathrm{s}^{-1}$
ω	wave frequency	s^{-1}

Note that only the symbols directly related to the description (Chap. 3) and results (Chaps. 5, 6 and 7) of the small-scale model are included in the List of Symbols.

List of Abbreviations

Abbreviation	Definition
ABL	atmospheric boundary layer
AIDJEX	Arctic Ice Dynamics Joint Experiment
BBM	brittle Bingham-Maxwell
BC	boundary condition
CDS	central differencing scheme
CFD	computational fluid dynamics
CICSAM	Compressive Interface Capturing Scheme for Arbitrary Meshes
CoG	centre of gravity
DEM	discrete element method
EB	elasto-brittle
EP	elastic-plastic
EVP	elastic-viscous-plastic
FDM	finite difference method
FEM	finite element method
FSI	fluid-structure interaction
FVM	finite volume method
HRIC	High-Resolution Interface Capturing scheme
LS	Level-set
MARIS	Marine and Antarctic Research Centre for Innovation and Sustainability
MEB	Maxwell-elasto-brittle
MIZ	marginal ice zone
MULES	Multidimensional Universal Limiter with Explicit Solution
NRF	National Research Foundation

ODE	ordinary differential equation
OpenFOAM	Open source Field Operation and Manipulation
PDE	partial differential equation
PDU	parameter dependent unit
PERG	Polar Engineering Research Group
PISO	Pressure Implicit solution by Split Operator method
PSU	particle salinity unit
QUICK	Quadratic Upwind Interpolation for Convection Kinetics
RMSE	root mean square error
SCALE	Southern oCean seAsonal Experiment
SIMPLE	Semi Implicit Method for Pressure Linked Equations
SO	Southern Ocean
UCT	University of Cape Town
UDS	upwind differencing scheme
VoF	volume of fluid
VP	viscous-plastic
WIIOS	waves-in-ice observation systems

Summary

The contribution of Antarctic sea ice in global climate models requires a more accurate estimation, as a relatively large part, approximately 4% of the Earth's surface in the winter season, is covered by sea ice. Understanding the dynamic and thermodynamic processes of sea ice results in a better comprehension of sea ice behaviour in the Antarctic marginal ice zone (MIZ) and thus leads to better predictions.

Large-scale sea ice models operate at regions of $10 - 100\text{km}^2$, describing sea ice in a smeared model approach. However, the highly dynamic sea ice behaviour in the Antarctic MIZ, which is represented by the area where sea ice and ocean waves interact, still eludes reliable prediction. A heterogeneous morphology, consisting of relatively small and mobile ice floes, governed by collisional dynamics and fracture mechanics, requires detailed finer-scale sea ice dynamics models. Therefore, this project focuses on small-scale modelling of sea ice dynamics in the Antarctic MIZ. The detailed newly-developed model considers a heterogeneous sea ice material composition, consisting of separately ice floes and grease ice with their distinct properties. The material behaviour of ice floes is implemented using a Hookean-like flow rule, whereas grease ice is governed by a viscous-plastic material law. The small-scale model developed in this study assumes that sea ice is isothermal, as only small time windows of less than a minute are considered. As a result, thermodynamic effects, such as sea ice melt and growth, are not taken into account.

This work describes key aspects of ice floe collision dynamics in wavy conditions, considering skin drag, the Froude-Krylov force acting at the circumference of ice floes from the wave pressure gradient, and form drag due to the surrounding grease ice deeper into the Antarctic MIZ in a low to medium wave energy regime. Ice floes that interact with each other and the interaction between ice floes and grease ice are analysed. The behaviour of the sea ice rheology of both ice floes and grease ice are studied in realistic sea ice layouts, subjected to different wave properties and grease ice viscosity values. The influence of inertia on the phase shift between the motion of the sea ice cover and the orbital wave velocity of the water layer underneath, is one of the most important aspects in the small-scale model. The phase shift directly affects the interrelation between the sea ice velocity, wave elevation and the ice floe collision dynamics. Additionally, the collision dynamics shows that the ice floe collision pattern in the sea ice domain becomes more random for larger wave periods, due to an increase of the kinetic wave energy. Lastly, strain rates exhibit high localised gradients due to form drag at the interface between ice floes and grease ice, which corresponds to low viscosity values.

The small-scale model, demonstrated in this study, shows the general applicability of a detailed continuum framework, contributing to the current research to small-scale atmosphere-ocean physical processes in the Antarctic MIZ. The obtained results provide insights into high-resolution behaviour of sea ice on the floe-scale. Furthermore, the newly-developed model can provide for the parametrisation of large-scale models, improving existing global climate models.

Chapter 1

Introduction

1.1 Background to study

Sea ice in the Antarctic is highly dynamic, covering a large area in the Southern Ocean (SO). From February to September each year, sea ice expands from approximately 2.5 million km^2 to 18 million km^2, which in winter is equivalent to approximately 4% of the Earth's surface [136, 160]. The formation of sea ice in the Antarctic is one of the most substantial seasonal variations on Earth [44]. It has a major impact on the global climate and life of marine organisms in and below the ice [114]. Sea ice acts as an insulating layer between the relatively warm ocean and cold atmosphere with a high albedo [7], resulting in a profound influence on the heat, gas, and momentum exchange. The extent to which sea ice has an impact on these processes depends on the distribution of the ice coverage, thickness, dynamics, ice type, and snow coverage [191, 200]. These processes determine the freshwater budget in the upper ocean layer, due to brine rejection during the formation and expulsion of freshwater during the melt [114].

A large number of dynamic and thermodynamic processes make, especially the Antarctic marginal ice zone (MIZ), a highly complex system. The MIZ represents the exterior area in the Antarctic, which is hundreds of kilometres in width, that covers the transition from the open ocean to consolidated sea ice [96, 142], requiring greater insight into sea ice dynamics and thermodynamics at the different stages of formation and melt during its seasonal cycle. Sea ice is crucial in the SO's biochemical cycles, growth of algal biomass, and the regulation of the marine carbon pump [114], which is the sequestration by transport of carbon from the atmosphere into the deep ocean [140].

Mostly young or first-year sea ice is encountered in the Antarctic MIZ, as most marine ice melts and does not survive the first summer after sea ice formation [130]. During the Antarctic winter, when temperatures are low, the formation of sea ice starts with randomly oriented loosely disk-shaped frazil crystals, which form in turbulent and supercooled water [142]. In calm waters, the frazil crystals aggregate into a thin uniform sheet of sea ice, called nilas. Subsequently, nilas grows downwards by freezing seawater onto its base. However, particularly for the more turbulent waters of the SO, frazil ice crystals accumulate at the ocean surface, forming a grease ice layer consisting of individual ice crystals [169]. Small irregular clumps of frazil ice crystals form into small circular discs with a diameter of approximately ten centimeters. Interaction of pancake ice by rafting, results in the aggregation of pancakes into larger pancakes, exhibiting the characteristic diameters

of $1-10$m, much smaller than ocean wavelengths [2].

Both polar regions, the Arctic and the Antarctic, play an important role in the global climate [167], but are distinctly different from one another. Firstly, the morphology of the polar regions. The area within the Arctic Circle, which includes the Arctic Ocean and is surrounded by open oceans and northern parts of continental landmasses, can be defined as the Arctic. Both the frozen Antarctic continent, with elevations exceeding 4km, and the surrounding SO, south of the Antarctic Convergence, can be defined as the Antarctic. The Antarctic Convergence is an oceanographic barrier that moves in space and time, approximately 58° south [117]. The SO and the atmospheric polar vortex, which is a band of strong winds that form in the stratosphere, thermally isolate the Antarctic continent from the rest of the world. The Arctic, on the other hand, is highly affected by rivers and seasonal atmospheric transport from the neighbouring northern continental parts [167]. Salinity in Antarctic waters is $3-4$ PSU higher than in the Arctic, while precipitation in the Antarctic is almost three times higher than in the Arctic. Secondly, the atmospheric conditions in the polar regions are different. The Antarctic is subjected to strong surface forcing, severe pressure gradients, and extreme storms, occurring frequently. Moreover, the Antarctic has a more dynamic circulation of the ocean surface, which is associated with the Antarctic Circumpolar Current and parts of the northern polar gyres [188]. These aspects all affect, and are affected by, sea ice concentration and distribution in the Antarctic. Lastly, the atmospheric variability, which affects scale and processes in the SO, is more complex than in the Arctic [167]. As a result, the Arctic is more accessible, as it is less remotely located, and weather conditions are less severe in the Arctic than in the Antarctic. This makes research in the Arctic both easier and more affordable. Atmosphere-ocean physical processes in the Antarctic MIZ are still poorly understood [188], due to limited observations. Therefore, more research and a better understanding of the Antarctic MIZ is required.

Several studies have been performed to gain a better understanding into the behaviour of sea ice in the polar regions. These studies range from in situ experimental studies to numerical modelling [2, 14, 67, 69, 118, 119, 123]. As in situ research in the Antarctic is expensive and difficult to access, numerical models have mostly been used. The majority of dynamic-thermodynamic sea ice models developed in the past are phenomenological, large-scale models, based on the Arctic, e.g. Hibler III [69], Keller [92], Wang and Shen [207], which are widely applied in global climate modelling and help to understand the impact of sea ice on seasonal changes.

The well-established viscous-plastic (VP) rheology by Hibler III [69] describes the large-scale drift of sea ice suitably with a certain level of accuracy. The VP sea ice rheology relates the internal ice stress with the strain rate. A large sea ice area with heterogeneous characteristics including fractures, leads, and open water is modelled using a smeared model approach, in which several different types of ice are modelled as one homogeneous material making use of averaged quantities. The model represent an ice-covered area at length scales of $10-100$km with a time scale in the order of days. This is the scale at which material properties have been developed and verified. It, however, fails at simulating the observed properties of sea ice deformation [38].

Small-scale sea ice modelling increases the resolution and provides a more detailed description of the actual behaviour of different types of ice. The majority of existing finer-scale numerical models are based on molecular dynamics schemes based on collision dynamics and discrete-element modelling [65, 75, 164], considering sea ice physics and dynamics processes taking place at a floe level [63]. The one-dimensional Discrete-Element bonded-particle Sea Ice model developed by Herman et al. [67] elucidates the significance of skin drag on wave attenuation and floe collision dynamics due to prolonged collision and reduced restitution

coefficient. The model makes use of a heuristic contact detection algorithm and includes simplified overwash, elastic and inelastic contact force contributions. Contact forces are linked to the restitution coefficient, but disregards tangential friction. Most Lagrangian models, including the discrete-element method (DEM) model of Herman et al. [67], have in common the limitation of using highly simplified modelling equations or ice floe geometries, which does not benefit the realistic behaviour of the model [65].

A direct link between sea ice characteristics and its mechanical properties is missing [218] and in situ data to verify the existing theoretical models are limited [128, 185]. In this sense, the accurate modelling of the interplay of temperature, waves, sea ice dynamics as well as wind and ocean currents is necessary not only to predict sea ice dynamics and wave energy dissipation [4, 200], but also to advance understanding of the governing mechanisms of sea ice growth in this region. In particular, deeper into the Antarctic MIZ, where up to 100% sea ice concentrations are observed, the wave-ice interaction is highly complex, and is typically characterised by floe collision, turbulent eddy generation at the ice-water interface due to skin drag and floe-grease ice interaction [97, 170, 171, 186]. Hence, understanding sea ice dynamics and thermodynamics can lead to a better comprehension of the Antarctic MIZ [65].

1.2 Problem identification

Sea ice modelling has helped to gain a better understanding of the polar regions, however, most of these models are based on the Arctic. Research in the Arctic is more accessible than in the Antarctic, due to its location and less severe weather conditions. Harsh atmospheric and oceanic conditions in the Antarctic MIZ highly affect the seasonal sea ice advance and retreat [168]. As a result, the dynamics of sea ice in the MIZ can be described by large variations both temporally and spatially, which is still insufficiently predicted by current climate models [71]. Therefore, the understanding of physical processes between the atmosphere and ocean in the Antarctic MIZ still requires attention. Observations that have been done in the Antarctic MIZ are not sufficient to resolve the rapidly evolving dynamics of the ocean surface layer [188].

Besides wind forcing, wave action is a determining feature of pancake ice formation and growth, although in situ data to verify the existing theoretical sea ice models is still very limited [128, 185]. Sea ice affects the propagation of waves, however, to what extent is still largely unknown [45]. Describing the distinctive nature of waves travelling through the Antarctic MIZ is essential for the understanding of sea ice dynamics.

Large- and meso-scale sea ice dynamics models are mainly continuum models, making use of effective sea ice properties, such as a spatially variable ice concentration and an empirically derived thickness [168]. As the observed sea ice properties and the scale dependency of sea ice are associated with specific sea ice constituents [38, 150, 168], it is essential to distinguish between materials, which can only be accurately accounted for on the small-scale. Large-scale models do not distinguish between different ice constituents with distinctively different material behaviour. Additionally, they do not describe the interaction between sea ice materials in a heterogeneous sea ice composition, considering the collision dynamics of realistically shaped ice floes, skin drag and form drag on ice floes from surrounding grease ice [3, 67].

Finer-scale models on a floe level commonly use either a molecular dynamics schemes based on Hertzian collision dynamics [18, 65, 75, 148, 164] or the Discrete-Element method [37, 67]. These models generally describe ice floes floating in water as a collection of interacting particles, which simplifies the ice floe solid

mechanics behaviour and the fluid-structure interaction significantly. Only a few continuum models are developed, which account for wave attenuation and dissipation effects in sea ice [207] or wave interaction with a single ice floe [14, 80], however, to the best of our knowledge, no model has explicitly described a collection of interacting ice floes surrounded by a viscous fluid.

In contrast to existing discrete particle and continuum models, the small-scale continuum approach developed in this project can account for the actual heterogeneous ice cover composition in terms of geometrical layout of ice floes and interstitial grease ice. Additionally, the respective material properties are described by a solid-like deformation behaviour of ice floes and a fluid-like viscous-plastic behaviour of grease ice by using two different material laws. This allows for the detailed quantification of the impact of floe and grease ice material properties, geometrical features including ice floe size, shape and concentration, as well as wave forcing on the mechanical response of the sea ice cover. For this, a realistic sea ice layout is extracted from in-situ image and video material recorded in the Antarctic MIZ [3] and suitable material parameter values are chosen to independently describe the mechanics of ice floes and grease ice. As a first step, this study investigates wave-ice and ice-ice interactions focusing on the high-resolution ice rheology. Specifically, the stress, strain and strain rate response of ice floe-grease ice interaction and ice floe collision dynamics is elucidated as linked to grease ice viscosity while being subjected to an imposed wave.

The sea ice rheology is controlled by floe collision, the floe-grease ice interaction, skin drag, as well as the heterogeneous ice cover composition in terms of geometrical layout and material properties. All aspects combined, describing the collisional dynamics of ice floes due to wave action, have not been considered before. This, however, based on recent observations by Alberello et al. [3, 4] and Vichi et al. [200], is crucial to accurately predict the sea ice dynamics of the Antarctic MIZ.

1.3 Aims and objectives

The primary aim of this project is to gain a better understanding of sea ice on a smaller scale. Understanding the motion of sea ice and its characteristic mechanical behaviour as linked to the rheology on the meter-scale specific to the Antarctic MIZ will contribute to solving the puzzle of the sea ice impact on seasonal changes and the global climate. The main objective is therefore to develop a small-scale model, describing the dynamics of sea ice in the Antarctic, focusing on the winter season. The large-scale model by Hibler III [69], as implemented in the computational fluid dynamics (CFD) software OpenFOAM[2], will serve as the basis for the current model.

In contrast to previously developed models, this work specifically focuses on the sea ice dynamics modelling deeper into the Antarctic MIZ in the low to medium wave energy regime during ice formation. The proposed framework will be used to quantify the impact of floe and grease ice material properties, geometrical features including ice floe size, shape, and concentration, as well as wave forcing on the mechanical response of the sea ice cover. The intended model distinguishes between two ice constituents, ice floes and grease ice. Atmospheric and oceanic conditions in the Antarctic MIZ are applied to the model, consisting of wave-dependent wind forcing and current-dependent wave loading. In the formulation, the current-dependent wave loading is implemented as an imposed harmonic propagating wave [72].

[2] https://www.openfoam.com/

In this study, the main research question is defined as follows:

> *How do oceanic and atmospheric conditions affect the dynamics of sea ice in the Antarctic MIZ on a small scale?*

Several objectives are set, to elaborate on the main research question and to assist in finding an answer:

1. The two-dimensional ocean's sea ice cover is considered to consist of two main constituents or ice types, namely, ice floes and grease ice, separately in a continuum fashion. Both materials are described by their own specific sea ice rheology, each with different material characteristics, due to their inherently different material behaviour. Ice floes are governed by solid mechanics, whereas grease ice by fluid dynamics. Therefore, the first objective is the implementation of both material laws, including the analyses of ice floe interaction with the corresponding interstitial grease ice.
2. The second objective is to implement more realistic atmospheric and oceanic conditions, taking into account that these external forces are dependent on each other.
3. The third objective is the implementation of realistic sea ice compositions, particularly focusing on ice floe shape and sea ice concentration. Corresponding in situ images, recorded by stereo cameras of the sea ice cover in the Antarctic MIZ [3], will be used for calibration and verification purposes of the small-scale model.

This project intends to demonstrate the suitability of the proposed computational framework and its algorithms to address the collisional dynamics of free-floating ice floes, in a detailed fashion, on a smaller scale. The small-scale model focuses on the interrelation between floe size, grease ice viscosity and wave forcing.

The newly-developed small-scale model contributes by resolving the lack of data of atmosphere-ocean physical processes on a smaller scale [188]. In future, the model could be linked to the larger-scale, to provide insights into parameter values used for global climate models.

1.4 Scope and limitations

Several general assumptions are applied to the small-scale model to limit the work and keep the scope of this project manageable. The assumptions are listed as follows:

1. The model will be exclusively focused on the dynamics and interactions of ice floes and grease ice. Thermodynamics does not fall within the scope of this project, as only small time periods of less than a minute are considered. As a result, the solver is isothermal, which means that the temperature is assumed constant and no energy equation is solved.
2. In reality, ice floes are a heterogeneous and anisotropic material [61, 115]. In this project, solid ice will, however, be treated as homogeneous and isotropic.
3. Due to the presence of grease ice, a highly viscous fluid, ice floe collisions taking place in the field are less energetic [66], therefore interactions between ice floes are not described by short violent collisions but rather continuous churning contact varying in intensity. Ice floe collisions barely exceed a maximum

compression strength of 2MPa [161, 168], therefore failure and fracture of sea ice are not considered to be part of the scope of this work. Additionally, ice floe cohesion and ridging are not considered in the ice floe collision dynamics, as it is seldom observed in the field, and unlikely to occur for the intended time scales.

4. The infinitesimal small strain theory is applied in this study [81, 83], as ice floe displacements are small compared to their dimensions. The geometry and material characteristics, such as stiffness and density, are spatially not affected by its deformation.

5. Wave forcing, applied as external forcing, is imposed on the sea ice domain, which means that wave scattering and dissipation effects are not part of the scope of work. The weight of the water affecting the water pressure gradient is included as an external force, however, the gravitational effect of sea ice on the velocity and acceleration in z-direction is not included in the two-dimensional model.

1.5 Layout of document

The thesis is structured as follows: in Chap. 2 a literature study is conducted, which elaborates on different sea ice rheologies used in existing sea ice models. Additionally, different modelling methods are described, and an overview of atmospheric and oceanic forcing is given. Chap. 3 describes the set of equations in the small-scale model and explains the most important aspects in the model. Chap. 4 explains in detail the implementation of the small-scale model in OpenFOAM. The model parameterisation and a plausibility study is presented in Chap. 5, showing basic examples for the validation and verification of the small-scale model. Subsequently, Chap. 6 discusses model results, focusing on the dynamics of realistic sea ice domains as influenced by ice floe geometry and studying its underlying mechanical behaviour. Chap. 7 studies in situ ice floe motions to demonstrate the applicability of the small-scale model to realistic sea ice layouts. Conclusions can be found in Chap. 8, whereas future work and recommendations are discussed in Chap. 9.

Chapter 2

Literature study

2.1 Introduction

Numerical sea ice modelling plays a key role in understanding the changing polar regions, allowing researchers to predict the dynamic and thermodynamic response of sea ice. In particular, the versatile behaviour of sea ice in the marginal ice zone (MIZ), which is subjected to melting, freezing and mechanical deformation, from solar radiation, wind, wave and ocean current forcing and from interactions with surrounding sea ice. The sea ice dynamics and morphology in the MIZ are characterised by a collection of relatively free-floating pancake ice floes within a mixture of interstitial water and grease ice, which are exposed to wind and wave action [4]. The presence of highly mobile round pancake ice floes, which vary in size, thickness, age and structure, that form in wavy conditions, is therefore a distinctive characteristic of the Antarctic MIZ during sea ice advance in the winter season [124]. Deeper into the Antarctic MIZ, larger pancakes cluster into ice floes, which eventually form a continuous, consolidated sea ice cover of almost a meter thick [7]. When consolidated sea ice breaks up during sea ice retreat in the spring season [181], it forms floes of various diameters, where the size is often comparable to the wavelengths typical for the Southern Ocean (SO), ranging from $100-200$m [19, 45].

Sea ice dynamics is generally modelled in horizontal directions, consisting of processes such as ice drift and deformation, whereas thermodynamics includes the one-dimensional growth and melt of sea ice in the vertical direction [23]. One of the most challenging aspects of modelling sea ice dynamics is capturing the behaviour across a wide range of spatial scales. Large-scale models, typically applied for global climate purposes, describe sea ice dynamics and thermodynamics on large temporal and spatial scales. They have proven their contribution to the understanding of sea ice behaviour on large-scale ($10-100\text{km}^2$), but at small scales ($< 10\text{km}^2$) the dynamics become highly discontinuous, resulting from interactions between many individual floes and discrete fracture events.

This chapter is structured as follows: Sec. 2.2 elaborates on large-scale continuum models, focusing on their sea ice rheology, and small-scale models. The latter, both developed in a continuum approach and an alternative discrete element approach, are discussed for comparison. Sec. 2.3 discusses pioneering studies related to wind, wave and ocean current forcing, as well as the interrelationship between the atmosphere and the ocean.

2.2 Sea ice rheology

Rheology is a branch of physics, which can be defined as the study of deformation and flow of a complex non-Newtonian liquid or gas. Solids, subjected to an applied force, can also be described by a rheology, behaving plastically rather than elastically [129]. A rheology, also known as a material law, or constitutive equation, describes the relationship between two physical quantities with material-dependent parameters. In sea ice dynamical models, a rheology describes the relationship between stress and strain rate, representing the internal ice forces and the corresponding deformation of sea ice [24, 50]. These quantities are affected by external forces and interactions of sea ice, such as interacting ice floes or ice floe-grease ice interactions.

This section describes five large-scale continuum sea ice models in the Eulerian framework, focusing on their sea ice rheology. These five models are selected as they have shown their contribution to the sea ice modelling community, each of them representing a distinctive sea ice rheology. Their objectives, pros and cons are discussed.

Prior to reviewing the types of rheology, it is crucial to understand the difference between plasticity and inelastic material laws. The latter, usually referred to as viscoplastic, is rate-dependent, which means that the material properties are time-dependent, whereas plasticity is rate-independent [33].

Coon et al. [34] developed a sea ice model, which is described by an elastic-plastic (EP) rheology. Their objective was to develop a model which includes sea ice dynamics and thermodynamics on a scale of 100 kilometres with temporal resolutions larger than one day. The drawback of this model is that no smaller time periods and spatial scales can be considered. The model by Hibler III [69], using a viscous-plastic (VP) rheology, has been recognised as the standard dynamic-thermodynamic sea ice model. The main objective of this work was to understand the role of sea ice during seasonal changes, by studying thermodynamics and the influence of ice dynamics on the distribution of ice thickness. Shortcomings in the model are the idealised treatments of the thermodynamics, the coupling of sea ice with the ocean and the distribution equations of the ice thickness [69].

Dansereau et al. [38], Rampal et al. [150] and Weiss et al. [209] believe that the VP rheology with its physical assumptions, is inconsistent with observations of the mechanical behaviour of sea ice. Accordingly, Dansereau et al. [38] presented the anisotropic Maxwell elasto-brittle (MEB) model, which considers observed sea ice behaviour, such as the anisotropic distribution of sea ice ridges and leads and the strength of sea ice in tension. This model considers both the elastic and viscous properties of sea ice. Their objective was to develop a continuum sea ice model including both damaging and healing mechanisms of sea ice. However, this model does not allow solving the elastic and permanent deformations separately, resulting in a sea-ice velocity that does not distinguish between reversible and irreversible deformations [38].

A model developed by Hunke and Dukowicz [81] describes an elastic-viscous-plastic (EVP) rheology, which improves the numerical behaviour of the previously developed VP model by Hibler III [69]. The elastic part does not alter the physical nature of the VP formulation. It is only added to improve numerical stability. The EVP model provides more accurate results for shorter time scales associated with physical forcing, reproduces VP model behaviour on longer time scales, and is computationally more efficient.

The discrete element method (DEM) is widely used to model granular media and discontinuous materials

in a variety of contexts [37]. This method treats sea ice as a collection of individual rigid bodies, or particles, [37, 64, 75, 73] that can interact independently, and therefore can capture the discontinuities in ice that are common at small scales. The collisional rheology by Shen et al. [164] is obtained by equating collisional energy losses to the deformational energy of colliding disk-shaped ice floes. This type of rheology stands out by providing quantification of the velocity fluctuation, however, it has rarely been used in sea ice modelling due to the applied unrealistic assumptions regarding collisional effects [65].

Nevertheless, DEM has been demonstrated as a promising tool for modelling sea ice dynamics [23]. The Lagrangian description used in DEM, to describe the interaction between numerous particles is however computationally expensive. For this reason, most global climate models resort to describing sea ice behaviour using an Eulerian frame of reference [37, 196]. To date, most DEM applications to modelling sea ice, resort to using simplified ice floe geometries, such as simple circular floes, and is therefore unable to account for the interaction between a number of irregularly shaped floes [65].

2.2.1 Large-scale numerical modelling

2.2.1.1 Elastic-plastic rheology

AIDJEX (Arctic Ice Dynamics Joint Experiment) two-dimensional sea ice model developed by Coon et al. [34] considers different types of sea ice, distinguished only by their thickness. Coon et al. [34], Rothrock [156] and Thorndike et al. [192] use an elastic-plastic (EP) constitutive equation to describe the sea-ice behaviour. The main variables in the model are the sea ice velocity vector, the stress tensor, and the sea ice thickness distribution function. The latter can be defined as the fractional area, consisting of ice with a sea ice thickness smaller than a given threshold.

The EP sea ice material law consists of a recoverable elastic part below the yield strength, in which energy does not dissipate during deformation. The energy is stored, which is completely released after unloading. This results in a full recovery of the deformed material, only if no plastic contribution is considered. The unrecoverable plastic part allows energy dissipation, which results in a permanently deformed material. Coon et al. [34] believe that an EP model can represent the mechanical behaviour of consolidated sea ice on a larger scale. In their model, the plastic behaviour of sea ice and the ice thickness distribution are related. However, on the condition that energy dissipation results in an increase of potential energy of sea ice, due to plastic deformation.

The plastic part in the EP rheology is based on sea ice deformation observations on a small scale, such as fractured sea ice and pressure ridges, which shows a characteristic of permanent deformation. There are two main reasons that allow for the justification of using a plastic analysis for sea ice. Firstly, a plastic material has successfully been used to simulate and describe granular materials, where sea ice and granular materials share similar visual characteristics. Secondly, Parmerter and Coon [139] and Ukita and Moritz [197] concluded, that energy during ridge formation, results in rate-independent work when a pressure ridge is formed.

The elastic part in the sea ice rheology by Coon [34] is more formally added to solve the system of equations. Nevertheless, individual ice floes show, to a certain degree, elastic behaviour under compression. Consolidated sea ice, consisting of an assemblage of thick ice floes with hardly any thin ice, has a high yield stress. As a

result, subcritical stress applied to the ice floes is likely to give rise to only elastic deformations, which are small in comparison to plastic deformations. Sub-critical stress values can still be significant, which means that stress assessment is required to determine the state of stress.

The yield function in two dimensional space used by Coon et al. [34] is illustrated by a curve in Fig. 2.1. The yield curve for isotropic materials can be written in terms of σ_1 and σ_2, representing the principal stresses. The orientation of the principal axes of stress does not affect the response. For isotropic materials, the yield curve must be symmetric in σ_{II}, representing the second stress invariant [34, 156]. Additionally, the plastic strain rate is projected normal to the yield curve and has an unknown magnitude. The principal axes of both stress and strain rate are aligned.

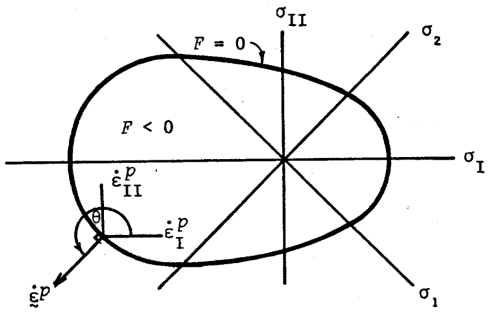

Figure 2.1: EP yield curve reproduced from Coon et al. [34] and Rothrock [156], where σ_1 and σ_2 denote the principal stresses, and σ_I and σ_{II} the stress invariants.

The infinitesimal small strain theory can be applied when material displacements are assumed small compared to their dimensions. As a result, the total strain increment can be additively decomposed into the elastic component and the plastic component of the strain increment. The elastic strain is related to stress by an elastic law, such as Hooke's law. Coon et al. [34] assumed that sea ice in its elastic behaviour is isotropic and linear. The plastic strain increment is found by using both the yield curve and the associated flow rule. When the stress state does not lie on the yield curve, the plastic strain increment equals zero. For plastic flow the total strain increment consists of both an elastic and plastic component, however, Coon et al. [34] assumed that the elastic component is negligible, which implies an ideal plastic.

2.2.1.2 Viscous-plastic rheology

The viscous-plastic (VP) model introduced by Hibler III [69], is based on the model previously developed by Coon et al. [34]. In comparison to the AIDJEX approach, the VP model is less detailed, however, accommodates larger time increments with more straightforward boundary conditions (BCs). Hibler III's objective was to contribute to climate modelling with long-term simulations. Therefore, Hibler III [69] replaced the elastic component in the constitutive equation by Coon et al. [34] with a viscous component, which allows modelling of non-linear plastic flow without limitations regarding time increments and eliminates the need to consider the elastic strain after unloading [50]. In addition to the momentum equation, two transport equations control the sea ice dynamics in Hibler III's model. The momentum equation links internal and external forces, the latter including the applied wind stress, ocean current stress, Coriolis force, caused by the Earth's rotation, and sea surface dynamic height, which includes the large-scale ocean circulation. Mass conservation is ensured by replacing the thickness distribution equation with the two transport equations, which describe the evolution of sea ice thickness and concentration accounting for deformation and growth-related effects.

The sea ice rheology by Hibler III [69] describes the sea ice stress as related to the sea ice strain rate and an internal sea ice strength parameter. The latter governs rate-independent compressibility behaviour and depends on both transport equations. Two types of sea ice are distinguished: thick and thin ice, including open water, which are intrinsically described by the sea ice concentration variable, where 100% ice concentration is often referred to as consolidated sea ice. In the case of open water, ice thickness equals zero, which leads to an ill-posed momentum equation, hence Hibler III [69] and Hutchings [82] introduced a lower limit on the sea ice thickness of 0.5m. The ice stress, modelled as a VP material law, describes the homogeneous and isotropic behaviour of sea ice. The VP rheology obeys the associated flow rule and the elliptical yield criterion [83, 82], shown in Fig. 2.2.

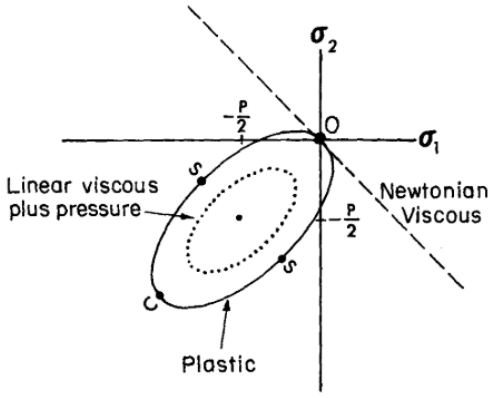

Figure 2.2: VP yield curve reproduced from Hibler III [69], where σ_1 and σ_2 denote the principal stresses and P the ice strength in compression.

The plastic part of the constitutive law is derived from the elliptical yield curve and the associated flow rule. The yield curve represents all stress states in which the limit of linear viscous behaviour in ice is reached. Once the limit is reached, ice starts behaving plastically. The yield curve and associated plastic flow rule are used to obtain the stress and strain rate iteratively. The ice strength parameter depends on the transport equations governing sea ice thickness and concentration, and two empirical constants, related to the sea ice strength and sea ice concentration.

The viscous part of the constitutive law is parameterised by two material-dependent viscosity parameters. These viscosities are strain rate dependent, and are coupled together. As strain rates approach zero, the viscosity tends to infinity. To avoid this, Hibler III [69] suggested imposing a lower limit on the effective deformation rate, $\Delta_{min} = 2 \times 10^{-9}\mathrm{s}^{-1}$. This marks a clear difference to the EP material law regarding the treatment of stationary sea ice. The EP formulation can preserve high-stress values without relative motion, whereas motionless sea ice in the VP framework slowly creeps. However, by increasing the viscosity in the VP model, the plastic strain rate can become insignificant. As a result, the difference between plastic and total strain rate is negligible [50].

The large viscosity values require implicit numerical methods, which are typically used to solve the system without time step restrictions, such as iterative over-relaxation and line relaxation methods [81]. These methods, however, suffer in several respects. Firstly, poor convergence characteristics with an increase in mesh resolution. Secondly, they are not well suited to parallelizing the solution procedure. Lastly, the simulation time of implicit numerical methods is time consuming. Additionally, the VP model by Hibler III [69] is inaccurate in computing transient behaviour, which can be defined as the response of a system to any change

from steady-state conditions. The VP formulation typically allows time steps in the order of a day, which results in a poor time response due to the semi-implicit time discretisation schemes used for the treatment of the VP rheology. For illustration, assuming daily time steps, the VP model works sufficiently accurate only for a slowly varying wind forcing on the order of weeks. The VP framework results in correct transient behaviour when time steps are chosen small enough, in the order of minutes for forcing of a daily period.

Most existing large-scale sea ice models are formulated on the VP approach by Hibler III [69], representing the mean global sea ice drift. Underlying physical assumptions, made in the VP formulation, are believed to be inconsistent with sea ice observations, namely the order of magnitude of strain rates, the anisotropic distribution of sea ice ridges and leads, the relationship between stress and strain rate and the strength of sea ice in tension are examples of such observations. Several more recent studies believe that the VP rheology requires re-evaluation [38, 150, 209].

2.2.1.3 Elastic-viscous-plastic rheology

The viscosity of sea ice in the VP model by Hibler III [69] endures a singularity, requiring implicit numerical methods, which suffer from numerical difficulties [81]. Therefore, Hunke and Dukowicz [81] introduced two different methods, to solve these numerical issues.

Firstly, a more efficient implicit numerical method is presented, which solves the equations in the VP model by making use of the preconditioned conjugate gradient method. The convergence rate of conjugate gradient methods is linear with the resolution, and therefore successfully used for computations in parallel. Secondly, Hunke and Dukowicz [81] suggested to modify the VP model, by adding an elastic component to the VP rheology. This modification results in a significant increase in numerical efficiency, is more accurate for transients, and shows original VP behaviour for long time-scales. At long time scales, the elastic component does not alter the physical nature of the viscous-plastic rheology, but is only added to improve numerical stability. This modification leads to a fully explicit numerical scheme, utilizing an elastic mechanism in regions of rigid ice to significantly increase the computational efficiency of the VP numerical model, using an acceptably long time step. The inaccurate computation of transient behaviour in the VP model by Hibler III [69] is resolved by Hunke and Dukowicz [81] in their EVP formulation, also when larger time steps are used. As a result, more accurate sea ice behaviour can be produced. The EVP rheology is equal to the VP formulation when Young's modulus goes to infinity, whereas the elastic equation is recovered [81] when the viscosity approaches infinity. In other words, the elastic component controls the behaviour in case the viscosity goes to infinity. Therefore, the EVP formulation serves as a regularisation of the VP rheology.

2.2.1.4 Viscous-elastic rheology

Fundamental assumptions in the VP model by Hibler III [69], are perceived to be conflicting with finer-scale sea ice observations [38, 150, 209], which has led to the development of the Maxwell-elasto-brittle (MEB) model by Dansereau et al. [38].

Dansereau et al. [38] developed a continuum model with a MEB rheology, derived from the existing elasto-brittle (EB) framework by Girard et al. [56] and the well-known Maxwell viscous-elastic model. Their objective was to consider a linear-elastic material law for small deformations with brittle fractures and a viscous-like

relaxation term for larger permanent post-fracture deformations [137], including a damage and healing mechanism.

The MEB rheology differs from the Maxwell model in how viscosity is treated. MEB treats it as an apparent viscosity that evolves, depending on the degree of damage and sea ice concentration, whereas in the Maxwell model viscosity describes a creep-response. The visco-elasticity of sea ice and the damage degree are coupled such that the viscosity is infinitely large for regions of undamaged sea ice with elastic deformations, whereas the elastic behaviour disappears for extremely damaged regions. When considering damaged ice, the viscous behaviour takes over, resulting in permanent deformations. Dansereau et al. [38] included a healing mechanism, which compensates for damaging over larger time periods. Both elastic and plastic deformations are solved concurrently, which results in naturally defined sea ice drift velocities.

The MEB rheology relates the stress and strain rate via Young's modulus and the apparent viscosity. In contrast to the Maxwell model, the MEB rheology considers these parameters as coupled mechanical parameters, which change with the gradually developing non-dimensional degree of damage over space and time [38]. Damage refers to evolving leads in sea ice, which arise from internal stress values exceeding the mechanical resistance of sea ice, leading to sea ice weakening. On the other hand, healing indicates the strengthening of only the damaged sea ice cover by refreezing of leads. This implies that healing stops when the mechanical parameters reached their undamaged values. The formulation of the degree of damage contains both the damaging and healing mechanisms.

In contrast to existing sea ice models, such as Coon et al. [34] and Hibler III [69], the MEB rheology makes use of the Mohr-Coulomb theory with a non-associated plastic flow rule in combination with the tensile stress criteria for the damage criterion. In case the critical stress is locally exceeded, Young's modulus decreases, causing strain softening. Spatially long-range interactions within an elastic material, which allow for small, local perturbations, in combination with strain softening, lead to redistribution of stress. This instigates damage in adjacent elements, resulting in damage propagation.

Olason et al. [137] more recently developed a one-dimensional brittle Bingham-Maxwell (BBM) model, which builds on the MEB framework presented above. The BBM model addresses two limitations encountered in the the MEB model by Dansereau et al. [38]. Firstly, the MEB model requires a high computational cost. Therefore, the momentum equation in the BBM model is solved by making use of an explicit scheme, which is in the spirit of Hunke and Dukowicz [81]. Note, however, in contrast to the EVP rheology by Hunke and Dukowicz [81], the elasticity component in the BBM rheology is implemented to represent the physical nature of elasticity. Secondly, ice piles up over time to an unrealistically thick layer of sea ice. This is due to inadequate resistance to compression for long-term simulations, when performing simulations for time scales longer than a year. Therefore, the BBM model considers an additional term that limits the ice thickness. Olason et al. [137] introduced a friction element, connected in parallel to a dash-pot, which are both connected to a spring in series. The dash-pot and spring still obey the viscous-elastic material law explained by Dansereau et al. [38], however, the friction element provides resistance to compression. A new parameter was further introduced, which represents the maximum pressure sea ice can resist before the ice starts ridging. In other words, there is a threshold between elastic and permanent deformations, which limits the thickness of ice piling up over time.

2.2.2 Small-scale numerical modelling

The continuum models, explained in the previous sections, are large-scale models making use of averaged sea ice properties, such as ice concentration and thickness. A single material, pack ice, is considered, in a smeared model approach. This implies a large sea ice area with heterogeneous characteristics, being modelled as one homogeneous material. The rheologies, however, differ in their relation, which link the internal ice stress with the strain rate.

Several parametrisations are developed to enhance continuum sea ice models in their performance, when granular effects significantly affect the behaviour of sea ice on large-scales. One group of parametrisations is associated with the collisional rheology, which is relevant especially closer to the edge in the MIZ. The stress response in fragmented sea ice is described by inelastic ice floe collisions. Ice floes show bumping and interlocking behaviour, allowing for a sea ice rheology that distinctively differs from the rheologies proposed by Coon [33], Dansereau et al. [38], Hibler III [69] and Hunke and Dukowicz [81].

A fundamentally different approach, focusing on ice floe collisions, was first studied by Solomon [174], who implemented a one-dimensional framework modelling the transfer of momentum due to the relative velocity of a pair of colliding ice floes. The influence of ice floe collisions on the sea ice rheology was discussed. Bratchie [26] also discussed the influence of ice floe collisions on the sea ice rheology, considering a two-dimensional domain with idealised uniformly-shaped disks, in which the deformation field describes the motion of the idealised disks. Bratchie [26] assumed a plastic rheology, based on the hypothesis that ice ridges are formed from ice floe collisions, resulting in energy dissipation from rate-independent ridging deformation.

According to Shen et al. [164], the theories by Bratchie [26] and Solomon [174] require a better understanding regarding the transfer of momentum, including stresses, which play a part in ice floe collisions. Velocity fluctuations caused by collisions were not considered in the models by Bratchie [26] and Solomon [174]. Shen et al. [164] derived a collisional rheology considering rigid body collisions between ice floes in a two-dimensional, fragmented, homogeneous sea ice area that slowly varies in time. The control volume consists of a cluster of idealised uniformly-shaped disks, and can be decomposed in a horizontal and vertical control surface, as illustrated in Fig. 2.3.

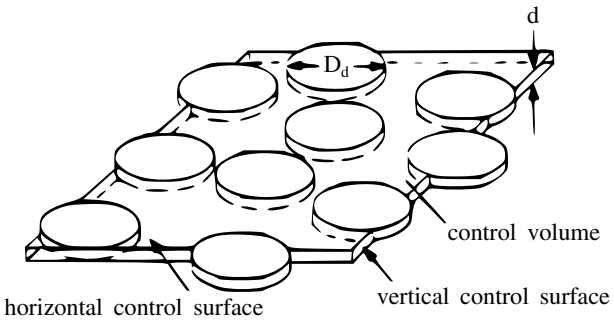

Figure 2.3: A control volume, reproduced from Shen et al. [164], with a cluster of idealised uniformly-shaped disks with diameter, D_d, and thickness d.

The translational motion of disks is represented by a mean component and a fluctuation component, derived from an ensemble of samples at a given time and location in the sea ice domain [164]. The method makes use of two general velocity-related assumptions. Firstly, a distribution function with prescribed floe velocity

fluctuations is assumed. Secondly, velocity magnitude fluctuation values are significantly larger than the mean relative velocity between adjacent ice floes.

The collisional rheology is found by relating losses of the collisional energy to the deformational energy. More specifically, the rate of work done by internal stresses in deformation, is equivalent to the rate of energy that is dissipated [164]. Existing plastic rheologies also use this approach. Note, however, that the collisional rheology by Shen et al. [164] distinctively differs from existing plastic rheologies as both the internal stresses and dissipation of energy are explicitly determined by rigid body collisions between ice floes. Both the impact force and the dissipation of energy are formulated in terms of the velocity of ice floe collisions, which implies that the collisional rheology cannot be classified as a plastic rheology.

Shen et al. [164] neglects the fluid in between ice floes, to focus on the main characteristics of the collisional rheology in the two-dimensional sea ice model. Two colliding ice floes with a relative velocity to each other, transfer linear momentum with energy dissipation. Stress acting on the vertical control surface, representing the vertical direction of the control volume, creates work which contributes to an increase in the internal energy inside the control volume. The internal energy is described by disk fluctuation, of which the fluctuation motion is comparable to the thermal motion of gas molecules [164].

Existing collisional rheology models [49, 105, 111, 162] have contributed to the understanding of sea ice dynamics in the MIZ, however, the collisional rheology has rarely been used in sea ice modelling, due to the rather unrealistic assumptions and idealised sea ice behaviour, resulting in an underestimation of the contribution of collisional stress to the total stress state [65].

Bai et al. [14] believe that computational fluid dynamics (CFD) models on the kinematics of ice floes in waves are limited. Accordingly, Bai et al. introduced a numerical model, which describes the kinematic response of a small rigid floe affected by waves. Their aim was to reproduce a previously conducted physical experiment [118, 119], which could not be properly calibrated, due to limited data available in literature. Both the potential flow model HydroStar, which disregards fluid viscosity, and the viscous flow CFD model in OpenFOAM are used to analyse the drift velocities for different shapes of ice floes. Their results found in OpenFOAM correspond better to the experimental data, confirming that the influence of viscosity is fundamental in the kinematics of ice floes.

Despite matching results with experiments [14], small rigid ice floes were assumed, limiting the model to dimensions only significantly smaller than the wave length. Therefore, Huang et al. [80] developed a numerical model considering larger ice floes, which require a fluid-structure interaction (FSI) approach that fully accounts for ice deformation and the hydro-elastic interaction between waves and ice. The fluid domain is described by the Navier-Stokes equations, whereas the solid domain is governed by the St. Venant Kirchhoff solid model. Additionally, a coupling scheme accounts for the interaction between the fluid and the solid. The model by Huang et al. [80] is validated using existing experiments, and showed satisfactory results regarding the prediction of overwash and the potential to include in wave-ice related studies.

The CFD models developed by Bai et al. [14] and Huang et al. [80] are recent examples of simulations, which describe the interaction between a single ice floe and waves. Additional relevant continuum models, considering wave-ice interaction, are explained in Sec. 2.3.2, mainly focusing on wave dissipation effects. All small-scale continuum models, mentioned in this chapter, do not explicitly account for a collection of inter-

acting floes in a viscous fluid. To the best of our knowledge, no detailed continuum model on small scale has considered this before.

According to Damsgaard et al. [37], continuum models are generally not well suited to simulate the behaviour of sea ice in the MIZ, due to strong changes in mechanical properties. Numerical models, that can simulate the dynamics of sea ice on a smaller scale and still produce the realistic behaviour of sea ice, are required. While Damsgaard et al. [37] have stated that a continuum model cannot adequately describe the dynamics of sea ice in a detailed fashion, the aim of the current study is to demonstrate that such a continuum model is possible, when using modern CFD techniques.

The discrete element method (DEM) is an established method, which models granular and discontinuous materials in many contexts [37]. This method models sea ice as a collection of individual rigid bodies, or particles [37, 64, 73, 75] that interact with each other independently, and captures discontinuities in sea ice on a small-scale. DEM is applied on an ice floe scale [78], where particles are represented by an assemblage of ice floes [106], generally representing one ice floe per particle.

One of the first sea ice models using the DEM approach, was developed by Hopkins and Hibler [74], showing a suitable method, modelling individual ice floe interactions. In the years that followed many sea ice models with the DEM approach were developed, using polygonal-shaped floes [77], or disk-shaped floes [62], to study the interaction of ice floes at the floe level.

A contact law, which describes the behaviour of particles in a DEM model, is used to compute the translational and rotational forces acting in between particles. Hopkins and Thorndike [77] introduced the representation of an assembly of floes, which are connected via inter-particle bonds. Alternatively, Hertzian contact models can be used. The latter refers to a classical theory of contact mechanics to calculate inter-particle forces [89]. Herman [65] considered disk-shaped ice floes, which move within a two-dimensional space, represented as individual grains and as an assemblage of bonded grains. Two independent mechanisms of interactions between neighbouring particles are described. In the first mechanism, particles only interact when they are in direct contact with each other. In the second, particles are connected via a semi-elastic bond, which can form when the neighbouring disks freeze together. In other words, these bonds represent new, usually thinner ice filling cracks, leads and other open spaces between thicker ice sheets. Both mechanisms described above transmit forces, however, bonds can also transfer momentum. Additionally, bonds can resist a certain tensile strength [65].

Rabatel et al. [148] proposed a DEM model focusing on collisions of individual ice floes. They were the only one in the community of sea ice modelling who modelled ice floes of arbitrary size and shape, derived from satellite images from the Arctic. Ice classified as 'new ice', which refers to recently frozen seawater that is not solid ice yet such as grease ice, was not considered in their model.

Blockley et al. [23] believe that DEM is promising for sea ice modelling, however, this type of Lagrangian approach suffers numerically, due to high computational costs. Hence, global climate models are still based on the Eulerian framework [37, 196]. Most DEM sea ice models apply simplified modelling equations or ice floe geometries, resulting in less realistic model behaviour [65]. Fundamental physical processes affecting floe evolution, such as floe splitting, pressure ridging or floe aggregation, cannot yet be represented in a DEM framework.

In future, a combination of modelling methods using different frameworks, is one of the solutions mentioned by Blockley et al. [23] to solve challenges the sea ice modelling community is currently facing related to multi-scale physics. Small-scale modelling and upscaling techniques will help parametrising large-scale models, to predict sea ice behaviour on both a regional and global scale.

2.3 Atmospheric and oceanic forcing

Sea ice dynamics in the Antarctic MIZ, which includes the direction and strength of ice movement, is governed by both the oceanic and atmospheric conditions, where atmosphere-ocean-sea ice interactions are most intense [4, 182]. Wind forcing is the main driver of sea ice drift in both the Arctic and Antarctic, counterbalanced by the internal stress of sea ice and the ice-ocean drag [103]. The Coriolis force acts perpendicular to the motion of sea ice, and is significantly smaller than the three major forces. Apart from the wind loading, waves potentially feature in the formation and growth of pancake ice floes, despite limited in situ data available for verification purposes of existing theoretical models [128, 185]. Ocean waves that travel through a sea ice cover, either consisting of individual ice floes typically found closer to the ice edge, or a continuous sheet deeper into the MIZ, decrease in amplitude at a rate that depends on the sea ice characteristics due to a combination of wave scattering and wave dissipation.

In global climate studies, the seasonal changes in the polar regions, in particular the rapid retreat of sea ice from winter to summer, including its driving forces, are topics that still require attention. Especially, the wind velocity close to the surface related to sea ice extent is ambiguous. Firstly, due to very limited, irregularly distributed wind velocity observations in the Arctic and Antarctic. Executing experiments and observations in the polar regions is challenging due to extreme weather conditions. Secondly, because of the unreliability regarding the dependency of wind simulations on subjective parametrisations of boundary layer stratification [6]. Therefore, computational modelling serves as a potential alternative regarding the assimilation of data and weather forecasting [46].

2.3.1 Wind forcing

The interaction between the atmospheric wind forcing and sea ice has mainly been studied on a large-scale [69, 120, 121], where the influence of the waves was not considered in the majority of the models, due to insufficient understanding [13]. Therefore, existing wind-wave coupling models only focus on the direct interaction between the wind forcing and ocean [72, 125, 147].

The work developed by Miles [125] is one of the well-known inviscid wind-wave coupling theories, used in leading wave-prediction models [72]. The interaction, with a resonant character, between the near-surface wind and the development of water waves for deep water in the atmospheric boundary layer (ABL) [215], is described by Miles [125] by a logarithmic wind profile [8, 126, 213]. According to Miles [125] the maximum air pressure is found on the windward side of the wave crest resulting in a pushing wind, moving the water surface downwards. The minimum air pressure is found at the leeward side of the wave crest resulting in a wind, which pulls the water surface up. As a result, energy transfers to the waves due to out-of-phase coupling between pressure and sea surface motion [72]. In the theory by Miles [125], both the gas and liquid phase

are assumed incompressible. Turbulent and viscosity effects are considered insignificant close to the ocean surface [28, 29], hence are excluded [79, 126].

Phillips [147] postulated that convection of pressure fluctuations within turbulent air results in wave development, starting from an initially smooth water surface, as opposed to the theory by Miles [125], which considered a prescribed wave. Phillips [147] suggested a stochastic model, which states that the variance in the water surface elevations grows linearly over time. Both wind-generation models are pioneering theories, which have been frequently used by many researchers [107].

The marine ABL over ocean waves can be subdivided into two layers. The surface layer and a mixed layer. The surface layer, which is approximately $1-100$m high, is important regarding the interaction with the ocean waves and is further subdivided (upwards from the water surface) into the viscous sub-layer, wave boundary layer, and the inertial sub-layer. The viscous sub-layer, just above the air-sea interface, is a layer with a thickness of just a few millimetres, where viscosity effects play an important role. Due to its insignificant thickness, most models disregard the viscous sub-layer. The wave boundary layer, which is just a few meters high, is in direct contact with the waves. In the inertial sub-layer, which lies above the wave boundary layer, waves and wind exchange most of the mass, moisture, momentum, and heat. Both the wave boundary layer and inertial sub-layer together are $10\% - 20\%$ of the entire marine ABL. The wind stress can be obtained by using a quadratic drag law, which can be applied to models on different spatial scales simulating the ABL [43].

Wind properties associated with an elevation of 10m are generally used in atmospheric models, however, some models provide values that correspond to heights of constant atmospheric pressure and ignore any vertical velocity component. The wind speed at 10m elevation can be written in terms of the friction velocity, which is not a physical velocity that can be measured, but a fictitious velocity instead [12]. The friction velocity, which requires an additional expression to compute, can then be related to the wind shear stresses acting along the water surface [72]. According to Deskos et al. [43] and Wu et al. [215] the wind shear stress can be decomposed into three components, consisting of the viscous, turbulent, and wave-coherent shear stresses. As previously mentioned, the viscous component is only prominent in the viscous sub-layer, which corresponds to the molecular viscosity of air [112]. The viscous shear stress [85] is generally disregarded due to high Reynolds numbers characterising the ABL, whereas the turbulent stress is parametrised by applying the mixing length theory.

When air flows over surface gravity waves, a considerable amount of momentum transfer takes place, resulting in wave generation. Due to the motion of waves at the water surface, a secondary airflow is induced, causing wave-induced stresses [190] which can significantly contribute to the total shear stress at the water surface [86]. Consequently, both the transfer of momentum and the air drag coefficient at 10m elevation rely on the ocean conditions [85]. It can be assumed that the total shear stress does not depend on height in the viscous sub-layer [190], resulting in a layer of constant flux [12, 85] and a constant friction velocity value. For wind-driven waves, the wave-induced stress decreases exponentially away from the ocean surface obeying an exponential wind profile [47, 85, 102]. Most climatological models describe the momentum flux of the wind at the air-water interface by making use of a roughness length parameter, which includes the viscous effects and turbulence at the ocean surface [215]. At a height referring to the roughness length parameter the wind velocity equals zero [85].

Buckley and Veron [28, 29] conducted an experimental study to investigate the detailed airflow above sur-

face waves, considering different wave conditions with wave ages. They were able to obtain high resolution, two-dimensional velocity measurements in the airflow above waves to get an estimate of the critical layer and three velocity components that can be distinguished: the phase-averaged velocities, wave-coherent, and turbulent momentum fluxes in a wave-following coordinate system. Measurements of the airflow were analysed just above the wave surface, using a curvilinear coordinate system. The wind velocity can be decomposed into a mean flow component, which depends on height, and a component considering turbulence with fluctuations [172]. The mean flow can be split again, into a phase-independent mean component, and a wave-coherent component [79]. The exponential velocity profile is used to describe the mean velocity profile [28, 29].

2.3.2 Wave forcing

Among small-scale processes in the Antarctic MIZ, waves play a crucial role in the formation of sea ice [163]. The propagation of waves from open ocean into the MIZ and wave-ice interaction are linked to wave scattering and dissipation through the momentum transfer to ice floes, which mainly depend on sea ice characteristics like ice floe geometry and floe size distribution [194]. Floe size distributions have only recently been introduced in numerical large-scale sea ice dynamics models [19, 152]. In particular, at the ice edge, close to the open ocean, high energy incident waves create complicated sea states resulting in violent ice floe motion and collision patterns [163, 178].

The poorly known wave attenuation and dissipation rates of sea ice in the MIZ depend on several factors, such as the type, thickness, and concentration of sea ice, as well as the wave properties, including wave energy [11]. Kinetic energy in waves is dissipated due to inelastic ice floe collisions, friction, ice floe rafting and ridging, and inelastic bending [130]. However, a better understanding of the more detailed physical processes affecting these rates is required. Unfortunately, due to limited available in-situ wind, wave, and sea ice data, research progress on wave attenuation and dissipation is challenging [127, 187]. Sea ice observations and theoretical studies conducted on wave propagation through a variety of sea ice types have recently become an area of interest [20, 25, 97, 124, 185].

In real life, waves at the ocean surface consist of a large number of random propagating harmonic wave components, travelling across the ocean with different wave directions, amplitudes, periods and phases [72]. The understanding of the behaviour of random (non-linear) waves is based on the concept of a harmonic propagating linear wave, described by the linear wave theory. Additionally, three classical wave theories of non-linear character have been developed. The Stokes wave theory [183] and the stream function theory [40] for steep waves, and the cnoidal wave theory [100] for waves in shallow water.

In the Stokes wave theory and stream function theory, wave corrections are added to the basic harmonic linear wave, to improve the approximation of a realistic propagating wave. In both theories the surface profile and the corresponding velocity components are expressed in terms of a series of harmonics. The difference between the two theories is that the Stokes theory is written in terms of the velocity potential, whereas the two-dimensional stream function is applied to derive the stream function theory [72]. Furthermore, corrections in the Stokes theory are successive, which implies that higher-order wave corrections are derived from previously obtained lower-order ones. The stream function theory obtains wave corrections simultaneously and satisfies the dynamic boundary condition. Both theories cannot be applied to very shallow water. Accordingly, the cnoidal wave theory is derived by Kordeweg and de Vries [100] similarly to the Stokes wave theory and the stream function theory, however, considering wave corrections which account for finite depth effects.

Two approaches can be distinguished to model wave effects in the MIZ. In the first approach, one finite solitary flexible ice floe is accurately modelled, which forms a sea ice cover consisting of a large number of ice floes. The second approach makes use of continuum models, in which a region in the MIZ is described mathematically with assumed a priori rheological properties. Generally, the second approach is preferred, however, it is difficult to find a mathematical framework that includes the physical characteristics of the MIZ accurately. According to Squire [178] this is challenging work which requires further investigation.

Floes in the MIZ are sensitive to the full six degrees of freedom of wave motion. Understanding the kinematic response of one individual ice floe in waves is essential in understanding its effect on shipping and offshore structures [14]. Several models on a smaller scale consider the motion of ice floes on waves and analyse ice floe collisions [64, 65, 66, 76].

One of these models is the microscopic Lagrangian DEM model developed by Herman [66]. The horizontal motion of ice floes in the x-direction is described as a function of various forces acting on individual floes. Collision patterns are analysed, considering different values of the wave properties and sea ice concentration, as well as ice floe size, drag, and restitution coefficients. This model distinguishes itself from existing models, due to its approach to computing the forces acting on the ice floe. Herman [66] used the method of integration to calculate the Froude-Krylov force. Wave diffraction, which is wave disturbance due to the presence of ice floes, is not considered by Herman [66].

The momentum balance equation in the one-dimensional model by Herman [66] represents forces acting on an individual ice floe. These forces consist of i) Froude-Krylov force, which is derived from the pressure gradient due to the undisturbed elevation of the waves. ii) force related to added mass, representing additional inertial forces either due to the imposed acceleration on a fluid by the acceleration of a body moving through the fluid, or due to the acceleration of the fluid relative to the body [99]. iii) drag force, which is the sum of skin drag and form drag. In densely packed ice floe areas, the form drag is generally small compared to skin drag, due to the small spacing between closely packed ice floes. The skin drag can be computed by integration of the local drag stress component over the bottom surface. iv) contact force, acting between ice floes due to collisions is derived from the Hertzian contact model. It represents the sum of all possible contact forces in one dimension acting on an individual ice floe. The contact force depends on the relative velocity in the x-direction between two ice floes, and includes an elastic constant and a viscous-elastic damping coefficient. Both the elastic constant and damping coefficient depend on properties related to elasticity. Rapid collisions are associated with high relative velocities, whereas more gentle collisions are linked to an almost zero relative velocity. Both collision types are included in the contact force in the model by Herman [66].

The simplified one-dimensional model by Herman [66] does not account for physical behaviour like wave scattering and wave dissipation, as well as turbulence effects and eddy generation due to the basal ice roughness. Additionally, aspects that are more essential in a two-dimensional domain, such as friction between ice floes, especially during ice floe collisions, which can result in ice floe rotation. More realistically, wave-ice interaction is modelled considering a two-layer model [207] or a three-layer model [219], as discussed below, starting with the three classical continuum models.

Three classical continuum models include the influence of waves on ice, which are the mass loading model, the thin elastic plate model and the viscous layer model. The aim of these continuum models is to describe the propagation of ocean waves travelling through a region in the MIZ. The mass loading model [146, 210]

emphasizes on the discontinuous nature of sea ice, considering the sea ice layer as an assemblage of non-interacting point masses. The thin-elastic plate model [53] considers sea ice as a homogeneous semi-infinite thin elastic plate, however, is unable to account for wave attenuation. Accordingly, additional mechanisms were introduced to account for energy loss [15, 176, 177, 180, 203]. In the viscous layer model, the ocean surface consists of a suspension of solid particles in water. Weber [208] introduced this model, which was improved by Keller [92], who derived a model which describes the wave dispersion relation, considering a layer of high viscous sea ice on top of a layer of water. Keller's model was developed to support laboratory experiments on grease ice by Newyear and Martin [133, 134]. The model, however, is not suitable for other ice types.

No comprehensive model has yet been developed which is capable of describing propagating gravity waves through all types of sea ice cover [207]. The mass loading model for example, produced poor results regarding the wave dispersion relationship when compared against laboratory experiments for high frequency waves in grease ice [133]. The viscous layer model, on the other hand, provided wave attenuation and dispersion results which corresponded well to laboratory results of Newyear and Martin [134]. Additionally, results from the viscous layer model were consistent with observations of a pancake ice field in the SO [204]. The thin-elastic plate model was developed to describe a continuous ice sheet, and more suited to studies of deep into the MIZ. Field observations from Liu et al. [108] in a region of consolidated sea ice correspond well with results obtained from the thin-elastic plate model.

Wang and Shen [207] developed a two-layer visco-elastic model which combines the three classical continuum models, and describes propagating gravity waves through an ice cover consisting of various ice types. The model consists of two layers of finite thickness, a homogeneous visco-elastic fluid layer on top of a layer of inviscid water. The viscous part in the first layer represents either frazil ice or small ice floes smaller than the wave length, whereas the elastic part represents larger ice floes equivalent to the wave length. Splitting of a wave into a large number of wave modes was observed when propagating through a sea ice surface, however, Wang and Shen [207] realised that only the dominant wave mode matters. Their model has been used as a tool for future wave-ice modellers, to parameterise for different ice types in the dynamic polar regions.

A three-layer model by Zhao and Shen [219] builds on the model of Wang and Shen [207], which consists of a visco-elastic ice layer, an upper ocean layer with eddy viscosity, and a lower ocean layer with inviscid water. The three-layer formulation by Zhao and Shen [219] accounts for energy dissipation effects due to the ice layer and the underlying boundary layer. The elastic part in the model is represented by undamaged ice floes or ice sheets. The viscous part includes a variety of mechanisms, such as inelastic bending of ice sheets, deformation of frazil ice, and ice floe collisions. All these processes result in wave dissipation, which are parametrised into an equivalent viscosity. The model results produced by Zhao and Shen [219] are similar to results previously found in models, such as the three classical continuum models, and the visco-elastic model by Wang and Shen [207], but obtained under more simplified conditions. Wave modelers do not need to choose between boundary layer damping and visco-elastic ice model, as it is all accounted for in the three-layer model. The model parameters still require calibration and verification, based on data from in situ field or the laboratory observations.

2.3.3 Ocean current forcing

The ice-ocean current stress can be calculated using a quadratic drag law, which depends on the relative velocity between the ocean current and sea ice. An alternative to the quadratic drag law is Stokes' law, also

known as the linear drag law, which is derived and suitable for spherical objects slowly moving through a viscous fluid without turbulence effects [104, 184].

Ocean waves are affected by an underlying ocean current velocity [30]. The direction of wave propagation, the wave length, and the wave frequency are wave parameters that mainly change close to the ocean surface [91, 166]. For this reason, the resultant flow of both the ocean current and wave forcing is dependent on the ocean current variation in both space and time, the wave properties, and the relative direction between the propagating wave and the ocean current. Two different types of currents can be distinguished: favourable and adverse currents. Favourable currents move in the same direction as the waves, whereas adverse currents move against the waves [166].

The ice-ocean boundary layer consists of a logarithmic boundary layer and an Ekman layer, representing two different ocean current profiles below the sea ice cover. The logarithmic boundary layer, with depth-independent stress, is a few meters deep, whereas the Ekman layer is one order of magnitude deeper and is affected by the rotation of the Earth [32].

Kim et al. [95] assumed that the velocity of the ocean current is insignificant in comparison to the drift of sea ice. Moreover, in-situ ocean current data below the sea ice cover in the MIZ is currently not available yet, as these are seldom observed. Therefore, several recent models, such as Alberello et al. [4] and Biddle and Swart [21] model free-drifting sea ice, where the ocean current velocity is assumed zero. In the case of a current velocity equal to zero, both the sea ice velocity and ocean current stress are in proportion to one another, but in opposite directions, resulting in damping [4].

2.4 Conclusion

Global climate models have significantly improved our knowledge regarding the polar regions, the majority of which is derived from data obtained in the Arctic. Due to inadequate observations and limited in situ data from the Antarctic MIZ, a better understanding of the various physical phenomena in this region is still required, especially to resolve the rapidly evolving dynamics of the sea ice cover [188]. The lack of in situ data complicates the calibration and verification of existing theoretical sea ice models [128, 185].

Large-scale sea ice models, such as Hibler III's VP formulation, are commonly used for climate modelling to gain a better understanding of the impact of sea ice on the seasonal cycle. The majority of these models use a smeared model approach, which implies no detailed and accurate description of the interaction between sea ice, the ocean and the atmosphere. The large-scale drift of sea ice can only be modelled to a certain degree of resolution, but fails to correctly capture all of the observed mechanical properties of sea ice [38].

Propagating waves are affected by the interaction with sea ice, however, to what extent is still poorly understood [45]. Simulating the characteristic properties of waves through a sea ice cover in the Antarctic MIZ is essential to understand the detailed dynamics of sea ice. By making use of small-scale models, where the resolution is increased, provides an opportunity to obtain a more detailed description of observed behaviour for different sea ice types. Existing small-scale models at a floe level [63], are mainly developed in a Lagrangian framework, applying the DEM [37, 65, 148, 164]. These models represent sea ice in the MIZ as rigid ice floes, focusing on individual ice floe collisions. Sea ice, which has not yet fully solidified, such as grease ice, has not

been considered in these models. Most existing Lagrangian models are limited in their usability, given the high number of simplifying assumptions, especially related the collision dynamics [65]. By contrast, the small-scale continuum models that were outlined in this chapter, are unable to explicitly describe the interaction between a collection of floes embedded within a viscous fluid.

The area of interest in this study is the region deeper into the Antarctic MIZ, consisting of realistically shaped, free-floating ice floes embedded in a layer of grease ice, in relatively calm wavy conditions. The implemented sea ice rheology is governed by ice floe collisions, the interaction between ice floes and grease ice, as well as skin drag at the ice-ocean interface. A heterogeneous layout, with distinctive material properties for both ice floes and grease ice, is subjected to a variety of waves and grease ice viscosity conditions. All these aspects combined, implemented in a continuum Eulerian framework, have not been investigated previously. Based on recent observations by Alberello et al. [3, 4] and Vichi et al. [200], these combined aspects are essential to accurately predict the sea ice dynamics of the Antarctic MIZ. Accordingly, unlike the existing small-scale models, the model developed as part of this study, will not only consider ice floe collisions, but also include the influence of the waves interacting with a realistic sea ice domain.

Chapter 3

Model description

3.1 Introduction

In this chapter the theory of the small-scale sea ice model is discussed, starting with an overview in which the aim and objectives of the model are highlighted. Then, the most important equations in the model are explained, regarding the sea ice rheology and the atmospheric and oceanic forcing. The implementation of both ice constituents in OpenFOAM, including the numerical stability and convergence of the model, the applied boundary conditions and divergence schemes are discussed in Chap. 4.

The primary aim of this study is to obtain a detailed insight in the mechanical behaviour of sea ice on a small scale. This numerical model contributes to the ongoing research into the impact of sea ice on seasonal changes and global climate change. The main objective is to develop a small-scale model in two-dimensions, which describes the high-resolution dynamics of sea ice in the Antarctic marginal ice zone (MIZ).

As previously mentioned in Chap. 1, this study focuses on the dynamics of sea ice deeper into the Antarctic MIZ, in the low to medium wave energy regime. In this region, the sea ice cover consists of relatively free-floating ice floes surrounded by grease ice, subjected to a wind and wave forcing [4]. The dynamics of sea ice is controlled by floe collision, the floe-grease ice interaction, skin drag, as well as the heterogeneous ice cover composition in terms of geometrical layout and material properties. All aspects in combination describing the collisional dynamics of ice floes due to wave action have not been considered before. This, however, based on recent observations by Alberello et al. [3, 4] and Vichi et al. [200], is crucial to accurately predict the sea ice dynamics of the Antarctic MIZ. Therefore, unlike the models previously developed, the ice floe collision dynamics is addressed, as well as wave action and the realistic embedment of ice floes in a mixture of grease ice.

The proposed framework can quantify the impact of floe and grease ice material properties, geometrical features including ice floe size, shape, and concentration, as well as wave forcing on the mechanical response of the sea ice cover. Two ice materials are distinguished in the intended small-scale model, ice floes and grease ice. Atmospheric and oceanic conditions in the Antarctic MIZ are applied to the model, consisting of wave-dependent wind forcing and current-dependent wave loading. In the formulation, the current-dependent wave loading is implemented as an imposed harmonic propagating wave [72].

The main research question in this study is defined as follows:

> *How do oceanic and atmospheric conditions affect the dynamics of sea ice in the Antarctic MIZ on a small scale?*

The numerical small-scale model provides high-resolution data regarding the interaction between the atmosphere, sea ice and the ocean.

3.2 Momentum balance equation

The momentum balance equation in the small-scale model describes the momentum transport of sea ice in a two-dimensional continuum solution domain, expressed as

$$m\left(\frac{\partial \boldsymbol{U}}{\partial t} + (\boldsymbol{U}\cdot\nabla)\boldsymbol{U}\right) = \nabla\cdot\boldsymbol{\sigma} + \boldsymbol{\tau}_a + \boldsymbol{\tau}_t, \tag{3.1}$$

where $\boldsymbol{U}$ represents the two-dimensional sea ice velocity vector and t the time parameter. The Coriolis force and sea surface dynamic height, which are part of Hibler III's large-scale momentum equation, are not included in Eq. (3.1), as they can be considered negligible in models with small spatial and temporal scales. The sea ice mass per unit area [69, 83, 197], m in kgm^{-2}, is written as

$$m = \rho h, \tag{3.2}$$

where ρ is the sea ice density and h the thickness. The Cauchy stress tensor, $\boldsymbol{\sigma}$, describes the sea ice stress state, which depends on the relevant ice type, either for ice floes, $\boldsymbol{\sigma}_f$, or for grease ice, $\boldsymbol{\sigma}_g$. The in-plane atmospheric and oceanic surface traction vectors are applied to the sea ice layer as external forcing, indicated by $\boldsymbol{\tau}_a$ and $\boldsymbol{\tau}_t$, respectively. Both terms are discussed in more detail in Sec. 3.4.

The velocity field of the sea ice domain is solved within the horizontal (x,y)-plane. Therefore, all terms in the momentum balance equation are normalised by the respective density, written as

$$h\left(\frac{\partial \boldsymbol{U}}{\partial t} + (\boldsymbol{U}\cdot\nabla)\boldsymbol{U}\right) = \nabla\cdot\boldsymbol{\sigma}' + \boldsymbol{\tau}_a' + \boldsymbol{\tau}_t', \tag{3.3}$$

where superscript $'$ represents the normalised terms, which are divided through by the sea ice density, ρ.

Accordingly, each term in Eq. (3.3) has a unit equal to $\mathrm{m}^2\mathrm{s}^{-2}$. The unit for stress, $\boldsymbol{\sigma}$, can be derived as

$$\left[\frac{\mathrm{m}^2}{\mathrm{s}^2}\right] = \nabla\cdot\boldsymbol{\sigma}' = \frac{\nabla\cdot\boldsymbol{\sigma}}{\rho} \rightarrow \left[\frac{\mathrm{m}^2}{\mathrm{s}^2}\right] = \left[\frac{1}{\mathrm{m}}\right]\left[\frac{\mathrm{m}^3}{\mathrm{kg}}\right]\boldsymbol{\sigma} \rightarrow \boldsymbol{\sigma} = \left[\frac{\mathrm{kg}}{\mathrm{s}^2}\right], \tag{3.4}$$

which results in a unit that deviates from the standard SI units. Generally, stress has SI units of force per area, Nm^{-2}, which is equivalent to $\mathrm{kgm}^{-1}\mathrm{s}^{-2}$.

The change of ice thickness over time is negligibly small compared to the size of the domain in the lateral direction. This allows for the assumption that both ice constituents are spatially constant. Only small time windows of less than a minute are considered in the model, which implies that the thickness of sea ice can be assumed unaffected by thermodynamic variation and rafting-related growth over time.

3.3 Sea ice rheology

The sea ice rheology in the small-scale model describes the relationship between the internal ice stresses, $\boldsymbol{\sigma}$, and the corresponding ice deformation, which is expressed in terms of strain rate, $\dot{\boldsymbol{\epsilon}}$. Strain rates, or velocity gradients, are defined as the change in strain, or displacement gradients, of a material with respect to time. This can be written as

$$\dot{\boldsymbol{\epsilon}}(t) = \frac{d\boldsymbol{\epsilon}}{dt} \approx \frac{\Delta\boldsymbol{\epsilon}}{\Delta t}, \qquad \text{with} \qquad \Delta\boldsymbol{\epsilon} = \boldsymbol{\epsilon}^{b+1} - \boldsymbol{\epsilon}^{b} \qquad \text{and} \qquad \Delta t = t^{b+1} - t^{b}, \tag{3.5}$$

where $\boldsymbol{\epsilon}$ represents the strain tensor. The time index, b, is discretised with time step Δt. The infinitesimal small strain theory is applied in this study, which means that the sea ice strain rate tensor, $\dot{\boldsymbol{\epsilon}}$ [81, 83], used in the sea ice rheology, can be written in terms of the sea ice velocity gradient, $\boldsymbol{\nabla U}$, as

$$\dot{\boldsymbol{\epsilon}} = \frac{1}{2}(\boldsymbol{\nabla U} + (\boldsymbol{\nabla U})^{T}). \tag{3.6}$$

The small-scale model distinguishes between two ice material constituents, grease ice and ice floes. Each are described separately, in Sec. 3.3.1 and Sec. 3.3.2, by their own sea ice rheology. Grease ice behaves as a viscous-plastic fluid, whereas ice floes have a solid-like character. The implementation of the combined set of equations in OpenFOAM, which requires the volume of fluid (VoF) method, is derived in Chap. 4.

3.3.1 Grease ice rheology

Grease ice is modelled as a viscous fluid, using a viscous-plastic (VP) material law, which is similar to the flow rheology developed by Hibler III [69] and Thorndike et al. [191], written as

$$\boldsymbol{\sigma}_g = 2\eta\dot{\boldsymbol{\epsilon}} + \boldsymbol{I}\left((\zeta - \eta)\mathrm{tr}(\dot{\boldsymbol{\epsilon}}) - \frac{P_g}{2}\right), \tag{3.7}$$

where the internal grease ice strength, P_g, dominates its compressibility. The spherical and deviatoric contributions of the viscosities, ζ and η, respectively, are both strain rate-dependent. $\boldsymbol{I}$ represents the identity tensor.

In the small-scale model, the internal grease ice strength parameter, P_g, is defined as

$$P_g = P_g^{*} h, \tag{3.8}$$

where P_g^{*} represents an empirical constant, excluding ice growth and concentration effects, as opposed to the large-scale model by Hibler III [69]. As previously mentioned in Sec. 2.2.1.2, the ice strength parameter in the VP model by Hibler III [69] depends on the sea ice thickness and sea ice concentration, which are formulated in terms of transport equations. Both transport equations represent the average of multiple ice types over time. The intended small-scale model does not compute averaged values, but differentiates between two ice materials. This implies that the average sea ice concentration parameter does not feature in the small-scale model, whereas the thickness parameter is separately parameterised for the two constituents. In other words, a constant, but different thickness is considered for both ice types.

Both strain rate-dependent viscosities are coupled via

$$\zeta = \frac{P_g}{2\Delta}, \qquad \eta = \frac{\zeta}{e_Y^2}, \tag{3.9}$$

where e_Y represents the ratio between the in-plane principal axes of the elliptical yield curve. The effective strain rate is indicated by Δ in s^{-1}, which can be written as

$$\Delta = \sqrt{(\dot{\epsilon}_{11}^2 + \dot{\epsilon}_{22}^2)(1 + e_Y^{-2}) + 4e_Y^{-2}\dot{\epsilon}_{12}^2 + 2\dot{\epsilon}_{11}\dot{\epsilon}_{22}(1 - e_Y^{-2})}, \tag{3.10}$$

where $\dot{\epsilon}_{11}$, $\dot{\epsilon}_{22}$ and $\dot{\epsilon}_{12}$ represent the Cartesian components of the symmetric strain rate tensor. The viscosity tends to infinity for strain rate values approaching zero, however, this is addressed by imposing a lower limit of the effective strain rate, i.e. $\Delta_{min} = 2 \cdot 10^{-7}\mathrm{s}^{-1}$ [104].

The units of both viscosities, as well as the unit of grease ice strength, deviate from the standard SI units due to the normalised momentum balance equation. In Eq. (3.4), the unit of stress is derived, kgs^{-2}. All terms in Eq. (3.7) have the same unit as stress. As a result, the unit of P_g is kgs^{-2}, whereas ζ and η have units in kgs^{-1}.

The grease ice rheology, shown in Eq. (3.7), can be written in terms of the velocity gradient, $\boldsymbol{\nabla U}$, after substitution of the strain rate tensor given in Eq. (3.6), as

$$\boldsymbol{\sigma}_g = \eta(\boldsymbol{\nabla U} + (\boldsymbol{\nabla U})^T) + \boldsymbol{I}\left((\zeta - \eta)\mathrm{tr}(\boldsymbol{\nabla U}) - \frac{P_g}{2}\right). \tag{3.11}$$

3.3.2 Ice floe rheology

A 'Hookean-like' flow rule is used to describe the constitutive law for the solid-like behaviour of ice floes, assuming relatively small deformations. Hooke's law can be written as

$$\boldsymbol{\sigma}_f = 2\mu\boldsymbol{\epsilon} + \lambda\boldsymbol{I}\mathrm{tr}(\boldsymbol{\epsilon}), \tag{3.12}$$

where the effective elastic Lamé parameters, μ and λ in kgs^{-2}, can be written as

$$\mu = \frac{E_Y}{2(1+\nu)}, \qquad \lambda = \frac{\nu E_Y}{(1+\nu)(1-2\nu)}. \tag{3.13}$$

Young's modulus is indicated by E_Y, and Poisson's ratio is represented by ν.

A sea ice rheology in CFD models, describes the relationship between stress and strain rate. Hooke's law is a function of strain, $\boldsymbol{\epsilon}$. Since the intended model solves a single continuity equation, the ice floe rheology must also be formulated in terms of velocity, and hence converted from strain, $\boldsymbol{\epsilon}$, into strain rate, $\dot{\boldsymbol{\epsilon}}$. As a result, the ice floe stress tensor, $\boldsymbol{\sigma}_f$, must be written in terms of the ice floe stress rate tensor, $\dot{\boldsymbol{\sigma}}_f$. Similarly, as done for the strain rate in Eq. (3.5), $\dot{\boldsymbol{\sigma}}_f$ can be given by

$$\dot{\boldsymbol{\sigma}}_f(t) = \frac{d\boldsymbol{\sigma}_f}{dt} \approx \frac{\Delta\boldsymbol{\sigma}_f}{\Delta t}, \qquad \text{with} \qquad \Delta\boldsymbol{\sigma}_f = \boldsymbol{\sigma}_f^{b+1} - \boldsymbol{\sigma}_f^{b} \qquad \text{and} \qquad \Delta t = t^{b+1} - t^{b}. \tag{3.14}$$

Substitution of Eqs. (3.6) and (3.14) into Eq. (3.12), results in

$$\boldsymbol{\sigma}_f^{b+1} = \boldsymbol{\sigma}_f^{b} + \Delta t \left(\mu(\boldsymbol{\nabla U} + (\boldsymbol{\nabla U})^T) + \lambda \boldsymbol{I}\mathrm{tr}(\boldsymbol{\nabla U})\right), \tag{3.15}$$

where the time index, b, is discretised with time step Δt [81]. The implementation of the ice floe rheology in the software OpenFOAM is discussed in Sec. 4.2.3.

3.4 Atmospheric and oceanic forcing

3.4.1 Wave-dependent wind loading

One of the founding wave-generation theories by Miles [125], describing the interaction between the wind and the wave forcing [72], is derived without the influence of sea ice. The main difference between Miles' theory, and the theory used for the wind forcing in the small-scale model, is the presence of sea ice. Wave-generation effects by the wind forcing are disregarded, because the small-scale model only considers an imposed wave. This is a reasonable assumption, as only small time windows are studied. Therefore, the wave-dependent wind loading considered in the small-scale model, represented by a wind stress on the apical plane, $\boldsymbol{\tau}_a$, is the external tangential force per unit area simply applied to the wavy sea ice surface at a height oscillating with the wave elevation by

$$\boldsymbol{\tau}_a = \rho_a C_a |\boldsymbol{U}_a| \left(\boldsymbol{U}_a \cos\theta_a + \boldsymbol{k} \times \boldsymbol{U}_a \sin\theta_a\right), \tag{3.16}$$

where ρ_a represents the air density, C_a the ice-air drag coefficient, and θ_a the wind turning angle. The turning angle describes the angle between the wind stress and the wind direction [31]. A positive angle corresponds to a stress vector that is oriented to the right of the wind direction. In other words, the angle is positive if the rotation from the wind direction to the stress vector is clockwise. In this study, the direction of the surface traction vector and the wind is assumed to be aligned, therefore $\theta_a = 0°$. The unit normal vector to the surface [69] is indicated by $\boldsymbol{k}$. The variable $\boldsymbol{U}_a$ represents the velocity of the wind boundary layer. The cross product, $\times$, of both vectors simply results in the tangential y-component of $\boldsymbol{\tau}_a$.

As previously mentioned in Chap. 2, Hutchings [82] enforced a lower limit on the ice thickness, $h = 0.5$m. The small-scale model does not make use of this lower limit, but includes the possibility of $h = 0$. This is done by treating a portion of the in-plane atmospheric and oceanic surface traction vectors semi-implicitly, ensuring that the mean sea ice velocity will be the velocity which satisfies the momentum balance equation, $\boldsymbol{\tau}_a' + \boldsymbol{\tau}_t' = 0$. Accordingly, Eq. (3.16) can be written with a semi-implicit and explicit component, as

$$\boldsymbol{\tau}_a = \underbrace{-\rho_a C_a |\boldsymbol{U}_a - \boldsymbol{U}| \cos\theta_a \boldsymbol{U}}_{\text{semi-implicit}} + \underbrace{\rho_a C_a |\boldsymbol{U}_a - \boldsymbol{U}| \left(\boldsymbol{U}_a \cos\theta_a + (\boldsymbol{U}_a - \boldsymbol{U})\boldsymbol{k} \times \sin\theta_a\right)}_{\text{explicit}}, \tag{3.17}$$

where $\boldsymbol{U}_a - \boldsymbol{U}$ represents the relative velocity between wind and sea ice.

The wind velocity, $\boldsymbol{U}_a$, above the wavy sea ice surface can be represented by the logarithmic wind profile, as previously studied by [8, 28, 29, 102, 126, 213], both in the presence and absence of sea ice. The logarithmic wind profile [85], $\boldsymbol{U}_a$, with height z above the water surface, is given by

$$\boldsymbol{U}_a(\zeta_c(z)) = \frac{\boldsymbol{U}^*}{\kappa} \ln\left(\frac{\zeta_c(z)}{z_0}\right), \qquad \text{with} \qquad z > z_0, \tag{3.18}$$

where the Von Kármán constant is given as $\kappa \approx 0.41$ [12, 43]. ζ_c represents a vertical curvilinear coordinate and $\boldsymbol{U}^*$ is the wind friction velocity. The sea surface roughness length parameter is indicated by z_0.

To find a value for the wind velocity close to the wind-wave interface, a wave-following curvilinear coordinate, ζ_c, is introduced [28, 29, 59]. Using a fixed Cartesian coordinate in the z-direction would result in velocity values that alternate in air and water. The curvilinear coordinate follows the wavy interface, where $\zeta_c(z) = 0$ corresponds to the ocean surface. ζ_c is related to the Cartesian z-coordinate, by

$$\zeta_c = z - \eta(x, t), \tag{3.19}$$

where $\eta(x, t)$ represents the wave elevation. The wave elevation of a linear wave propagating in positive x-direction can be written as

$$\eta(x, t) = a \sin(\omega t - kx), \tag{3.20}$$

which is derived from the Laplace equation and a kinematic boundary condition (BC) at $z = 0$. The wave amplitude is denoted by a, the wave frequency by ω, and k represents the wave number. The wave frequency, $\omega = 2\pi/T$, and wave number, $k = 2\pi/\Lambda$, are computed from the wave period T and the wave length Λ, using the deep water dispersion relation $\omega^2 = gk$. The gravitational acceleration is indicated by g.

The wind friction velocity vector in ms^{-1} in the apical plane, can be written as

$$\boldsymbol{U}^* = \begin{pmatrix} U_x^* \\ U_y^* \\ 0 \end{pmatrix}, \tag{3.21}$$

which is not physically a velocity, but the square root of the downward flux of eddy momentum. In two-dimensions, the component in the z-direction equals zero. The total wind shear stress vector, $\boldsymbol{\tau}$, representing the downward transport of the turbulence towards the surface, can be written as

$$\boldsymbol{\tau} = \rho_a \boldsymbol{U}^{*2} = \rho_a \boldsymbol{U}_{10}^2 C_{10}, \tag{3.22}$$

where $\boldsymbol{U}_{10}$ and C_{10} denote the wind speed and air drag coefficient at 10m height above the mean water level.

Turbulent and viscous effects just above the surface are parametrised by the sea surface roughness length parameter, z_0, and the layer of critical height, z_c [138, 157, 214, 215]. The sea surface roughness length can be calculated by

$$z_0 = \frac{\alpha_C U^{*2}}{g}, \qquad \text{with} \qquad U^* = \sqrt{U_x^{*2} + U_y^{*2}}, \tag{3.23}$$

where α_C indicates the Charnock coefficient.

Ocean's surface waves consist of a large number of wave components with random wave amplitudes, periods and phases, that travel in arbitrary wave direction [72]. A layer of turbulent airflow, with a height equal to the so-called critical height, z_c, passes over this random wave surface only if the primary wind and wave components face in the same direction. The height of the critical layer can be found by comparing the speed of the wave to the velocity profile of the wind. If $z_c > 0$, a cat's eye is formed, due to a wind velocity acting

in the opposite wave direction below z_c [157]. Obtaining the height of the critical layer is of importance. If $z_c = 0$m, the wind velocity profile starts increasing from zero at a height equal to the surface roughness length, z_0. The height of the critical layer, z_c, can be calculated by equating the wave speed, c, to the wind velocity profile, $\boldsymbol{U}_a(\zeta_c(z))$. The small-scale model does not include any viscous and turbulence effects from the interaction between the wind and the water waves, allowing the assumption that $z_c \approx 0$. This implies no turbulence layer, and results in a velocity profile that starts increasing from zero at a height $z = z_0$, just above the emerged ice floes.

A sketch of the logarithmic wind profile is shown in Fig. 3.1, indicating the curvilinear coordinate, the sea surface roughness and critical height.

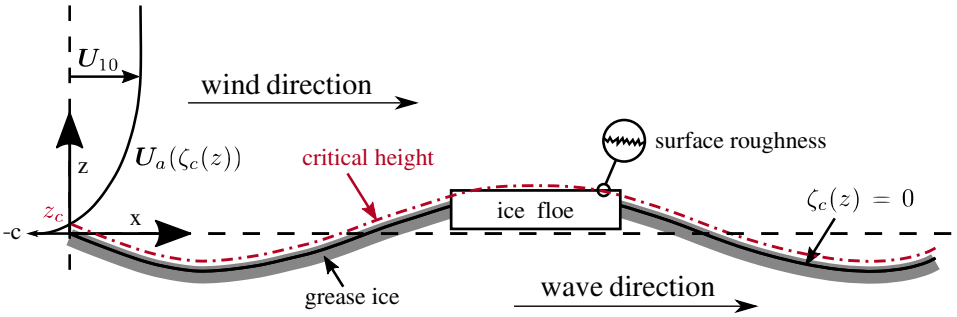

Figure 3.1: Logarithmic wind profile adapted from Buckley and Veron [28] and Sajjadi et al. [157].

Multiple studies have been conducted on the air drag coefficient, C_a. Paulson et al. [143] and Hidy [70] proposed a constant drag coefficient. Garratt [54] and Smith [173] demonstrated a wind speed dependent drag coefficient, whereas Wu et al. [214] and Amory et al. [8] suggest a drag coefficient in terms of the sea surface roughness z_0,

$$C_a(\zeta_c(z)) = \left(\frac{\kappa}{\ln(\zeta_c(z)/z_0)} \right)^2, \tag{3.24}$$

with a distinctive correlation between C_a and z_0. An increase in the sea surface roughness results in an increase in the drag coefficient.

An air drag multiplication factor, C_{a_λ}, is introduced in the small-scale model. This multiplication factor simply multiplies the wave dependent air drag coefficient in the entire domain with an arbitrary factor. A factor equal to one corresponds to air drag coefficient values found by Wu et al. [214] and Amory et al. [8]. Inclusion of C_{a_λ} in Eq. 3.24, results in

$$C_a(\zeta_c(z)) = C_{a_\lambda} \left(\frac{\kappa}{\ln(\zeta_c(z)/z_0)} \right)^2. \tag{3.25}$$

A detailed investigation into the multiplication factor, C_{a_λ}, is performed in Chap. 5.

3.4.2 Current-dependent wave loading

The current-dependent wave loading implemented in the small-scale model is based on the linear wave theory, describing the propagation of a harmonic wave in water. The linear wave theory, or the Airy wave theory, is

based on both a mass balance equation and a momentum balance equation. Both can be expressed in terms of the velocity potential, $\phi(x, y, z, t)$, which is a scalar function indicating the particle velocities in water. Note that the velocity potential function can only be used if the water particles are irrotational. This implies that particles may not rotate around their own axis. Water particles, under a harmonic wave, move with orbital motion in the x- and z-direction.

Substitution of the velocity potential in the mass balance equation results in the Laplace equation, which is a second-order differential equation. It is derived from the mass balance equation, but mass or mass density as such has disappeared from the equation. Substitution of the velocity potential in the momentum balance equation results in the linearised Bernoulli equation [72], which provides, in conjunction with the Laplace equation, the wave-induced pressure, p_{wi}, below the wavy water surface.

The linear wave theory only considers waves with a moderate wave steepness in shallow to deep waters. Wave steepness is defined as the ratio between the wave height, H, and the wave length, Λ [122]. A moderate wave steepness is equivalent to waves with $H/\Lambda \ll 1$ [132]. Shallow water refers to a water depth, d_w, which satisfies $d_w \ll \Lambda/2$, whereas deep water is defined as $d_w \gg \Lambda/2$ [72]. In deep water, $kd_w \to \infty$, the water particles move through circles, with an exponentially decreasing radius with water depth. In shallow water, $kd_w \to 0$, the particles move in ellipses, which grow flatter towards the bottom.

Furthermore, only free waves and forced waves are considered in this theory. A free wave is subjected to only gravity and can only be considered 'free' when the atmospheric pressure at the air-water interface is zero. A forced wave, on the other hand, is a free wave which is also exposed to external forcing. Substitution of both the wave elevation and the velocity potential function into the dynamic BC of zero atmospheric pressure at $z = 0$, results in a correlation between the wave frequency, ω, and the wave number, k. This correlation is also known as the dispersion relation.

Herman [66] applied the linear wave theory, assuming that the ice floes do not influence the motion of the waves. In Herman's model wave scattering and other wave-ice interaction effects were not considered. As with Herman [66], the small-scale model also makes use of the linear wave theory. We, however, impose the wave forcing, which implies that the wave elevation is known before solving the equations and that no wave dissipation is considered.

The linear wave theory is still valid for harmonic propagating waves travelling on currents. However, waves are affected by the current, resulting in a shift of the wave frequency and shape modification [30]. The intrinsic, or relative frequency, represents the wave frequency in a shifted reference system, preserving the correlation with the wave number and water depth [72]. The wave number is affected by the ocean current velocity and can be found by rewriting the dispersion relation, after adding the influence of the ocean current velocity.

The resultant velocity of a wave travelling on an ocean current can simply be obtained by taking the sum of both the velocity of the current and the wave [30, 166], where the current profile can be assumed constant along the depth. For waves propagating within a current field, the oceanic surface traction vector, $\boldsymbol{\tau}_t$, is represented by the sum of the flow due to the current and the wave as [30, 91, 94, 166]

$$\boldsymbol{\tau}_t = \boldsymbol{\tau}_o + \boldsymbol{\tau}_w, \tag{3.26}$$

where $\boldsymbol{\tau}_o$ represents the ocean current drag and $\boldsymbol{\tau}_w$ the wave traction, which in turn depends on the current dependent skin drag, $\boldsymbol{\tau}_{sd}$, and Froude-Krylov stress due to the wave forcing, $\boldsymbol{\tau}_{fk}$, [66]. The ocean current drag, acting at the basal plane of the ice due to the relative velocity of the ocean current and the ice is given by

$$\boldsymbol{\tau}_o = \rho_w C_w |\boldsymbol{U}_o - \boldsymbol{U}|((\boldsymbol{U}_o - \boldsymbol{U})\cos\theta_w + (\boldsymbol{U}_o - \boldsymbol{U}) \times \boldsymbol{k}\sin\theta_w), \tag{3.27}$$

where ρ_w represents the water density, θ_w the ice-ocean turning angle and C_w the ice-ocean drag coefficient. The constant ocean current velocity, $\boldsymbol{U}_o$, at $z = 0$m, is given as

$$\boldsymbol{U}_o = \begin{pmatrix} U_{o_x} \\ U_{o_y} \\ 0 \end{pmatrix}, \tag{3.28}$$

where U_{o_x} and U_{o_y} represent the constant ocean current velocity in the x- and y-direction, respectively. The component in the z-direction equals zero in the two-dimensional small-scale model.

Eq. (3.27) can be written in terms of a semi-implicit and explicit component, as

$$\boldsymbol{\tau}_o = \underbrace{-\rho_w C_w |\boldsymbol{U}_o - \boldsymbol{U}| \cos\theta_w \boldsymbol{U}}_{\text{semi-implicit}} + \underbrace{\rho_w C_w |\boldsymbol{U}_o - \boldsymbol{U}| \left(\boldsymbol{U}_o \cos\theta_w + (\boldsymbol{U}_o - \boldsymbol{U})\boldsymbol{k} \times \sin\theta_w\right)}_{\text{explicit}}, \tag{3.29}$$

where $\boldsymbol{U}_o - \boldsymbol{U}$ denotes the relative velocity between ocean current and sea ice.

The in-plane traction due to the waves, $\boldsymbol{\tau}_w$, derived from the linear wave theory [66, 72], consists of two components, given by

$$\boldsymbol{\tau}_w = \boldsymbol{\tau}_{sd} + \boldsymbol{\tau}_{fk}, \tag{3.30}$$

where $\boldsymbol{\tau}_{sd}$ is the viscous component representing the current-dependent skin drag. It acts on the entire ice-ocean interface as controlled by the drag coefficient. Both ice floes and grease ice have a different surface roughness, affecting the drag coefficient. Therefore, the ice constituents have a constant, but different drag coefficient. The small-scale model differentiates between both drag coefficients, via the non-dimensional parameter α of the VoF method.

The current-dependent skin drag, $\boldsymbol{\tau}_{sd}$, is given by

$$\boldsymbol{\tau}_{sd} = \rho_w C_w |\boldsymbol{U}_w - \boldsymbol{U}|((\boldsymbol{U}_w - \boldsymbol{U})\cos\theta_w + (\boldsymbol{U}_w - \boldsymbol{U}) \times \boldsymbol{k}\sin\theta_w), \tag{3.31}$$

which can be written in terms of a semi-implicit and explicit component, as

$$\boldsymbol{\tau}_{sd} = \underbrace{-\rho_w C_w |\boldsymbol{U}_w - \boldsymbol{U}| \cos\theta_w \boldsymbol{U}}_{\text{semi-implicit}} + \underbrace{\rho_w C_w |\boldsymbol{U}_w - \boldsymbol{U}| \left(\boldsymbol{U}_w \cos\theta_w + (\boldsymbol{U}_w - \boldsymbol{U})\boldsymbol{k} \times \sin\theta_w\right)}_{\text{explicit}}, \tag{3.32}$$

where $\boldsymbol{U}_w - \boldsymbol{U}$ indicates the relative velocity between ocean current affected wave motion and sea ice.

As a wave travels, water passes energy along by moving in a circle. In deep water this movement is called circular orbital motion [195]. In order to create orbital wave motion, the velocity components in the basal plane must be coupled with the component in the z-direction. As a result, the current-dependent orbital wave

velocity, $\boldsymbol{U}_w$, is given as

$$\boldsymbol{U}_w = \begin{pmatrix} U_{w_x} \\ U_{w_y} \\ U_{w_z} \end{pmatrix} = \begin{pmatrix} a(\omega - k_1 U_{o_x}) \sin(\omega t - k_1 x) \cos(\theta_{wa}) \\ a(\omega - k_2 U_{o_y}) \sin(\omega t - k_2 y) \sin(\theta_{wa}) \\ a(\omega - k_1 U_{o_x} - k_2 U_{o_y}) \cos(\omega t - k_1 x - k_2 y) \end{pmatrix}, \tag{3.33}$$

where the current-affected wave number, k, is determined by the modified dispersion relation [94, 166], as

$$\left(\omega - k\sqrt{U_{o_x}^2 + U_{o_y}^2}\right)^2 = gk. \tag{3.34}$$

This results in wave numbers in the x- and y-direction, as

$$k_1 = k\cos(\theta_{wa}), \qquad k_2 = k\sin(\theta_{wa}), \tag{3.35}$$

where θ_{wa} represents the wave direction angle, measured with respect to the x-axis and positive in the counter-clockwise rotation direction. A value of $\theta_{wa} = 0°$ is equivalent to a wave that propagates in the x-direction only.

The Froude-Krylov stress vector, $\boldsymbol{\tau}_{fk}$, accounts for the horizontal surge force due to the wave-induced pressure [66], acting on the ice floe circumference, at the interface between ice floes and grease ice

$$\boldsymbol{\tau}_{fk} = -\int_{h_w} p_{wi} \boldsymbol{n} \, \mathrm{d}z, \tag{3.36}$$

where h_w represents the height of submersion for an ice floe portion and $\mathrm{d}z$ the differential length in the z-direction. The unit vector $\boldsymbol{n}$ acts normal to the circumference of the ice floes directed outwards. The wave-induced pressure, p_{wi}, is written as

$$p_{wi} = \rho_w g a \sin(\omega t - kx), \tag{3.37}$$

where the gravitational acceleration is denoted as g. Eqs. (3.36) and (3.37) can be rewritten as

$$\boldsymbol{\tau}_{fk} = \boldsymbol{n} \cdot h_w a \omega^2 \cos(\omega t - kx). \tag{3.38}$$

Additionally, Herman [66] considered a collisional force and a force related to the added mass. The latter is not considered in the small-scale model as Herman [66] concluded that the contribution of added mass is small, especially considering that ice floe sizes in the small-scale model are much smaller than the wave length. Interaction between colliding ice floes which resist collisional forces, are included in the small-scale model via the stress and strain rate response. The same applies to form drag acting on the ice floe circumference due to velocity differences of floes and surrounding grease ice. Both are implicitly included by the continuity requirement of the velocity field throughout the domain which is modelled in a continuum fashion.

Chapter 4

Computational framework

4.1 Introduction to OpenFOAM

OpenFOAM is an open-source platform that allows for the solutions of computational fluid dynamics (CFD) problems. CFD is a tool in mathematics, physics and computational software, which is the field of solving fluid flow problems numerically. OpenFOAM which stands for Open source Field Operation and Manipulation makes use of the C^{++} programming language. A variety of numerical problems can be solved in OpenFOAM, such as problems related to turbulent fluid flows, fluid-structure interaction, and heat transfer [14, 57].

In CFD simulations a set of partial differential equations (PDEs) describes the fluid flow. The PDEs represent the mass, momentum, and energy conservation equations. Firstly, the conservation of mass states that the rate of change of mass, in an arbitrary control volume, is equal to the mass production rate in the control volume. Secondly, momentum conservation equates the rate of change of momentum in a control volume to the total force acting on the volume. In the event where no external forces are applied, momentum is unchanged in the system [39]. Lastly, the conservation of energy is controlled by the first law of thermodynamics. The latter does not allow generation or demolition of energy, however, energy phase transformation is allowed to take place [9, 39, 211].

Fluid flow can be described either in a Lagrangian or an Eulerian frame of reference. In the Lagrangian approach, known as the material description or convective form, the fluid can be described in terms of fluid particles. Each fluid particle is tracked as it moves through space and time. Contrastingly, the Eulerian framework, known as the spatial description or conservation form, considers a fixed domain through which a fluid flows [39, 212]. Spatial positions are occupied by different particles at different times.

The intended small-scale model in OpenFOAM is developed in an Eulerian frame of reference, making use of the approach of multiphase flow. This approach refers to any fluid flow consisting of more than one phase or component. Multiphase flow can be described as 'interpenetrating continua', including the concept of phase volume fractions. This concept describes the space which is occupied by each phase. Additionally, the mass and momentum conservation equations are met by each phase individually.

The most sophisticated multiphase model is the Eulerian-Eulerian multiphase model, because of a strong

coupling between the dispersed and continuous phases [1]. For each phase a set of n momentum and continuity equations are solved [216]. Eulerian-Eulerian multiphase modelling can be subdivided into two flows, dispersed flows with dispersed-continuous phase interactions and separated flows with continuous-continuous phase interactions. Dispersed flows consist of particles, which include droplets and bubbles, in a continuous phase. Separated flows can be identified as phases, which are separated by an interface [27, 36, 175].

Two alternative models, derived from the Eulerian-Eulerian multiphase model, are volume of fluid (VoF) models, which describe separated flows, and mixture models, which represent dispersed flows. Both models are a simplification of the Eulerian-Eulerian multiphase model, as all phases only share a single set of momentum and continuity equations. The VoF model, applied to a fixed Eulerian grid, is a surface-tracking method for two or more immiscible phases. The term 'immiscible' implies that phases cannot mix together. Volume fractions of each phase are tracked in the problem domain, with the primary aim to find the position of the interface between phases. The mixture model is different from the VoF model in three aspects. Firstly, phases in the mixture model can interpenetrate, which means that they can mix or merge together. Secondly, phases in the mixture model can move with a different velocity, applying the concept of slip velocities. Lastly, the mixture model allows interaction between phases in terms of transfer of mass and momentum [48].

PDEs describe the fluid flow, which can be formulated in their strong or weak form. In the strong or differential form [144], which refers to the PDE and corresponding boundary conditions, the PDEs are not directly solvable. The weak form is an integral form of the PDEs, which can be approximated when discretised [52]. Most commonly used discretisation schemes and solution methods include the finite difference method (FDM), the finite element method (FEM), and the finite volume method (FVM). All three methods approximate governing ordinary or partial differential equations [144]. Note, however, that these methods only apply to the spatial discretisation. FEM is mainly used in structural mechanics, in which forces are applied to a solid body and stress and deformation are modelled [109]. FDM is used for simple boundary value problems with simple geometries [58], whereas FVM can be applied to more complex CFD geometries.

In 2018, Roenby et al. [153] released a new VoF method in OpenFOAM, called the isoAdvector method. Their objective was to design a VoF-based interface advection method, that operates on arbitrary meshes, preserves accuracy of the geometric schemes by explicit approximation of the interface. Additionally, minimizes the geometric operations to reduce computational times.

Two important features within the OpenFOAM software, applied in the small-scale model, are the FVM and the VoF method, in particular the isoAdvector method. Therefore, these methods are discussed thoroughly in this chapter.

4.1.1 Finite Volume Method

OpenFOAM is a utility and a set of libraries that facilitate solving PDEs by predominantly using the FVM. The solution domain is subdivided, by means of a mesh, into a finite number of small control volumes, or cells. Each control volume is bounded by a control surface [51]. The rate of change of a quantity within a control volume, plus the flux through the boundary is equal to the rate of production [145].

The fundamental physical principles, consisting of the conservation of mass and momentum, are applied to the fluid inside a control volume. These conservation equations are expressed in terms of coupled partial

differential equations, which are integrated over each control volume. Subsequently, the divergence theorem is applied to both convective and diffusive terms. As a result a volume integral is converted into a surface integral, considering the flux through the cell faces of the control volume. Fluxes at the cell faces are obtained by making use of differencing schemes, which are different in order, stability, accuracy, and convergence. As a result, discretised momentum equations are obtained.

Per control volume three equations are required, to solve three unknown variables in the two-dimensional Navier-Stokes equations. These variables are the velocities in the x- and y-direction, U_x and U_y, and the pressure, p. In this section the notation of the velocities in the x- and y-direction is different, by simply writing them as U and V, respectively. The momentum equations only provide two equations, which means that one more equation is needed. The continuity equation is used, however, it does not explicitly contain the pressure gradient for incompressible flows. Consequently, the continuity equation is rewritten in terms of the pressure gradient by pressure-velocity coupling. The discretised momentum equations are used to find the pressure-explicit continuity equation, written in a solvable algebraic form. As a result, each control volume in two-dimensions has now three equations and three unknowns. This means that an algebraic system of equations is obtained, which can be solved.

4.1.1.1 Collocated grid

Methods that make use of a collocated grid, store all variables at the central node of a cell, of which five cell centres are illustrated by P, N, E, S, W in a two-dimensional uniform grid in Fig. 4.1. The cell faces of central cell P are indicated by n, e, s, w. This configuration of storing variables at one location is beneficial regarding computational costs [193], however, interpolation between cell centres is needed to find variable values at the faces of each cell.

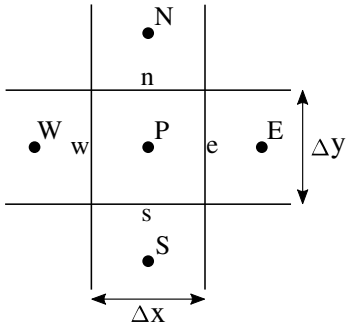

Figure 4.1: Two-dimensional collocated uniform grid [35].

.

The FVM will be explained in detail in this section by making use of the following continuity and momentum equations in two dimensions. The continuity equation is written as

$$\frac{\partial \rho}{\partial t} + \rho \frac{\partial U}{\partial x} + \rho \frac{\partial V}{\partial y} = 0, \tag{4.1}$$

where ρ represents the density of an arbitrary fluid. Note that an incompressible fluid can be assumed when changes in density are non-existent. When considering an incompressible fluid, where $D\rho/Dt = 0$ [39], the

continuity equation, given in Eq. (4.1), can be rewritten as

$$\frac{\partial U}{\partial x} + \frac{\partial V}{\partial y} = 0. \tag{4.2}$$

The momentum equation in the x-direction is written as

$$\rho\frac{\partial U}{\partial t} + \rho U\frac{\partial U}{\partial x} + \rho V\frac{\partial U}{\partial y} = -\frac{\partial p}{\partial x} + \frac{\partial}{\partial x}\left(\mu_d\frac{\partial U}{\partial x}\right) + \frac{\partial}{\partial y}\left(\mu_d\frac{\partial U}{\partial y}\right) + S_u, \tag{4.3}$$

and in the y-direction given as

$$\rho\frac{\partial V}{\partial t} + \rho U\frac{\partial V}{\partial x} + \rho V\frac{\partial V}{\partial y} = -\frac{\partial p}{\partial y} + \frac{\partial}{\partial x}\left(\mu_d\frac{\partial V}{\partial x}\right) + \frac{\partial}{\partial y}\left(\mu_d\frac{\partial V}{\partial y}\right) + S_v, \tag{4.4}$$

where the material derivative is shown on the left-hand side of both momentum equations, which represents the change of velocity in both space and time. The first term on the left-hand side of both momentum equations indicates the transient term, whereas the second and third terms describe the convective fluxes [17, 22, 39]. On the right-hand side, the first term represents the pressure gradient, whereas the second and third terms describe diffusive fluxes with the dynamic viscosity, μ_d. Remaining source terms before volume integration are included by S_u and S_v in the x- and y-direction, respectively [84].

The discretised equations are linearised in time, by decomposition of time into discrete time steps. Both implicit and explicit iterative methods can be applied to discretise the time-dependent terms, of which one of the most basic is the Euler method. A first-order accurate method, which is used to solve ordinary differential equations (ODEs). The following first-order ODE with initial condition [51, 82] is considered for illustration, written as

$$\frac{d\phi(t)}{dt} = F(t,\phi), \qquad \text{with} \qquad \phi(t_0) = \phi^0, \tag{4.5}$$

where the initial condition is denoted by $\phi(t_0)$. Values of ϕ are obtained at time steps $t_1 = t_0+\Delta t$, $t_2 = t_0+2\Delta t$, $t_3 = t_0 + 3\Delta t$, etc. A method is required to approximate the integration from t_n to t_{n+1}, which is given as

$$\int_{t_n}^{t_{n+1}} \frac{d\phi(t)}{dt}dt = \phi^{n+1} - \phi^n = \int_{t_n}^{t_{n+1}} F(t,\phi)dt, \tag{4.6}$$

where ϕ^{n+1} represents the value of ϕ at t_{n+1}. An approximation of the integral in Eq. (4.6) can be obtained by using the value of the integrand at the initial point, as

$$\phi^{n+1} = \phi^n + F(t_n,\phi^n)\Delta t, \tag{4.7}$$

which is referred to as the explicit or forward Euler method. If one would use the final point to approximate the integral, this would be written as

$$\phi^{n+1} = \phi^n + F(t_{n+1},\phi^{n+1})\Delta t, \tag{4.8}$$

which is called the implicit or backward Euler method. Potentially, the accuracy can be increased by splitting the time step, or by applying a second-order method, such as the Mid-point Rule, or the Trapezium Rule.

The Mid-point Rule can be mathematically formulated as

$$\phi^{n+1} = \phi^n + F(t_{n+\frac{1}{2}}, \phi^{n+\frac{1}{2}})\Delta t, \tag{4.9}$$

and the Trapezium Rule is given by

$$\phi^{n+1} = \phi^n + \frac{1}{2}\left(F(t_n, \phi^n) + F(t_{n+1}, \phi^{n+1})\right)\Delta t, \tag{4.10}$$

The four different schemes are illustrated in Fig. 4.2.

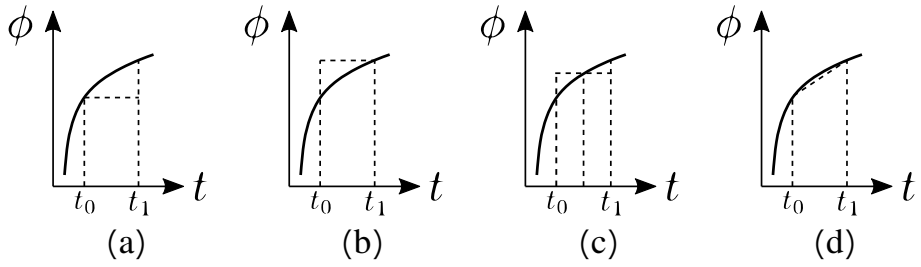

Figure 4.2: Linear approximations of the time integral of ϕ, with **(a)** the Euler Explicit Method, **(b)** the Euler Implicit Method, **(c)** the Mid-point Rule and **(d)** the Trapezium Rule. The figure is reproduced from Ferziger et al. [51] and Hutchings [82].

The temporally-dependent terms in the momentum equations are constant over the cell volume, because the FVM integrates cell centred values by multiplying the value by the volume. Accordingly, the temporally-dependent terms are not included in the spatial discretisation scheme explained below.

The explanation of the FVM commences by integration of the momentum equations over the volume of cell P. The equation in the x-direction can be written as

$$\int_{V_P}\left(\rho U\frac{\partial U}{\partial x} + \rho V\frac{\partial U}{\partial y}\right)dV = -\int_{V_P}\frac{\partial p}{\partial x}dV + \int_{V_P}\left(\frac{\partial}{\partial x}\left(\mu_d\frac{\partial U}{\partial x}\right) + \frac{\partial}{\partial y}\left(\mu_d\frac{\partial U}{\partial y}\right)\right)dV. \tag{4.11}$$

The divergence theorem, also known as the Gauss' theorem, is used to convert a volume integral into a surface integral. The theorem implies that the net flux of a vector field through a closed surface is equal to the total volume of all sources and sinks over the region inside the surface [39]. In mathematical notation the divergence theorem can be written as

$$\int_V (\nabla \cdot \boldsymbol{F})dV = \int_{\partial V}(\boldsymbol{F}\cdot\boldsymbol{n})dS, \tag{4.12}$$

where the left-hand side represents the volume integral of vector field $\boldsymbol{F}$, and the right-hand side the surface integral of $\boldsymbol{F}$. V represents a region in space with ∂V as its boundary surface. $\boldsymbol{n}$ indicates the unit normal vector to the boundary edges. dV denotes the differential volume, and dS the differential surface.

Applying the divergence theorem used in Eq. (4.12) to the convective and diffusive terms in Eq. (4.11), results after rearrangement in

$$\int_{\partial V_P}(\rho UU + \rho VU)\cdot\boldsymbol{n}dS - \int_{\partial V_P}\left(\mu_d\frac{\partial U}{\partial x} + \mu_d\frac{\partial U}{\partial y}\right)\cdot\boldsymbol{n}dS = -\int_{V_P}\frac{\partial p}{\partial x}dV, \tag{4.13}$$

with on the right-hand side the pressure gradient term. Integrating the pressure gradient over the volume of cell P results in source term, S_{U_P}. It is approximated by interpolating pressure values of neighbouring cells and then multiplied by the volume of cell P in two-dimensions, as

$$S_{U_P} = -\int_{V_P} \frac{\partial p}{\partial x} dV \approx \left(\frac{\partial p}{\partial x}\right)_P \Delta x \Delta y, \tag{4.14}$$

where $(\partial p/\partial x)_P$ represents the pressure gradient at the centre of cell P. The length of a uniform cell in the x- and y-direction is indicated by Δx and Δy, respectively. On a uniform grid, as shown in Fig. 4.1, S_{U_P} can be written as

$$S_{U_P} = \frac{(p_e - p_w)}{\Delta x}(\Delta x \Delta y) = (p_e - p_w)\Delta y = 0.5(p_E - p_W)\Delta y, \tag{4.15}$$

where p_e and p_w represent the pressure at faces e and w.

The surface integrals in Eq. (4.13) are rearranged, such that the components in the x- and y-direction are separated, and approximated in discretised form by

$$\int_{\partial V_P} \left(\rho UU - \mu_d \frac{\partial U}{\partial x}\right) \cdot \boldsymbol{n} dS \approx \sum_k \left(\rho UU - \mu_d \frac{\partial U}{\partial x}\right)_k \cdot (\boldsymbol{n}\Delta y)_k, \qquad \text{with} \qquad k = e, w, \tag{4.16}$$

$$\int_{\partial V_P} \left(\rho VU - \mu_d \frac{\partial U}{\partial y}\right) \cdot \boldsymbol{n} dS \approx \sum_k \left(\rho VU - \mu_d \frac{\partial U}{\partial y}\right)_k \cdot (\boldsymbol{n}\Delta x)_k, \qquad \text{with} \qquad k = n, s. \tag{4.17}$$

Substitution of cell faces $k = e, w$ into Eq. (4.16) results in the discretised convective and diffusive terms in the x-direction, given in Eq. (4.18). Substitution of $k = n, s$ into Eq. (4.17), results in the discretised convective and diffusive terms in the y-direction, given in Eq. (4.19), as

$$\left(\rho UU - \mu_d \frac{\partial U}{\partial x}\right)_e (\Delta y)_e - \left(\rho UU - \mu_d \frac{\partial U}{\partial x}\right)_w (\Delta y)_w, \tag{4.18}$$

$$\left(\rho VU - \mu_d \frac{\partial U}{\partial y}\right)_n (\Delta x)_n - \left(\rho VU - \mu_d \frac{\partial U}{\partial y}\right)_s (\Delta x)_s. \tag{4.19}$$

Collecting the convective flux terms in both Eqs. (4.18) and (4.19), results in

$$(\rho UU)_e(\Delta y)_e - (\rho UU)_w(\Delta y)_w + (\rho VU)_n(\Delta x)_n - (\rho VU)_s(\Delta x)_s. \tag{4.20}$$

Eq. (4.20) can be rewritten as

$$C_{xe}U_e - C_{xw}U_w + C_{yn}U_n - C_{ys}U_s, \tag{4.21}$$

where $C_{xe} = \rho(U\Delta y)_e$, $C_{xw} = \rho(U\Delta y)_w$, $C_{yn} = \rho(V\Delta x)_n$ and $C_{ys} = \rho(V\Delta x)_s$, represent the max flux through the relevant cell faces. The velocity values at the cell faces, U_e, U_w, U_n, and U_s are calculated by means of interpolation between cell centred values.

Collecting the diffusive flux terms in both Eqs. (4.18) and (4.19), results in

$$-\left(\mu_d \frac{\partial U}{\partial x}\right)_e (\Delta y)_e + \left(\mu_d \frac{\partial U}{\partial x}\right)_w (\Delta y)_w - \left(\mu_d \frac{\partial U}{\partial y}\right)_n (\Delta x)_n + \left(\mu_d \frac{\partial U}{\partial y}\right)_s (\Delta x)_s, \tag{4.22}$$

where $\partial U/\partial x$ and $\partial U/\partial y$ denote the gradients at the cell faces. These are obtained by making use of the central difference scheme, resulting in diffusive flux terms, given by

$$-\mu_d(\Delta y)_e \frac{U_E - U_P}{\Delta x} + \mu_d(\Delta y)_w \frac{U_P - U_W}{\Delta x} - \mu_d(\Delta x)_n \frac{U_N - U_P}{\Delta y} + \mu_d(\Delta x)_s \frac{U_P - U_S}{\Delta y}, \tag{4.23}$$

which represents a second-order approximation. Eq. (4.23) can be rewritten as

$$a_e^d U_E + a_w^d U_W + a_n^d U_N + a_s^d U_S - a_P^d U_P, \tag{4.24}$$

where $a_e^d = -\mu_d(\Delta y/\Delta x)_e$, $a_w^d = \mu_d(\Delta y/\Delta x)_w$, $a_n^d = -\mu_d(\Delta x/\Delta y)_n$, $a_s^d = \mu_d(\Delta x/\Delta y)_s$ and $a_P^d = a_e^d + a_w^d + a_n^d + a_s^d$.

4.1.1.2 Interpolation schemes

The choice of interpolation scheme influences the stability and accuracy of the obtained results [16, 51]. Frequently-used schemes [39, 51, 87, 198] are outlined below, focusing on cells P and E with cell face e in between. Note that in the explanation of the schemes the words 'positive' and 'negative' are used figuratively, only to distinguish between two opposite flow directions.

- First Order Upwind Scheme [198]: scheme applicable to the convective flux terms, depending on the flow direction. $U_e = U_P$ when the flow direction is in 'positive' direction and $U_e = U_P$ when the flow direction is in 'negative' direction. This implies a constant value of U_e between the centre and the face of the cell. Hence, this upwind scheme is only first-order accurate.

- Central Difference Scheme [39]: second-order accurate scheme. To find U_e, the cell centred velocity values U_P and U_E are linearly interpolated, as

$$U_e = U_P + \frac{U_E - U_P}{x_E - x_P}(x_e - x_P), \tag{4.25}$$

  where the x-coordinates of cell centres P and E are indicated by x_P and x_E, respectively. The x-coordinate of cell face e is given by x_e.

- Linear Upwind Scheme [87]: the second-order accurate scheme is generally applied to convective flux terms, which essentially combines the First-Order Upwind and Central Difference schemes. A 'positive' or 'negative' flow direction results in a value of U_e equal to a linear equation

$$U_e = U_P + \phi_g(\nabla U)_P \cdot \boldsymbol{r}, \qquad \text{or} \qquad U_e = U_E + \phi_g(\nabla U)_E \cdot \boldsymbol{r}, \tag{4.26}$$

  respectively. ∇U indicates the known gradient at the centre of cell P, which is applied to enhance the accuracy of the extrapolation. Additionally, ϕ_g, which is the gradient limiter representing a value between zero and one, ensures that values do not exceed the local minimum or maximum values. $\boldsymbol{r}$ denotes a vector between either the centre of cells P or E and face e, depending on the direction of the fluid flow.

- QUICK scheme [51]: third-order accurate scheme, which stands for Quadratic Upwind Interpolation for Convection Kinetics scheme. The velocity at cell face e, U_e, is approximated by making use of cell centred values from cell P and two consecutive neighbouring cells, fitted by a parabolic function.

If one would consider the First Order Upwind Scheme, the convective terms can be rewritten as

$$-a_e^c U_E - a_w^c U_W - a_n^c U_N - a_s^c U_S + a_P^c U_P, \tag{4.27}$$

where $a_e^c = \max(-C_{xe}, 0)$, $a_w^c = \max(C_{xw}, 0)$, $a_n^c = \max(-C_{yn}, 0)$, $a_s^c = \max(-C_{ys}, 0)$ and $a_P^c = a_e^c + a_w^c + a_n^c + a_s^c + (C_{xe} - C_{xw} + C_{yn} - C_{ys})$, resulting in positive a_i^c coefficients, with $i = e, w, n, s$. As the net mass flux in cell P needs to be equal to zero, one could simply write $a_P^c = a_e^c + a_w^c + a_n^c + a_s^c$.

The generalised diffusive-convective flux expression results in a discretised equation of the form

$$a_P U_P = a_e U_E + a_w U_W + a_n U_N + a_s U_S + S_{U_P}, \tag{4.28}$$

where $a_e = a_e^d + a_e^c$, $a_w = a_w^d + a_w^c$, $a_n = a_n^d + a_n^c$, $a_s = a_s^d + a_s^c$ and $a_P = a_e + a_w + a_n + a_s$. As previously noted, S_{U_P} represents the source derived from the pressure gradient. As a result, a relation has been obtained which links the velocity at the centre of cell P, U_P, to neighbouring cell-centred velocity values. Eq. (4.28) can be rewritten as

$$a_P U_P = \sum a_i U_i + S_{U_P} + S_U, \tag{4.29}$$

which includes S_U, representing remaining source terms after volume integration. a_i indicates the sum of convective and diffusive coefficients at the neighbouring cell faces and U_i denotes the velocity components of the adjacent cell centres.

In the collocated grid approach interpolation of stored values, p_P, p_E and p_W, is required to obtain the pressure value at cell faces e and w. Fig. 4.3 illustrates linear interpolation of both cell faces on a one-dimensional uniform grid. Additionally, the equation of the pressure gradient, given by

$$\left(\frac{\partial p}{\partial x}\right)_P = \frac{(p_e - p_w)}{\Delta x} = \frac{(p_E - p_W)}{2\Delta x}, \tag{4.30}$$

shows that this approach results in a weak relation between the velocity values and the pressure field, as p_P is not directly used. This, however, can cause a numerical complication, namely chequerboard oscillations, discussed in greater detail in Sec. 4.1.1.6. Two main methods do not suffer from chequerboard oscillations. These methods are the staggered grid approach, explained in Sec. 4.1.1.4, and the collocated grid approach in combination with the Rhie and Chow interpolation, described in Sec. 4.1.1.6.

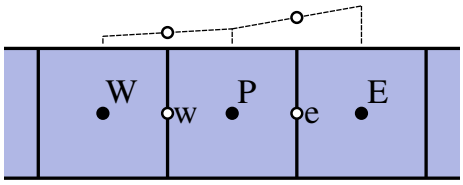

Figure 4.3: One-dimensional uniform grid resulting in a chequerboard pattern.

For the calculation of the Linear Upwind Scheme, the velocity gradient, ∇U, at cell centroid P is required. Several differencing schemes can be used to approximate the gradient, such as the Green-Gauss gradient scheme. This study opted to make use of the least-squares gradient scheme, which is explained in Sec. 4.1.1.3, using an arbitrary variable ϕ.

4.1.1.3 Least squares gradients

Consider a two-dimensional collocated uniform grid with primary cell centroid P with neighbour cells N, E, S, W as shown in Fig. 4.4. The value of an arbitrary variable ϕ at the cell centre of cell P can be extrapolated to the values of neighbouring cell centres N, E, S, W by making use of the gradient at P. The extrapolated values at cell centroid are compared to the actual value at N, E, S, W. The difference between these two values is expressed as the error. Minimizing the sum of the errors squared at all neighbours of cell P with respect to the gradient, results in a good approximation of the gradient.

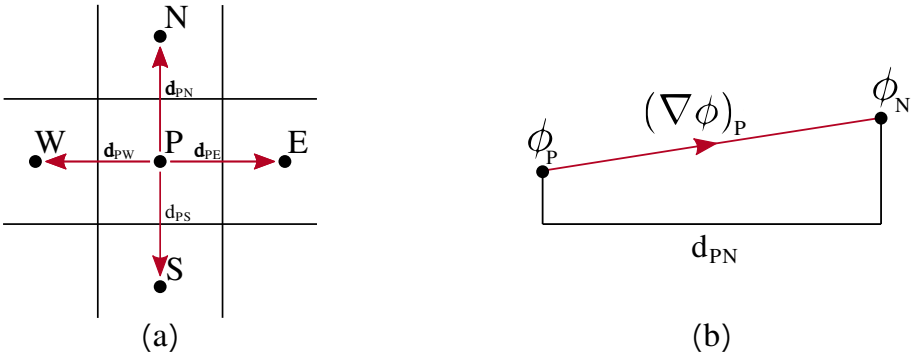

Figure 4.4: A schematic diagram of the least-squares method, showing **(a)** a two-dimensional uniform grid with distance vectors and **(b)** linear interpolation of an arbitrary variable, ϕ, between cell centres P and N.

The least-squares method [189] starts by expressing the value of ϕ at a neighbour cell, for example N, crossing a single face, as

$$\phi_N = \phi_P + \boldsymbol{d}_{PN} \cdot (\boldsymbol{\nabla}\phi)_P, \tag{4.31}$$

where $\boldsymbol{d}_{PN}$ is the distance vector between cell centres P and N. $(\boldsymbol{\nabla}\phi)_P$ is the unknown in Eq. (4.31). An additional equation is written for every cell face, resulting in a set of equations

$$\phi_i = \phi_P + \boldsymbol{d}_{Pi} \cdot (\boldsymbol{\nabla}\phi)_P, \tag{4.32}$$

where $i = N, E, S, W$. In each of these equations the gradient, $(\boldsymbol{\nabla}\phi)_P$, is the same and is unknown. In the uniform grid, as shown in Fig. 4.4, the distance vectors between cell centres are all equal.

Subtract ϕ_P from both sides of Eq. (4.32), results in

$$[\phi_i - \phi_P] = [\boldsymbol{d}_{Pi}][(\boldsymbol{\nabla}\phi)_P], \tag{4.33}$$

which can be written in terms of a matrix equation, $\boldsymbol{M}\boldsymbol{x} = \boldsymbol{b}$, as

$$[\boldsymbol{d}_{Pi}][(\boldsymbol{\nabla}\phi)_P] = [\phi_i - \phi_P], \tag{4.34}$$

where vector $\boldsymbol{x}$ represents the unknown gradient vector $(\boldsymbol{\nabla}\phi)_P$, with $i = N, E, S, W$. $\boldsymbol{M}$ is the matrix of coefficients, $\boldsymbol{d}_{Pi}$. Vector $\boldsymbol{b}$ indicates the variable difference vector. If one would write out Eq. (4.34), this

would result in

$$\begin{pmatrix} d_{PN_x}, d_{PN_y}, d_{PN_z} \\ d_{PE_x}, d_{PE_y}, d_{PE_z} \\ d_{PS_x}, d_{PS_y}, d_{PS_z} \\ d_{PW_x}, d_{PW_y}, d_{PW_z} \end{pmatrix} \begin{pmatrix} \left(\frac{\partial \phi}{\partial x}\right)_P \\ \left(\frac{\partial \phi}{\partial y}\right)_P \\ \left(\frac{\partial \phi}{\partial z}\right)_P \end{pmatrix} = \begin{pmatrix} \phi_N - \phi_P \\ \phi_E - \phi_P \\ \phi_S - \phi_P \\ \phi_W - \phi_P \end{pmatrix}, \tag{4.35}$$

which shows matrices which are not square, which implies that an exact solution cannot be obtained. Therefore, an approximate solution is computed for $(\boldsymbol{\nabla}\phi)_P$, resulting in an error in each equation

$$e_i = \phi_i - (\phi_P + (\boldsymbol{\nabla}\phi)_P \cdot \boldsymbol{d}_{Pi}, \tag{4.36}$$

where e_i represents the error for $i = N, E, S, W$. The least-squares solution minimises the sum of the errors squared, which can be mathematically expressed as

$$(\nabla\phi)_P = \boldsymbol{G}^{-1}\boldsymbol{d}^T(\phi_N - \phi_P), \tag{4.37}$$

where $\boldsymbol{G} = (\boldsymbol{d}^T\boldsymbol{d})$. As a result, $\boldsymbol{G}$ is always a (3×3) matrix, which allows an easy computation of its inverse.

Note, however, that the least-squares gradient scheme does not work sufficiently well for thin cells. This applies to a mesh, in which, for example, the cells in the y-direction, with corresponding distance vectors, are small, whereas the cells in the x-direction, with corresponding distance vectors, are large. This would result in a dominating gradient calculation in the x-direction. The trick to solve this dominant effect is to introduce a weighting function, $w = 1/|\boldsymbol{d}|$, as

$$[\boldsymbol{w}][\boldsymbol{d}_{Pi}][(\boldsymbol{\nabla}\phi)_P] = [\boldsymbol{w}][\phi_i - \phi_P], \tag{4.38}$$

where $\boldsymbol{w}$ is a diagonal weighting matrix, $w_i = 1/|\boldsymbol{d}_i|$. The least-squares solution in Eq. (4.37) can now be written as

$$(\nabla\phi)_P = \boldsymbol{G}^{-1}\boldsymbol{d}^T\boldsymbol{w}^T\boldsymbol{w}(\phi_N - \phi_P), \tag{4.39}$$

where $\boldsymbol{G} = \boldsymbol{d}^T\boldsymbol{w}^T\boldsymbol{w}\boldsymbol{d}$. In a static mesh, the distance vectors do not change in time. This means that the quantity $\boldsymbol{G}^{-1}$ multiplied by $\boldsymbol{d}^T\boldsymbol{w}^T\boldsymbol{w}$ does not change in time. Accordingly, the values are calculated only once for each cell in the mesh. Hence, the least-squares gradient is efficient to compute.

The second- and fourth order least-squares gradient schemes differ in their number of neighbouring cells included in the calculation of the gradient. The second-order least-squares makes use of only direct neighbours, whereas the fourth-order includes cells further away from the primary cell.

4.1.1.4 Staggered grid

Stronger coupling between the cell centred values of velocity and pressure can be obtained by making use of a staggered grid approach. This configuration stores pressure values in the cell centres of the main grid, while velocity values are stored in an additional offset grid. As a result, the velocity values are essentially stored at the cell faces of the main grid, as shown in Fig. 4.5 for a system which is solved in two-dimensions using

a staggered uniform grid. All other parameters are stored in the cell centres of the main grid. The staggered grid approach is beneficial because interpolation is not required, due to the already calculated velocity values in the displaced grid, representing the cell faces of the main grid [93]. A disadvantage of the staggered grid approach is that two separate grids need to be generated and maintained. Additionally, it is difficult to handle non-orthogonal grids in the staggered grid approach. As a result, this method is much more computationally expensive than the collocated grid approach.

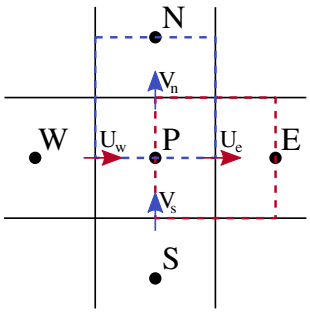

Figure 4.5: Two-dimensional staggered uniform grid [35].

The pressure gradient source term, S_{U_P}, for U_e between cell centres P, and E are shown in Eq. (4.15) for a collocated grid approach. In a staggered grid approach, the pressure gradient source term is given as

$$S_{U_P} = (p_P - p_E)\Delta y, \tag{4.40}$$

showing strong coupling between the velocity and pressure, because it directly depends on the values of cell centre P.

As previously mentioned, the momentum balance equation presents discretised equations, which are solved for U and V, once the pressure values are known. However, the continuity equation is not directly linked to pressure. As a result, pressure is modified by making use of an iterative procedure, to ensure that the obtained velocity meets the continuity requirement. The pressure is corrected in each iteration step, which iteratively modifies the velocity to a value that meets both the continuity and momentum equations. The coupling between pressure and velocity is known as the Pressure Correction scheme, which is explained in Sec. 4.1.1.5.

4.1.1.5 Pressure-velocity coupling

A well-known Pressure Correction scheme is the SIMPLE scheme, which stands for Semi Implicit Method for Pressure Linked Equations scheme, developed by Patankar [141]. The discretised momentum equation for U_e and V_n, can be given as

$$a_e U_e = \sum a_i U_i + S_{U_P} + S_U, \qquad a_n V_n = \sum a_i V_i + S_{V_P} + S_V. \tag{4.41}$$

In a staggered grid approach, U_e and V_n are cell-centred values in the displaced grid. Input from adjacent cell-centred values are represented on the right-hand side of Eq. (4.41) by the summations. S_{U_P} and S_{V_P} indicate pressure-gradient source terms, whereas S_U and S_V represent the remaining source terms after volume

integration. Eq. (4.41) can be rewritten as

$$U_e = \sum \frac{a_i U_i}{a_e} + D_U(p_P - p_E) + s_U, \qquad V_n = \sum \frac{a_i V_i}{a_n} + D_V(p_P - p_N) + s_V, \tag{4.42}$$

where $D_U = \Delta y/a_e$, $D_V = \Delta x/a_n$, $s_U = S_U/a_e$ and $s_V = S_V/a_n$. If one would assume initial values for the pressure, Eq. (4.42) could be solved to find values for U and V, which, generally, do not meet the continuity equation. Therefore, pressure and velocity corrections are introduced, resulting in the following corrected variables, as

$$p^* = p + p', \qquad U^* = U + U', \qquad V^* = V + V', \tag{4.43}$$

which meet both the continuity and momentum equations. p, U and V represent the mean components, whereas p', U' and V' indicate the fluctuation components of pressure and velocity. The first step in solving the corrections, is to substitute Eq. (4.43) into Eq. (4.42), which results into

$$(U_e + U'_e) = \sum \frac{a_i}{a_e}(U_i + U'_i) + D_U(p_P - p_E) + D_U(p'_P - p'_E) + s_U, \tag{4.44}$$

$$(V_n + V'_n) = \sum \frac{a_i}{a_n}(V_i + V'_i) + D_V(p_P - p_N) + D_V(p'_P - p'_N) + s_V. \tag{4.45}$$

Subsequently, subtracting Eq. (4.42) from Eqs. (4.44) and (4.45), gives

$$U'_e = \sum \frac{a_i U'_i}{a_e} + D_U(p'_P - p'_E), \qquad V'_n = \sum \frac{a_i V'_i}{a_n} + D_V(p'_P - p'_N), \tag{4.46}$$

which results in a relationship between pressure and velocity corrections that still meets the momentum equation. This method can be simplified by subdividing the corrections in two components as

$$p' = p'_1 + p'_2, \qquad U' = U'_1 + U'_2, \qquad V' = V'_1 + V'_2, \tag{4.47}$$

which are substituted in Eq. (4.46), resulting in

$$U'_{e1} + U'_{e2} = \sum \frac{a_i U'_i}{a_e} + D_U(p'_{P1} - p'_{E1}) + D_U(p'_{P2} - p'_{E2}), \tag{4.48}$$

$$V'_{n1} + V'_{n2} = \sum \frac{a_i V'_i}{a_n} + D_V(p'_{P1} - p'_{N1}) + D_V(p'_{P2} - p'_{N2}). \tag{4.49}$$

The SIMPLE scheme considers the two correction components as

$$U'_{e1} = D_U(p'_{P1} - p'_{E1}), \qquad U'_{e2} = \sum \frac{a_i U'_i}{a_e} + D_U(p'_{P2} - p'_{E2}), \tag{4.50}$$

$$V'_{n1} = D_V(p'_{P1} - p'_{N1}), \qquad V'_{n2} = \sum \frac{a_i V'_i}{a_n} + D_V(p'_{P2} - p'_{N2}), \tag{4.51}$$

establishing a relation between U'_1, V'_1, p'_1. The pressure and velocity components, indicated with subscript $_2$ on the right-hand side of Eq. (4.47), include the intricate part, which represents velocity corrections from adjacent cell-centred values. The corrected velocity values have to meet the continuity equation, shown in Eq. (4.2). After integration over cell volume P, the continuity equation can be written in discretised form as

$$(U^*_e - U^*_w)\Delta y + (V^*_n - V^*_s)\Delta x = 0, \tag{4.52}$$

which can be rewritten as

$$(U'_e - U'_w)\Delta y + (V'_n - V'_s)\Delta x = -S_m, \tag{4.53}$$

where $S_m = (U_e - U_w)\Delta y + (V_n - V_s)\Delta x$ represents the mass imbalance due to the original variables U and V. The SIMPLE scheme disregards the second correction components U'_2, V'_2, and P'_2, which, after substitution of Eqs. (4.50) and (4.51) into Eq. (4.53), results in

$$\begin{aligned}&\Delta y\left[(D_U)_e(p'_{P1} - p'_{E1}) - (D_U)_w(p'_{W1} - p'_{P1})\right]\\&+ \Delta x\left[(D_V)_n(p'_{P1} - p'_{N1}) - (D_V)_s(p'_{S1} - p'_{P1})\right] = -S_m,\end{aligned} \tag{4.54}$$

which after rearrangement can be written as

$$a_P p'_{P1} = a_e p'_{E1} + a_w p'_{W1} + a_n p'_{N1} + a_s p'_{S1} + S_U, \tag{4.55}$$

where $a_e = \Delta y(D_U)_e$, $a_w = \Delta y(D_U)_w$, $a_n = \Delta x(D_V)_n$, $a_s = \Delta x(D_V)_s$, $a_P = a_e + a_w + a_n + a_s$ and $S_U = -S_m$.

A drawback of the SIMPLE scheme is potentially slow convergence, which is due to the assumption that the second velocity and pressure correction components can be disregarded.

Several alternatives to the SIMPLE scheme have been developed, mainly to enhance the speed of convergence. One of these alternatives is the PISO scheme, which stands for Pressure Implicit solution by Split Operator method scheme, developed by Issa et al. [84]. The approach of the PISO scheme is identical to the SIMPLE scheme, however, the PISO scheme takes into account the previously abandoned second correction components, U'_2, V'_2, and P'_2.

In the PISO scheme the second part of Eqs. (4.50) and (4.51) are computed by

$$U'_{e2} = \sum \frac{a_i U'_{i1}}{a_e} + D_U(p'_{P2} - p'_{E2}), \qquad V'_{n2} = \sum \frac{a_i V'_{i1}}{a_n} + D_V(p'_{P2} - p'_{E2}). \tag{4.56}$$

Eq. (4.56) is substituted into the discretised continuity equation, shown in Eq. (4.52), as

$$(U'_{e2} - U'_{w2})\Delta y + (V'_{n2} - V'_{s2})\Delta x = 0. \tag{4.57}$$

As a result

$$\begin{aligned}&\Delta y\left[(D_U)_e(p'_{P2} - p'_{E2}) - (D_U)_w(p'_{W2} - p'_{P2})\right] + \Delta x\left[(D_V)_n(p'_{P2} - p'_{N2}) - (D_V)_s(p'_{S2} - p'_{P2})\right] =\\&\Delta y\left[\sum \frac{a_i U'_{i1}}{a_P}\right]_w - \Delta y\left[\sum \frac{a_i U'_{i1}}{a_P}\right]_e + \Delta x\left[\sum \frac{a_i V'_{i1}}{a_P}\right]_n - \Delta x\left[\sum \frac{a_i V'_{i1}}{a_P}\right]_s,\end{aligned} \tag{4.58}$$

can be generically written as

$$a_P p'_{P2} = a_e p'_{E2} + a_w p'_{W2} + a_n p'_{N2} + a_s p'_{S2} + S_U, \tag{4.59}$$

where the coefficients related to a_i with $i = n, e, s, w$ are identical to the ones in Eq. (4.55). Note, however, that S_U represents the terms on the right-hand side of Eq. (4.58). This set of linear equations for the pressure corrections p'_1 and p'_2, shown in Eqs. (4.55) and (4.59) can be solved, using the same methods employed for

solving the discretised momentum equations mentioned above. The corresponding corrections to the velocities, U_1', U_2', V_1' and V_2' are then obtained from Eqs. (4.50) and (4.51), and the pressure and velocities are thus all updated.

4.1.1.6 Chequerboard oscillations

Chequerboard oscillations are undesirable numerical instabilities, associated with collocated FVM schemes, which are encountered in the OpenFOAM software, causing poor distributions in a continuous domain. Variables alternate from cell to cell with under- and overestimated values, causing a jigsaw pattern, which resembles a chequerboard pattern [88, 165]. Several approaches are known to reduce or prevent chequerboard oscillations, of which two main methods are discussed below.

A method to avoid chequerboard oscillations is by making use of the previously explained staggered grid approach [141] in Sec. 4.1.1.4, which stores the pressure and velocity values at the cell centres of the main grid and an additional displaced grid. A strong coupling between velocity and pressure values is obtained, due to a direct relation with cell-centred values of cell P.

An alternative, frequently-used method to eliminate chequerboard oscillations, when utilizing a collocated grid, is through Rhie and Chow interpolation [151]. Rhie and Chow interpolation mimics a staggered grid approach and obtains the mass flux across cell faces by means of interpolation [217]. A correction term is introduced, which calculates the difference in pressure gradient at the cell face between the actual value and its interpolated value.

The derivation of the Rhie and Chow correction is explained on a one-dimensional uniform grid considering cell centres P and E with face e, as partly shown in the two-dimensional collocated uniform grid in Fig. 4.1. The second term on the right-hand side is defined as the Rhie and Chow correction [16]

$$U_e = \overline{U_e} - \overline{d_e}\left(\left.\frac{\partial p}{\partial x}\right|_e - \overline{\left.\frac{\partial p}{\partial x}\right|_e}\right), \tag{4.60}$$

where e represents the face in between cell centroids P and E. The component representing the interpolated pressure gradient, shown in Eq. (4.60) with an overbar notation, $\overline{\partial p/\partial x}$, is subtracted from the actual calculated value of the pressure gradient at cell face e, resulting in a modified value of the interpolated velocity at cell face e. $\overline{d_e}$ indicates the volume of the cell divided by the diagonal coefficients, (V_P/a_P), interpolated onto cell face e. The difference in values of the actual and interpolated pressure gradients contributes to the damping of the chequerboard oscillations, which gently vanishes with the convergence rate of the solution [16].

Before explaining the derivation of the Rhie and Chow correction technique, the origin of chequerboard oscillations requires more attention. Chequerboard oscillations are an undesirable effect, emerging from the discretisation of the momentum equation. However, it depends on what discretisation scheme is applied.

The origin of oscillations is shown by explaining the process of discretisation and interpolation in more detail below. For simplicity, only steady-state conditions are considered, which means that time-dependent terms and source terms in the momentum equation are excluded from this derivation. The discretised momentum

equation can be written as

$$a_P U_P + \sum a_i U_i = -\left.\frac{\partial p}{\partial x}\right|_P V_P, \tag{4.61}$$

which is identical to the discrete momentum equation shown in Eq. (4.29), however, without the source term S_U. The momentum equation essentially represents, on the left-hand side of the equation, convective and diffusive fluxes from adjacent cells into cell P, which has to be in equilibrium with the pressure gradient across cell P, written on the right-hand side of the equation. Eq. (4.61) can be rewritten as

$$U_P = -\frac{1}{a_P}\sum a_i U_i - \frac{V_P}{a_P}\left.\frac{\partial p}{\partial x}\right|_P, \tag{4.62}$$

which, again, can be rewritten as

$$U_P = \tilde{U}_P - d_P \left.\frac{\partial p}{\partial x}\right|_P, \qquad \text{where} \qquad \tilde{U}_P = -\frac{1}{a_P}\sum a_i U_i \qquad \text{and} \qquad d_P = \frac{V_P}{a_P}. \tag{4.63}$$

The discretised momentum equations can also be obtained for cells E and W, shown in Fig. 4.1, using the same approach, resulting in

$$U_E = \tilde{U}_E - d_E \left.\frac{\partial p}{\partial x}\right|_E, \qquad\qquad U_W = \tilde{U}_W - d_W \left.\frac{\partial p}{\partial x}\right|_W, \tag{4.64}$$

which are used later in this section. However, first, the pressure gradient component is studied, computed here using a central differencing scheme, where the gradient then becomes

$$\left.\frac{\partial p}{\partial x}\right|_P = \frac{p_e - p_w}{\Delta x} = \frac{p_E - p_W}{2\Delta x}, \tag{4.65}$$

which is the primary cause of the chequerboard oscillations. The pressure gradient of cell centre P does not depend on the pressure gradient values of cell P itself, but is rather only dependent on the cell-centred values of the east- and west-side neighbours of cell P, cells E and W. To understand why this leads to chequerboard oscillations, the continuity equation is discretised first, as

$$(U_e - U_w)\Delta y = 0, \tag{4.66}$$

which is identical to the first term shown in Eq. (4.52). It can be assumed that the momentum equation is solved before the continuity equation, which implies that velocity values at the cell centres are known. As a result, values at the cell faces, U_e and U_w, can be computed by means of linear interpolation, as

$$U_e = \frac{1}{2}(U_P + U_E), \qquad\qquad U_w = \frac{1}{2}(U_W + U_P). \tag{4.67}$$

Then, Eq. (4.67) is substituted into the discretised continuity equation, given in Eq. (4.66), as

$$\left(\frac{1}{2}(U_P + U_E)\right) - \left(\frac{1}{2}(U_W + U_P)\right) = 0, \tag{4.68}$$

which can be simplified as

$$U_E - U_W = 0. \tag{4.69}$$

The momentum equations for cells E and W, shown in Eq. (4.64), are substituted into Eq. (4.69), resulting in

$$\left(\tilde{U}_E - d_E \frac{\partial p}{\partial x}\bigg|_E\right) - \left(\tilde{U}_W - d_W \frac{\partial p}{\partial x}\bigg|_W\right) = 0. \tag{4.70}$$

Lastly, the pressure gradient terms of cells E and W can be substituted into Eq. (4.70), as

$$\left(\tilde{U}_E - d_E \frac{p_{EE} - p_P}{2\Delta x}\right) - \left(\tilde{U}_W - d_W \frac{p_P - p_{WW}}{2\Delta x}\right) = 0, \tag{4.71}$$

which represents the pressure calculation at cell centre P. p_{EE} and p_{WW} indicates the cell-centred pressure values of cells EE, located on the east-side of cell E, and cell WW, located on the west-side of cell W. Note that the pressure in cell P depends on the pressure in cells EE and WW, however, it does not depend on the pressure in adjacent cells E and W. As a result, two separate solutions for the pressure field are obtained, as illustrated in Fig. 4.6 by two different colours. Most software does not recognize chequerboard oscillations as an error, but as two separate solutions instead. Therefore, it is the task of the user to recognize chequerboard oscillations and to find a method to remove it.

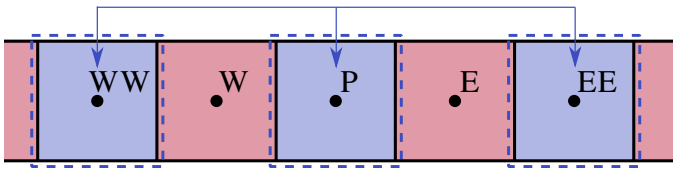

Figure 4.6: Two separate solutions resulting in a chequerboard pattern.

Rhie and Chow [151] derived a technique that removes the chequerboard oscillations on a collocated grid. They introduced a correction term, which is added to the method of linear interpolation. To obtain the velocity value at cell face e, linear interpolation is used

$$U_e = l_x U_P + (1 - l_x) U_E, \qquad \text{with} \qquad l_x = \frac{x_e - x_P}{x_E - x_P}, \tag{4.72}$$

resulting in an equation, which is identical to Eq. (4.25). The distance fraction is indicated by l_x, which equals 0.5 for a uniform grid. A correction term is added to the linear interpolation equation, resulting in

$$U_e = l_x U_P + (1 - l_x) U_E + \text{Correction}, \tag{4.73}$$

which can be rewritten as

$$U_e = \overline{U_e} + \text{Correction}, \tag{4.74}$$

where the overbar notation indicates linear interpolation [16]. Hence, $\overline{U_e}$ represents the velocity at cell face e, which is linearly interpolated from velocity values at cell centres P and E. The concept behind the correction term needs to be explained first. A staggered grid is introduced, as shown in Fig. 4.5, with cell centres of the staggered grid aligned with cell faces of the main grid. Momentum equations for the staggered grid are obtained, however, these will not be solved. Instead, these equations will be rearranged and rewritten in terms of the variables at cell centres P and E.

The discretised momentum equation of cell face e can be written similarly as done for the momentum equations

of cell E and W in Eq. (4.64), resulting in

$$U_e = \tilde{U}_e - d_e \left.\frac{\partial p}{\partial x}\right|_e , \tag{4.75}$$

where U_e is the desired velocity on cell face e. Rearrangement of Eq. (4.75) is required, because $\tilde{U}_e$ is unknown. Consequently, the main crux in the derivation of the correction term is the substitution of $\tilde{U}_e$, by using linear interpolation as

$$\tilde{U}_e = l_x \tilde{U}_P + (1 - l_x)\tilde{U}_E, \tag{4.76}$$

with $\tilde{U}_P$ and $\tilde{U}_E$ as known values from Eqs. (4.63) and (4.64). Substitution of these equations into Eq. (4.76), gives

$$\tilde{U}_e = l_x \left[U_P + d_P \left.\frac{\partial p}{\partial x}\right|_P \right] + (1 - l_x) \left[U_E + d_E \left.\frac{\partial p}{\partial x}\right|_E \right], \tag{4.77}$$

which can be rearranged by collecting the velocity and pressure gradient values, as

$$\tilde{U}_e = [l_x U_P + (1 - l_x) U_E] + \left[l_x d_P \left.\frac{\partial p}{\partial x}\right|_P + (1 - l_x) d_E \left.\frac{\partial p}{\partial x}\right|_E \right]. \tag{4.78}$$

The first two terms on the right-hand side in square brackets can be written in overbar notation, as the first term represents the linearly interpolated face velocity $\overline{U_e}$ and the second term indicates the interpolated gradient on cell face e. This results in

$$\tilde{U}_e = \overline{U_e} + \overline{d_e \left.\frac{\partial p}{\partial x}\right|_e} , \tag{4.79}$$

which is substituted back into the momentum equation of the staggered cell e, shown in Eq. (4.75), resulting in

$$U_e = \overline{U_e} - \overline{d_e} \left(\left.\frac{\partial p}{\partial x}\right|_e - \overline{\left.\frac{\partial p}{\partial x}\right|_e} \right), \tag{4.80}$$

which assumes that $d_e \approx \overline{d_e}$ [16]. Eq. (4.80), of which the second term is defined as the Rhie and Chow correction, is identical to Eq. (4.60), which implies that the derivation is complete.

4.1.2 Volume of Fluid Method

The volume of fluid (VoF) method is a numerical FVM technique, used in software, such as OpenFOAM, to describe the interface between two immiscible and incompressible fluids. This method determines volume fractions of one of the fluids across cell faces per time step, to describe a sharp interface [55, 153]. Two VoF methods can be distinguished, a geometric and algebraic approach. Geometric methods use information obtained from volume fractions to explicitly reconstruct the interface. This in contrast to the algebraic method, which solves a linear algebraic system to advect the interface, resulting in high computational efficiency [113]. Additionally, the algebraic approach does not have mesh restrictions. However, results are not as accurate as the geometric method, due to the inability to maintain a constant width of the interface. The implementation of the geometric method is more complex, with higher computational cost [153, 154].

An alternative numerical technique for multiphase flows, similar to the VoF method, is the Level-set (LS) method. This approach is more accurate than the VoF method at preserving a sharp interface, and in its interfacial properties, such as normal and curvature, which are mainly used for surface tension effects. However, a disadvantage of the LS method, compared with the VoF method, is the lack of mass conservation, which can result in poorly computed flow regions [42].

VoF methods comprise three steps. The first step is the interface reconstruction method, in which an isosurface concept is used for modelling the interface inside cells. The second step is the interface advection, which computes the total fluid volume transported across a cell face over a single time step. The third step is the surface tension method, which includes interfacial surface tension effects. This step is generally incorporated into the momentum equation as a source term, following the continuous surface force model [55], which is not included in the small-scale model. Therefore, the surface tension method is not further elaborated on in this section.

To explain the VoF method in more detail, an arbitrary domain D, with two incompressible isothermal and immiscible fluids, A and B, are considered, see Fig. 4.7. The interface between fluid A and B is indicated by surface S.

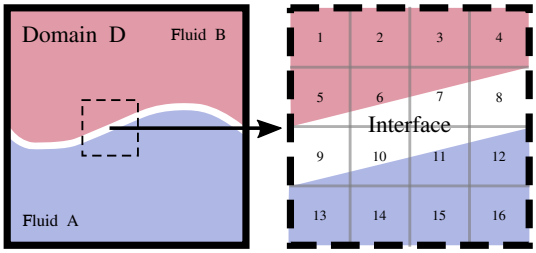

Figure 4.7: Cell 1-4: $\alpha_1 = 0$, cell 5-12: $0 < \alpha_1 < 1$, cell 13-16: $\alpha_1 = 1$.

The evolution of the interface can be described by the continuity equation [159], which can be written as

$$\frac{d}{dt}\int_{V_P} \rho dV + \int_{\partial V_P} (\rho \boldsymbol{U} \cdot \boldsymbol{n}) dS = 0, \tag{4.81}$$

in which the change of mass in a cell is written as the mass flux through the faces of the cell. V_P represents the volume of cell P with dV as the differential volume and ∂V_P its volume boundaries. dS indicates the differential surface, with $\boldsymbol{n}$ the unit normal vector pointing out of the volume. A prescribed velocity, $\boldsymbol{U}$, is assumed. Roenby et al. [155] disregarded viscous and surface tension effects for simplification. As a result of incompressibility, both fluids are constant in density ρ_A and ρ_B [153]. Density, or any other composite material parameter, shows a discontinuity at the interface, which therefore can be written in terms of the Heaviside function, H, as

$$\rho = \rho_A H + \rho_B (1 - H). \tag{4.82}$$

However, pure advection is considered in this example of incompressible fluids, resulting in a density-independent solution. Hence, the Heaviside function, H, is used to eliminate density from the equation

$$H = \frac{\rho - \rho_B}{\rho_A - \rho_B}, \tag{4.83}$$

where $H = 1$ for $\rho = \rho_A$ and $H = 0$ for $\rho = \rho_B$.

Solution domain D is, by means of the FVM, discretised into a finite number of cells. Substitution of Eq. (4.83) into Eq. (4.81) and additionally integrating Eq. (4.81) from time t to time $t + \Delta t$, results after some rearrangement in the updated volume fraction of cell P as

$$\alpha_P(t + \Delta t) = \alpha_P(t) - \frac{1}{V_P} \sum_k \int_t^{t+\Delta t} \int_{\partial V_P} (H\boldsymbol{U} \cdot \boldsymbol{n}) dS d\tau, \tag{4.84}$$

where $\alpha_P(t)$ is the volume fraction of cell P. A differential time frame within time step t to $t+\Delta t$ is represented by $d\tau$. The double integral indicates the total volume of fluid A transported across all cell faces $k = n, e, s, w$ of cell P for a given time interval, which is given as

$$\Delta V_k(t, \Delta t) = \int_t^{t+\Delta t} \int_{\partial V_P} (H\boldsymbol{U} \cdot \boldsymbol{n}) dS d\tau, \tag{4.85}$$

resulting in a fundamental equation, rewritten as

$$\alpha_P(t + \Delta t) = \alpha_P(t) - \frac{1}{V_P} \sum_k \Delta V_k(t, \Delta t). \tag{4.86}$$

Eq. (4.86) represents the fundamental continuity equation of cell P from which one must derive any consistent interface advection method. A continuity equation is solved for the volume fraction for each additional phase in a multiphase model. For two fluids A and B, as shown in the example given in Fig. 4.7, only one continuity equation has to be solved, as a constraint condition requires that in each cell in the domain the sum of the volume fractions equals one. The volume fraction of fluid A can be calculated as

$$\alpha_P(t) = \frac{1}{V_P} \int_{V_P} H dV. \tag{4.87}$$

Both the velocity field at the cell centres and the velocity field across the cell faces can be written similar to Eq. (4.87), as

$$\boldsymbol{U}_P(t) = \frac{1}{V_P} \int_{V_P} \boldsymbol{U} dV, \qquad \phi_k(t) = \int_{\partial V_P} (\boldsymbol{U} \cdot \boldsymbol{n}) dS, \tag{4.88}$$

where $\phi_k(t)$ is the volumetric face flux.

The evolution of the interface is described by an additional continuity equation for the volume fraction, which can be obtained by integration and discretisation of the continuity equation [153, 155], as shown in Eqs. (4.81) and (4.84).

Numerical difficulties are related to the discretisation of the continuity equation for the volume fraction. One of these difficulties is ensuring an interface that is constant in thickness. In other words, the prevention of artificial diffusion. Another difficulty is assuring a monotonic change of variables, also known as the boundedness criterion [202]. Commonly used discretisation schemes, such as the upwind differencing scheme (UDS) and the central differencing scheme (CDS) result in numerical diffusion or dispersion [201]. Accordingly, higher-order discretisation schemes, such as CICSAM (Compressive Interface Capturing Scheme for Arbitrary Meshes) and HRIC (High-Resolution Interface Capturing scheme) are introduced by Wacławczyk and Koronowicz [202], which focus on the convective term in Eq. (4.81), to preserve a sharp interface between

phases [131].

Wacławczyk and Koronowicz [202] compared both high-resolution schemes, CICSAM and HRIC. It can be concluded that CICSAM is less sensitive to diffusion and preserves the shape of the interface better. The main disadvantage of both schemes is their low order of accuracy, which requires further investigation [202]. The difficulty regarding boundedness is tackled using MULES (Multidimensional Universal Limiter with Explicit Solution).

Roenby et al. [153] developed the isoAdvector algorithm, which is an alternative to MULES. The isoAdvector method presents promising results, showing a sharper interface, shorter computations, and a lower sensitivity to mesh size and element types [153, 154, 155]. The algorithm is explained, utilizing domain D presented in Fig. 4.7, in Sec. 4.1.2.1.

4.1.2.1 IsoAdvector algorithm

The isoAdvector algorithm, based on the VoF method, has been developed by Roenby et al. [153]. The algorithm combines advantages of both the algebraic and geometric methods. It performs on an arbitrary mesh, preserves the accuracy, and minimizes the geometric operations to ensure acceptable calculation times. The objective of the isoAdvector method is to find an approximation for the volume transport, $\Delta V_k(t, \Delta t)$, of a fluid across a cell face for a given time interval. New features are developed, consisting of two parts, which are combined with existing VoF characteristics.

In the first part, the surface reconstruction step, an isosurface concept is considered, which redistributes fluids inside interface cells that are occupied by two fluids. Both sides of the cell occupy exclusively a single fluid. The second part, the interface advection step, models the motion of the face-interface intersection lines and quantifies the fluid, which after integration over the time step, results in a good approximation of the transported volume across the cell face for a given time interval [155]. The fundamental equation, given in Eq. (4.86), does not contain information about the distribution of fluids inside a cell. Hence, a sub-grid model has been introduced in the isoAdvector method. The sub-grid model can only be applied on the condition that the cell size is small enough so that the interface is fully absorbed by the mesh. When meeting that requirement, computation of the isosurface results in an adequate distribution of fluids in the cell [153].

Cell P represents one of the interface cells shown in Fig. 4.7. The volume fraction of fluid A in cell P over a single time step t to $t + \Delta t$ is represented by $\alpha_P(t + \Delta t)$, and obtained by completing two parts. The first part starts with the reconstruction of the fluid interface inside cell P from data at the previous time step, t, using an isosurface approach that primarily interpolates volume fractions from the centre to all vertices of cell P [153, 155].

By making use of an isovalue, α_0, a constructed isosurface inside cell P can be obtained. A correct value for α_0 can be found by investigating all edges of cell P. Cut edges refer to edges with volume fractions at one end of a vertex larger than α_0 and at the other end of the same vertex smaller than α_0. For these relevant edges, intersection points are computed by linear interpolation, which are connected across cell faces resulting in the cell-isosurface intersection. Fig. 4.8 shows cell P with vertices in red and intersection points in blue. The intersection points form an isoface indicated in grey. The isoface cuts cell P into two sub-cells and redistributes fluids A and B, such that fluid A is placed next to adjacent cells containing fluid A and

fluid B is placed next to adjacent cells containing fluid B [153, 155].

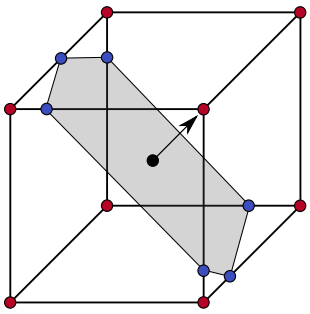

Figure 4.8: Schematic diagram adapted from Roenby et al. [155], showing interface cell P with a reconstructed isoface in grey. Vertices and intersection points are illustrated in red and blue. The centre of the isoface and unit normal vector are depicted in black.

If one would take α_0 values ranging from the minimum to the maximum α values found in the vertices of cell P, the isosurface would travel across the volume of cell P. The selected isovalue, α_0, is based on the volume fraction from the previous time step, $\alpha_P(t)$, with the corresponding isoface that has subdivided the cell into two sub-cells [155].

In the second part, the interface advection step, the position of the interface inside cell P at the previous time step t is used to approximate the quantities of fluids A and B that moved across cell face k over the time step t to $t + \Delta t$ [155]. To obtain $\alpha_P(t + \Delta t)$, the velocity on the interval is required, which is found by assuming a constant velocity over the time step t to $t + \Delta t$. Additionally, the velocity on the face dotted with the differential face normal vector can be approximated in terms of the volumetric face flux, $\phi_k(t)$, as

$$(\boldsymbol{U} \cdot \boldsymbol{n}) dS \approx \frac{\phi_k(t)}{|\boldsymbol{S}_k|} dS, \qquad \text{with} \qquad \boldsymbol{S}_k = \int_{\partial V_P} \boldsymbol{n} dS. \tag{4.89}$$

where $dS = d|\boldsymbol{S}|$ and $\boldsymbol{S}_k$ is the mean normal vector of cell faces k pointing in outward direction of cell P. $\Delta V_k(t, \Delta t)$ can be approximated by substitution of Eq. 4.89 into Eq. 4.85, resulting in

$$\Delta V_k(t, \Delta t) \approx \frac{\phi_k(t)}{|\boldsymbol{S}_k|} \int_t^{t+\Delta t} A_k d\tau, \tag{4.90}$$

representing an approximation of the total volume of fluid A that moves across cell face k for a time interval t to $t + \Delta t$, with the submerged area of cell face k defined as

$$A_k = \int_{\partial V_P} H dS. \tag{4.91}$$

Fig. 4.9 shows a schematic diagram of the top face of cell P, illustrating face-interface intersection lines at t and $t + \Delta t$. To find an estimate of how much the velocity moves the isoface within cell P, it is of importance to find estimations of the variation of A_k over time within time step t to $t + \Delta t$.

Note that first the velocity is interpolated to the centre of the isoface at time t, shown in Fig. 4.8 by a black dot. The dot product is taken with the unit normal vector of the isoface, also shown in Fig. 4.8, resulting in the velocity perpendicular to the isoface. The location of all vertices and the centre of the isoface at time step t are known, which means that the perpendicular distance between each vertex and the centre of

the isoface can be computed [153, 155].

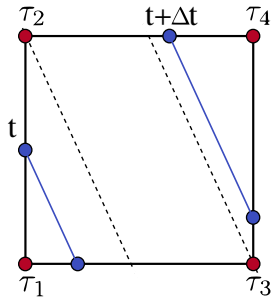

Figure 4.9: Schematic diagram adapted from Roenby et al. [155], showing face interface intersection lines in blue at time interval t to $t + \Delta t$. The black dotted lines represent the 'time of arrival' of all vertices with the shaded area illustrating a subinterval between τ_2 and τ_3, which should not be confused with the isoface shown in Fig. 4.8.

As a result, the 'time of arrival' of all vertices can be obtained, shown in Fig. 4.9 by τ_i with $i = 1, 2, 3, 4$ with τ_1 and τ_4 positioned outside of the of time interval t to $t + \Delta t$. Between τ_2 and τ_3 the face-interface intersection line has moved in a quadrilateral-shaped volume. Assuming that the motion of the line is constant in time, then A_k can be expressed in terms of τ on the subinterval between τ_2 and τ_3.

If one would repeat this exercise for all subintervals, a value for A_k is obtained. Integration over time results in a good approximation of the total volume that has been moved across the cell face, meaning a value for $\Delta V_k(t, \Delta t)$ has been found [153, 155].

4.1.3 Boundary conditions

Boundary conditions (BCs) are required to solve the system of differential equations, used as additional constraints to the system. The obtained solution satisfies both the differential equation and the BCs. Generally, a boundary is subdivided into a set of patches. A patch comprises one or more enclosed areas of the boundary surface, which do not have to be physically linked.

OpenFOAM has a large variety of BCs available. However, this section will only focus on two types: the zero-gradient BC and the periodic BC. The zero-gradient BC and periodic BC are explained in more detail, because these ones are applied in the small-scale model.

The zero-gradient BC simply extrapolates the quantity to the patch from the nearest cell value. This implies that the quantity developed in space and its gradient is equal to zero in the direction perpendicular to the boundary. In mathematical notation a zero-gradient BC can be written as

$$\frac{\partial}{\partial \boldsymbol{n}}\phi = 0, \tag{4.92}$$

where $\boldsymbol{n}$ represents the normal vector and ϕ an arbitrary variable in the domain. Fig. 4.10(a) illustrates the zero-gradient BC by means of a schematic drawing. The boundary is named 'right'. The values of an arbitrary variable, ϕ, are shown at the cell centre, indicated by black arrows. The red arrows represent the extrapolated values, assuming a gradient equal to zero.

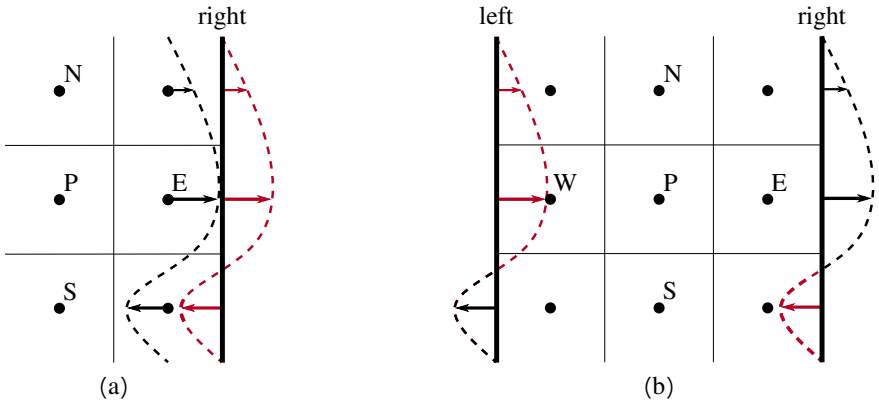

Figure 4.10: Schematic drawing of the two types of BCs used in this study, illustrating **(a)** zero-gradient BCs **(b)** periodic BCs.

The periodic BC can only be used when the expected flow pattern is of a periodically repeating nature, which implies for example a forcing either spatially or temporally constant. Periodic BCs are used to approximate a larger (infinite) domain by using a smaller part, a unit cell, to reduce computational effort. This BC represents a coupling condition between a pair of patches.

Fig. 4.10(b) illustrates the periodic BC. The boundaries are named 'left' and 'right'. Values at the cell faces are indicated by a black arrow, which are linearly interpolated from their adjacent cell values. The red arrows represent the coupled values. Cell faces on each coupled patch must have the same topology, which means that the patches must have collocated points such that a one-to-one mapping exists between the faces on each side. Patches are strictly paired, with variable values at the one boundary equal to variable values at the matched boundary. The coupling is treated implicitly using the cell values adjacent to each pair of periodic patches. The values at the cell faces are obtained, using linear interpolation between the cell values.

4.2 Implementation details of the small-scale sea ice model in OpenFOAM

The OpenFOAM features, explained in Sec. 4.1, are applied in this section to the small-scale sea ice model. The implementation in OpenFOAM is described, by making use of the FVM and VoF method. Both the ice floe rheology and grease ice rheology are discussed thoroughly, showing a combined set of equations. The numerical stability and convergence of the model are described and the applied boundary conditions, as well as the divergence schemes in the small-scale model are mentioned.

4.2.1 Ice type separation via the Volume of Fluid Method

In order to spatially distinguish between the material constituents, the VoF method is used. The VoF method is a numerical technique, describing the interface between two immiscible and incompressible fluids in a computational fluid dynamics model. This method determines volume fractions of fluids across the cell faces per time step and distinguishes both materials based on the non-dimensional parameter α [153, 154, 155].

The VoF method is complemented with an interface compression scheme, that enforces a sharp interface

between dominantly solid-like ice floes and viscous-plastic fluid-like interstitial grease ice. This project specifically makes use of the IsoAdvector scheme, discussed in Sec. 4.1.2.1. Cells containing exclusively ice floes or grease ice have phase fractions, α, of 1 or 0, respectively. All intermediate values ($0 < \alpha < 1$) have no physical interpretation, but are needed in the FVM to ensure a smoothly varying continuous field. The region of $0 < \alpha < 1$ should be numerically constrained to the thin interface between the two ice materials.

The VoF method in the small-scale model, with its non-dimensional parameter α, differentiates between ice floes and grease ice. This can be formulated as

$$\alpha_2 = 1 - \alpha_1, \tag{4.93}$$

where $\alpha_1 = 1$ represents ice floes and $\alpha_1 = 0$ (and thus $\alpha_2 = 1$) represents grease ice.

With the VoF approach in mind, the normalised momentum balance equation, shown in Eq. (3.3), can be written as

$$h\left(\frac{\partial \boldsymbol{U}}{\partial t} + (\boldsymbol{U}\cdot\nabla)\boldsymbol{U}\right) = \alpha_1\left(\nabla\cdot\boldsymbol{\sigma}'_f\right) + \alpha_2\left(\nabla\cdot\boldsymbol{\sigma}'_g\right) + \boldsymbol{S}', \tag{4.94}$$

where the normalised Cauchy stress tensor, $\boldsymbol{\sigma}'$, is written either in terms of the normalised ice floe stress, $\boldsymbol{\sigma}'_f$, or grease ice stress, $\boldsymbol{\sigma}'_g$. The normalised source terms, which originate from the atmospheric and oceanic forcing, are included in the source term $\boldsymbol{S}'$.

Eq. (4.94) shows how the VoF method distinguishes between the normalised ice floe stress and grease ice stress. The same method is applied to all material parameters, such as the sea ice density and thickness, given as

$$\rho = \alpha_1\rho_f + \alpha_2\rho_g, \qquad\qquad h = \alpha_1 h_f + \alpha_2 h_g, \tag{4.95}$$

where ρ_f and ρ_g represent the density of ice floes and grease ice, respectively, with corresponding thickness, indicated by h_f and h_g.

The momentum equation is written to solve the system of the form

$$\boldsymbol{M}\boldsymbol{x} = \boldsymbol{b}, \tag{4.96}$$

where matrix $\boldsymbol{M}$ represents a sparsely populated, diagonally dominant matrix. Additionally, implicit and explicit terms are distinguished. Implicit terms are included within matrix $\boldsymbol{M}$, whereas explicit terms are incorporated as a source within vector $\boldsymbol{b}$. The variables that need to be solved are represented by vector $\boldsymbol{x}$. The momentum equation is treated semi-implicitly, which requires iteration until convergence is obtained.

Substitution of Eqs. (3.11) and (3.15) in Eq. (4.94), results, after rearrangement, in

$$h\left(\frac{\partial \boldsymbol{U}}{\partial t}+(\boldsymbol{U}\cdot\boldsymbol{\nabla})\boldsymbol{U}\right)=\alpha_1\left(\underbrace{\nabla\cdot\boldsymbol{\sigma}_f'^b+\nabla\cdot(\Delta t\mu'(\boldsymbol{\nabla U}+(\boldsymbol{\nabla U})^T)+\nabla\cdot(\lambda'\boldsymbol{I}\mathrm{tr}(\boldsymbol{\nabla U}))}_{\text{explicit}}\right) \tag{4.97}$$
$$+\alpha_2\left(\underbrace{\nabla\cdot(\eta'\boldsymbol{\nabla U})}_{\text{implicit}}+\underbrace{\nabla\cdot(\eta'\boldsymbol{\nabla U})^T)+\nabla\cdot(\zeta'-\eta')\boldsymbol{I}\mathrm{tr}(\boldsymbol{\nabla U})-\boldsymbol{\nabla}p_g'}_{\text{explicit}}\right)+\boldsymbol{S}',$$

where $p_g'=P_g'/2$. As a result, a combined set of equations is obtained. The implicit and explicit terms are indicated in Eq. (4.97) for both the ice floe and grease ice rheology. The normalised viscosities, Lamé parameters and grease ice strength parameter are represented by a superscript $'$.

Both ice floes and grease ice are modelled in a continuum fashion, using the FVM implementation in OpenFOAM. As a result, the form drag, acting at the circumference of the ice floes due to the velocity differences of floes and the surrounding grease ice, is implicitly accounted for by the continuity requirement of the velocity field throughout the domain. This requirement, in a continuum approach comprising of two ice constituents, enforces the velocity continuity at the interface.

The continuity requirement also governs the interaction between colliding ice floes, which resists the collision forces via the stress and strain rate response. As a result, the floe-floe and the floe-grease ice interactions are naturally accounted for in terms of their normal and tangential force components.

4.2.2 Numerical stability and convergence

The numerical solution of the combined set of equations, shown in Eq. (4.97), can be stabilised to improve convergence. This is done through the addition of implicit terms, which are subtracted as explicit terms. Both the implicit and explicit terms cancel each other out at convergence within a single time step, which implies that the net contribution is zero. This trick is referred to as matrix conditioning [82].

The reason for adding implicit terms into matrix $\boldsymbol{M}$, is to increase the portion of implicit terms. Otherwise, the explicit portion of the diffusive terms would be larger than the implicit part. As a result the solution would be driven by the set of explicit source terms, which negatively impact convergence rates [82]. It has the further additional benefit of improving the diagonal dominance of the matrix, which improves the convergence speeds of sparse, iterative, linear solvers.

The term $\nabla\cdot(\Delta t(2\mu'+\lambda')\boldsymbol{\nabla U})$ is added to the ice floe rheology as implicit term and subtracted as explicit term, whereas $\nabla\cdot(\zeta'\boldsymbol{\nabla U})$ is implicitly added to the grease ice rheology and subtracted explicitly. This

results in the momentum equation, which can be written as

$$
\begin{aligned}
h\left(\frac{\partial \boldsymbol{U}}{\partial t}+(\boldsymbol{U}\cdot\boldsymbol{\nabla})\boldsymbol{U}\right) =& \alpha_1\left(\underbrace{\nabla\cdot(\Delta t(2\mu'+\lambda')\boldsymbol{\nabla U})}_{\text{implicit}}\right) \\
&+\alpha_1\left(\underbrace{\nabla\cdot\boldsymbol{\sigma}_f'^b+\nabla\cdot(\Delta t\mu'(\boldsymbol{\nabla U}+(\boldsymbol{\nabla U})^T)+\nabla\cdot(\lambda'\boldsymbol{I}\mathrm{tr}(\boldsymbol{\nabla U}))-\nabla\cdot(\Delta t(2\mu'+\lambda')\boldsymbol{\nabla U})}_{\text{explicit}}\right) \\
&+\alpha_2\left(\underbrace{\nabla\cdot(\eta'+\zeta'\boldsymbol{\nabla U})}_{\text{implicit}}+\underbrace{\nabla\cdot(\eta'\boldsymbol{\nabla U})^T)+\nabla\cdot(\zeta'-\eta')\boldsymbol{I}\mathrm{tr}(\boldsymbol{\nabla U})-\nabla\cdot(\zeta'\boldsymbol{\nabla U})-\boldsymbol{\nabla}p_g'}_{\text{explicit}}\right)+\boldsymbol{S}'.
\end{aligned}
\tag{4.98}
$$

A more detailed explanation regarding the implicit and explicit contribution of the ice floe rheology, is discussed in Sec. 4.2.3.

When a coupled system is solved by means of iteration, changes in one variable can affect the coefficients determining another. This could lead to slow convergence or even divergence. The convergence can be improved by limiting the change in each variable between corrector steps. This is done by means of relaxation of the solution. To do this for the velocity between iterations, velocity is updated before each solution of the momentum equation [82].

The easiest method is choosing a fixed value for the relaxation parameter, ω, for all time steps. The relaxation parameter is, however, extremely problem specific, which implies that a fixed value is most ineffective. The value of the relaxation parameter needs to be small enough to ensure that the iteration does not diverge, but should be as large as possible to make most use of the new solution and to avoid unnecessary iterations. Therefore, the optimal ω value is problem specific and unknown beforehand, as it may vary between time steps. Even an optimal fixed value leads to more iterations than a suitable dynamic relaxation parameter [101].

Accordingly, the small-scale model applies Aitken's dynamic relaxation method, which is commonly used within the community of fluid-structure interactions. The main concept of Aitken's method is to utilize values from two previous iterations, to improve the current solution. The update of the velocity, including a relaxation factor, ω_k, results in

$$
\boldsymbol{U}_{k+1}=\boldsymbol{U}_k+\omega_k\boldsymbol{r}_{k+1}, \tag{4.99}
$$

where k represents the current coupling iteration count and $\boldsymbol{r}_{k+1}$ the solution residual. Aitken's dynamic relaxation defines an update rule to dynamically modify the relaxation parameter using the residual results from two previous iterations. This relaxation method has proven to significantly accelerate the overall behaviour of convergence.

4.2.3 Implementation of the ice floe rheology

The generalised Hooke's law ideally represents the elastic ice floe rheology with small deformations, where ice floes undeform to their original unstressed state after unloading. However, the method proposed in the small-scale model has a Hookean-like flow rule for solid regions. Given the implementation of the floe rule, while the model is capable of representing 'solid-like' behaviour, it does not account for elastic unloading

back to the original undisplaced configuration. In other words, once an ice floe has been deformed, it won't undeform to its original state. This issue, however, is effectively limited as only ice floes are considered deeper into the MIZ, where gentle floe collisions take place. Therefore, the kinetic energy of colliding ice floes can be considered to be largely dissipated due to inelastic deformations of the soft outer rim of ice floes.

A detailed description of the implementation of the ice floe rheology is discussed, explaining the phenomenon of chequerboard patterns which is a major complication of the stress distribution, when solving the solid flow rule using the FVM method. Given the limitations of the FVM method, fully avoiding chequerboarding is not possible, when considering the solid flow rule. This section will therefore elaborate on an alternative formulation to avoid chequerboard oscillations.

The normalised momentum balance equation, shown in Eq. (4.94), is given as

$$h\left(\frac{\partial \boldsymbol{U}}{\partial t}+(\boldsymbol{U}\cdot\nabla)\boldsymbol{U}\right)=\alpha_1\left(\nabla\cdot\boldsymbol{\sigma}'_f\right)+\alpha_2\left(\nabla\cdot\boldsymbol{\sigma}'_g\right)+\boldsymbol{S}', \tag{4.100}$$

showing the divergence of the normalised ice floe stress tensor, $\nabla\cdot\boldsymbol{\sigma}'_f$.

As previously mentioned in Chap. 3, Hooke's law can be rewritten in linearised form, as

$$\underbrace{\boldsymbol{\sigma}'^{b+1}_f}_{\text{current time step}} = \underbrace{\boldsymbol{\sigma}'^{b}_f}_{\text{previous time step}} + \underbrace{\Delta t\left(\mu'(\boldsymbol{\nabla U}+(\boldsymbol{\nabla U})^T)+\lambda'\boldsymbol{I}\mathrm{tr}(\boldsymbol{\nabla U})\right)}_{\text{current time step}}, \tag{4.101}$$

where the stress is defined in terms of the velocity. The calculation of the stress at the current time step, shown on the left-hand side of Eq. (4.101), depends on the stress from the previous time step plus a sea ice velocity-dependent stress component at the current time step. Stress from the previous time step, $\boldsymbol{\sigma}'^{b}_f$, is entirely decoupled from $\boldsymbol{U}$ and is essentially a constant for a given time step, which cannot be updated.

A collocated FVM approach, however, cannot track the stress state without a numerical complication, which is the chequerboard pattern in the stress distribution, leading to undesirable stress results. Chequerboard oscillations can occur under two circumstances i) stress from the previous time step, as the stress is essentially a constant, ii) stress from the current time step. The same issue arises when solving for the pressure gradient, explained in Sec. 4.1.1.1. The main difference, however, is that unlike the pressure gradient, $\boldsymbol{\sigma}'^{b}_f$ is a constant, and therefore cannot be updated within the current time step. This is an unsolvable problem given the current choice of the implemented framework and requires an alternative stress approach.

As previously mentioned in Sec. 4.2.2, the divergence of the normalised ice floe stress tensor, $\nabla\cdot\boldsymbol{\sigma}'_f$, can be split, and written in implicit and explicit terms, as

$$\begin{aligned}\nabla\cdot\boldsymbol{\sigma}'_f =& \alpha_1\left(\underbrace{\nabla\cdot(\Delta t(2\mu'+\lambda')\boldsymbol{\nabla U})}_{\text{implicit}}\right)\\ &+\alpha_1\left(\underbrace{\nabla\cdot\boldsymbol{\sigma}'^{b}_f+\nabla\cdot(\Delta t\mu'(\boldsymbol{\nabla U}+(\boldsymbol{\nabla U})^T)+\nabla\cdot(\lambda'\boldsymbol{I}\mathrm{tr}(\boldsymbol{\nabla U}))-\nabla\cdot(\Delta t(2\mu'+\lambda')\boldsymbol{\nabla U})}_{\text{explicit}}\right),\end{aligned} \tag{4.102}$$

where, $\nabla \cdot (\Delta t(2\mu' + \lambda')\boldsymbol{\nabla U})$, is added implicitly and subtracted explicitly for stabilisation, to improve convergence and to resolve chequerboard oscillations. If the implicit and explicit terms were not included, then chequerboarding would occur when considering the stress from the current time step. Mathematically, at convergence, both the added implicit and explicit terms cancel each other out, however, they are included to add crucial computational stability in the spirit of the Rhie and Chow interpolation. Note, however, as mentioned in Sec. 4.1.1.6, that the Rhie and Chow interpolation solves chequerboard oscillations referring to the current time step. This implies that chequerboard oscillations in the small-scale model, are not fixed by the Rhie and Chow interpolation, as these oscillations originate from stress at the previous time step.

In the alternative stress approach, implicit and explicit terms are separately implemented, starting with the normalised explicit part of the stress divergence, which can be written as

$$\nabla \cdot \boldsymbol{\sigma}_f'^{b+1} = \nabla \cdot (\boldsymbol{\sigma}_D' - \Delta t(2\mu' + \lambda')\boldsymbol{\nabla U}), \tag{4.103}$$

where $\boldsymbol{\sigma}_D'$ represents the stress at the current time step, given as

$$\boldsymbol{\sigma}_D' = \Delta t(\mu'(\boldsymbol{\nabla U} + (\boldsymbol{\nabla U})^T) + \lambda' \boldsymbol{I}\mathrm{tr}(\boldsymbol{\nabla U})). \tag{4.104}$$

The second term on the right-hand side of Eq. (4.103), subtracted from $\boldsymbol{\sigma}_D'$, is implicitly added to the left-hand side of the equation of motion as a Laplacian term. The Laplacian operator is mathematically the divergence of the gradient of a function. A Laplacian term computes gradients at the cell centres, and subsequently interpolates gradients to face centres, whereas an explicit divergence term interpolates cell centred values to face centres. Hence, it includes both gradient and cell centred values for corrections.

Including the stability terms resolved the oscillations associated with stress from the current time step. As shown in Eq. (4.102), an additional benefit of adding a Laplacian term to the equation of motion is the inclusion of an implicit stress component, which is velocity dependent. However, the stability terms do not address the chequerboard oscillations associated with stress from the previous time step. Therefore, this stress component requires a different approach, which is discussed below.

The second normalised explicit part of the stress divergence can be written as

$$\nabla \cdot \boldsymbol{\sigma}_f'^{b}, \tag{4.105}$$

which represents the divergence of the stress tensor from the previous time step. Stress from the previous time step is a constant and cannot be updated within the current time step. Accordingly, in the alternative stress approach, the stress from the previous time step is advected, to ensure that the old stress moves along with the moving ice floes, as

$$\left(\frac{\partial \sigma_{f,ij}'^{b}}{\partial t} + \nabla \cdot (\sigma_{f,ij}'^{b} \boldsymbol{U}) \right) = 0, \tag{4.106}$$

where $\sigma_{f,ij}'^{b}$ is a scalar, which represents each stress component from the previous time step, with i and $j = 1, 2, 3$. The cell-centred values of $\nabla \cdot \boldsymbol{\sigma}_f'^{b}$ are computed explicitly by using the formal definition of the divergence, as

$$\nabla \cdot \boldsymbol{T}_i = \mathrm{tr}(\boldsymbol{\nabla T}_i), \tag{4.107}$$

rather than the default divergence operator in OpenFOAM. The default operator makes use of Gauss' theorem. This, however, as previously explained in Sec. 4.1.1.1, results in chequerboard oscillations.

By manually redefining the divergence operator, using a combination of gradient terms, a higher order gradient stencil can be used. Three separate vectors are created, $\boldsymbol{T}_i$, with $i = 1, 2, 3$. Each vector represents a part of $\boldsymbol{\sigma}_f'^b$, as

$$\boldsymbol{\sigma}_f'^b = \begin{pmatrix} \boldsymbol{T}_1 \\ \boldsymbol{T}_2 \\ \boldsymbol{T}_3 \end{pmatrix} = \begin{pmatrix} \sigma_{f,11}'^b & \sigma_{f,12}'^b & \sigma_{f,13}'^b \\ \sigma_{f,21}'^b & \sigma_{f,22}'^b & \sigma_{f,23}'^b \\ \sigma_{f,31}'^b & \sigma_{f,32}'^b & \sigma_{f,33}'^b \end{pmatrix}, \tag{4.108}$$

where the gradient operators are set to fourth-order least-squares [57], allowing the inclusion of information from more neighbouring cells.

If one could account for the full historical stress then it would be possible to solve for the full stress state, and therefore be able to account for elastic unloading. While the above treatment resolves chequerboard oscillations, when considering partial information from the previous time steps, chequerboarding does still happen if the full previous time step stress is retained. This is discussed in more detail in Sec. 5.3.4.

4.2.4 Spatial and temporal discretisation schemes

Ice floes and interstitial grease ice are spatially discretised in OpenFOAM with the finite volume approach, as shown in the Appendix in Chap. 10. The discretisation of the divergence and gradient terms of an arbitrary variable ϕ, at cell centroids and faces, is essential to compute the discretised set of equations [39].

In the small-scale model, the second- and fourth-order least-squares gradient schemes and the Gauss linear divergence scheme are used for the spatial discretisation. The Gauss divergence scheme is the default choice for the computation of the finite volume discretisation of Gaussian integration. It requires the interpolation of values from cell centres to cell faces. The Gauss entry requires a more specific interpolation scheme. The small-scale model makes use of the linear interpolation scheme, also known as the central differencing scheme.

The Euler implicit method is applied for temporal discretisation. The spatially, and temporal discretisation schemes are explained in Sec. 4.1.

4.2.5 Applied boundary conditions

The zero-gradient BC, explained in Sec. 4.1, is used in the majority of the simulations in this project. This BC is, however, restricted in its implementation. The domain boundary is numerically approximated by horizontal zero-gradient BCs, which implies that the gradient of all variables in the direction perpendicular to the boundary is assumed zero. This is incorrect, as for any non-boundary cell in the domain, cell face values are found by means of linear interpolation. This results in an error, which is introduced to cell values directly adjacent to the boundary.

It is, potentially, possible to solve this boundary issue, by developing a BC from scratch. However, a truly

suitable solution in the application of the small-scale model, has not been found yet. This boundary error does, however, not affect the variable values further away from the boundary. To overcome this inconsistency in all numerical test cases performed in this study, the sea ice domain is enlarged. Subsequently, only the inner portion of the domain is used for the analysis of the results, to ensure that any inconsistencies resulting from the boundary does not influence the results.

The period BC is used in Chap. 5. Applying this BC to all variables in the sea ice domain, essentially means that ice floes and grease ice leaving the domain on for example the right-hand side, enter the domain on the paired left-hand side.

Chapter 5

Model parameterisation and preliminary numerical studies

In this chapter all general parameters used in all simulations conducted in this project, are presented in Sec. 5.1. Preliminary numerical convergence analyses are described in Sec. 5.2, creating conditions for simulations conducted in Chap. 6. In Sec. 5.3 plausibility studies are discussed, describing simplified sea ice dynamics problems, which contribute to the validation and verification of the small-scale model.

5.1 Model parameterisation

Both the theory and the implementation of the small-scale model, as described in Chaps. 3 and 4, respectively, are applied to a wide range of simulations, with different domain sizes, sea ice layouts and external forcings. Parameter values that are the same in all simulations throughout this thesis, are listed in Tab. 5.1.

Table 5.1: General parameters used in all simulations conducted in this project.

Parameter	**Definition**	**Value**	**Unit**
C_{10}	air drag coefficient at a height of 10m	0.0015 [172]	-
e_Y	yield surface axes ratio	2 [68, 81, 104]	-
E_Y	Young's modulus	8.7×10^6 [161]	Nm^{-1}
g	gravitational acceleration	9.81	ms^{-2}
$h_{f,g}$	thickness ice floes and grease ice	0.31, 0.1 [116]	m
h_w	submerged ice floe thickness	0.189	m
α_C	Charnock constant	0.011 [43, 158]	-
Δ_{min}	lower limit of the effective deformation rate	2×10^{-7} [104]	s^{-1}
$\theta_{a,w}$	air and water turning angle	0 [182]	rad
κ	von Kármán constant	0.41 [12, 43]	-
λ	first Lamé parameter	6.4×10^6 [161]	Nm^{-1}
μ	second Lamé parameter	3.3×10^6 [161]	Nm^{-1}
ν	Poisson's ratio	0.33 [66]	-
$\rho_{f,g}$	density ice floes and grease ice	879, 997 [149]	kgm^{-3}
$\rho_{a,w}$	air and sea water density	1.3 [104], 1026 [120]	kgm^{-3}

The thickness and density of ice floes are based on averaged values of in situ measurements taken in the Antarctic during the SCALE[1] winter cruise in 2019 by Skatulla et al. [168]. The thickness and density of grease ice are based on values found in literature [116, 149], assuming that grease ice is a two-phase mixture, consisting of a solid, pure ice, and a liquid, seawater. A solid ice fraction of 20% is considered [116]. The yield surface axes ratio of grease ice is derived from values found in Hibler [68], Hunke and Dukowicz [81] and Leppäranta and Hibler [104].

The effective elastic ice floe parameters are approximated in the spirit of characteristics for uncompacted snow [161], considering the very soft rim of ice floes [44], dominating the floe deformation behaviour for gentle collisions.

According to Wu [213] the Charnock coefficient, α_C, is a constant between 0.012 and 0.035. Growing wave heights result in increasing aerodynamic roughness, which increases the Charnock coefficient value. The Charnock coefficient, α_C, is dependent on parameters such as wave age and wind speed [112], which represents to some extent how much the wind is decelerated by the waves. Andreas [10] suggests a Charnock coefficient for snow and sand between 0.010 and 0.016. Saucier et al. [158] has modelled the sea ice-ocean seasonal cycle in Hudson Bay, Foxe Basin, and Hudson Strait in Canada and used a Charnock coefficient equal to 0.011.

5.2 Convergence analyses

The convergence analyses concerning grid and domain size are conducted to find i) the optimal cell size to be used in the discretisation of FVM, in Sec. 5.2.1, and ii) the critical ratio of floe diameter to domain size as linked to the imposed wave forcing, in Sec. 5.2.2. The domain size convergence analysis allows to find the threshold between large- and small-scale modelling, where detailed small-scale modelling is required to actually capture the mechanical response.

Simplified ice layouts are used, consisting of randomly distributed disk-shaped ice floes of constant diameter, $D_d = 20\text{m}$. Loset et al. [110] defined a small ice floe as any relatively flat piece of sea ice, which is $20 - 100\text{m}$ across. The disks are surrounded by grease ice with a temporally and spatially varying viscosity, $\nu_k \approx 0.04\text{m}^2\text{s}^{-1}$, as found in literature [134, 142, 205, 206], corresponding to a constant grease ice strength parameter, $P_g^* = 0.02\text{Nm}^{-2}$. The wave parameters are chosen to maintain a constant wave steepness, $ak = 0.06$, across the considered cases. This corresponds to storm waves propagating into the marginal ice zone (MIZ), to highlight their effect on heterogeneous sea ice conditions [5]. The time step, $\Delta t = 0.01\text{s}$, for the Euler implicit method is chosen, providing stable simulations. All variables at the boundary of the domain are numerically approximated by zero-gradient boundary conditions (BCs).

In the grid size convergence analysis the domain is exposed to a harmonic propagating wave with period $T = 18\text{s}$, which is equivalent to a wave length of $\Lambda = 506\text{m}$, and amplitude $a = 4.8\text{m}$, typically encountered in the Antarctic MIZ [4]. In the domain size convergence analysis three different wave forcing scenarios are considered with periods $T = 6\text{s}$, $T = 12\text{s}$ and $T = 18\text{s}$, equivalent to wave lengths of $\Lambda = 56\text{m}$, $\Lambda = 225\text{m}$ and $\Lambda = 506\text{m}$, respectively, to cover the majority of occurring wave conditions and amplitudes $a = 0.5\text{m}$, $a = 2.1\text{m}$ and $a = 4.8\text{m}$, respectively.

[1] Southern oCean seAsonal Experiment http://scale.org.za/

5.2.1 Grid size

A convergence analysis is conducted, to find the most suitable cell size to study ice floe dynamics. A $100 \times 100\text{m}^2$ inner domain size is considered, with disk-shaped ice floes of 20m-diameter [110]. As zero-gradient BCs are applied, the domain is enlarged to $300 \times 300\text{m}^2$ to exclude undesired boundary effects for the inner domain, as shown in Fig. 5.1 by the black box. Multiple simulations are carried out, each time with an increasing number of cells in the problem domain.

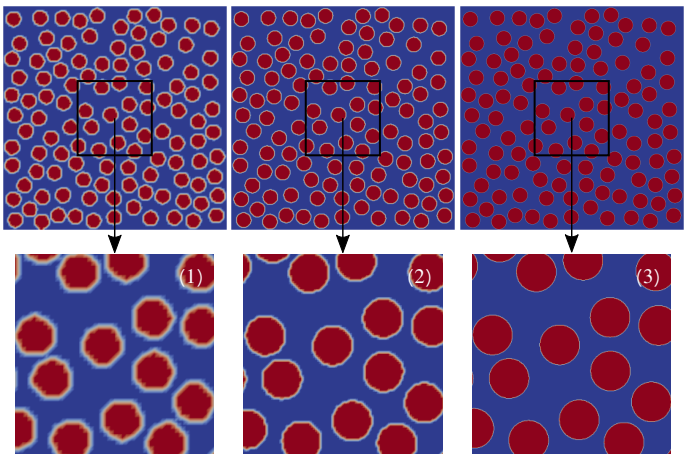

Figure 5.1: Three different grid refinement levels of a $300 \times 300\text{m}^2$ domain of uniformly distributed disk-shaped pancake floes each with $100 \times 100\text{m}^2$ inner domains with discretisations of **(1)** 2500 cells with a 2×2m cell size, **(2)** 10000 cells with a 1×1m cell size and **(3)** 160000 cells with a 0.25×0.25m cell size.

To accurately resolve the interface of ice floes and the surrounding grease ice, discretisations featuring a higher number of cells provide a sharper boundary as indicated by the white colour in the ice floe-grease ice layouts depicted in Fig. 5.1 at $t = 0$s. For each discretisation refinement level, the spatial average of ice floe stress and grease ice strain rate magnitudes, σ_{mag} and $\dot{\epsilon}_{mag}$, respectively, as well as the grease ice bulk viscosity, ζ, are computed. The stress and strain rate magnitude are calculated as

$$\sigma_{mag} = \sqrt{\sigma_{ij}\sigma_{ij}}, \qquad \dot{\epsilon}_{mag} = \sqrt{\dot{\epsilon}_{ij}\dot{\epsilon}_{ij}}, \tag{5.1}$$

where σ_{ij} and $\dot{\epsilon}_{ij}$ represent the Cartesian components of both the stress and strain rate tensor, respectively. Once the average is unaffected by changes in cell size, a suitable mesh is deemed to be found.

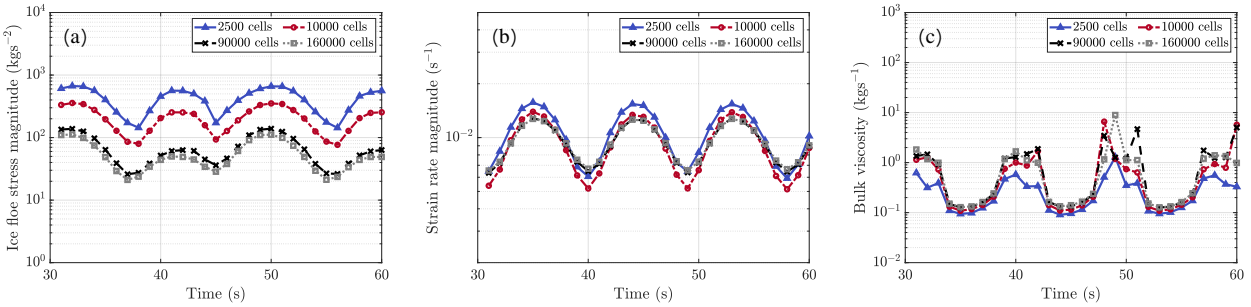

Figure 5.2: Comparing the domain-averaged sea ice rheology variables for four different discretisations, showing **(a)** the stress magnitude [kgs^{-2}], **(b)** the strain rate magnitude [s^{-1}] and **(c)** the bulk viscosity [kgs^{-1}].

Fig. 5.2 shows the main sea ice rheology variables for four different number of cells in the $100 \times 100\text{m}^2$ inner domain. The black and grey curves, representing 90000 and 160000-cell inner domains, respectively, show similar values indicating convergence. From the grid-size convergence analysis performed, the required cell size providing mesh-independent results was determined as $0.33 \times 0.33\text{m}^2$. Therefore, the problem domain of all simulations conducted in the upcoming chapters have a cell size of at least $0.33 \times 0.33\text{m}^2$.

5.2.2 Domain size

If large-scale regional models are to be informed by the actual material behaviour as originated on a smaller scale, averaged material parameters need to be obtained from homogenisation and upscaling procedures. These rely on the identification of the minimum domain size threshold where the actual kinematics and material composition of the problem must be addressed in detail and the averaged quantities are statistically representative for larger domains. Here, the focus is placed on the ice floe interaction as influenced by interstitial grease ice and wave dynamics.

A total domain size of $3600 \times 3600\text{m}^2$ is considered with disk-shaped ice floes of 20m-diameter [110], from which results are extracted for smaller inner domains, ranging from $100 \times 100\text{m}^2$ to $3200 \times 3200\text{m}^2$. This ensures a boundary zone of at least 400m around each of the inner domains to exclude unwanted boundary effects due to the zero-gradient BCs. Fig. 5.3 shows the smallest three inner domain sizes ranging from $100 \times 100\text{m}^2$ to $400 \times 400\text{m}^2$.

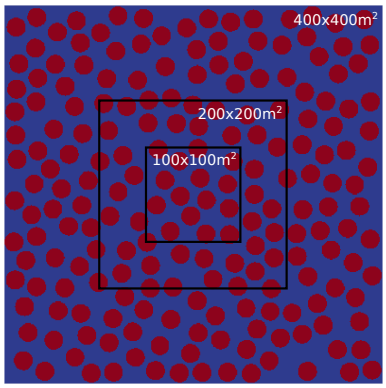

Figure 5.3: Inner domain sizes ranging from $100 \times 100\text{m}^2$ to $400 \times 400\text{m}^2$ with constant ice floe-grease ice ratios. Ice floes are modelled as disk-shaped floes of 20m-diameter. Red and blue represent ice floes and grease ice, respectively, considering constant ice floe and grease ice thicknesses of 0.31m and 0.1m, respectively.

The ice floe concentration from the largest domain size, $3200 \times 3200\text{m}^2$, to the smallest, $100 \times 100\text{m}^2$, ranges from 40% to 38%, due to a randomly distributed sea ice layout. The domain is discretised, using a constant cell size of $2 \times 2\text{m}^2$. The threshold for convergence concerning the minimum required domain size is found by calculating the domain-averaged stress and strain rate magnitudes, σ_{mag} and $\dot{\epsilon}_{mag}$, respectively, as well as bulk viscosity, ζ, for increasing inner domain sizes. Once the average is unaffected by changes in the domain size, the transition from small to large-scale modelling is identified, and the link to a phenomenological model using homogeneous material properties is established. This allows to study the detailed mechanical response of the sea ice rheology on a smaller scale, which is different for any domain size smaller than the threshold.

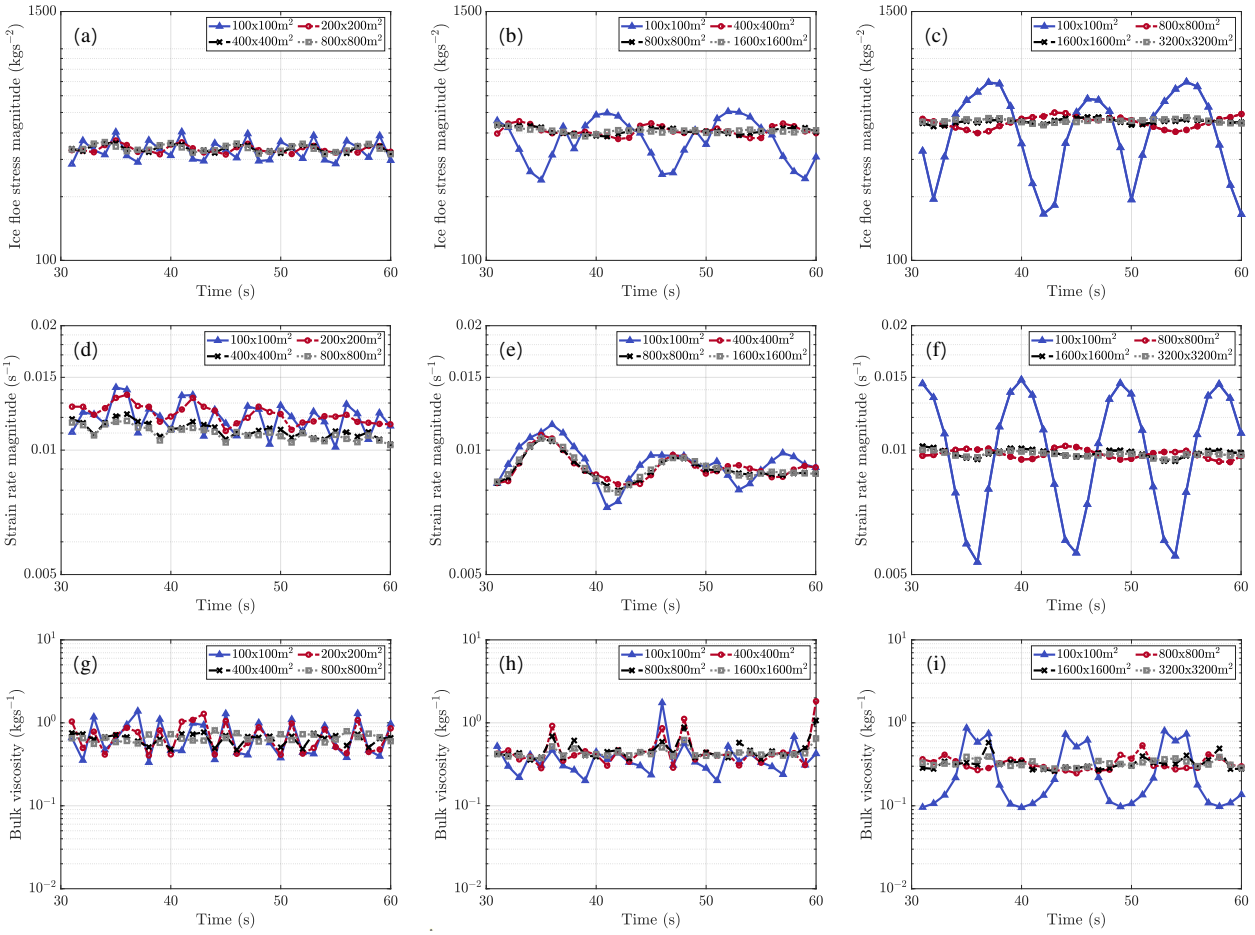

Figure 5.4: Comparing the domain-averaged sea ice rheology variables for different inner domain sizes. Three different wave periods are considered, $T = 6$s, $T = 12$s and $T = 18$s, showing **(a)** the stress magnitude [kgs^{-2}] for $T = 6$s, **(b)** the stress magnitude [kgs^{-2}] for $T = 12$s, **(c)** the stress magnitude [kgs^{-2}] for $T = 18$s, **(d)** the strain rate magnitude [s^{-1}] for $T = 6$s, **(e)** the strain rate magnitude [s^{-1}] for $T = 12$s, **(f)** the strain rate magnitude [s^{-1}] for $T = 18$s, **(g)** the bulk viscosity [kgs^{-1}] for $T = 6$s, **(h)** the bulk viscosity [kgs^{-1}] for $T = 12$s and **(i)** the bulk viscosity [kgs^{-1}] for $T = 18$s.

Figs. 5.4(a-c) show the overall domain-averaged stress in both ice floes and grease ice for different domain sizes and three different wave periods. Clearly, smaller wave periods reduce the required domain size for convergence. For the largest wave period of $T = 18$s, the threshold is identified at an inner domain size of 1600×1600m^2, where the blue and red curves in Figs. 5.4(c), (f) and (i), representing an inner domain size of 1600×1600m^2 and 3200×3200m^2, respectively, show very similar values. In contrast to the smallest wave period of $T = 6$s, the minimum needed inner domain size is only 400×400m^2.

Accordingly, to justify small-scale modelling a domain-size threshold is identified as smaller than 400×400m^2 where temporal and spatial fluctuations of the sea ice rheology variables become significant for all considered wave periods $T = 6 - 18$s with uniformly disk-shaped ice floes with a 20m diameter. This wave period-dependent threshold marks the transition from small- to large-scale modelling, where a phenomenological model with homogenised material properties can be utilised. Finding the threshold, allows studying the detailed mechanical response of the sea ice rheology on a smaller scale, which is different for any domain size smaller than the threshold.

5.3 Preliminary plausibility studies

In this section, plausibility studies are undertaken, showing simplified problems of ice floe-grease ice interaction, from which straightforward results are expected. These simulations contribute to the validation and verification of the small-scale model. Flaws in the model are shown and points for future improvements are presented.

Test case 1 studies the ice floe and grease ice behaviour of a simplified ice layout, named Layout A. The initial layout is shown in Fig. 5.5(a). Two disk-shaped ice floes with a diameter of $D_d = 10\text{m}$ move towards each other until collision. Both ice floes are given an initial velocity only, acting in opposite x-direction, equal to $|0.5|\text{ms}^{-1}$. The ice floes are embedded in a grease ice domain, $D = 50 \times 30\text{m}^2$, which is initially at rest. The domain is discretised, using a constant cell size of $0.25 \times 0.25\text{m}^2$. The simulation time is $t = 30\text{s}$, with a time step size of $\Delta t = 0.01\text{s}$. The boundaries of all fields in the domain are set to zero-gradient BCs.

Test cases 2, 3 and 4 discuss the response of a simplified ice layout, named Layout B. The initial layout, shown in Fig. 5.5(b), is subjected to atmospheric and/or oceanic forcing. One disk-shaped ice floe with a diameter of $D_d = 10\text{m}$ is embedded in a $D = 50 \times 30\text{m}^2$ grease ice domain. These test cases have a constant cell size of $0.25 \times 0.25\text{m}^2$. The simulation time, time step size and BCs are defined in the relevant sections, as these differ per test case.

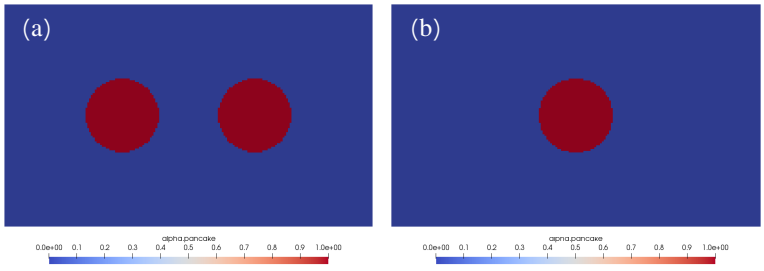

Figure 5.5: Initial layout, showing **(a)** Layout A for Test case 1 and **(b)** Layout B for Test cases 2, 3 and 4.

Test case 5 describes a more advanced example of two ice floes hitting an obstacle. Flaws observed in the set of the ice floe rheology equations are explained. These flaws, however, do not affect model results in Chap. 6. All basic simulations in this chapter allow for a small uniform write interval of 0.1s, which capture a more detailed response. As a result, curves in this chapter are shown without markers, to keep the graphs clean.

5.3.1 Test case 1: Colliding ice floes

This test case shows four simple numerical examples, making use of Layout A. Ice floe and grease ice material properties are discussed, by conducting a sensitivity study. The behaviour of both ice constituents is analysed, contour plots are shown and the stress and velocity magnitude are plotted.

In the first three examples, focus is on the stiffness, the initial ice floe position and the ice floe resistance in the domain. Default parameter values are set for Young's modulus, $E_Y = 8.7 \times 10^6\text{Nm}^{-1}$, the initial vertical distance between the centre of the two ice floes, $\Delta h = 0\text{m}$, and the constant grease ice strength parameter, $P_g^* = 0.02\text{Nm}^{-2}$. The last example elaborates on the behaviour of grease ice in the domain, explaining the

grease ice rheology, by discussing the contour plots of the velocity (gradient), strain rate, and stress magnitude.

5.3.1.1 Example 1: Ice floe stiffness

The sensitivity of ice floe stiffness is studied in the first example by variation of the value of Young's modulus, E_Y in Nm^{-1}. Note that the units of Young's modulus, Nm^{-1}, deviate from the standard SI-units, Nm^{-2}, because all terms in the momentum equation are normalised with respect to the density of sea ice in the domain.

Fig. 5.6 shows ice floe collisions for three different values of Young's modulus, $E_Y = 1 \times 10^5 \mathrm{Nm}^{-1}$, $E_Y = 5 \times 10^5 \mathrm{Nm}^{-1}$ and $E_Y = 1 \times 10^8 \mathrm{Nm}^{-1}$. As one would expect, the ice floe stiffness increases for increasing Young's modulus.

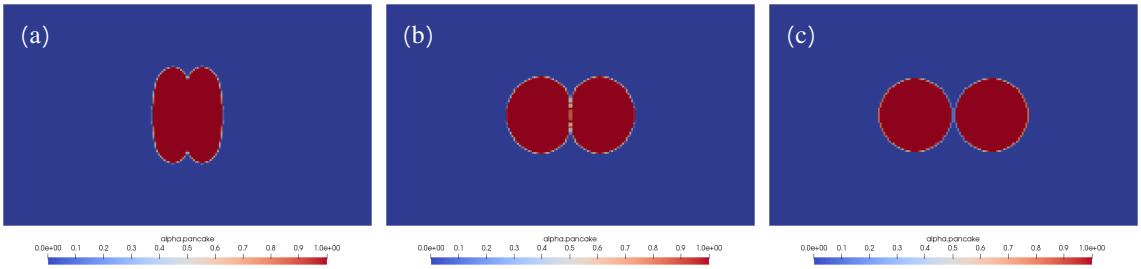

Figure 5.6: Ice layout at $t = 30$s, showing **(a)** $E_Y = 1 \times 10^5 \mathrm{Nm}^{-1}$, **(b)** $E_Y = 5 \times 10^5 \mathrm{Nm}^{-1}$ and **(c)** $E_Y = 1 \times 10^8 \mathrm{Nm}^{-1}$.

The impact of ice floe collisions for varying ice floe stiffness is mapped by plotting the stress and velocity magnitude curves over time in Fig. 5.7. Note that the x-axis shows values between $t = 5 - 15$s, to emphasize the stress and velocity response just before, during, and just after ice floe collision. The highest average stress magnitude value over both ice floes, $4701\mathrm{kgs}^{-2}$, representing the largest collision stress intensity, corresponds to Young's modulus of $E_Y = 1 \times 10^8 \mathrm{Nm}^{-1}$. The velocity curves, presented in Fig. 5.7(b), show a discontinuity at the time of the collision, due to the rapid decrease of the velocity to zero. The discontinuity in the curves is smoother for decreasing stiffness because the collision is dampened for lower stiffness values. Young's modulus used in the simulations of the small-scale model, $E_Y = 8.7 \times 10^6 \mathrm{Nm}^{-1}$, is based on values found in literature [161], resulting in a numerically stable simulation.

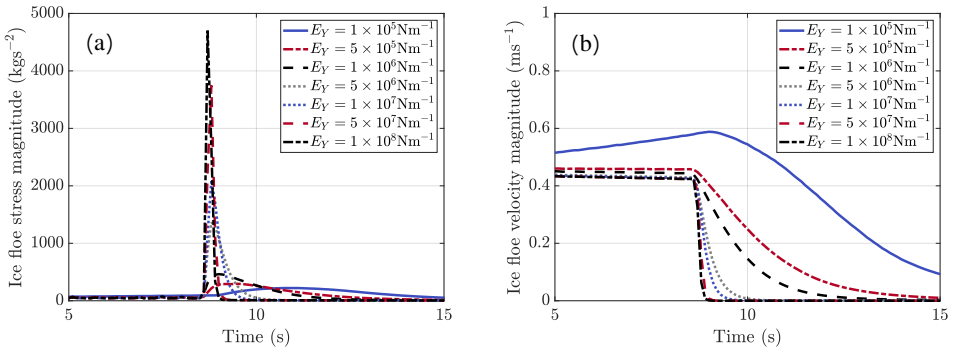

Figure 5.7: Seven different values of Young's modulus, showing **(a)** the ice floe stress magnitude [kgs^{-2}] and **(b)** the ice floe velocity magnitude [ms^{-1}]. All simulations have a simulation time of 30s, however, only $t = 5 - 15$s is shown to emphasize on the ice floe collision.

In Fig. 5.8 contour plots show the stress magnitude and velocity distribution in the x-direction before, during and after ice floe collision with ice floe stiffness, $E_Y = 8.7 \times 10^6 \text{Nm}^{-1}$. Before collision, both ice floes have a velocity in the x-direction equal to $|0.45|\text{ms}^{-1}$, acting in opposite directions, with a low ice floe stress magnitude close to 50kgs^{-2}, which is equally distributed over the floes. Once the ice floes collide, the initial velocity reduced, but minimally, due to the low resistance of the grease ice viscosity. At the instance of collision, a local stress concentration of approximately 20500kgs^{-2} is observed. However, the average stress magnitude over both floes is approximately 1936kgs^{-2}. After the collision, the ice floe velocity and stress magnitude are zero.

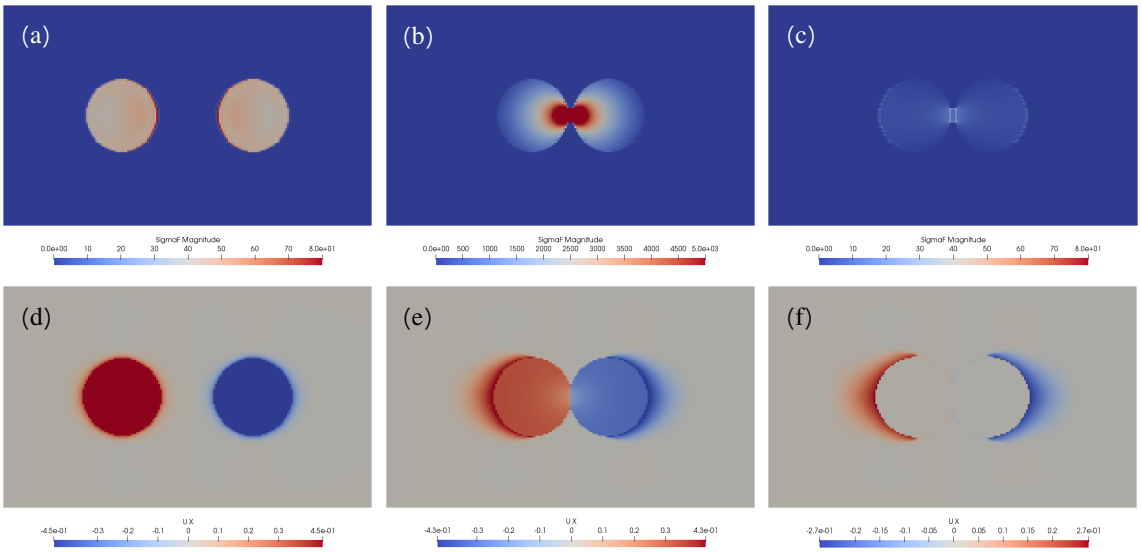

Figure 5.8: The ice floe stress magnitude [kgs^{-2}], showing **(a)** before, **(b)** during, and **(c)** after ice floe collision, as well as the ice floe velocity in the x-direction [ms^{-1}], showing **(d)** before, **(e)** during and **(f)** after ice floe collision with $E_Y = 8.7 \times 10^6 \text{Nm}^{-1}$.

The velocity magnitude curve for $E_Y = 1 \times 10^5 \text{Nm}^{-1}$ in Fig. 5.7 is highly unreliable, due to an increasing velocity magnitude before collision. This cannot be true as the ice floes are only subjected to an initial velocity. Therefore, the resistance of grease ice viscosity should result in a decreasing ice floe velocity before the collision. This counter-intuitive behaviour is due to a relatively high initial velocity of $|0.5|\text{ms}^{-1}$ in combination with an ice floe stiffness that is too low. This implies that the relation between velocity and Young's modulus is crucial. Results are unreliable when the ratio of velocity to Young's modulus is too high.

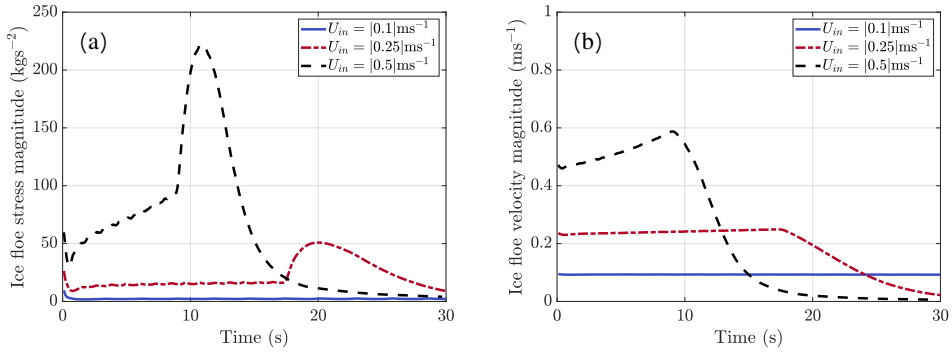

Figure 5.9: Three different initial velocity values with Young's modulus, $E_Y = 1 \times 10^5 \text{Nm}^{-1}$, showing **(a)** the ice floe stress magnitude [kgs^{-2}] and **(b)** the ice floe velocity magnitude [ms^{-1}].

The relation between velocity and Young's modulus is investigated in more detail, by studying the lowest Young's modulus separately, mainly focusing on the time before ice floe collision. Fig. 5.9 shows the ice floe stress and velocity magnitude response for $E_Y = 1 \times 10^5 \text{Nm}^{-1}$ with three different initial velocity values of $|0.1|\text{ms}^{-1}$, $|0.25|\text{ms}^{-1}$ and $|0.5|\text{ms}^{-1}$. The latter shows an ice floe stress magnitude curve, which increases before collision. This results in an increase in the ice floe velocity magnitude, shown in Fig. 5.9(b). Reducing the initial velocity, U_{in}, results in improved ice floe stress steady-state conditions before collision, and therefore a more controlled velocity magnitude curve. Note that for $U_{in} = |0.1|\text{ms}^{-1}$, the ice floes have not yet collided, hence no stress peak and decreasing velocity magnitude is observed.

This example has shown that a critical stability criteria forms the foundation of the physics and solution method. Therefore, it can be stated that the model is numerically stable only for values of Young's modulus larger than $E_Y = 1 \times 10^5 \text{Nm}^{-1}$.

5.3.1.2 Example 2: Ice floe position

In the second example, the initial position of ice floes relative to each other are studied. The purpose of this example is to show that the ice floe response results in expected behaviour. The collision stress intensity should decrease for increasing vertical distance between ice floes, measured from the centres of the ice floes. Three initial layouts are considered, as shown in Fig. 5.10, each with a different vertical distance, Δh, between the floes. Both ice floes are only given an initial ice floe velocity acting in opposite x-direction equal to $|0.5|\text{ms}^{-1}$.

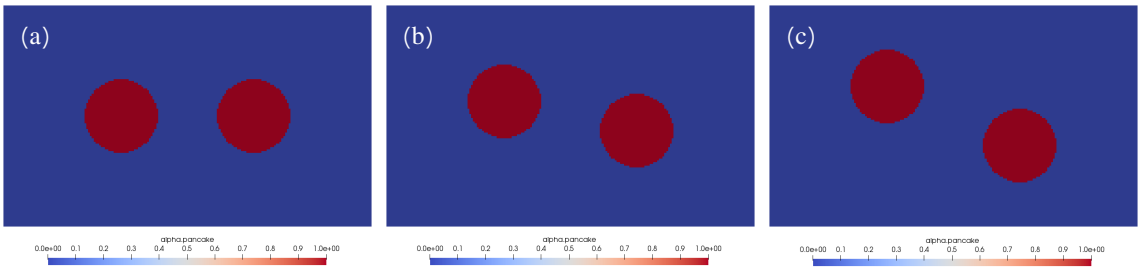

Figure 5.10: Ice layout at $t = 0$s, showing **(a)** $\Delta h = 0$m, **(b)** $\Delta h = 4$m and **(c)** $\Delta h = 8$m.

Both ice floe stress and velocity magnitude curves are plotted in Fig. 5.11 for three simulations with the different initial positions. No vertical distance between the centre of the ice floes corresponds to a frontal collision, resulting in the highest average ice floe stress magnitude value over both ice floes, shown in Fig. 5.11(a). The shape of the collision peak in the stress curve is wider for increasing vertical distance, due to shearing taking place between ice floes when they move past each other.

Additionally, the stress curves indicate that an increasing vertical distance between ice floe positions results in a delayed collision response, which corresponds to the velocity plot where the discontinuity in the curve occurs at a later time step for increasing vertical distance. The stress curve of the largest vertical distance, $\Delta h = 8$m, is significantly smaller because the ice floes barely touch each other. This can also be seen in the velocity plots shown in Fig. 5.11(b), where the discontinuity in the curve is much smoother.

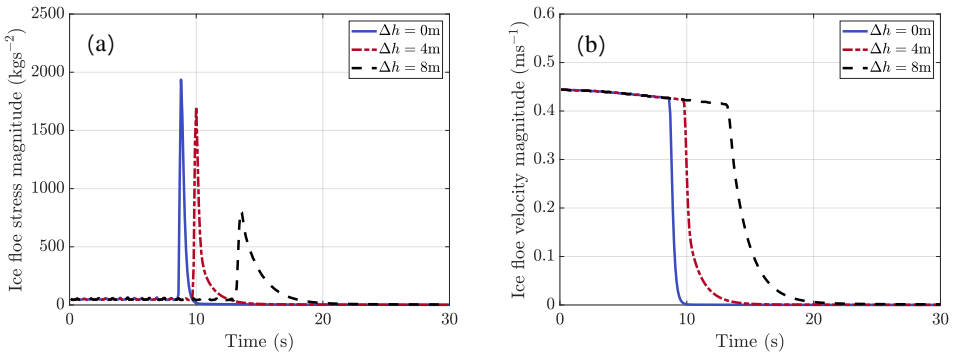

Figure 5.11: Three different values of the vertical distance between the initial ice floe position, showing **(a)** the ice floe stress magnitude [kgs^{-2}] and **(b)** the ice floe velocity magnitude [ms^{-1}].

Fig. 5.12 illustrates the velocity vector plots of the three simulations, emphasizing ice floe rotations. The contour plots are shown at a time step of $t = 10$s. This time step corresponds to the moment in time when the ice floes, with an initial vertical distance of $\Delta h = 4$m, collide. Fig. 5.12(a) represents the velocity vectors of $\Delta h = 0$m just after the frontal ice floe collision, with ice floe velocity vectors close to zero. Fig. 5.12(b) exemplifies the velocity vectors of $\Delta h = 4$m at the instance of ice floe collision, with ice floe velocity vectors of approximately $U_{mag} = 0.4$ms^{-1}, pointing in opposite directions. Fig. 5.12(c) shows the velocity vectors of $\Delta h = 8$m before the ice floe collision, with ice floe velocity vectors close to $U_{mag} = 0.4$ms^{-1}, acting in opposite direction.

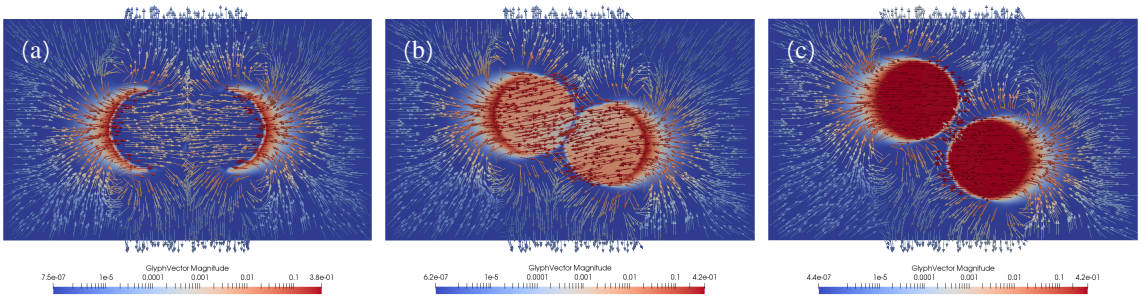

Figure 5.12: Velocity magnitude contour plots with overlaying velocity vectors [ms^{-1}] at $t = 10$s, showing **(a)** $\Delta h = 0$m, **(b)** $\Delta h = 4$m and **(c)** $\Delta h = 8$m.

5.3.1.3 Example 3: Ice floe resistance

In the third example, the influence of grease ice viscosity on the stress and velocity response of ice floes in grease ice is studied. Different constant grease ice strength parameter values are considered, focusing on the ice floe behaviour. The grease ice behaviour is discussed in Sec. 5.3.1.4. The purpose of this example is to show that the response of ice floes results in expected behaviour. An increase in grease ice viscosity should result in a higher floe resistance, which in turn results in a smaller distance travelled.

The constant grease ice strength parameter values range from $P_g^* = 0.02$Nm^{-2} to $P_g^* = 2$Nm^{-2}. The ice floes only have an initial velocity in opposite direction equal to $|0.5|$ms^{-1}, which implies that an increase in grease ice viscosity results in increased resistance and therefore a delayed response with damped collision impact.

In Fig. 5.13, three ice layouts are shown at $t = 7.5$s for increasing viscosity. It can be seen that the ice floes have covered a smaller distance in a higher grease ice viscosity.

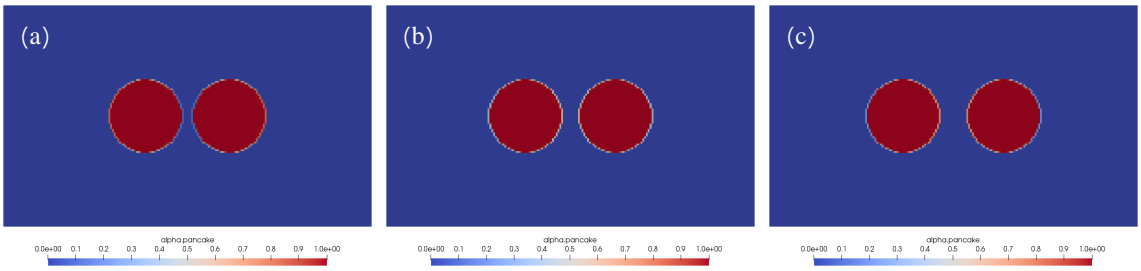

Figure 5.13: Ice layout at $t = 7.5$s, showing **(a)** $P_g^* = 0.02\text{Nm}^{-2}$, **(b)** $P_g^* = 0.2\text{Nm}^{-2}$ and **(c)** $P_g^* = 2\text{Nm}^{-2}$.

Ice floe stress and velocity magnitude curves are shown in Fig. 5.14, for the three different grease ice viscosities. The average ice floe stress magnitude over both ice floes is higher for a lower viscosity, which confirms that the grease ice viscosity acts as a dampening effect between colliding ice floes.

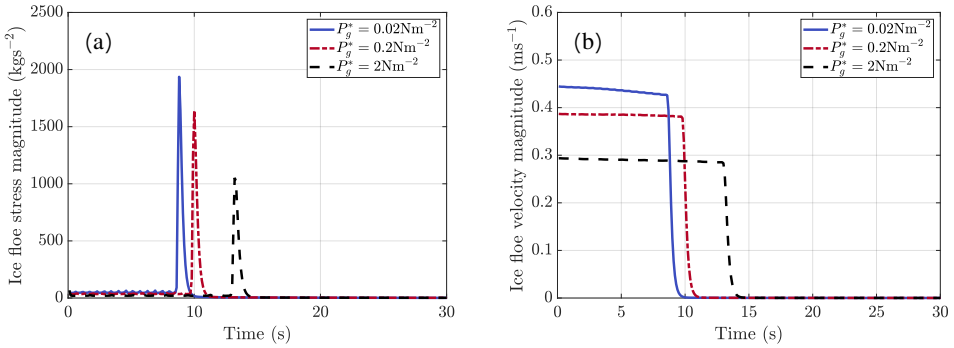

Figure 5.14: Three different values of the grease ice viscosity parameter, showing **(a)** the ice floe stress magnitude [kgs^{-2}] and **(b)** the ice floe velocity magnitude [ms^{-1}].

The stress magnitude curves show that a higher grease ice viscosity results in a delayed collision response, due to a higher floe resistance. This corresponds to the velocity curves, where the discontinuity in the curve represents the ice floe collision. An increase in viscosity results in an increase in inertia, which in turn results in a decreasing sea ice velocity.

5.3.1.4 Example 4: Grease ice behaviour

In this example, the emphasis is on the behaviour of the grease ice in the domain, to discuss intricacies of modelling the grease ice strain rate in the viscous-plastic model. Both ice floes are only subjected to an initial ice floe velocity of $|0.5|\text{ms}^{-1}$, acting in opposite x-direction. Three different constant grease ice viscosity parameter values are considered, $P_g^* = 0.02\text{Nm}^{-2}$, $P_g^* = 0.2\text{Nm}^{-2}$ and $P_g^* = 2\text{Nm}^{-2}$. The grease ice velocity (gradient), stress and strain rate magnitudes are discussed, showing contour plots of these variables over time.

The grease ice velocity is initially equal to zero. Due to the moving ice floes, surrounding stationary grease ice is affected and starts moving. An increase in the constant grease ice strength parameter, results in an increased amount of grease ice affected in the domain. This is shown in bulk viscosity contour plots at $t = 7.5$s,

depicted in Fig. 5.15, for an increasing constant grease ice strength parameter. High viscosity values are illustrated at the boundary, which decrease for an increasing constant grease ice strength parameter, P_g^*.

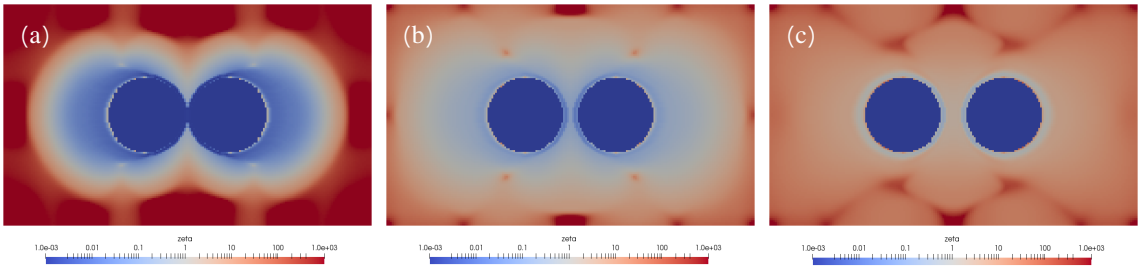

Figure 5.15: Bulk viscosity contour plots at $t = 7.5$s, showing **(a)** $P_g^* = 0.02\text{Nm}^{-2}$, **(b)** $P_g^* = 0.2\text{Nm}^{-2}$ and **(c)** $P_g^* = 2\text{Nm}^{-2}$.

Fig. 5.16 shows velocity magnitude contour plots and overlaying velocity vectors for the three different constant grease ice strength parameter values at $t = 7.5$s. The velocity vectors in grease ice point in the direction of the moving ice floes, as stationary grease ice is dragged in by the moving ice floes. The centre of rotational motion in grease ice are indicated above and below the ice floes. These rotations move away from the ice floes for an increasing viscosity. Moreover, a higher viscosity shows a larger turning radius in the grease ice, as a higher viscosity results in a higher inertia. As the ice floes move closer to each other, grease ice in between is squeezed in the vertical directions.

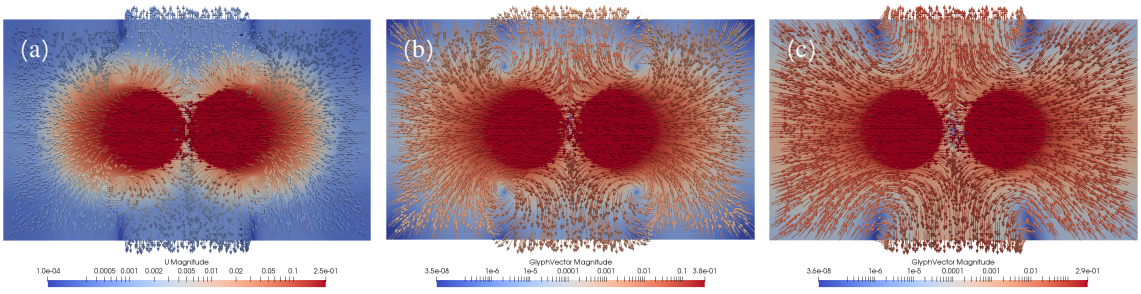

Figure 5.16: Velocity magnitude contour plots and overlaying velocity vectors [ms^{-1}] at $t = 7.5$s, showing **(a)** $P_g^* = 0.02\text{Nm}^{-2}$, **(b)** $P_g^* = 0.2\text{Nm}^{-2}$ and **(c)** $P_g^* = 2\text{Nm}^{-2}$.

As previously mentioned in Chap. 3, the strain rate magnitude, $\dot{\boldsymbol{\epsilon}}$, and grease ice rheology can be expressed in terms of the velocity gradient, $\boldsymbol{\nabla U}$. Fig. 5.17 shows the velocity gradient, strain rate and stress magnitude contour plots before collision, at $t = 7.5$s, and after collision, at $t = 15$s.

The rate of change in velocity per unit of distance is known as the velocity gradient. Figs. 5.17(a) and (d) illustrate high velocity gradient values at the ice floe-grease ice interface, whereas low values are shown at the boundary of the domain. The gradient is high at the ice floe-grease ice interface, due to a velocity difference between ice floes and grease ice, resulting in high strain rate magnitude values. The bulk viscosity is inversely related to the strain rate, which in turn results in low bulk viscosity values at the interface, as can be observed in Fig. 5.15.

As strain rate is directly related to the velocity gradient, the strain rate magnitude contour plots, shown in Figs. 5.17(b) and (e), are similar to the contour plots of the velocity gradient. The lower strain rate values

indicated above and below the ice floes in Figs. 5.17(b) and (e) represent the centre of the rotational motion in the grease ice.

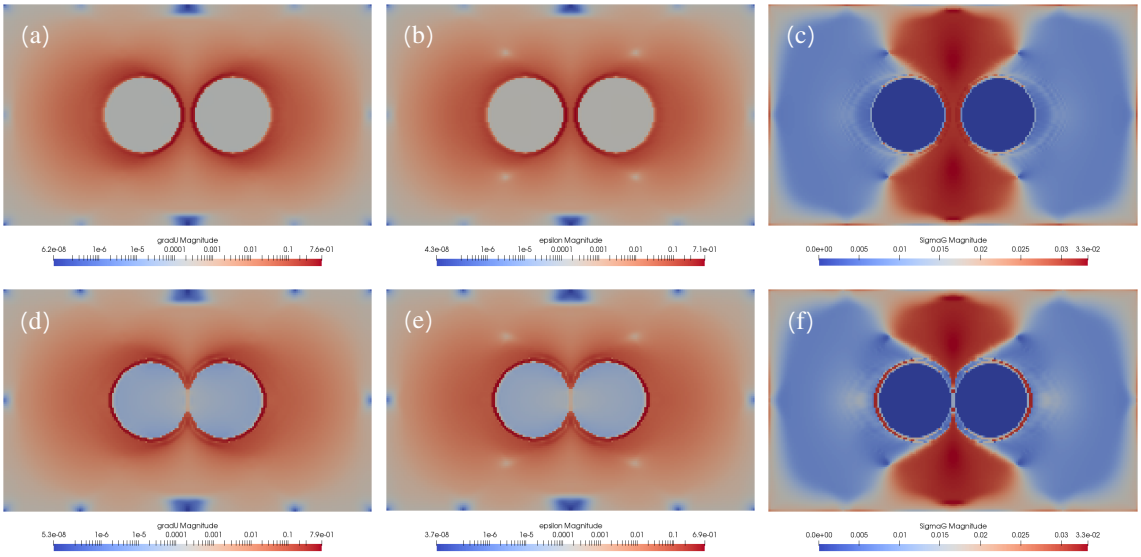

Figure 5.17: Contour plots showing **(a)** the velocity gradient magnitude [s^{-1}] at $t = 7.5$s, **(b)** the strain rate magnitude [s^{-1}] at $t = 7.5$s, **(c)** the grease ice stress magnitude [kgs^{-2}] at $t = 7.5$s, **(d)** the velocity gradient magnitude [s^{-1}] at $t = 15$s, **(e)** the strain rate magnitude [s^{-1}] at $t = 15$s and **(f)** the grease ice stress magnitude [kgs^{-2}] at $t = 15$s.

The grease ice stress depends on both the viscosity and strain rate variables. Accordingly, similar grease ice stress contour plots are shown in Figs. 5.17(c) and (f). Before ice floe collision, the ice floes move towards each other, resulting in a high grease ice stress magnitude in between the ice floes, whereas the magnitude is small on the left- and right-hand side of the ice floes. The centre of the grease ice rotations is the boundary between large and small stress magnitudes. After ice floe collision, grease ice on the outer side of the ice floes builds up, resulting in large magnitude values.

5.3.2 Test case 2: Bulk velocity

During the winter cruise to the Antarctic MIZ in 2017 and 2019, sea ice characteristics and the dynamics of ice floes and grease ice have been observed. Additionally, in situ image material is recorded by stereo cameras of the sea ice cover in the Antarctic MIZ [3]. From observations, researchers noticed that ice floes with interstitial grease ice move together as a whole, covering large distances due to oceanic and atmospheric drivers. Ice floes and grease ice can only move collectively, if both constituents have a similar bulk velocity, representing the average flow velocity. If not, ice floes and grease ice would separate from one another.

The water drag coefficient is one of the parameters affecting ice floe and grease ice displacements. Both ice constituents considered in the small-scale model, ice floes and grease ice, do not have the same water drag coefficient. Accordingly, it is of importance to find a ratio between both drag coefficients, to ensure that the bulk velocity of both ice constituents is similar.

This test is conducted with Layout B. The sea ice domain is subjected to a harmonic propagating wave with wave period, $T = 15.06$s and wave amplitude, $a = 2.77$m. The wave properties are based on values

obtained by Alberello et al. [4]. This test case has a simulation time of $t = 60$s with time steps between $\Delta t = 0.01 - 0.001$s. Zero-gradient BCs are applied to all variables in the domain.

The water drag coefficient value for ice floes, initially considered in this section, is equal to $C_{w_f} = 0.01$. Corresponding grease ice drag coefficient values range between $C_{w_g} = 0.001 - 0.01$ with increments equal to 0.001. Once the bulk velocity of both constituents, i.e. the averaged velocity magnitude curves, are similar for both ice floe and grease ice, the ratio between both drag coefficient values is found. Subsequently, water drag coefficient values of ice floes are increased from $C_{w_f} = 0.01$ to $C_{w_f} = 0.05$, using the obtained ratio to find the corresponding C_{w_g} values. This is done, to confirm that the obtained ratio can also be applied to higher water drag coefficient values for ice floes. Once this is established, the final value of the ratio is found.

In Fig. 5.18(a), a velocity magnitude curve is shown for ice floes with a water drag coefficient value equal to $C_{w_f} = 0.01$ and three velocity magnitude curves for grease ice with water drag coefficient values ranging between $C_{w_g} = 0.002 - 0.06$. A similar bulk velocity for both ice constituents is found for $C_{w_g} = 0.004$, resulting in a drag coefficient ratio of ice floe to grease ice equal to $2.5 : 1$.

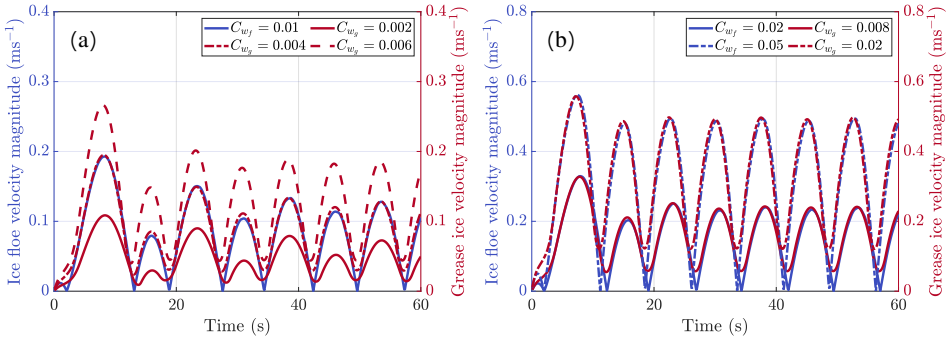

Figure 5.18: Ice floe velocity magnitude [ms^{-1}] for different water drag coefficient values for ice floe and grease ice, showing **(a)** $C_{w_f} = 0.01$ with $C_{w_g} = 0.002 - 0.06$, respectively, and **(b)** $C_{w_f} = 0.02$ and $C_{w_f} = 0.05$ with obtained drag coefficient ratio, resulting in $C_{w_g} = 0.008$ and $C_{w_g} = 0.02$, respectively.

Fig. 5.18(b) shows the ice floe velocity magnitude curves with water drag coefficients, $C_{w_f} = 0.02$ and $C_{w_f} = 0.05$, and corresponding water drag coefficients for grease ice, which meet the obtained drag coefficient ratio. Higher water drag coefficient values also result in similar velocity magnitude values for both ice constituents. Accordingly, a drag coefficient ratio of ice floe to grease, $2.5 : 1$, is hereby confirmed.

Higher water drag coefficient values result in velocity curves that reach equilibrium faster. However, the velocity magnitude is fairly high for ice floe drag coefficient values larger than $C_{w_f} = 0.02$. According to Alberello et al. [4], the average measured daily drift velocity, in the sector that was the focus of their study in the Antarctic MIZ, was 0.35ms^{-1}. The value measured by Alberello et al. [4] is more than 50% higher than velocity values previously reported by Heil and Allison [60].

Accordingly, in the small-scale model, an ice floe drag coefficient value of $C_{w_f} = 0.02$ is used in future simulations, with corresponding grease ice drag coefficient value equal to $C_{w_g} = 0.008$. In this example, these coefficients result in a bulk velocity value equivalent to an averaged velocity magnitude value of approximately 0.15ms^{-1}.

Inertia effects on the sea ice velocity are investigated, by modifying the sea ice density. The x-component of

the orbital wave velocity is maximum at the crest of a wave propagating in water, minimum at the trough of the wave, and zero at the mean sea water level. If one would plot the wave elevation and the orbital wave velocity in the x-direction, both curves would be in phase. In other words, both variables have the same frequency, and as a result, their maximum and minimum would coincide.

Considering sea ice implies the inclusion of inertia, which affects the sea ice velocity response. Fig. 5.19 shows the wave elevation and both the ice floe and grease ice velocity curves for an increasing ice floe and grease ice density.

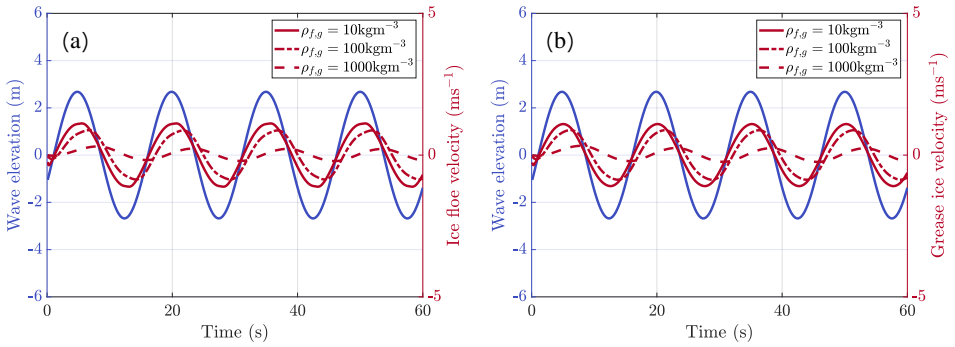

Figure 5.19: Comparing the phase between the wave elevation [m] and the velocity in the x-direction [ms^{-1}] for three different density values, for **(a)** ice floes and **(b)** grease ice.

Density values equal to zero correspond to a water wave. Note that the density values are unrealistic, however, that is not of importance here. The purpose of this example is to show the effect of inertia on the velocity. An increase in density, and therefore an increase in inertia, results in a shift of the velocity curve in the positive x-direction. In other words, the wave elevation and sea ice velocity in the x-direction are out of phase. Moreover, an increase in inertia results in a decrease of the velocity amplitude.

5.3.3 Test case 3: Atmospheric and oceanic forcing

The air drag multiplication factor is one of the parameters affecting ice floe and grease ice displacements. In this example, the sensitivity of the air drag coefficient, C_a, on ice floe displacement is studied in Layout B. Values of the air drag multiplication factor, C_{a_λ}, range between 1 - 10. A multiplication factor is included, shown in Eq. (3.25) in Chap. 3, which simply multiplies the wave-dependent air drag coefficient in the entire domain by a certain value.

This test case consists of two examples. In the first example the ice floe is subjected to a wind forcing only. The initial ice floe velocity is equal to zero, which increases until steady-state conditions are reached. In the second example, the ice floe is subjected to a wind and wave forcing, using the steady-state conditions from the first example as input.

In the first example, the sea ice domain is subjected to a wind forcing in the x-direction with a true wind speed of 18.9ms^{-1}. This test case has a simulation time of $t = 300$s with a time step size of $\Delta t = 0.01$s. Periodic BCs are applied to all variables in the domain, allowing the ice floe to reach steady-state conditions, so that the applied wind forcing is fully developed.

Fig. 5.20 shows the ice floe stress and velocity magnitude curves for three different values of the air drag multiplication factor. Both the stress and velocity magnitude curves show that ice floes reach equilibrium conditions earlier for larger air drag coefficient values. After approximately $t = 200$s all three simulations have reached steady-state conditions.

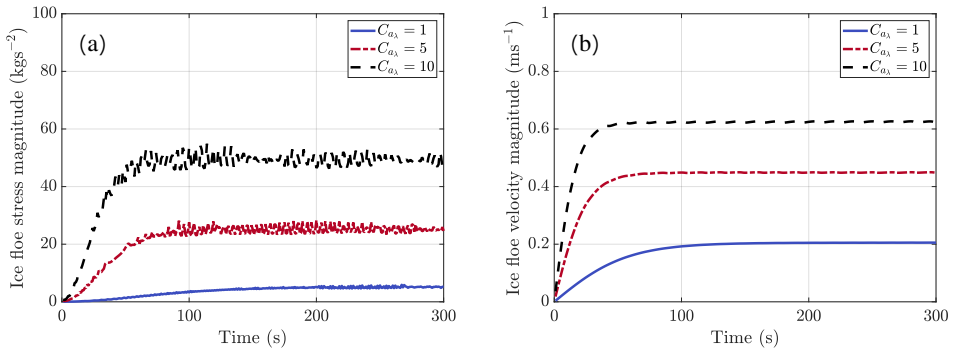

Figure 5.20: Three different air drag multiplication factor values, showing **(a)** the ice floe stress magnitude [kgs^{-2}] and **(b)** the ice floe velocity magnitude [ms^{-1}].

The second example has a simulation time of $t = 60$s, with a time step size of $\Delta t = 0.01$s. Zero-gradient BCs are applied to all variables in the domain. The wind forcing has a true wind speed of 18.9ms^{-1} with a wind direction angle of 321.7°, which corresponds to a north-western wind. The wind properties are based on values found by Vichi [199] during the winter cruise in 2017. The wind forcing is applied in combination with a wave forcing propagating in the x-direction with wave period $T = 15.06$s and wave amplitude $a = 2.77$m [3], resulting in a 45° angle between the wind and wave forcing. A north-western wind requires x- and y-components of the velocity, which are derived from the obtained steady-state velocity magnitude values, shown in Fig. 5.20(b).

Results of the second example are illustrated in Fig. 5.21, showing the ice floe trajectories, by tracking the centre of the ice floe. The trajectories are indicated in black with increments of $\Delta t = 0.1$s until $t = 60$s for three different values of the multiplication factor, $C_{a_\lambda} = 1, 5$ and 10. These values correspond to a domain-averaged air drag coefficient equal to $C_a = 0.0026, 0.0128$ and 0.0251, respectively.

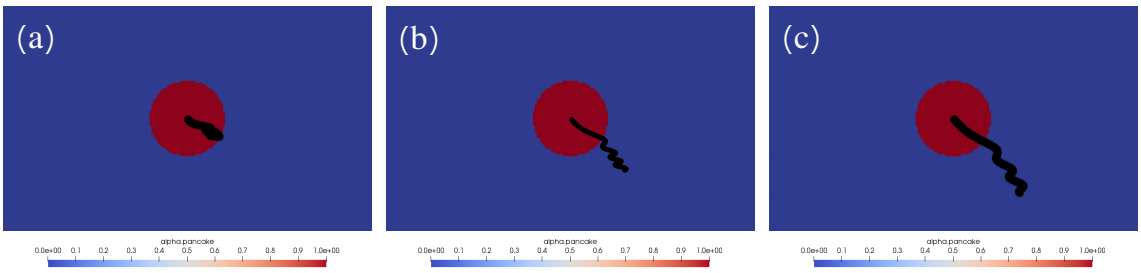

Figure 5.21: Ice floe trajectory for three different values of the air drag multiplication factor, showing **(a)** $C_{a_\lambda} = 1$, **(b)** $C_{a_\lambda} = 5$ and **(c)** $C_{a_\lambda} = 10$.

Fig. 5.22(a) shows the stress magnitude curves, which increase in magnitude for increasing air drag multiplication factor. An increasing wave-dependent air drag coefficient results in an increasing wind forcing, which in turn, depending on the wind direction, enhances the wave amplitude on the one side and reduces the wave amplitude on the other side.

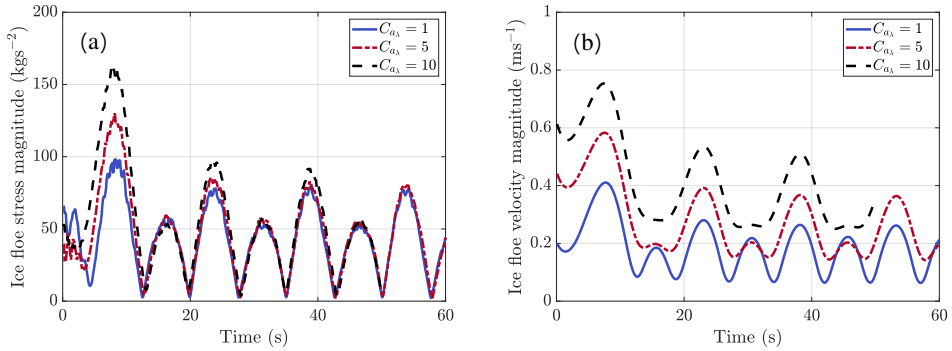

Figure 5.22: Three different air drag multiplication factor values, showing **(a)** the ice floe stress magnitude [kgs^{-2}] and **(b)** the ice floe velocity magnitude [ms^{-1}].

This phenomenon can be seen in the ice floe velocity magnitude curves in Fig. 5.22(b), where the smaller velocity magnitude amplitudes at approximately $t = 15$s, $t = 30$s and $t = 45$s gradually disappear for larger multiplication factors. Note that the velocity magnitude at $t = 0$s is equal to the steady-state conditions found in Fig. 5.20(b). Additionally, the stress and velocity curves for $C_{a_\lambda} = 10$ end at $t = 50$s, as the floe moves out of the domain.

5.3.4 Test case 4: Chequerboard oscillations

This test case focuses on the elastic ice floe rheology in OpenFOAM. The implementation of the Hookean-like flow rule is explained, discussing an associated numerical complication, named chequerboard oscillations. The problem of chequerboard oscillations is visualised and the alternative stress implementation method is presented.

The sea ice domain, Layout B, is subjected to a wave with a wave period, $T = 12$s, and a wave amplitude, $a = 2.1$m. This example has a simulation time of $t = 60$s, with a time step size of $\Delta t = 0.01$s. Only the last 30s are used for the analysis, as only near steady-state conditions are considered.

For ease of reading, the normalised, linearised form of Hooke's law is shown here again, written as

$$\underbrace{\boldsymbol{\sigma}_f'^{b+1}}_{\text{current time step}} = \underbrace{\boldsymbol{\sigma}_f'^{b}}_{\text{previous time step}} + \underbrace{\Delta t \left(\mu'(\boldsymbol{\nabla U} + (\boldsymbol{\nabla U})^T) + \lambda' \boldsymbol{I}\text{tr}(\boldsymbol{\nabla U})\right)}_{\text{current time step}}, \tag{5.2}$$

which shows a constant stress component from the previous time step and a velocity-dependent contribution from the current time step. However, as mentioned previously in Sec. 4.2.3, the stress component from the previous time step results in chequerboard oscillations.

Accordingly, this test case shows an alternative stress implementation, to avoid chequerboard oscillations. The normalised ice floe stress at the previous time step, $\boldsymbol{\sigma}_f'^{b}$, is treated either considering the total stress state or a partial stress state.

Both stress states are explained by substituting values for parameter b. When $b = 1$

$$\underbrace{\boldsymbol{\sigma}_f'^{2}}_{\text{time step 2}} = \underbrace{\boldsymbol{\sigma}_f'^{1}}_{\text{time step 1}} + \underbrace{\Delta t(\mu'(\boldsymbol{\nabla U}_2 + (\boldsymbol{\nabla U}_2)^T) + \lambda' \boldsymbol{I}\mathrm{tr}(\boldsymbol{\nabla U}_2))}_{\text{time step 2}}, \tag{5.3}$$

where $\boldsymbol{U}_i$ represents $\boldsymbol{U}$ with time step indicator i. The first term on the right-hand side is a constant stress component from time step 1. The second term on the right-hand side is a velocity dependent stress component from time step 2. When $b = 2$

$$\underbrace{\boldsymbol{\sigma}_f'^{3}}_{\text{time step 3}} = \underbrace{\boldsymbol{\sigma}_f'^{2}}_{\text{time step 2}} + \underbrace{\Delta t(\mu'(\boldsymbol{\nabla U}_3 + (\boldsymbol{\nabla U}_3)^T) + \lambda' \boldsymbol{I}\mathrm{tr}(\boldsymbol{\nabla U}_3))}_{\text{time step 3}}. \tag{5.4}$$

Note that only three values, $b = 1, 2, 3$ are shown here to explain the difference between a total and a partial stress state, containing values from both the current and previous time steps. However, this does not apply to these three time steps only, but to all time steps throughout a simulation. The total and partial stress states differ in their approach when Eq. (5.3) is substituted into Eq. (5.4). The substitutions are explained separately in Secs. 5.3.4.1 and 5.3.4.2.

5.3.4.1 Example 1: Total stress state

In this first example the total stress state is shown, which refers to the stress state from the previous time step, including both the constant stress component and the velocity-dependent contribution. Including the total stress state would allow for the floes to elastically unload after a collision. However, this leads to severe chequerboarding issues. Substitution of the total stress state, given in Eq. (5.3), into Eq. (5.4), results in

$$\begin{aligned}\underbrace{\boldsymbol{\sigma}_f'^{3}}_{\text{time step 3}} = \underbrace{\boldsymbol{\sigma}_f'^{1}}_{\text{time step 1}} &+ \underbrace{\Delta t(\mu'(\boldsymbol{\nabla U}_2 + (\boldsymbol{\nabla U}_2)^T) + \lambda' \boldsymbol{I}\mathrm{tr}(\boldsymbol{\nabla U}_2))}_{\text{time step 2}} \\ &+ \underbrace{\Delta t(\mu'(\boldsymbol{\nabla U}_3 + (\boldsymbol{\nabla U}_3)^T) + \lambda' \boldsymbol{I}\mathrm{tr}(\boldsymbol{\nabla U}_3))}_{\text{time step 3}},\end{aligned} \tag{5.5}$$

which results in ice floe stress magnitude contour plots shown in Fig. 5.23 for time steps $t = 31$s, $t = 45$s and $t = 60$s. The black box in the top-right corners shows the top part of the ice floe in more detail to highlight chequerboard oscillations. Stress distribution results are unreliable due to chequerboard patterns. This problem cannot be solved with the current set of equations using a collocated FVM grid, as is used within OpenFOAM. Consequently, stress from the previous time step is only partially implemented, explained in the second example in Sec. 5.3.4.2.

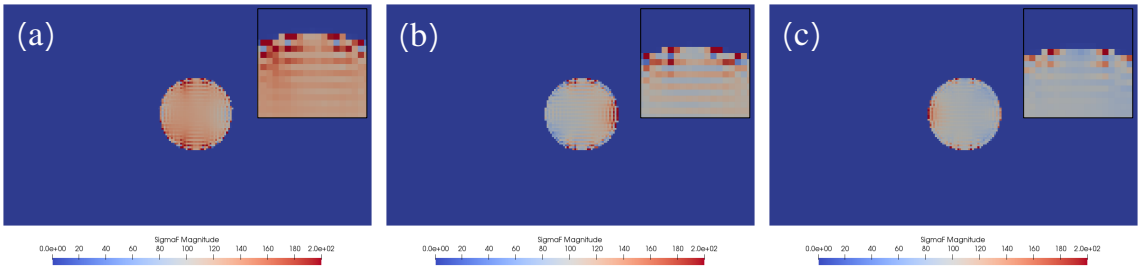

Figure 5.23: Total stress state including stability terms resulting in chequerboard oscillations, showing for three different time steps **(a)** $t = 31$s, **(b)** $t = 45$s and **(c)** $t = 60$s.

5.3.4.2 Example 2: Partial stress state

In this second example the partial stress state is shown, referring to the previous time step which retains the velocity-dependent stress component, but disregards the constant component from the previous time step. This alternative stress implementation solves the chequerboard complication. However, the stress magnitude value is underpredicted, as the previous time step is only partially considered.

In case of the partial stress state, the second time step, shown in Eq. (5.3) should only depend on the velocity-dependent stress component from time step 2, as the constant stress component from time step 1 is disregarded. Substitution of the partial stress state in Eq. (5.3) into Eq. (5.4), results in

$$\underbrace{\boldsymbol{\sigma}^3}_{\text{time step 3}} = \underbrace{\Delta t(\mu(\boldsymbol{\nabla U} + (\boldsymbol{\nabla U})^T) + \lambda \boldsymbol{I}\text{tr}(\boldsymbol{\nabla U}))}_{\text{time step 2}} + \underbrace{\Delta t(\mu(\boldsymbol{\nabla U} + (\boldsymbol{\nabla U})^T) + \lambda \boldsymbol{I}\text{tr}(\boldsymbol{\nabla U}))}_{\text{time step 3}}, \tag{5.6}$$

which leads to underprediction of the stress state. The extent to which stress is underestimated is discussed below.

The partial stress state solely considers the velocity-dependent stress component. Fig. 5.24 shows the stress magnitude distribution at time steps $t = 31$s, $t = 45$s and $t = 60$s. The black box in the top-right corners shows the top part of the ice floe in more detail to highlight the absence of chequerboard patterns.

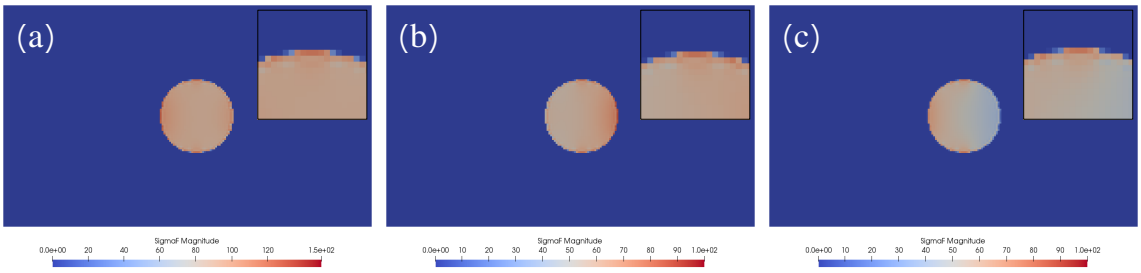

Figure 5.24: Partially implemented stress state resulting in no chequerboard oscillations, showing for three different time steps **(a)** $t = 31$s, **(b)** $t = 45$s and **(c)** $t = 60$s.

Differences between the total and partial stress states are mapped by plotting ice floe stress and velocity magnitude values in Fig. 5.25. Note that both curves start at $t = 31$s, as only the velocity response at near steady-state conditions is considered. The total stress state is approximately twice the stress of the partial stress state. Bear in mind, however, that the results of the total stress state cannot be trusted due to the chequerboard oscillations. Therefore, the plotted total stress state might not be the actual stress state, but fundamentally incorrect. As a result, stress states are preferably underpredicted, rather than completely unreliable. The velocity is significantly less affected by the chequerboard problem, as both the total and partial stress states show similar ice floe velocity magnitude curves.

By accounting for the partial stress state, the Hookean elastic equation, given in Eq. (3.12), is changed to a Hookean-like flow rule. Any deformation is permanent, where the floes will not return to their undeformed configuration once the external forcing has been removed. The floes do, however, still behave solid like, where any internal stress state, leads to a large resistance to deformation. This will further be demonstrated in the subsequent test case in Sec. 5.3.5.

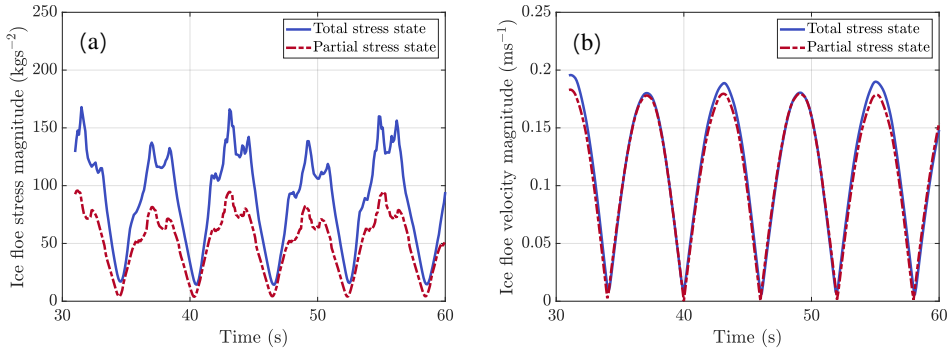

Figure 5.25: Total and partial stress states including stability terms, showing **(a)** the ice floe stress magnitude [kgs^{-2}] and **(b)** the ice floe velocity magnitude [ms^{-1}].

5.3.5 Test case 5: Ice floes hitting an obstacle

This test case elaborates on the ice floe rheology, specifically focusing on the Hookean-like behaviour of ice floes. Two disk-shaped ice floes with a diameter of $D_d = 10$m are subjected to a 0.4ms^{-1} ocean current velocity. An obstacle is placed in the middle of a $D = 50 \times 30$m^2 domain, obstructing the flow of the ice floes. Ice floes 1 and 2 refer to the ice floes in their initial position on the left- and right-hand side of the obstacle, respectively, shown in Fig. 5.26(a). This test case has a simulation time of $t = 160$s. A constant cell size, 0.125×0.125m^2, is used with a time step size of $\Delta t = 0.01$s. The left- and right-hand boundaries are implemented as periodic BCs. Ice floes leaving the domain on the right-hand side, move into the domain on the left-hand side. Slip BCs are imposed along the obstacle boundaries, to allow for non-zero velocity values.

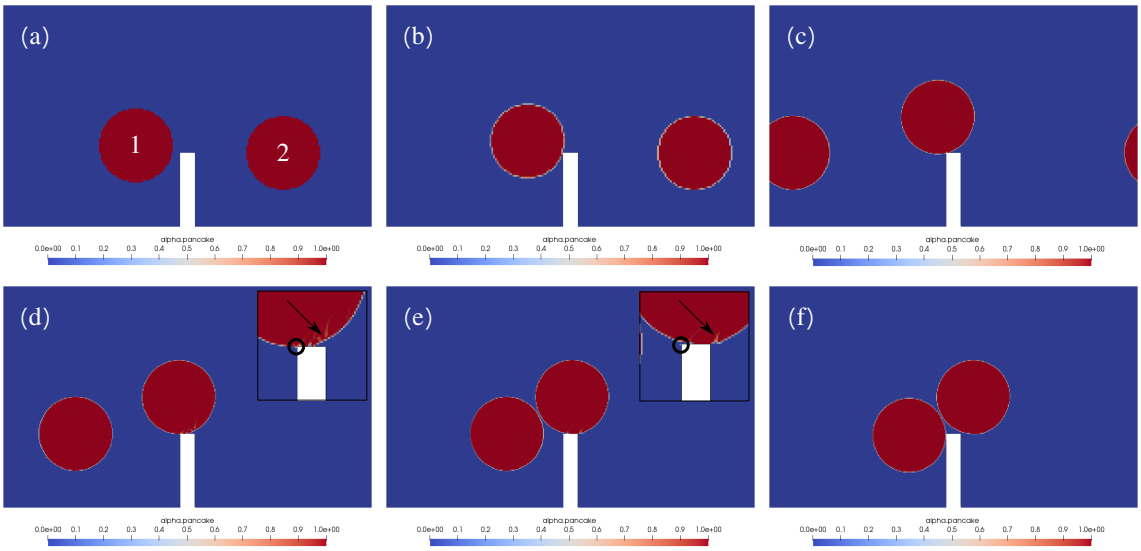

Figure 5.26: Two ice floes are subjected to an uninterrupted constant ocean current forcing obstructed by an obstacle, showing **(a)** $t = 0$s, **(b)** $t = 15$s, **(c)** $t = 77.7$s, **(d)** $t = 100$s, **(e)** $t = 120.8$s and **(f)** $t = 132$s. Ice floe inaccuracies are highlighted by an arrow, whereas cells of minor separation are highlighted by a black circle.

Two ice floes move from left to right due to a constant, uninterrupted ocean current forcing. Ice floe 1 hits the obstacle and rotates across. Ice floe 2 moves out of the domain on the right-hand side and enters the domain on the left-hand side. Subsequently, ice floe 2 collides with ice floe 1. Ice layouts are depicted in Fig. 5.26 for

six different time steps, $t = 0$s, $t = 15$s, $t = 77.7$s, $t = 100$s, $t = 120.8$s and $t = 132$s, representing a specific stress and velocity response. The corresponding average stress and velocity magnitude curves of both ice floes are depicted in Fig. 5.27.

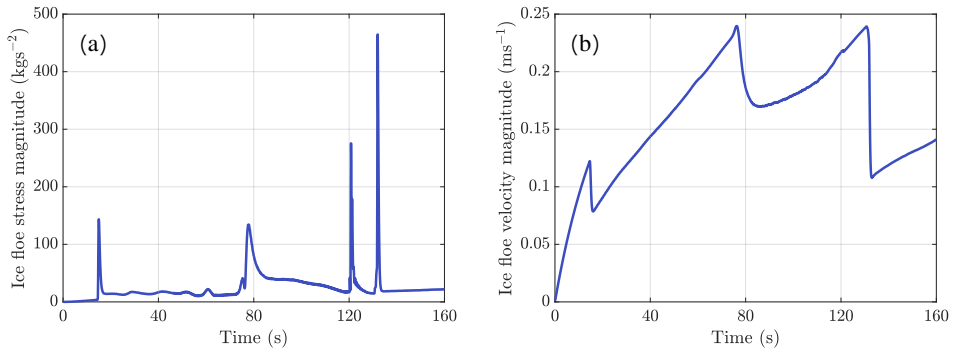

Figure 5.27: Ice floe response, showing **(a)** the ice floe stress magnitude [kgs^{-2}] and **(b)** the ice floe velocity magnitude [ms^{-1}].

At $t = 77.7$s a peak in the stress magnitude curve is observed, together with a decreasing ice floe velocity magnitude. The corresponding stress magnitude contour plots are shown in Figs. 5.28(b) and (c). The latter shows the same time step as Fig. 5.28(b), however, the stress legend bar was rescaled to highlight concentrated peak stresses.

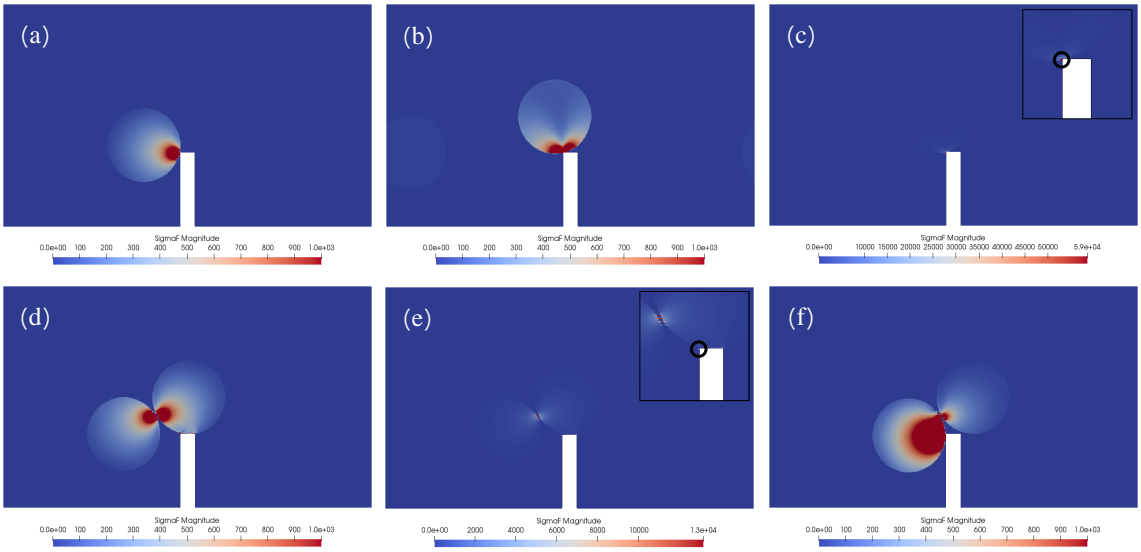

Figure 5.28: Stress magnitude contour plots [kgs^{-2}] at four time steps, **(a)** $t = 15$s, **(b)** $t = 77.7$s, **(c)** $t = 77.7$s, **(d)** $t = 120.8$s, **(e)** $t = 120.8$s and **(f)** $t = 132$s. Ice floe cells of minor separation are highlighted by a black circle.

The black box in the top-right corner zooms in on the peak stress, highlighted by a black circle at the tip of the obstacle. This excessively high peak stress cannot be explained physically but originates from permanent deformations in the solid floe, described as a numerical complication in the small-scale model. Due to this numerical complication, the ice floe struggles to move over the obstacle without inaccuracies. Fig. 5.29(b) shows the velocity magnitude distribution, highlighting the velocity at the tip of the obstacle. The cells with extremely high peak stress correspond to velocity magnitude values close to zero.

In Fig. 5.26(d) the sea ice layout is shown at $t = 100$s, highlighting inaccuracies in the ice floe by an arrow. Due to the implementation of Hookean-like ice floe behaviour, minor deformations are permanent. In other words, once a relative deformation has occurred, the ice floe cannot deform back. Permanent deformations, in combination with a stationary obstacle, result in minor separation of the ice floe. This is observed at the tip of the obstacle and highlighted by a black circle. The stress magnitude values in the ice floe cells of minor separation are extremely high. This is incorrect, however, it is a consequence of the implementation of the Hookean-like ice floe behaviour. Similar behaviour can be observed in Fig. 5.26(e) at $t = 120.8$s.

The stress magnitude peak at $t = 120.8$s is due to the collision of both ice floes, depicted in Figs. 5.28(d) and (e). The latter shows the same time step as Fig. 5.28(d), however, the stress legend bar was rescaled to highlight the peak stresses. Fig. 5.29(c) shows the velocity magnitude distribution, highlighting velocity values at the tip of the obstacle close to zero. Note that the velocity magnitude curve, shown in Fig. 5.27, barely drops at $t = 120.8$s, despite the collision between the two ice floes. This is because of a high velocity of ice floe 2 before the collision, pushing ice floe 1 forward.

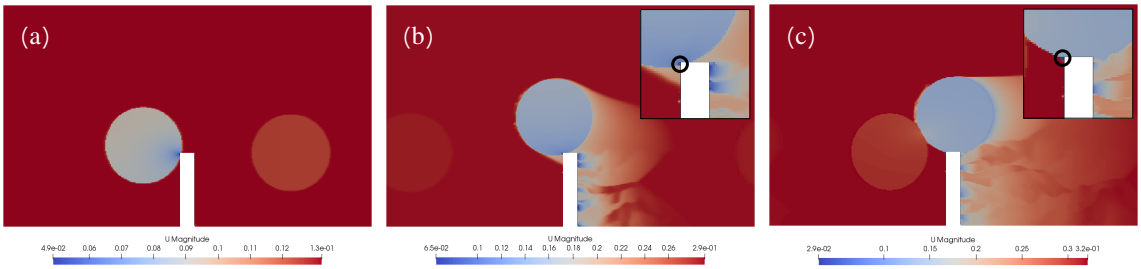

Figure 5.29: Velocity magnitude contour plots [ms^{-1}] at three time steps, **(a)** $t = 15$s, **(b)** $t = 77.7$s and **(c)** $t = 120.8$s. Ice floe cells of minor separation are highlighted by a black circle.

This test case shows what still needs to be improved in the model, however, fixing this separation issue at the obstacle is currently not a requisite. The approach works for colliding ice floes, as shown by Test case 1 in Sec. 5.3.1.

Chapter 6

Numerical investigation of mechanical behaviour of ice floe-grease ice interaction

From the domain-size convergence analysis conducted in Chap. 5, it was found that any inner domain size smaller than $400 \times 400\text{m}^2$ results in clear differences in mechanical response for any wave period larger than $T = 6\text{s}$. For that reason, results in this section consider an inner domain size of $100 \times 100\text{m}^2$, which is expected to produce temporal and spatial fluctuations of the stress and strain rate distributions, depending on the ratio of ice floe diameter and wave length, and thus, warrant detailed small-scale modelling.

In this chapter the high-resolution mechanical response of sea ice due to wave-ice interaction is studied. The sea ice domain is subjected to a simplified imposed harmonic wave forcing with different wave characteristics. The sea ice rheology variables, consisting of sea ice stress, strain rate, viscosity, and velocity, are separately analysed for ice floes and grease ice to better understand the behaviour of both ice constituents. The distribution of variables is analysed in a realistic sea ice domain, which is extracted from in situ image and video material recorded by stereo cameras of the dynamics of sea ice in the Antarctic marginal ice zone (MIZ) [3]. The sea ice domain is subjected to a simplified harmonic wave forcing with different wave characteristics.

Sec. 6.1 concentrates on the ice composition in terms of ice type as well as floe shape and diameter. Three images were taken in close proximity to each other, during the 2017 winter cruise to the Antarctic MIZ. Homogeneous sea ice conditions were observed with only slightly differing sea ice properties in terms of ice floe concentration and median ice floe caliper diameter. From these images, realistic sea ice layouts were obtained, implemented in the small-scale model as initial sea ice composition.

Sec. 6.2 focuses on the motion of sea ice, ice floe collisions, and the interaction between waves, ice floes, and grease ice. Additionally, the effect of grease ice viscosity is mapped on both stress and strain rate response of sea ice, considering different grease ice viscosities.

As the focus of this section is on the mechanics of wave-ice interaction, wind and ocean current veloci-

ties are set to zero. Accordingly, the external forcing of the sea ice domain only considers the wave action via the Froude-Krylov force acting on the submerged floe circumference below the grease ice layer, and the skin drag on the entire ice-ocean interface controlled by the water drag coefficient.

All simulations conducted in Secs. 6.1 and 6.2 have a simulation time of $t = 60$s, with a time step size of $\Delta t = 0.01$s, and a uniform write interval of 1s and 0.5s, respectively, illustrated by markers in the curves. A write interval indicates what interval is used to write data as output to a file [57]. Only near steady-state conditions are considered in the upcoming analyses, which are reached after 30s.

Zero-gradient BCs are applied to all boundaries in the sea ice domain, which simply extrapolates the quantity to the patch from the nearest cell value, effectively dampening the wave propagation and introducing an error that only affects the immediate boundary cells. To exclude these boundary effects, the $100 \times 100\text{m}^2$ inner domain are embedded in an outer domain of $300 \times 300\text{m}^2$, to which the boundary conditions are applied. The domain is discretised, using a constant cell size of $0.33 \times 0.33\text{m}^2$, found as the optimal cell size in the grid-size convergence analysis, conducted in Chap. 5.

6.1 Numerical study on the geometry of ice floes embedded in grease ice

The objective of this numerical study is to map the influence of the ice floe geometry on the stress, strain rate and bulk viscosity response on a small-scale. Additionally, the different sea ice layouts help to verify the robustness of the numerical framework with respect to the natural variability of the ice floe distribution in the MIZ.

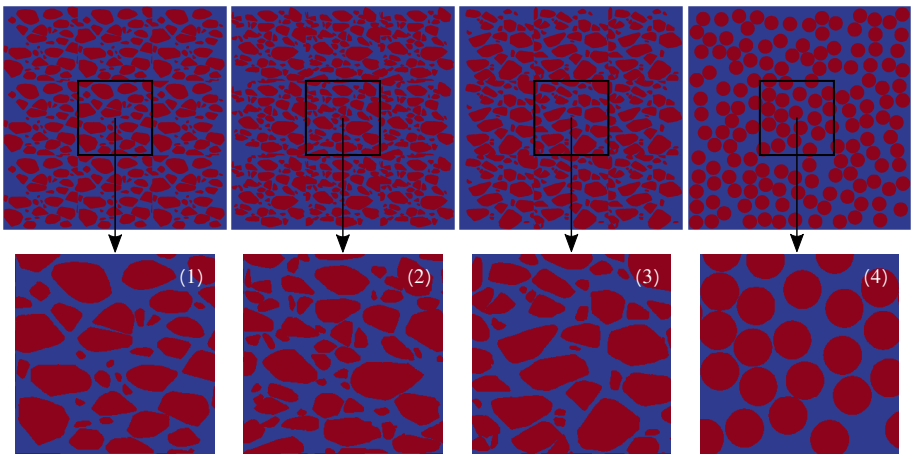

Figure 6.1: (**1-3**) Realistic sea ice layouts and (**4**) idealised with disk-shaped floes, each with a $100 \times 100\text{m}^2$ inner domain embedded in a $300 \times 300\text{m}^2$ outer domain.

Three realistic layouts and one idealised sea ice configuration with disk-shaped floes, comparable in terms of sea ice concentration, are illustrated in Fig. 6.1. Geometric properties of ice floes for all four layouts are summarised in Tab. 6.1, including both the ice floe caliper diameter and standard deviation in the x- and y-direction, ice floe concentrations, wave characteristics, and grease ice viscosity values.

All sea ice layouts are subjected to three different wave forcing, using wave periods ranging between $T = 8-16$s with constant wave steepness, $ak = 0.06$ [41]. The domain-averaged grease ice viscosity value, $\nu_k \approx 0.04\text{m}^2\text{s}^{-1}$, is in agreement with literature values [134, 205, 206]. The viscosity of the grease ice rheology is strain rate-dependent via the grease ice strength parameter, P_g, which in turn depends on the empirical constant, P_g^*. The value of P_g^* is chosen so that the domain-averaged viscosity provides a close match to the predefined value of $\nu_k \approx 0.04\text{m}^2\text{s}^{-1}$.

Table 6.1: Parameters specifically used in the analysis of sea ice composition and rheology, where XCD and YCD denote the ice floe caliper diameter in the x- and y-directions [m], respectively. The standard deviation in the x- and y-directions [m] is indicated by XSD and YSD, respectively.

Parameter	**Definition**	**Value**	**Unit**
a	wave amplitude	1, 2.1, 3.8	m
ak	wave steepness	0.06 [41]	-
A_f	ice floe concentration Layout 1, 2, 3, 4	54.7, 59.7, 57.3, 59.7	%
$C_{w_{f,g}}$	water drag coefficient for ice floes and grease ice	0.02, 0.008	-
$D_{x,m}$	median XCD Layout 1, 2, 3, 4	13.0, 11.0, 9.3, 9.7	m
$D_{y,m}$	median YCD Layout 1, 2, 3, 4	10.0, 7.0, 8.0, 9.7	m
n_f	number of ice floes Layout 1, 2, 3, 4	41, 60, 49, 23	-
P_g^*	grease ice strength parameter	0.024	Nm^{-2}
SD_x	XSD Layout 1, 2, 3, 4	8.8, 7.3, 9.2, 0	m
SD_y	YSD Layout 1, 2, 3, 4	5.5, 4.3, 5.6, 0	m
T	wave period	8, 12, 16	s
Λ	wave length	100, 225, 400	m
ν_k	kinematic grease ice viscosity	0.04	m^2s^{-1}

The ice floe concentration differs slightly between the different layouts, with an average value equal to 57.9% ($\pm$3.2%). The median ice floe caliper diameter in both the x- and y-direction is equal 10.8m ($\pm$2.2m) and 8.7m ($\pm$1.7m), respectively.

The distribution of the ice floe caliper diameter is mapped for all realistic sea ice layouts through the use of box plots, as shown in Fig. 6.2. Layout 2 has the smallest interquartile range, which refers to the distance between the bottom, 25$^{\text{th}}$ percentile, and the top, 75$^{\text{th}}$ percentile, of the box plot. This is also reflected in the standard deviation, which shows the lowest values in both the x- and y-direction for Layout 2. This indicates that Layout 2 features the largest portion of medium-size floes and is the most homogeneous in size. Layout 3, on the other hand, exhibits the largest spread of floe sizes, in particular concerning large floes.

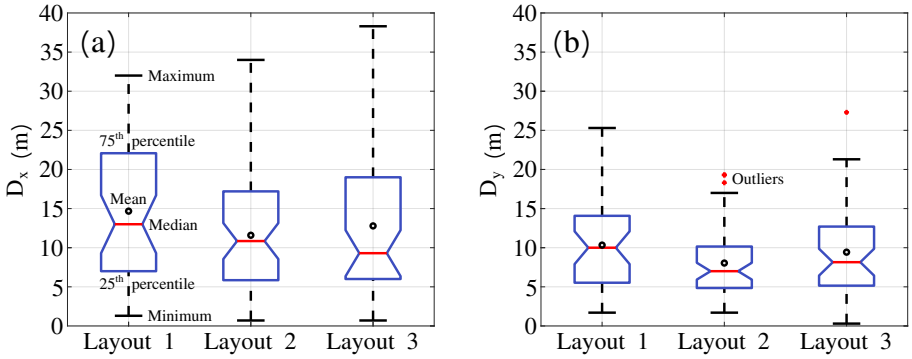

Figure 6.2: Box plots for all three realistic sea ice layouts, showing the distribution of (**a**) the caliper diameter in the x-direction [m] and (**b**) the caliper diameter in the y-direction [m].

As Layout 2 is the most homogeneous, its mechanical response is expected to be closest to the idealised sea ice Layout 4. Therefore, Layout 4 is chosen to study the error introduced by completely disregarding floe shape and variations in floe diameter. To specifically focus on the sensitivity regarding ice floe shape and diameter, and study their effect on the stress, strain rate, and viscosity variables, in both the grease ice and ice floe rheology, the ice floe concentration of Layout 4 is chosen to be the same as the concentration in Layout 2. Additionally, the mean ice floe caliper diameter in Layout 4 has been derived from Layout 2, such that the average area per ice floe, $A_{floe} = 293\text{m}^2$, is identical.

Fig. 6.3 shows the spatially-averaged stress in both ice floes and grease ice for wave periods $T = 8$s, $T = 12$s and $T = 16$s. An increasing wave period results in an increasing stress amplitude and a decreasing stress frequency.

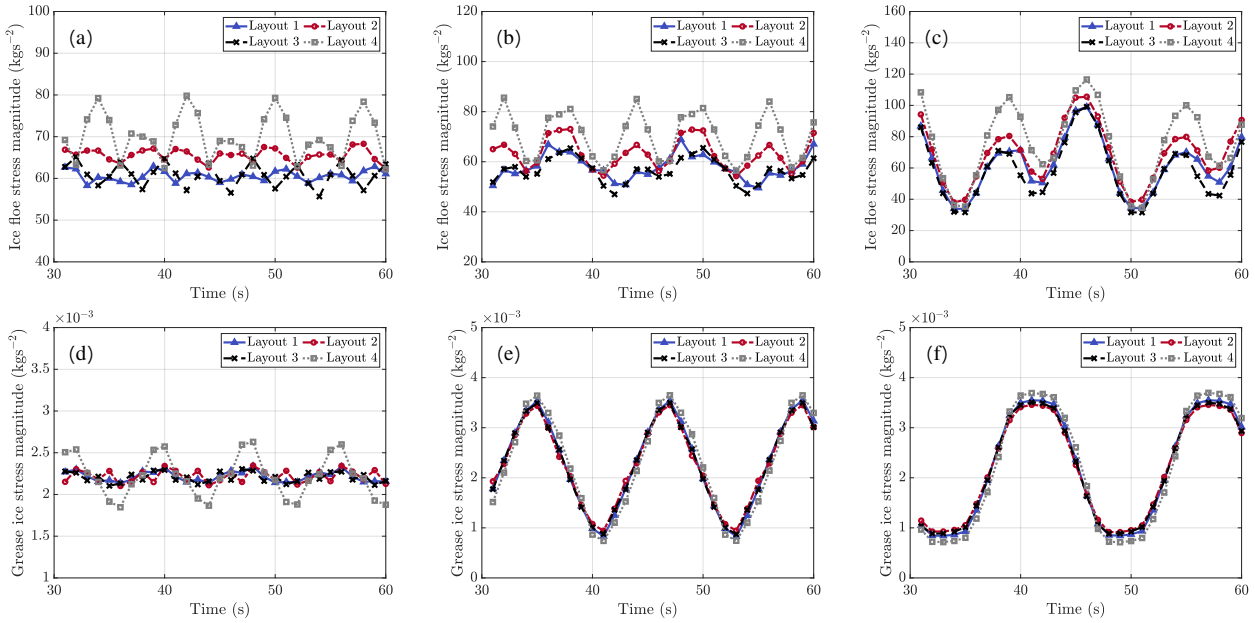

Figure 6.3: Spatially-averaged mechanical sea ice response for layouts 1-4 with $\nu_k \approx 0.04\text{m}^2\text{s}^{-1}$, showing the ice floe stress magnitude [kgs^{-2}] for (**a**) $T = 8$s, (**b**) $T = 12$s and (**c**) $T = 16$s and the grease ice stress magnitude [kgs^{-2}] for (**d**) $T = 8$s, (**e**) $T = 12$s and (**f**) $T = 16$s.

The discrepancy between the curves of the four considered layouts is investigated and expressed in terms of the root mean square error ($RMSE$), which can be calculated by

$$RMSE = \sqrt{\frac{\sum_{i=1}^{N_i}(l_i - \hat{l}_i)^2}{N_i}}, \tag{6.1}$$

where l_i and $\hat{l}_i$ represent the values of stress, strain rate and bulk viscosity, of two layouts to be compared with each other for a particular wave period. The number of values, which is one value per time step, is indicated by N_i, equal to 30. The unit of the $RMSE$ is the same as the quantity being estimated and should be close to zero for good approximations. Tabs. 6.2-6.4 show the $RMSE$ values obtained from the ice floe stress curves for all wave periods and corresponding sea ice layouts. Note that the zero $RMSE$ values on the diagonal are excluded from the calculation of the average $RMSE$.

Table 6.2: Comparison of the ice floe stress response in all layouts. The discrepancy between the stress curves is expressed in terms of the $RMSE$ [kgs^{-2}], for a wave forcing with wave period of $T = 8$s.

$RMSE$ (kgs^{-2})	**Layout 1**	**Layout 2**	**Layout 3**	**Layout 4**	**Average**
Layout 1	0	5.4	2.8	11.0	6.4
Layout 2	5.4	0	6.0	6.4	5.9
Layout 3	2.8	6.0	0	11.9	6.9
Layout 4	11.0	6.4	11.9	0	9.8
Average	6.4	5.9	6.9	9.8	

Table 6.3: Comparison of the ice floe stress response in all layouts. The discrepancy between the stress curves is expressed in terms of the $RMSE$ [kgs^{-2}], for a wave forcing with wave period of $T = 12$s.

$RMSE$ (kgs^{-2})	**Layout 1**	**Layout 2**	**Layout 3**	**Layout 4**	**Average**
Layout 1	0	7.3	3.4	15.6	8.8
Layout 2	7.3	0	7.8	8.8	8.0
Layout 3	3.4	7.8	0	15.8	9.0
Layout 4	15.6	8.8	15.8	0	13.4
Average	8.8	8.0	9.0	13.4	

Table 6.4: Comparison of the ice floe stress response in all layouts. The discrepancy between the stress curves is expressed in terms of the $RMSE$ [kgs^{-2}], for a wave forcing with wave period of $T = 16$s.

$RMSE$ (kgs^{-2})	**Layout 1**	**Layout 2**	**Layout 3**	**Layout 4**	**Average**
Layout 1	0	8.1	5.2	16.8	10.0
Layout 2	8.1	0	11.4	11.4	10.3
Layout 3	5.2	11.4	0	20.0	12.2
Layout 4	16.8	11.4	20.0	0	16.1
Average	10.0	10.3	12.2	16.1	

Visually the discrepancy in the ice floe stress curves seems to decrease for increasing wave period. However, the $RMSE$ values increase for increasing wave period, due to increased ice floe stress magnitudes. Layout 4 exhibits a higher ice floe stress magnitude with a larger amplitude, compared to the realistic sea ice layouts. This coincides with the largest average $RMSE$ values for Layout 4, shown in Tabs. 6.2-6.4, signifying the mounting influence of the detailed heterogeneous sea dynamics description. High stress values are the result of ice floe collisions. Accordingly, if the domain-averaged ice floe stress value at a certain point in time is higher, then more floes and floe interfaces are involved in collisions. The small distance in between ice floes on the left-hand side of the inner domain in Layout 4, causes collisions and therefore high stress values. This also explains why Layout 2 shows the highest ice floe stress curve, when comparing only the realistic sea ice layouts, shown in Figs. 6.3(a-c).

With regards to the influence of floe shape and diameter variations, the ice floe stress response of the idealised sea ice composition Layout 4 is distinctly different from realistic Layout 2, with increasing discrepancy for increasing wave period. The reason is that the stress response of Layout 4 is being overestimated by the idealisation of ice floe geometry. The total interface area is maximised using the constant average diameter for all floes, resulting in the largest potential collision surface area. The $RMSE$ values calculated from the discrepancy in the ice floe stress curves between Layout 2 and 4 for wave periods, $T = 8$s, $T = 12$s and $T = 16$s are 6.4kgs^{-2}, 8.8kgs^{-2} and 11.4kgs^{-2}, respectively.

Figs. 6.3(d-f) show the spatially-averaged grease ice stress for sea ice Layouts 1-4. Results of the three realistic sea ice layouts (Layout 1-3) are very similar for all wave periods, due to a comparable concentration

of grease ice in all layouts. However, not only the grease ice concentration in the domain is of importance, also the fact that the grease ice field is influenced by the motion of ice floes during interaction. Layout 4 has a significant number of ice floes within a small distance, resulting in ice floe-ice floe interaction. This, in turn, affects the grease ice stress response in between these ice floes, similar to the behaviour observed in the ice floe collision test case investigated in 5.3.1. This explains the deviating grease ice stress curves for Layout 4, more pronounced for the smallest wave period. This results in average $RMSE$ values for Layouts 1-3 which are lower than the average $RMSE$ for Layout 4.

In Tabs. 6.5-6.7 the $RMSE$ of the grease ice stress magnitudes is given for all four layouts, subjected to wave periods $T = 8$s, $T = 12$s and $T = 16$s. The uniformity of floe diameter and shape results in a discrepancy in grease ice stress between realistic Layout 2 and the idealised composition Layout 4, mainly visible for the lowest wave period, $T = 8$s, in Fig. 6.3(d). The $RMSE$ values calculated from the discrepancy in the grease ice stress curves between Layout 2 and 4 for wave periods, $T = 8$s, $T = 12$s and $T = 16$s are 0.00023kgs^{-2}, 0.00025kgs^{-2} and 0.00024kgs^{-2}, respectively.

Table 6.5: Comparison of the grease ice stress response in all layouts. The discrepancy between the stress curves is expressed in terms of the $RMSE$ [kgs^{-2}], for a wave forcing with wave period of $T = 8$s.

$RMSE$ (kgs^{-2})	**Layout 1**	**Layout 2**	**Layout 3**	**Layout 4**	**Average**
Layout 1	0	0.00007	0.00005	0.00020	0.00011
Layout 2	0.00007	0	0.00010	0.00023	0.00013
Layout 3	0.00005	0.00010	0	0.00020	0.00012
Layout 4	0.00020	0.00023	0.00020	0	0.00021
Average	0.00011	0.00013	0.00012	0.00021	

Table 6.6: Comparison of the grease ice stress response in all layouts. The discrepancy between the stress curves is expressed in terms of the $RMSE$ [kgs^{-2}], for a wave forcing with wave period of $T = 12$s.

$RMSE$ (kgs^{-2})	**Layout 1**	**Layout 2**	**Layout 3**	**Layout 4**	**Average**
Layout 1	0	0.00010	0.00005	0.00019	0.00011
Layout 2	0.00010	0	0.00008	0.00025	0.00014
Layout 3	0.00005	0.00008	0	0.00021	0.00011
Layout 4	0.00019	0.00025	0.00021	0	0.00022
Average	0.00011	0.00014	0.00011	0.00022	

Table 6.7: Comparison of the grease ice stress response in all layouts. The discrepancy between the stress curves is expressed in terms of the $RMSE$ [kgs^{-2}], for a wave forcing with wave period of $T = 16$s.

$RMSE$ (kgs^{-2})	**Layout 1**	**Layout 2**	**Layout 3**	**Layout 4**	**Average**
Layout 1	0	0.00009	0.00005	0.00016	0.00010
Layout 2	0.00009	0	0.00005	0.00024	0.00013
Layout 3	0.00005	0.00005	0	0.00020	0.00010
Layout 4	0.00016	0.00024	0.00020	0	0.00020
Average	0.00010	0.00013	0.00010	0.00020	

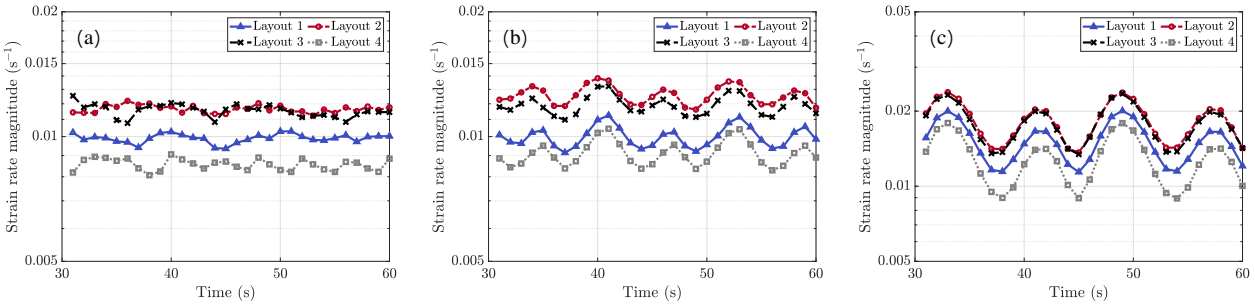

Figure 6.4: Spatially-averaged mechanical sea ice response for layouts 1-4 with $\nu_k \approx 0.04\text{m}^2\text{s}^{-1}$, showing the strain rate magnitude [s^{-1}] for (**a**) $T = 8$s, (**b**) $T = 12$s and (**c**) $T = 16$s.

The spatially-averaged grease ice strain rate curves are shown in Figs. 6.4(a-c) for all sea ice layouts. Looking only at the realistic sea ice layouts a distinctly smaller strain rate magnitude is exhibited for Layout 1, which can be explained by investigating both the ice floe concentration differences and the number of ice floes in the domain. Layout 1 has both, the smallest number of ice floes and concentration of ice floes, but largest average floe size in the domain. The latter means less interface area in relation to total floe area.

Strain rates at the interface between ice floes and grease ice are higher than strain rates away from the interface, hence strain rate at the interface dominate the spatially-averaged grease ice strain rate curves. A smaller concentration of ice floes results in a higher grease ice concentration, which implies a higher ratio between grease ice further away from the interface and grease ice at the interface. This in turn results in lower spatially-averaged grease ice strain rate values, and together explains the lower strain rate magnitude curves for Layout 1. Layout 2 has both, a higher number of ice floes and a higher ice floe concentration, compared to Layout 3 but also a larger average floe size. In combination, it results that both strain rate magnitude curves are close together.

Comparing the grease ice strain rate curves of Layout 2 and 4, it can be seen that the average strain rate is lower for the idealised Layout 4, due to fewer ice floes in the domain but effectively same floe size. In Tabs. 6.8-6.10 the $RMSE$ is calculated for the grease ice strain rate magnitude curves of all four layouts subjected to wave periods $T = 8$s, $T = 12$s and $T = 16$s. The discrepancy in the grease ice strain rate between Layouts 2 and 4 increases for increasing wave period, as for, $T = 8$s, $T = 12$s and $T = 16$s $RMSE$ values are equal to 0.0031s^{-1}, 0.0035s^{-1} and 0.0055s^{-1}, respectively.

Table 6.8: Comparison of the grease ice strain rate response in all layouts. The discrepancy between the strain rate curves is expressed in terms of the $RMSE$ [s^{-1}], for a wave forcing with wave period of $T = 8$s.

$RMSE$ (s^{-1})	**Layout 1**	**Layout 2**	**Layout 3**	**Layout 4**	**Average**
Layout 1	0	0.0018	0.0017	0.0014	0.0016
Layout 2	0.0018	0	0.0005	0.0031	0.0018
Layout 3	0.0017	0.0005	0	0.0030	0.0017
Layout 4	0.0014	0.0031	0.0030	0	0.0025
Average	0.0016	0.0018	0.0017	0.0025	

Table 6.9: Comparison of the grease ice strain rate response in all layouts. The discrepancy between the strain rate curves is expressed in terms of the $RMSE$ [s^{-1}], for a wave forcing with wave period of $T = 12$s.

$RMSE$ (s^{-1})	**Layout 1**	**Layout 2**	**Layout 3**	**Layout 4**	**Average**
Layout 1	0	0.0026	0.0019	0.0009	0.0018
Layout 2	0.0026	0	0.0007	0.0035	0.0023
Layout 3	0.0019	0.0007	0	0.0028	0.0018
Layout 4	0.0009	0.0035	0.0028	0	0.0024
Average	0.0018	0.0023	0.0018	0.0024	

Table 6.10: Comparison of the grease ice strain rate response in all layouts. The discrepancy between the strain rate curves is expressed in terms of the $RMSE$ [s^{-1}], for a wave forcing with wave period of $T = 16$s.

$RMSE$ (s^{-1})	**Layout 1**	**Layout 2**	**Layout 3**	**Layout 4**	**Average**
Layout 1	0	0.0032	0.0028	0.0023	0.0028
Layout 2	0.0032	0	0.0005	0.0055	0.0031
Layout 3	0.0028	0.0005	0	0.0051	0.0028
Layout 4	0.0023	0.0055	0.0051	0	0.0043
Average	0.0028	0.0031	0.0028	0.0043	

Eq. (3.9) in Chap. 3 shows that the relation between the grease ice strain rate and bulk viscosity is inversely proportional. An increase in grease ice viscosity results in a decreasing strain rate and vice versa. This explains why the bulk viscosity curves of Layout 1 are higher than the curves of Layouts 2 and 3, mainly observable in Figs. 6.5(a) and (b).

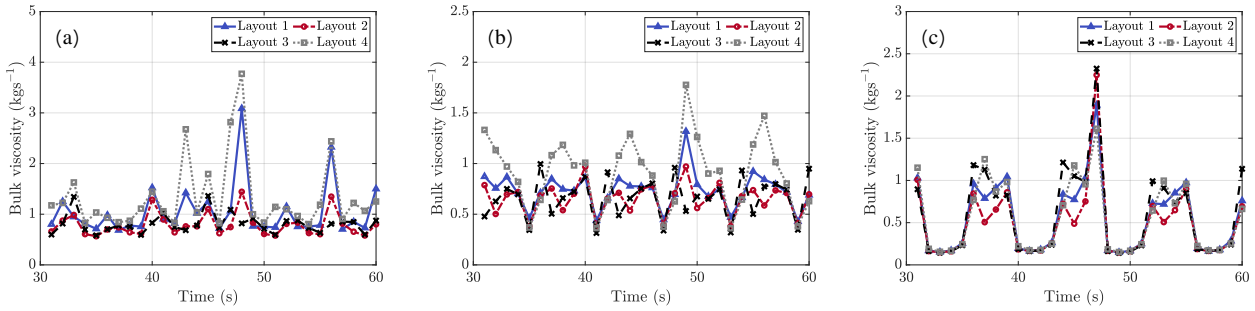

Figure 6.5: Spatially-averaged mechanical sea ice response for layouts 1-4 with $\nu_k \approx 0.04 m^2 s^{-1}$, showing the bulk viscosity [kgs^{-1}] for (**a**) $T = 8$s, (**b**) $T = 12$s and (**c**) $T = 16$s.

In Tabs. 6.11-6.13 the $RMSE$ is calculated for the grease ice bulk viscosity curves of all four layouts subjected to wave periods $T = 8$s, $T = 12$s and $T = 16$s. Due to the direct interrelation between the strain rate and bulk viscosity variables, the average discrepancy in grease ice viscosity between Layout 2 and 4 is also high for wave periods, $T = 8$s, $T = 12$s and $T = 16$s, with $RMSE$ values decreasing for increasing wave period, equal to $0.782 kgs^{-1}$, $0.386 kgs^{-1}$ and $0.247 kgs^{-1}$, respectively.

Table 6.11: Comparison of the grease ice bulk viscosity response in all layouts. The discrepancy between the bulk viscosity curves is expressed in terms of the $RMSE$ [kgs^{-1}], for a wave forcing with wave period of $T = 8$s.

$RMSE$ (kgs^{-1})	**Layout 1**	**Layout 2**	**Layout 3**	**Layout 4**	**Average**
Layout 1	0	0.429	0.568	0.488	0.495
Layout 2	0.429	0	0.212	0.782	0.474
Layout 3	0.568	0.212	0	0.843	0.541
Layout 4	0.488	0.782	0.843	0	0.704
Average	0.495	0.474	0.541	0.704	

Table 6.12: Comparison of the grease ice bulk viscosity response in all layouts. The discrepancy between the bulk viscosity curves is expressed in terms of the $RMSE$ [kgs^{-1}], for a wave forcing with wave period of $T = 12$s.

$RMSE$ (kgs^{-1})	**Layout 1**	**Layout 2**	**Layout 3**	**Layout 4**	**Average**
Layout 1	0	0.135	0.238	0.270	0.214
Layout 2	0.135	0	0.177	0.386	0.233
Layout 3	0.238	0.177	0	0.450	0.288
Layout 4	0.270	0.386	0.450	0	0.369
Average	0.214	0.233	0.288	0.369	

Table 6.13: Comparison of the grease ice bulk viscosity response in all layouts. The discrepancy between the bulk viscosity curves is expressed in terms of the $RMSE$ [kgs^{-1}], for a wave forcing with wave period of $T = 16$s.

$RMSE$ (kgs^{-1})	**Layout 1**	**Layout 2**	**Layout 3**	**Layout 4**	**Average**
Layout 1	0	0.140	0.176	0.147	0.154
Layout 2	0.140	0	0.232	0.247	0.206
Layout 3	0.176	0.232	0	0.218	0.209
Layout 4	0.147	0.247	0.218	0	0.204
Average	0.154	0.206	0.209	0.204	

6.2 Numerical study on the mechanical behaviour of ice floe-grease ice interaction

The objective of this numerical study is to map the high-resolution mechanical behaviour of interacting ice floes embedded in grease ice. Additionally, the effect of grease ice viscosity on both the stress and strain rate response of sea ice is discussed, considering an imposed wave forcing.

A detailed analysis is performed of sea ice dynamics and its characterizing rheology variables. Ice floe and grease ice properties and wave characteristics used in this section are summarised in Tab. 6.14. A 100×100m^2 realistic heterogeneous sea ice layout, shown in Fig. 6.6, is subjected to five different wave characteristics propagating in the x-direction, where the wave periods with corresponding wave amplitude have a prescribed wave steepness, $ak = 0.06$ [41], found by varying the amplitude of the waves. The chosen three kinematic grease ice viscosity values are in-line with Newyear and Martin [134], Paul et al. [142], Wadhams et al. [205], Wang and Shen [206]. The bulk viscosity is directly related to the grease ice strength parameter, P_g, as shown in

Eqs. (3.8) and (3.9). Accordingly, values for P_g^* are determined such that the resulting domain-averaged bulk viscosity provides a close fit to the corresponding kinematic grease ice viscosity values.

Table 6.14: Parameters used in the sea ice dynamics analysis in this section.

Parameter	**Definition**	**Value**	**Unit**
a	wave amplitude	2.1, 2.9, 3.8, 4.8, 6	m
ak	wave steepness	0.06 [41]	-
$C_{w_{f,g}}$	water drag coefficient for ice floes and grease ice	0.02, 0.008	-
P_g^*	grease ice strength parameter	0.006, 0.024, 0.096	Nm^{-2}
T	wave period	12, 14, 16, 18, 20	s
Λ	wave length	225, 306, 400, 506, 625	m
ν_k	kinematic grease ice viscosity	0.01, 0.04, 0.16 [134, 142, 205, 206]	$\mathrm{m}^2\mathrm{s}^{-1}$

The presentation of the sea ice dynamics analysis results in Sec. 6.2 is split into two subsections. In Sec. 6.2.1, the response of the sea ice velocity field and the relative motion between ice floes are studied. Additionally, the interaction between ice floes is discussed, focusing on the number of ice floe collisions with corresponding collision stress intensity. Contour plots are shown for a time window of one wave length, allowing for a comparison between the different wave periods and to illustrate the most important time frames within one wave length. Furthermore, the impact of the stress response on changes in grease ice viscosity is discussed.

Sec. 6.2.2 studies the interaction between two ice floe pairs and the interface between ice floes and grease ice. The detailed stress, strain rate, viscosity and velocity gradient distributions are shown, by means of contour plots in a realistic heterogeneous sea ice domain. The strain rate is highly dependent on the velocity gradient, as shown in Eq. (3.6) in Chap. 3. Additionally, the impact of the strain rate response on changes in grease ice viscosity is mapped.

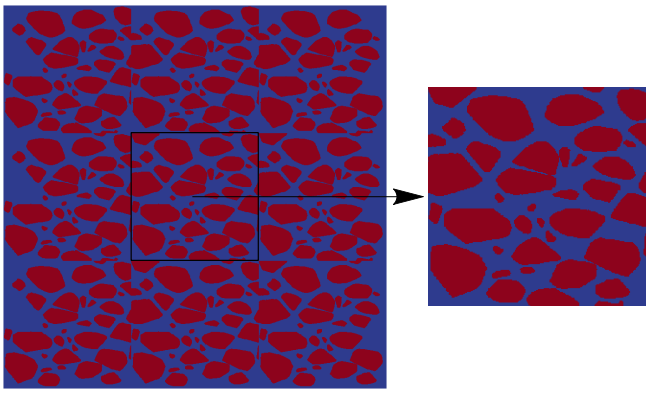

Figure 6.6: Realistic sea ice layout, showing a $100 \times 100\mathrm{m}^2$ inner domain with a total of 90000 FVM cells indicated by a black rectangle, embedded in a $300 \times 300\mathrm{m}^2$ outer domain with a total of 810000 FVM cells.

6.2.1 Sea ice velocity and ice floe stress response

The wave elevation of an imposed gravity wave with a period of $T = 12\mathrm{s}$ is illustrated in Fig. 6.7, shown for a time window of one wave length between $t = 38\mathrm{s}$ and $t = 50\mathrm{s}$. The wave propagates in the horizontal x-direction through the $100 \times 100\mathrm{m}^2$ inner domain with a total of 90000 FVM cells, consisting of grease ice with a domain-averaged kinematic viscosity of $\nu_k \approx 0.04\mathrm{m}^2\mathrm{s}^{-1}$.

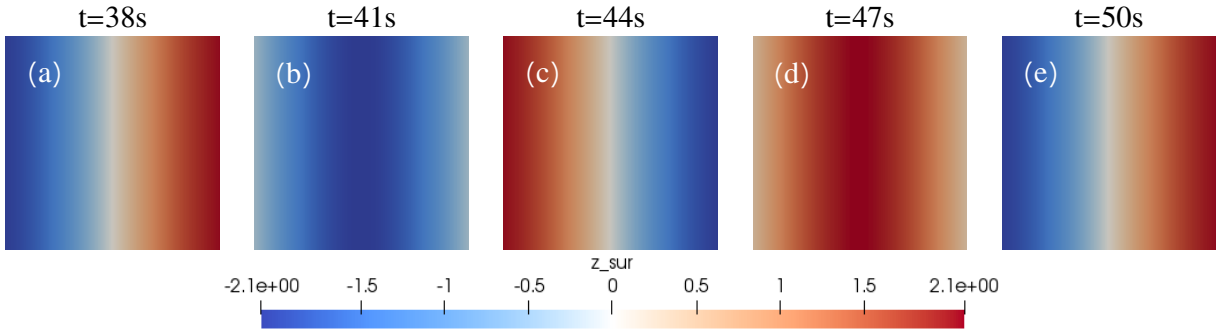

Figure 6.7: Wave elevation [m] for an imposed wave forcing exemplified for $T = 12$s and kinematic grease ice viscosity $\nu_k \approx 0.04\text{m}^2\text{s}^{-1}$, illustrating **(a-e)** one wave length between $t = 38$s and $t = 50$s.

The five time steps show characteristic positions within one wave length. Figs. 6.7(a,c,e) show a domain-averaged wave elevation equal to zero, with a descending wave flank in Figs. 6.7(a,e) and an ascending wave flank in Fig. 6.7(c). The wave trough is depicted in Fig. 6.7(b), whereas the wave crest is shown in Fig. 6.7(d).

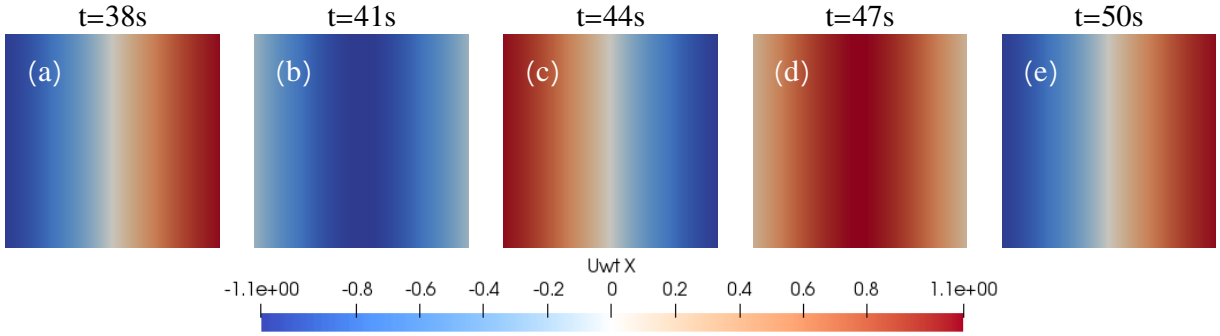

Figure 6.8: Orbital wave velocity [ms^{-1}] for an imposed wave forcing exemplified for $T = 12$s and kinematic grease ice viscosity $\nu_k \approx 0.04\text{m}^2\text{s}^{-1}$, illustrating **(a-e)** one wave length between $t = 38$s and $t = 50$s.

The imposed orbital wave velocity in the x-direction, shown in Fig 6.8, results in the sea ice velocity (in the x-direction), depicted in Fig. 6.9. The sea ice velocity distribution is characterised by a delayed response and exhibits clear floe size-dependent differences, both due to the effect of inertia. Temporary contact between ice floes is indicated when sharing the same velocity magnitude. The predominantly oscillatory nature of the induced orbital wave velocity yields a negligible net-resultant horizontal movement of ice floes over time, due to ice floes that move back and forth in an orbital motion.

Ice floes at the centre of Fig. 6.9(a) at $t = 38$s, are located in an ascending wave flank with an orbital wave velocity in the x-direction equal to zero and a maximum positive floe velocity in the x-direction indicating a sliding motion of ice floes in forward direction. At $t = 41$s, the centrally located ice floes are in the wave trough, showing a largest negative orbital wave velocity and, due to inertia, a floe velocity in the x-direction close to zero indicating a clear phase shift between both. Considering that subsequently at $t = 44$s at the centre of Fig. 6.9(c) the ice floe velocity is maximum negative, it is clear that the ice floe motion is diverging in the wave trough. Similarly, looking the contour plots at $t = 47$s and $t = 50$s, respectively, one finds converging ice floe motion at the wave crest. The effect of gravitation-caused sliding of ice floes downwards both wave flanks would lead to the opposite motion behaviour but can be considered negligible [66].

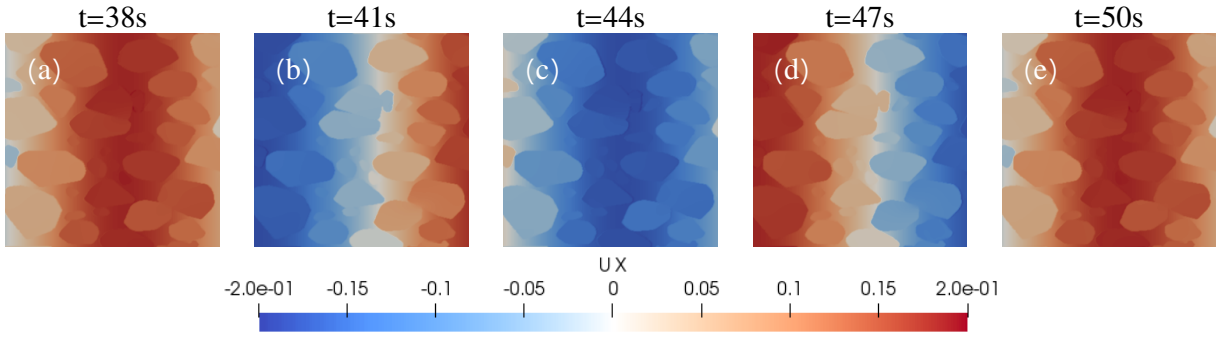

Figure 6.9: Sea ice velocity [ms^{-1}] for an imposed wave forcing exemplified for $T = 12$s and kinematic grease ice viscosity $\nu_k \approx 0.04\mathrm{m}^2\mathrm{s}^{-1}$, illustrating **(a-e)** one wave length between $t = 38$s and $t = 50$s.

Fig. 6.10 highlights the velocity differences of ice floes and the surrounding grease ice, where only the former are affected by form drag and collision-induced rotation. Due to the orbital sea ice motion, vertical bands, along which the velocity vectors point in opposite direction on either side, indicate floes being located between trough and crest according to the wave elevation plots illustrated in Fig. 6.7. Colliding ice floes temporarily show shared velocity values and velocity directions at contact.

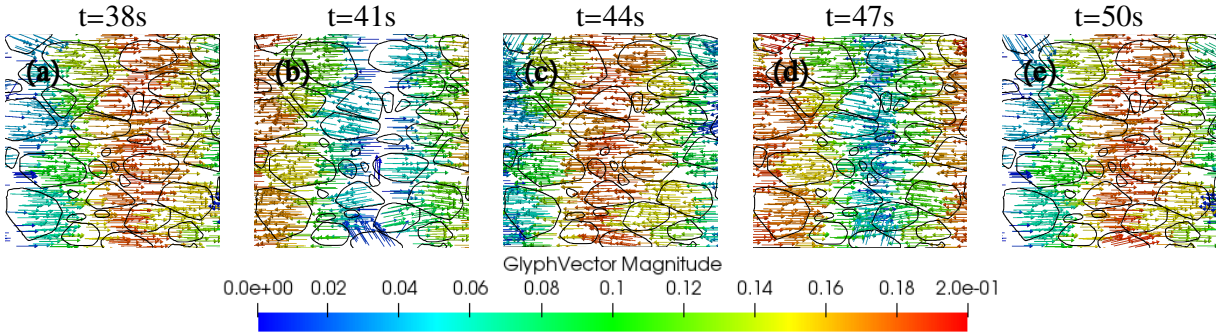

Figure 6.10: Sea ice velocity vectors [ms^{-1}] for an imposed wave forcing exemplified for $T = 12$s and kinematic grease ice viscosity $\nu_k \approx 0.04\mathrm{m}^2\mathrm{s}^{-1}$, illustrating **(a-e)** one wave length between $t = 38$s and $t = 50$s.

In Fig. 6.11 the areas marked by white rectangles highlight the evolution of two ice floe collisions over time for a wave forcing with $T = 12$s, characterised as points of highly localised stress magnitudes. The floe interaction is not characterised by short violent collisions but rather continuous churning contact varying in intensity.

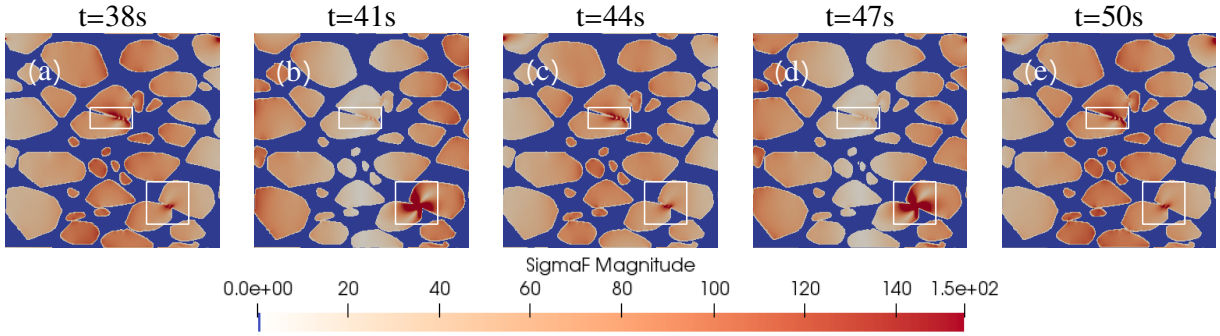

Figure 6.11: Ice floe stress magnitude [kgs^{-2}] for an imposed wave forcing exemplified for $T = 12$s and kinematic grease ice viscosity $\nu_k \approx 0.04\mathrm{m}^2\mathrm{s}^{-1}$, illustrating **(a-e)** one wave length between $t = 38$s and $t = 50$s. The white rectangles at the bottom-right (Zone I) and centre (Zone II) mark floe collisions.

For the more prominent ice floe collision in the bottom-right (Zone I), the collision stress intensity is most pronounced when the two colliding floes left the trough at $t = 41$s and passed the crest $t = 47$s as shown in Figs. 6.11(b) and (d) which can be determined from Figs. 6.7(b) and (d), respectively. Similarly, the floe collision found in the domain centre (Zone II) exhibits a high stress intensity when the two involved floes passed the crest at $t = 38$s, left the trough at $t = 44$s and passed the crest again at $t = 50$s. This is studied in more detail, later in this section, for specific floe collisions.

The minimum principal stress, σ_{min}, if negative, is the maximum compressive stress, acting normal to the plane where shear stress is zero, and provides an indication of the collision stress intensity. Contour plots of the minimum principal ice floe stress for wave forcing with $T = 12$s and $T = 20$s are illustrated in Figs. 6.12 and 6.13, showing the evolution of ice floe collisions over time. Note that the legends differ, as they are wave period dependent. $T = 20$s yields a higher number of ice floe collisions, whereas for $T = 12$s only a few selected pairs of floes directly interact with each other, specifically, floes which have been in close vicinity at $t = 0$s already, for example as marked by the white rectangles (Zones I and II). Differences in ice floe collision patterns are due to an increasing wave kinetic energy for increasing wave period on condition that a prescribed wave steepness is considered.

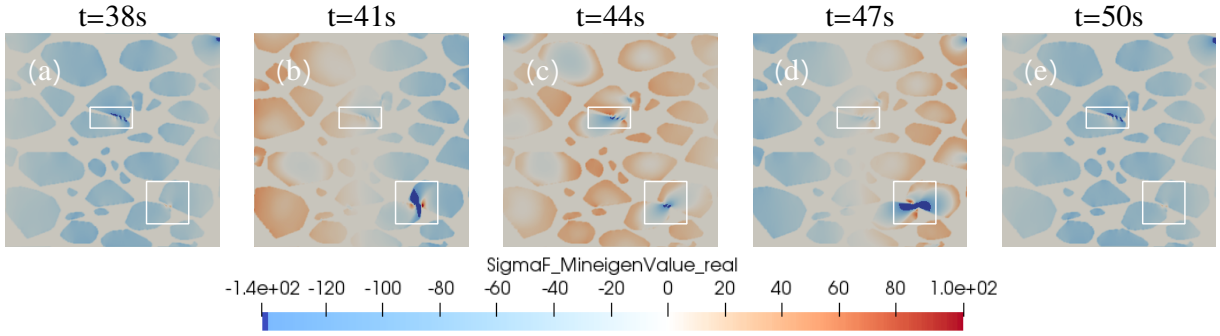

Figure 6.12: Minimum principal ice floe stress [kgs^{-2}] for an imposed wave forcing exemplified for $T = 12$s and kinematic grease ice viscosity $\nu_k \approx 0.04$m^{2}s^{-1}, illustrating **(a-e)** one wave length between $t = 38$s and $t = 50$s. The white rectangles at the bottom-right (Zone I) and centre (Zone II) mark floe collisions.

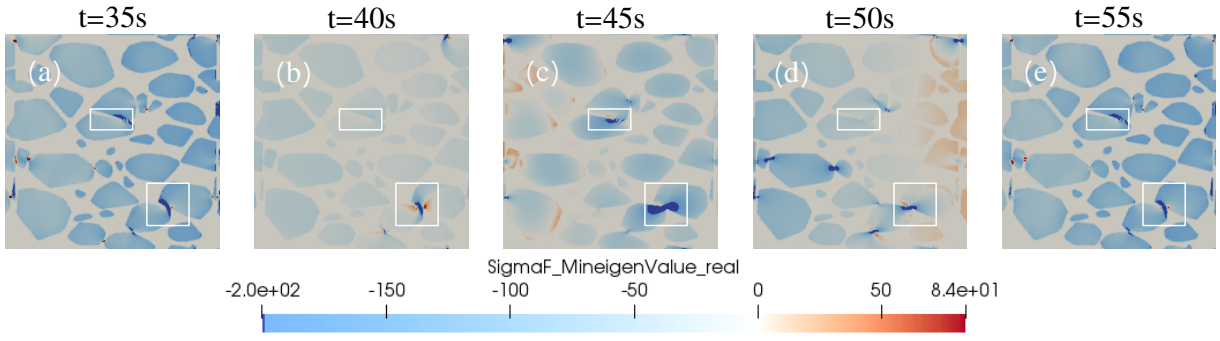

Figure 6.13: Minimum principal ice floe stress [kgs^{-2}] for an imposed wave forcing exemplified for $T = 20$s and kinematic grease ice viscosity $\nu_k \approx 0.04$m^{2}s^{-1}, illustrating **(a-e)** one wave length between $t = 35$s and $t = 55$s. The white rectangles at the bottom-right (Zone I) and centre (Zone II) mark floe collisions.

The interrelation between wave elevation, velocity in the x-direction and ice floe collision stress intensity over time are discussed for the ice floe collisions occurring in Zone I and Zone II. Considering wave forcings with

$T = 12$s, $T = 16$s and $T = 20$s, the minimum principal stress collision intensity observed over a time window of one wave length yields a peak collision stress intensity in Zone I equal to $\sigma_{col}^{peak} = -973\text{kgs}^{-2}$, -1186kgs^{-2}, and -1535kgs^{-2}, respectively, and in Zone II equal to $\sigma_{col}^{peak} = -371\text{kgs}^{-2}$, -410kgs^{-2}, and -541kgs^{-2}, respectively.

Ice floe collisions occur for all five wave periods considered, but their number increases with the wave period, as found by visual inspection of Fig. 6.12 as opposed to Fig. 6.13. This is also reflected by the percentages of FVM cells exhibiting highly localised minimum principal stress values (> 2MPa [161, 168]) which is only 0.10%, 0.50% and 1.18% for wave periods $T = 12$s, $T = 16$s and $T = 20$s, respectively. These results support the assumption of no ice floe failure and fracture in the small-scale model, as mentioned in Chap. 1. Mainly the same ice floes collide for wave periods with $T < 16$s. A larger variety of ice floes collide for the larger wave periods with $T \geq 16$s, due to a higher kinetic wave energy in the system.

In Fig. 6.14(a) box plots show the minimum principal stress values of all FVM ice floe cells in the inner domain accumulated (collection of all the ice floe stress values) between one wave length with $\nu_k \approx 0.04\text{m}^2\text{s}^{-1}$ for the five wave forcing increasing from $T = 12 - 20$s. All wave periods show sample skewness, representing

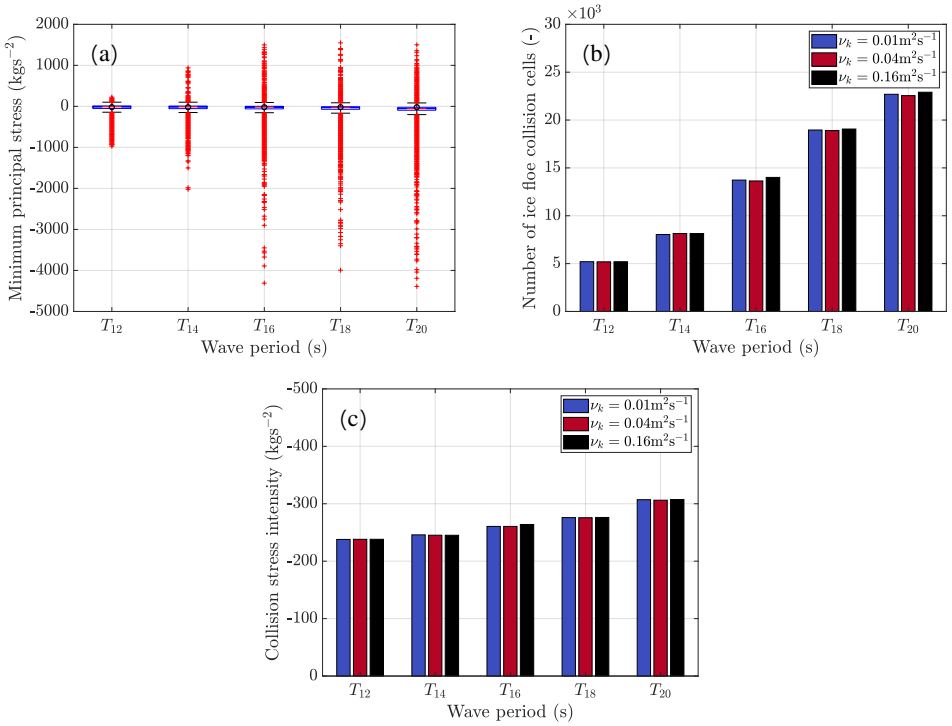

Figure 6.14: Five waves with a wave period $T = 12 - 20$s, showing **(a)** box plots with minimum principal stress values [kgs^{-2}] of all ice floe cells in the inner problem domain with $\nu_k \approx 0.04\text{m}^2\text{s}^{-1}$, **(b)** number of ice floe collision cells [−] for kinematic grease ice viscosity ranging from $\nu_k \approx 0.01 - 0.16\text{m}^2\text{s}^{-1}$ and **(c)** temporally- and spatially-averaged collision stress intensity [kgs^{-2}] for kinematic grease ice viscosity ranging from $\nu_k \approx 0.01 - 0.16\text{m}^2\text{s}^{-1}$.

the mean minimum principal stress in ice floes indicated by a black circle ranging between $\sigma_{col} = -18.88\text{kgs}^{-2}$ and -62.01kgs^{-2}. The median is indicated by a red horizontal line, ranging between $\sigma_{col} = -10.15\text{kgs}^{-2}$ and -53.60kgs^{-2}. The maximum and minimum whisker length, representing the upper and lower adjacent, respectively, are calculated by $q_3 + w(q_3 - q_1)$. w denotes the multiplier whisker, which is equal to 1.5. The 25$^{\text{th}}$

percentile is indicated by q_1 and the 75^{th} percentile is given by q_3. All FVM cell-values in the inner problem domain beyond the maximum and minimum whisker length are defined in statistical outliers, indicated by red plus symbols in Fig. 6.14(a). Specifically, the negative minimum principal stress outliers refer to ice floe portions under severe compression as found in floe collision zones illustrated in Figs. 6.12 and 6.13. The corresponding lower adjacent in the box plot, shown in Fig. 6.14(a), is used to define the collision stress threshold, which equals $\sigma_{col}^{thres} = -142.8\text{kgs}^{-2}$, -149.5kgs^{-2}, -154.4kgs^{-2}, -166.3kgs^{-2}, -200.8kgs^{-2} for wave forcings with $T = 12$s, $T = 14$s, $T = 16$s, $T = 18$s and $T = 20$s, respectively. The number of extreme minimum principal stress outliers, referred to as collision stress in the following, indicate the number of cells directly affected by floe collisions, where their number increases with the frequency and severity of floe collisions. Fig. 6.14(b) shows the total number of minimum principal stress outliers accumulated during one wave length in the inner domain and Fig. 6.14(c) shows the temporally and domain-averaged collision stress value for all five wave forcing with kinematic grease ice viscosities $\nu_k \approx 0.01\text{m}^2\text{s}^{-1}$, $\nu_k \approx 0.04\text{m}^2\text{s}^{-1}$, and $\nu_k \approx 0.16\text{m}^2\text{s}^{-1}$, respectively. The number of cells associated with collisions show a clear gradual increase for increasing wave period. Consequently, the temporally- and spatially-averaged collision stress intensity also increases for increasing wave period. The stress response is not significantly impacted by changes in viscosity within the given range as found in situ [134, 142, 205, 206]. The main reason is that the used range of viscosity values is relatively small. Therefore, differences in viscosity values only result in relatively small changes. Additionally, the small-scale model considers an imposed wave. If the wave would freely propagate and dissipate energy after entering the ice field, both the strain rate and the stress distribution would be affected and decrease further due to the presence of sea ice. However, this effect would be small in a small sea ice domain.

To study the two ice floe collisions occurring in the bottom-right corner (Zone I) and in the centre (Zone II), as shown in Figs. 6.12 and 6.13, in more detail, the mean wave elevation, velocity in the x-direction and collision stress intensity of both floes combined are plotted over time for wave forcing with $T = 12$s, $T = 16$s and $T = 20$s. Firstly, the most prominent ice floe collision is discussed in Fig. 6.15, which refers to the collision in Zone I. Figs. 6.15(a,d,g) show the absolute value of the mean collision stress intensity and wave elevation over time for wave forcing with $T = 12$s, $T = 16$s and $T = 20$s, respectively. All wave periods show a similar correlation, where the collision stress intensity shows minimum and maximum collision stress magnitudes just before and after both, the wave crest and the wave trough, respectively. The time-averaged collision stress intensity in Zone I over one entire wave length passing through increases for increasing wave period, namely $\sigma_{col}^{avg} = -233\text{kgs}^{-2}$ for $T = 12$s and $t = 38 - 50$s, -248kgs^{-2} for $T = 16$s and $t = 30 - 46$s, and -303kgs^{-2} for $T = 20$s and $t = 35 - 55$s. The absolute value of the collision stress intensity and the number of ice floe collision FVM cells involved, show a direct relation, that is, an increase in the collision stress intensity results in an increasing number of ice floe collision cells, as depicted in Figs. 6.15(b,e,h). The total number of ice floe collision FVM cells accumulated for all time steps during one entire wave length passing through Zone I are equal to 4168, 5991 and 7608 for wave periods $T = 12$s, $T = 16$s and $T = 20$s, respectively. Discontinuities in the curves of the domain-averaged collision stress intensity, as depicted in Figs. 6.15(a,b,d,e,g,h), indicate that the minimum principal stress of the two floes is below the previously defined collision stress threshold, σ_{col}^{thres}. This is either due to ice floes that have temporarily detached themselves leading to the absence of ice floe collision cells or due to ice floe contact with low stress intensity.

Secondly, the interrelations between mean wave elevation, velocity in the x-direction and collision stress intensity are shown for the two ice floes close in the centre (Zone II) of the inner domain in Fig. 6.16. The time-averaged collision stress intensity values over a time window of one wave length are equal to $\sigma_{col}^{avg} = -184\text{kgs}^{-2}$, -190kgs^{-2}, and -250kgs^{-2} for a wave period with $T = 12$s, $T = 16$s and $T = 20$s, respectively, showing that

this collision is less violent. These values, in addition to the time-averaged collision stress intensity values found for the collision in Zone I, correspond to the increasing collision stress intensity with increasing wave period, as shown in Fig. 6.14(c) for all collisions occurring in the inner domain.

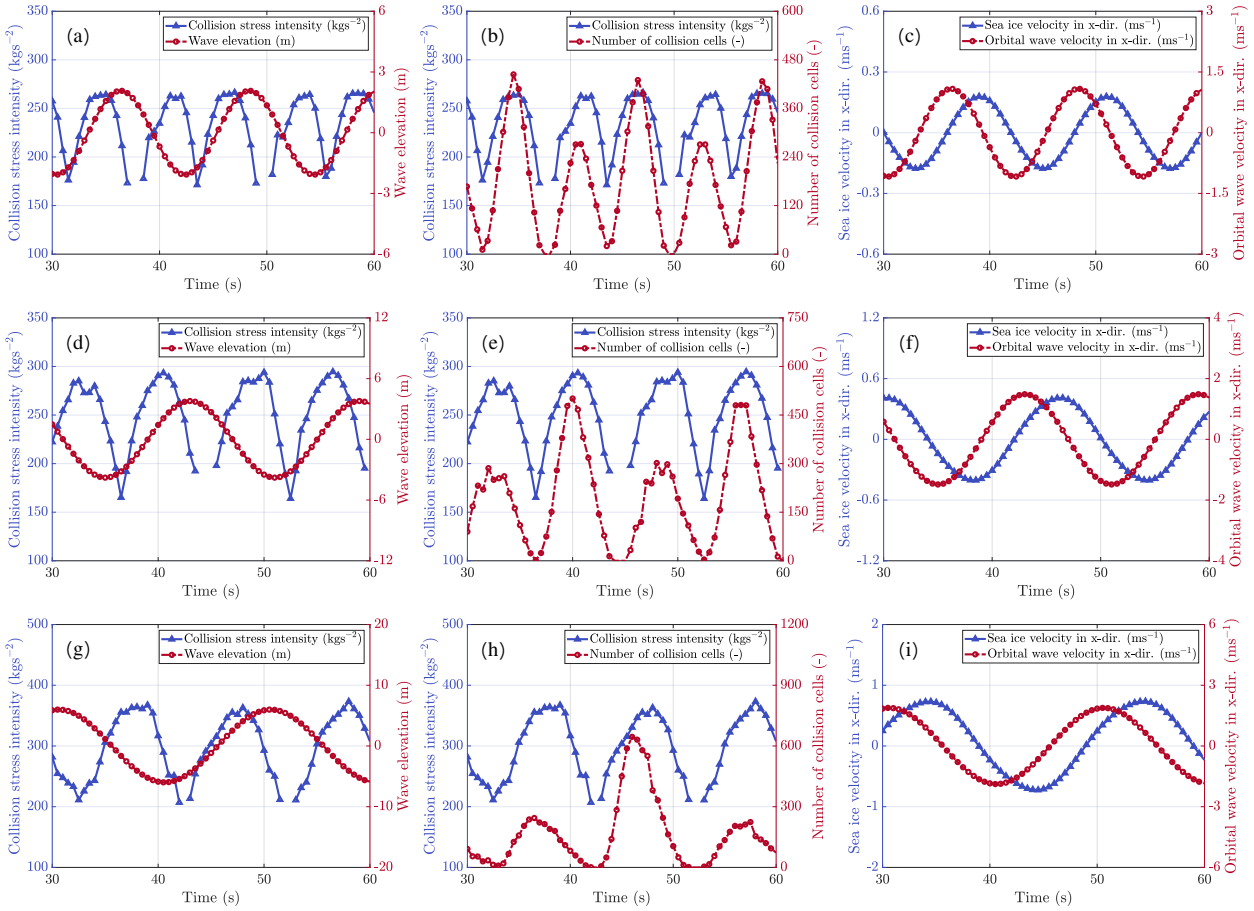

Figure 6.15: Correlation between variables of the collision in the bottom-right corner (Zone I) of the inner domain. **(a,d,g)** absolute value of the ice floe collision stress intensity [kgs^{-2}] vs. wave elevation [m], **(b,e,h)** absolute value of the ice floe collision stress intensity [kgs^{-2}] vs. the number of ice floe collision cells over time [−], **(c,f,i)** sea ice velocity in the x-direction [ms^{-1}] vs. orbital wave velocity in the x-direction [ms^{-1}], shown for three different wave forcings with $\nu_k \approx 0.04\text{m}^2\text{s}^{-1}$ **(a-c)** $T = 12$s, **(d-f)** $T = 16$s and **(g-i)** $T = 20$s.

The total number of ice floe collision cells involved in the collision in Zone II is equal to 545, 843 and 1206, for wave periods $T = 12$s, $T = 16$s and $T = 20$s, respectively. Comparing these numbers with the numbers of the collision in Zone I, a similar trend can be observed. The same applies to the total number of ice floe collision cells in the entire inner domain, illustrated in Fig. 6.14(b). Fig. 6.16 shows similar collisional behaviour as observed previously in Fig. 6.15 for the collision in Zone I. The collision is less violent, as the collision stress intensity and the number of collisions are lower than for the collision occurring in Zone I. This is to be expected, considering that the two colliding floes in Zone I are positioned subsequently of each other with respect to the horizontal wave propagation direction. The two floes in Zone II, however, are positioned parallel to each other, which limits the momentum transfer. More interruptions are observed in the collision stress intensity curve where the minimum principal stress values $\sigma_{min} < \sigma_{col}^{thres}$ and the two floes are not engaged in full collision contact.

The local sea ice velocity and the orbital wave velocity in the x-direction, shown in Figs. 6.15(c,f,i) and 6.16(c,f,i)

for three different wave periods, $T = 12$s, $T = 16$s and $T = 20$s, respectively, show similar behaviour for both ice floe collisions. Note, however, that the curves are slightly shifted, due to a different location of the ice floe collisions in the inner domain. Hypothetically speaking, ice floe collisions in the inner domain would not occur when the sea ice cover is at rest, which implies that the sea ice velocity and wave elevation are in phase and equal to zero. However, due to the influence of sea ice inertia, the collision stress intensity is out of phase with the velocity and wave elevation. As a result, the interrelation between sea ice velocity, wave elevation and collision stress intensity is not straight-forward.

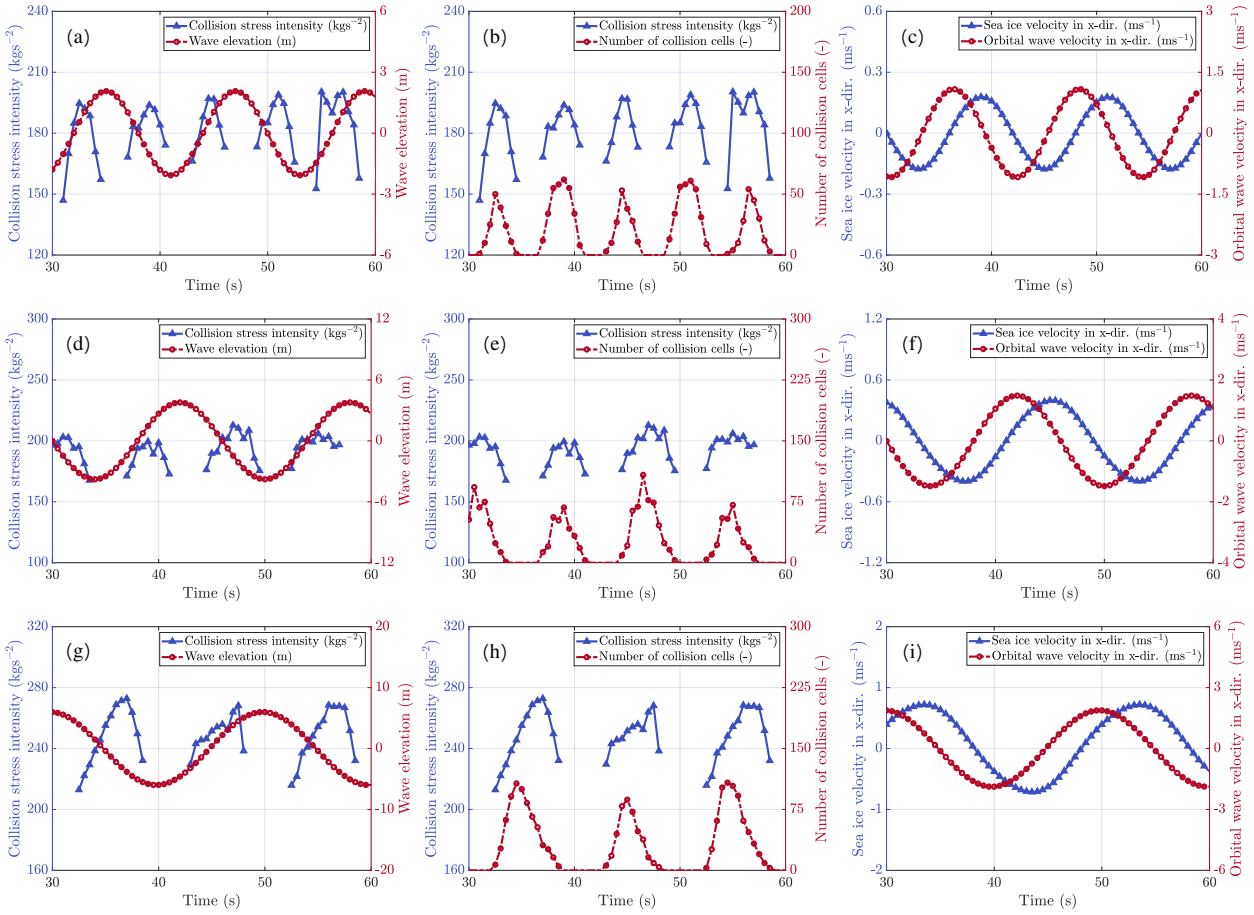

Figure 6.16: Correlation between variables of the collision in the centre (Zone II) of the inner domain. **(a,d,g)** absolute value of the ice floe collision stress intensity [kgs^{-2}] vs. wave elevation [m], **(b,e,h)** absolute value of the ice floe collision stress intensity [kgs^{-2}] vs. the number of ice floe collision cells over time [−], **(c,f,i)** sea ice velocity in the x-direction [ms^{-1}] vs. orbital wave velocity in the x-direction [ms^{-1}], shown for three different wave forcings with $\nu_k \approx 0.04$m^{2}s^{-1} **(a-c)** $T = 12$s, **(d-f)** $T = 16$s and **(g-i)** $T = 20$s.

The relative motion of the ice layer with respect to the ocean layer underneath is generally influenced by the wave forcing and the ice composition [171]. In particular, inertia of the ice cover opposing the oscillatory orbital wave velocity and the frictional contact at the ice basal plane, result in a lag of the sea ice velocity behind the orbital wave velocity. The phase shift between the sea ice velocity and the orbital wave velocity in the x-direction is constant over time and equal to 2.5s, 3.5s and 4s, for wave periods $T = 12$s, $T = 16$s and $T = 20$s, respectively. Thus, the constant phase shift is not the same for all wave periods, but increases for increasing wave period.

From Fig. 6.17, it can be seen that the effect of grease ice viscosity on the phase shift in Zone I is negligible

considering the lowest and highest kinematic grease ice viscosity values, $\nu_k \approx 0.01\text{m}^2\text{s}^{-1}$ and $\nu_k \approx 0.16\text{m}^2\text{s}^{-1}$, respectively. The effect of inertia, on the interrelation between the sea ice velocity and wave elevation, has also been discussed in Test case 2 in Sec. 5.3.2.

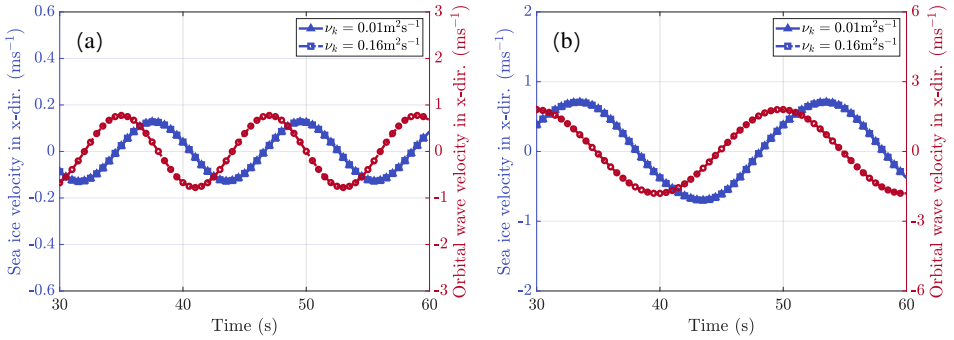

Figure 6.17: The influence of grease ice viscosity values, $\nu_k \approx 0.01\text{m}^2\text{s}^{-1}$ and $\nu_k \approx 0.16\text{m}^2\text{s}^{-1}$, on the phase shift in Zone I, showing for a wave period of **(a)** $T = 12$s and **(b)** $T = 20$s.

6.2.2 Grease ice stress, viscosity and strain rate response

The previously observed heterogeneous ice motion characteristics are caused by the heterogeneous sea ice composition and distinct differences in material behaviour of its two constituents, ice floes and grease ice, respectively. The viscous stress response of grease ice is non-linear and highly strain rate-dependent and generally several orders of magnitude smaller than the ice floe stress. The magnitude of the velocity gradient is shown in Fig. 6.18. The distribution of the strain rate magnitude, illustrated in Fig. 6.19, is qualitatively similar to the velocity gradient magnitude distribution. Note that the legends of both variables are capped to improve clarity of the contour plots. The inner domain contains values up to $\dot{\epsilon}_{mag} \approx 0.15\text{s}^{-1}$ and $\nabla U_{mag} \approx 0.15\text{s}^{-1}$ at the interface between ice floes and grease ice. The sea ice velocity gradient, and therefore the strain rate, approaches zero when the sea ice velocity is either at its maximum or minimum, which corresponds to a wave elevation close to zero, in between the wave crest and the wave trough.

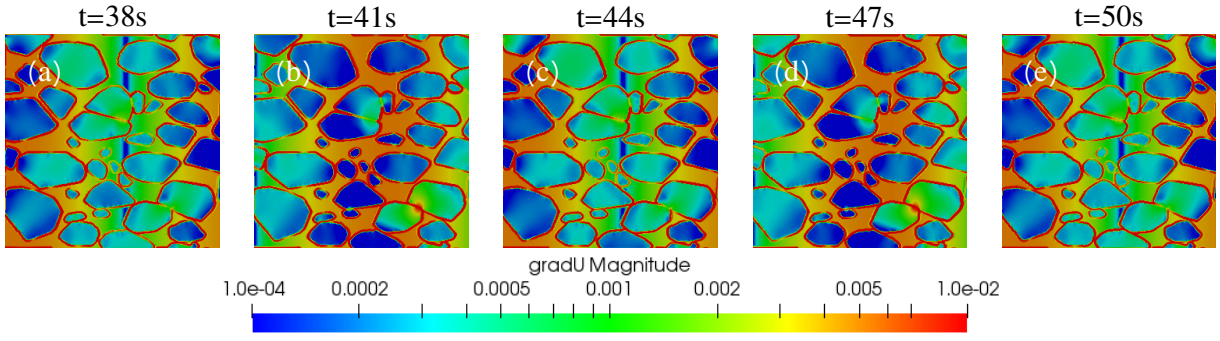

Figure 6.18: Velocity gradient magnitude [s^{-1}] for an imposed wave forcing exemplified for $T = 12$s and kinematic grease ice viscosity $\nu_k \approx 0.04\text{m}^2\text{s}^{-1}$, illustrating **(a-e)** one wave length between $t = 38$s and $t = 50$s.

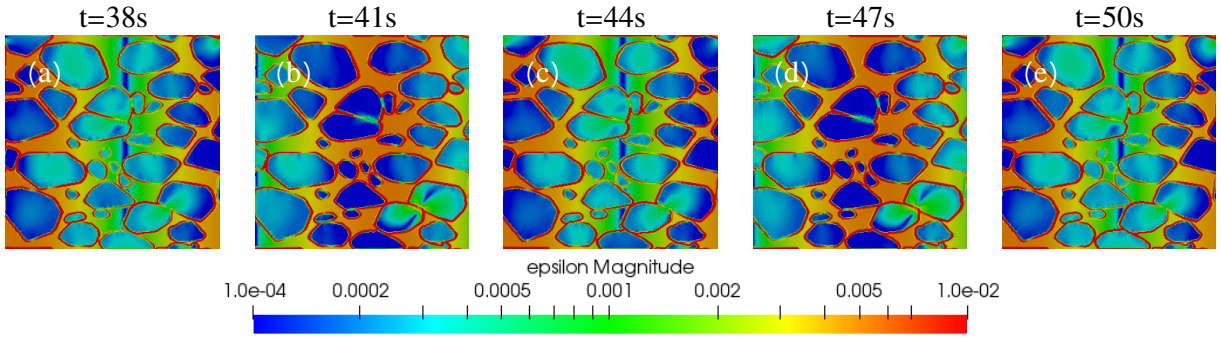

Figure 6.19: Strain rate magnitude [s^{-1}] for an imposed wave forcing exemplified for $T = 12$s and kinematic grease ice viscosity $\nu_k \approx 0.04 m^2 s^{-1}$, illustrating **(a-e)** one wave length between $t = 38$s and $t = 50$s.

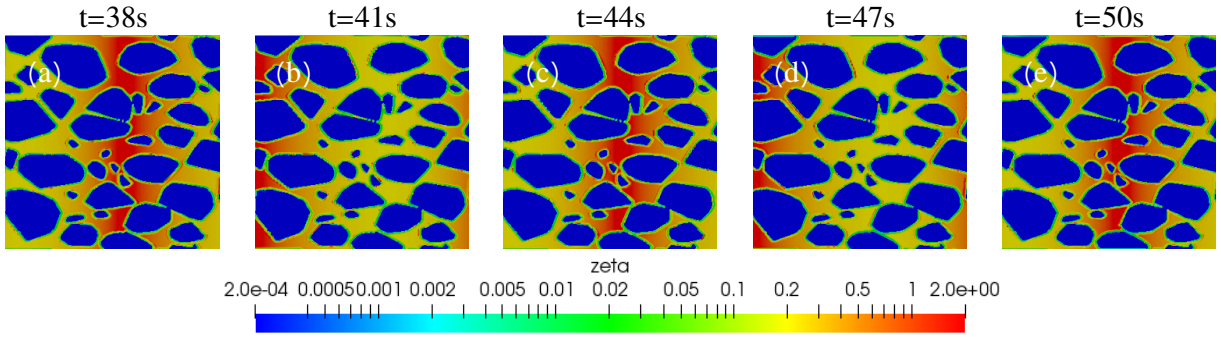

Figure 6.20: Bulk viscosity [kgs^{-1}] for an imposed wave forcing exemplified for $T = 12$s and kinematic grease ice viscosity $\nu_k \approx 0.04 m^2 s^{-1}$, illustrating **(a-e)** one wave length between $t = 38$s and $t = 50$s.

The grease ice bulk viscosity, ζ, is a nonlinear function of the strain rate. The viscosity distribution, shown in Fig. 6.20, and the strain rate suffer from a singularity with locally very high viscosity values when strain rates approach zero, despite matching temporally and spatially-averaged grease ice viscosity with values found in literature [134, 205, 206]. Note, however, that the inner domain locally contains bulk viscosity values of $\zeta \approx 100 kgs^{-1}$, which are capped in the legend at $\zeta = 2 kgs^{-1}$, to enhance clarity in the contour plots. As expected for shear thinning behaviour, the bulk viscosity exhibits clear minima where the strain rate has maxima, in particular at the floe-grease ice interfaces.

The grease ice stress distribution, shown in Figs. 6.21(a-e), is through its dependency on the strain rate a function of the velocity gradient. A sharp interface, shown in Figs. 6.21(a,c,e), corresponds to the position in the domain, where the velocity gradient and strain rate magnitude approach zero, leading to locally very high viscosity values. The grease ice stress magnitude distribution, including sharp interface, is studied in detail by plotting the spherical part of the grease ice stress tensor given by its trace, $\text{sph}(\boldsymbol{\sigma}_g) = \frac{1}{3}\text{tr}(\boldsymbol{\sigma}_g)$, in kgs^{-2} in Figs. 6.21(f-j), over a horizontal line, as illustrated by white arrows in Figs. 6.21(a-e).

The spherical part of the grease ice stress tensor refers to stress linked to volume change (tension or compression). The graphs are directly placed under the distributions and equal in size, allowing direct comparison between the grease ice stress magnitude distributions and the evolution of $\text{sph}(\boldsymbol{\sigma}_g)$ over the horizontal line. Note that the white arrows also cross ice floes, resulting in $\text{sph}(\boldsymbol{\sigma}_g)$ values equal to zero, shown by discontinuities in the stress curves in Figs. 6.21(f-j).

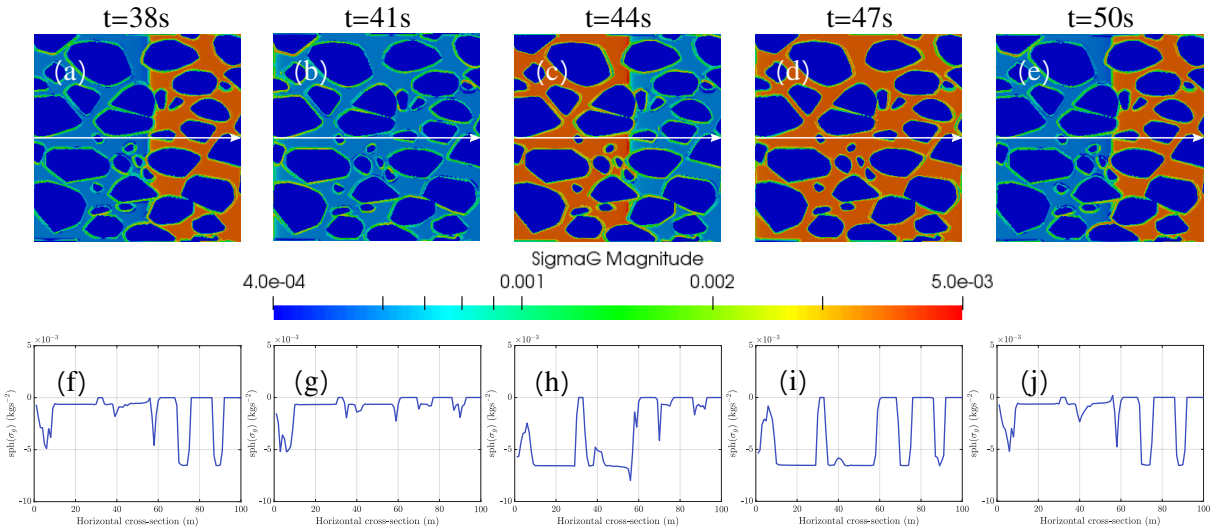

Figure 6.21: Grease ice stress magnitude [kgs^{-2}] for an imposed wave forcing exemplified for $T = 12$s and kinematic grease ice viscosity $\nu_k \approx 0.04\text{m}^2\text{s}^{-1}$, illustrating **(a-e)** one wave length between $t = 38$s and $t = 50$s and **(f-j)** the spherical part of the grease ice stress tensor, sph($\boldsymbol{\sigma}_g$) [kgs^{-2}], plotted over a horizontal line, represented by white arrows for all five time steps.

As expected for fluid-like behaviour, defined by the VP rheology in Eq. (3.7), sph($\boldsymbol{\sigma}_g$) ≤ 0 is found, indicating resistance capacity only in compression and shear. The diverging velocity distribution in the wave trough at $t = 41$s (Fig. 6.9(b)) therefore leads to very small spherical stress values whereas the converging velocity distribution at the crest at $t = 47$s (Fig. 6.9(d)) results in large spherical stress values indicating compression. At the interface, high strain rate values dominate the stress response, resulting in intermediate grease ice stress magnitude values, indicated in green.

The effect of grease ice viscosity on strain rate distributions is investigated, by creating box plots, showing the differences in mechanical response over all five wave periods, averaged over a time period of one wave length, as depicted in Fig. 6.22(a). These box plots specifically provide information regarding interface effects between ice floes and grease ice. Each box plot, shown in Fig. 6.22(a), represents strain rate magnitude values of all grease ice FVM cells in the inner domain with $\nu_k \approx 0.04\text{m}^2\text{s}^{-1}$ for the five wave forcings within the range of $T = 12 - 20$s. All wave periods show sample skewness, with mean values, indicated by a black circle, ranging between $\dot{\epsilon}_{mag} = 0.0105 - 0.0212\text{s}^{-1}$. The median is indicated by a red horizontal line, ranging between $\dot{\epsilon}_{mag} = 0.0044\text{s}^{-1}$ and $\dot{\epsilon}_{mag} = 0.0074\text{s}^{-1}$. The maximum whisker lengths of $\dot{\epsilon}_{mag} = 0.0098\text{s}^{-1}$, $\dot{\epsilon}_{mag} = 0.0196\text{s}^{-1}$, $\dot{\epsilon}_{mag} = 0.0332\text{s}^{-1}$, $\dot{\epsilon}_{mag} = 0.0460\text{s}^{-1}$, $\dot{\epsilon}_{mag} = 0.0555\text{s}^{-1}$ for wave forcing with $T = 12$s, $T = 14$s, $T = 16$s, $T = 18$s and $T = 20$s, respectively, represent the upper adjacent that serves as the threshold between the 75$^{\text{th}}$ percentile and the outliers. Each outlier illustrates a FVM cell in the inner domain with an extreme strain rate value, which is located at the ice floe-grease ice interface. The number of extreme strain rate values indicate the number of interface FVM cells and how pronounced the form drag on the ice floe-grease ice interface is. Fig. 6.22(b) shows the number of outliers accumulated over one wave length, which are cells of extreme strain rate magnitude values. Fig. 6.22(c) shows the temporally and domain-averaged strain rate outliers found at the interface for all five wave forcing with $\nu_k \approx 0.01\text{m}^2\text{s}^{-1}$, $\nu_k \approx 0.04\text{m}^2\text{s}^{-1}$, and $\nu_k \approx 0.16\text{m}^2\text{s}^{-1}$. The number of interface FVM cells gives an indication for strain rate localisation due to form drag, and shows a similar trend as previously found for the ice floe collision pattern. The smaller wave periods, with $T < 16$s, show a higher number of interface FVM cells, whereas the number of interface FVM cells is smaller for the larger wave periods, with $T \geq 16$s. The mean strain rate at the interface, however, increases

for increasing wave period. From this inverse relationship it can be concluded that larger wave periods lead to stronger strain rate localisation due to form drag in terms affected interface area and magnitude.

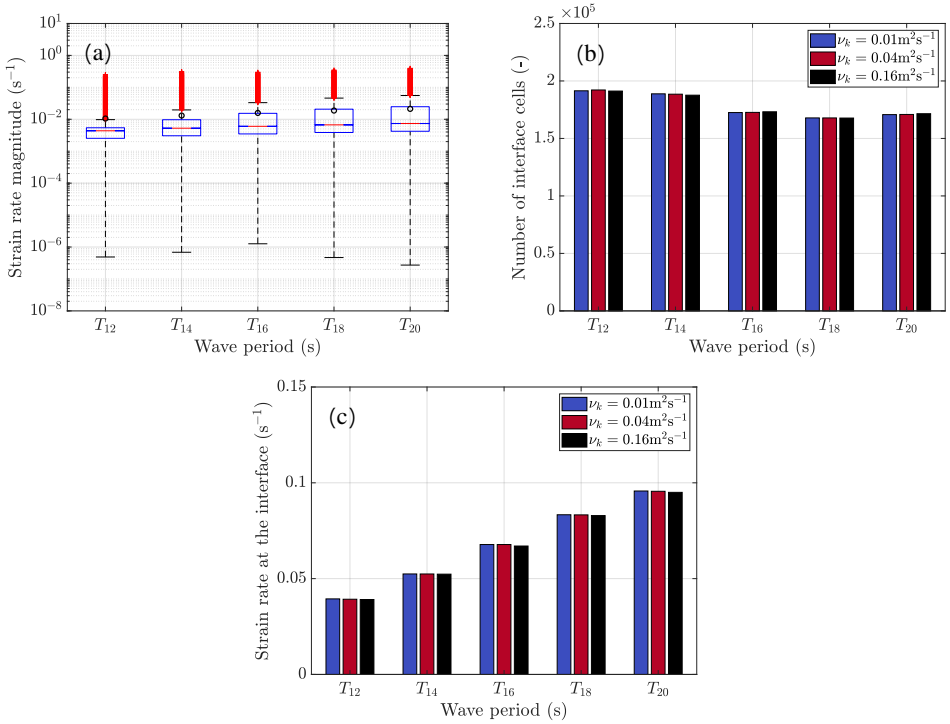

Figure 6.22: Five waves with a wave period $T = 12 - 20$s, showing **(a)** box plots with strain rate magnitude values [s^{-1}] of all grease ice cells in the inner domain with $\nu_k \approx 0.04\text{m}^2\text{s}^{-1}$, **(b)** number of interface cells [−] for kinematic grease ice viscosity ranging from $\nu_k \approx 0.01 - 0.16\text{m}^2\text{s}^{-1}$ and **(c)** mean strain rate at the interface [s^{-1}] for kinematic grease ice viscosity ranging from $\nu_k \approx 0.01 - 0.16\text{m}^2\text{s}^{-1}$.

As for the ice floe collision stress previously discussed in Sec. 6.2.1, variations in viscosity do not significantly affect the number of outliers and mean strain rate values at the interface. This is mainly due to the relatively small range of viscosity values away from the singularity values, and because the small-scale model considers an imposed wave. A freely propagating wave would dissipate energy, affecting both the strain rate and the stress distributions, which would decrease further due to the presence of sea ice. However, this effect can be assumed small in a small sea ice domain.

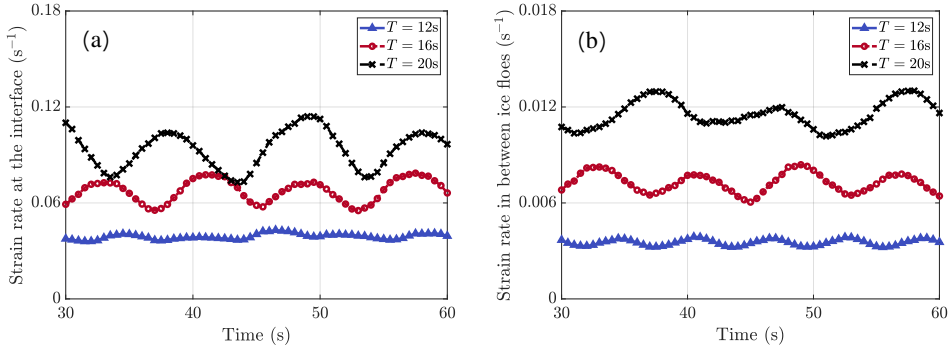

Figure 6.23: Effect of varying wave forcing on the strain rate response of grease ice, $\dot{\epsilon}_{mag}$, over time, showing **(a)** at the ice floe-grease ice interface and **(b)** in between ice floes (away from the interface).

Lastly, Fig. 6.23 shows the spatially averaged strain rate values at the interface (values > maximum whisker length, Fig. 6.23(a)) and in between ice floes, away from the interface (values < maximum whisker length, Fig. 6.23(b)), for wave forcing with $T = 12$s, $T = 16$s and $T = 20$s. Both, the strain rate magnitude values at the ice floe interface and away from the interface show a direct correlation with increasing wave period. Moreover, the values at the interface are approximately one order of magnitude greater than the grease ice strain rate magnitudes in between ice floes.

Chapter 7

Numerical study of in situ ice floe motions

In this chapter the ability of the small-scale sea ice dynamics to reproduce actual ice floe motion characteristics is investigated. For this purpose, sea ice observation data from the 2017 winter cruise are used. Data was obtained approximately 100km from the edge of the Antarctic marginal ice zone (MIZ) at ±62-64° south and ±30° east. Images and wave buoy data were collected to monitor the ocean surface during an intense storm on the 4^{th} of July 2017. This data can assist in gaining a better understanding of the sea ice cover, such as the sea ice concentration, pancake ice shape, and floe size distribution [3].

In Sec. 7.1 the procedure of image processing in Matlab is explained, from which ice floe displacement data in the horizontal plane is obtained. Subsequently, a sensitivity analysis is conducted in Sec. 7.2, discussing the sensitivity of the unknown parameter values, which require calibration. The final parameter calibration and model verification results are discussed in Sec. 7.3.

7.1 Image processing

A system of two GigE monochrome industrial CMOS cameras with a 2/3 inch sensor, installed on the monkey bridge of the S.A. Agulhas II, at a height of approximately 34m from the ocean surface, recorded in situ image and video material [3]. Two waves-in-ice observation systems (WIIOS) [98], deployed in close proximity to one another, acquired wave data for 12 minutes and generated a value averaged over that time. The main parameters of the wave data from the WIIOS include time, latitude, longitude, wave height, wave period, and ship velocity components in the x- and y-direction.

A large number of consecutive in situ images with corresponding WIIOS data are used for the calibration of the small-scale model, to map the motion of first-year sea ice in the horizontal plane. Three consecutive samples of in situ images of the sea ice cover, taken during the 2017 winter cruise, are shown in Fig. 7.1.

Figure 7.1: Three consecutive sample images of the sea ice cover taken during the 2017 winter cruise.

Before images can be used for calibration purposes, they were processed by rotating each image, optimising the colour contrast, and eliminating the ship, using a mask in the bottom-right corner. Approximately 5% of the processed images were removed after quality control, due to poor reconstruction of the floes [3]. The resulting field of view, found by Alberello et al. [3], is $28 \times 28\text{m}^2$. Figs. 7.2(a) and (b) show an example of a successfully processed image. The red box, shown in Fig. 7.2(b) and (c), represents the domain that is implemented in OpenFOAM, equal to $21 \times 21\text{m}^2$.

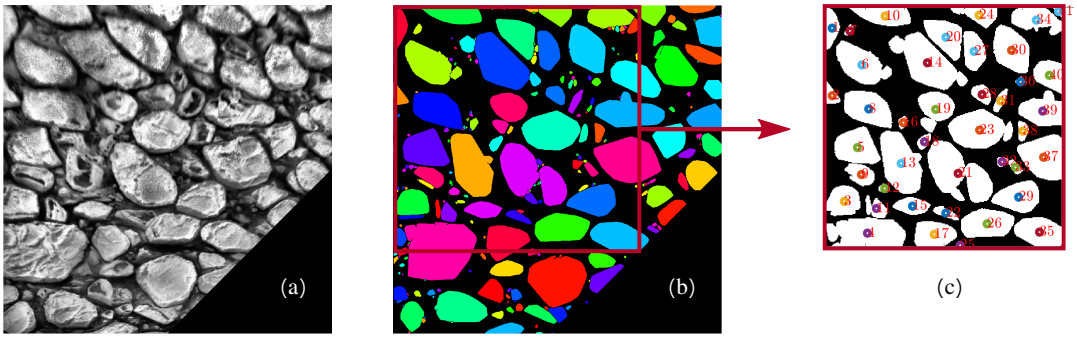

Figure 7.2: In situ images as processed in Matlab [3], showing **(a)** and **(b)** the rotation, colour optimisation and the ship elimination using a mask and **(c)** the box in the top-left corner with the floe layout implemented as realistic sea ice layout in OpenFOAM.

According to data obtained from the WIIOS, images were taken in wave conditions with a dominant wave period of $T = 15$s and a significant wave height of $H_s = 5.5$m. The photo acquisition is 2Hz, which is equal to a time step size of $\Delta t = 0.5$s between photos. To ensure no relative motion between ice floes and the ship, only photos that were taken when the ship was stationary were considered. All floes in the domain are labeled with numbers. An example is shown in Fig. 7.3 for three consecutive time steps.

The centre of gravity (CoG) of each ice floe is known, assuming a constant density distribution over the ice floes. The CoG is illustrated by circles in Fig. 7.3, from which the x- and y-coordinates can be obtained. As the coordinates of all ice floes in each time step are known, it allows for tracking the motion of ice floes in the horizontal plane. The layout from which tracking of ice floes starts, is referred to as the initial layout.

Note that the numbering of ice floes in Fig. 7.3 is different for each time step. This is because floes enter and/or leave the domain, or due to sub-optimal ice floe reconstruction. Accordingly, each ice floe in the initial layout, shown in Fig. 7.3(a), is additionally labelled with a letter, which allows referring to the same ice floe over time. The letter labelling is illustrated in Fig. 7.4.

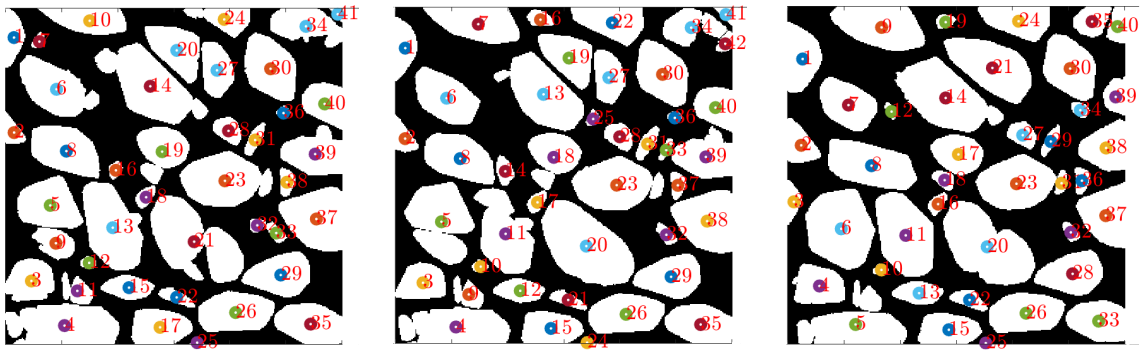

(a) (b) (c)

Figure 7.3: Three consecutive layouts, in which each ice floe is labeled with a number. The centre of gravity of each ice floe is represented by a circle, showing **(a)** the initial layout, from which tracking of ice floes starts, **(b)** and **(c)** consecutive layouts.

The imaging analysis allows for tracking the majority of the ice floes. To ensure the reliability of the imaging analysis, the area and the equivalent diameter of the ice floes are calculated per time step. The area and equivalent diameter of several ice floes in the domain are significantly different between time steps, due to a poor reconstruction of the ice floes during processing in Matlab. Therefore, only floes with a dissimilarity in area and equivalent diameter, less than 5% between all steps of motion, are considered in this analysis.

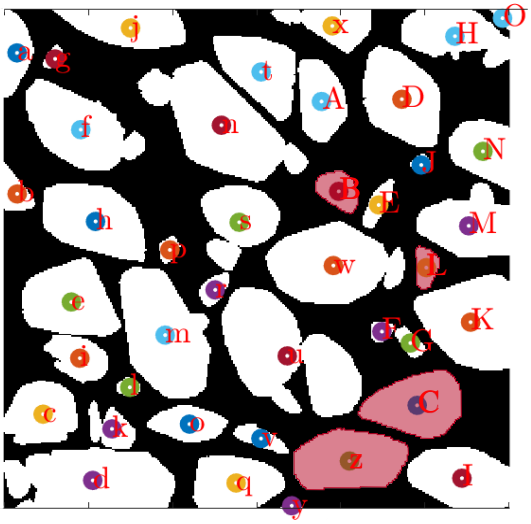

Figure 7.4: Initial sea ice layout labeled with letters. Ice floes B, C, L and z are highlighted in red.

As previously mentioned, two external forcings drive the sea ice motion in the small-scale model, current-dependent wave forcing and wave-dependent wind forcing. In terms of the wave forcing, both the wave period and wave height, are acquired by the WIIOS [3, 98], during the 2017 winter cruise. These are, together with the wave direction, θ_{wa}, the only required wave parameters to describe a simplified imposed sinusoidal harmonic propagating wave as implemented in the small-scale model.

In terms of the wind forcing, the wind magnitude at 10m above sea level and wind direction, are measured by Vichi [199] during the 2017 winter cruise. Both θ_w and θ_a are set to zero, as it can be assumed that on a small-scale the ocean current and air drag point in the same direction as the ocean current and wind velocity [182]. This means that, besides the already known parameters shown in Tab. 7.1, only four parameters in

the small-scale model need to be calibrated based on the image-derived motion data: the constant grease ice strength parameter, P_g^*, both air and water drag coefficient values, C_a and C_w, respectively, and the wave direction, θ_{wa}.

Table 7.1: Acquired wind and wave parameters from the 2017 winter cruise, used for the calibration of small-scale model results.

Parameter	**Definition**	**Value**	**Unit**
a	wave amplitude	2.769	m
U_{10}	true wind speed at 10m above sea level	18.9	ms^{-1}
T	wave period	15.06	s
θ_{wi}	true wind direction	321.7	$^\circ$

Ice floes B, C, L and z in the sea ice domain, highlighted in red in Fig. 7.4, show the highest number of uninterrupted time steps with a dissimilarity in area and equivalent diameter less than 5%. Accordingly, these four ice floes are used for calibration. The small-scale model is considered successfully calibrated when floe displacements obtained from the imaging analysis and simulation results from OpenFOAM correspond to each other. The difference between floe displacement is expressed in terms of the root mean square error ($RMSE$). Values close to zero imply a successful calibration.

Figs. 7.5 and 7.6 show blue triangular data points, which represent displacements of ice floes B, C, L and z obtained from the imaging analysis. Ice floe displacements in the x- and y-direction are calculated using $\Delta i = i(t) - i(t - \Delta t)$, with i representing x and y, respectively. While the photo sampling rate is 2Hz, which is equivalent to Δt = 0.5s, the actual time step between two consecutive data points can be larger than 0.5s due to the previously mentioned quality control of images during post-processing and due to the reliability requirement used in the imaging analysis.

Before proceeding with the calibration of the model, however, the sensitivity of the involved parameters is studied focusing on floe C. The four involved parameters in the small-scale model, which require calibration are the constant grease ice strength parameter, P_g^*, both air and water drag coefficient values, C_a and C_w, respectively, and the wave direction angle, θ_{wa}.

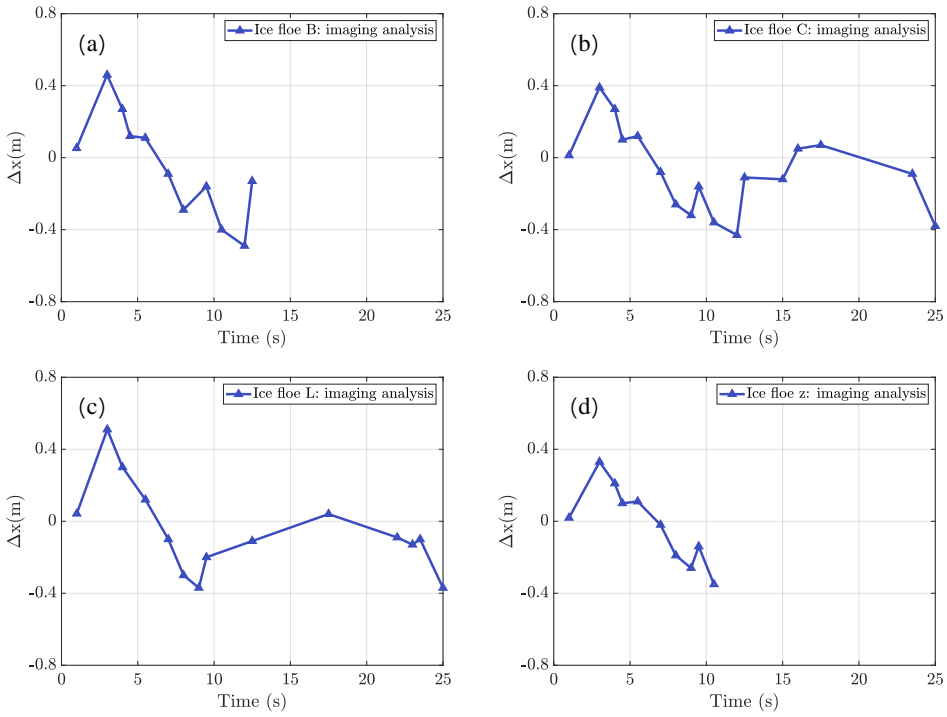

Figure 7.5: Displacements in the x-direction, Δx [m], showing for ice floe **(a)** B, **(b)** C, **(c)** L and **(d)** z.

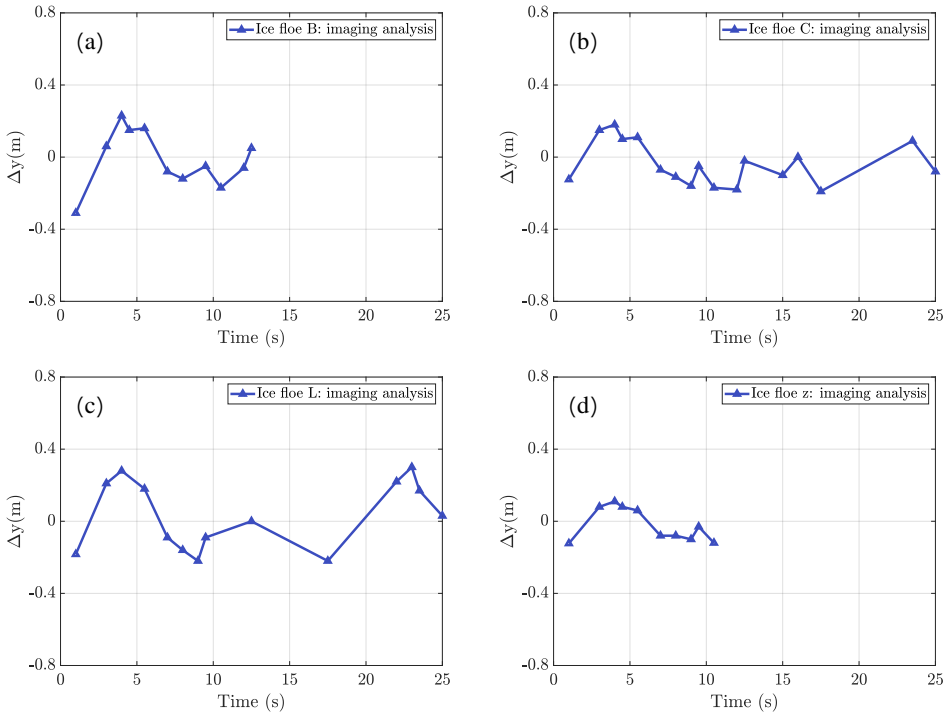

Figure 7.6: Displacements in the y-direction, Δy [m], showing for ice floe **(a)** B, **(b)** C, **(c)** L and **(d)** z.

7.2 Parameter sensitivity analysis - ice floe C

A sensitivity study is conducted, applied to ice floe C for all four parameters to be calibrated. To perform the sensitivity analysis, each of the parameters is varied around a set of base parameters, where the base parameters are: $C_{w_f} = 0.02$, $C_{w_g} = 0.008$, $C_{a_\lambda} = 1$, $P_g^* = 0.02\text{Nm}^{-2}$, and $\theta_{wa} = 45°$. Parameters influence each other, which means that matching ice floe displacement results depend on a combination of the parameter values. Therefore, the sections below only give an indication of how sensitive the displacement of ice floe C is towards a particular parameter. The most suitable combinations of parameter values, fitting motion of all four ice floes is determined in Sec. 7.3.

All simulations conducted for the sensitivity analysis of the small-scale model have a simulation time, $t = 60$s. Note that some simulations finish earlier because tracking of ice floe C stopped after it has moved out of the domain. Simulations have a time step size of $\Delta t = 0.01$s, providing computationally stable simulations. A uniform write interval is set to 0.5s. The domain is discretised with a constant cell size of $0.20 \times 0.20\text{m}^2$. The boundaries of all fields in the domain are set to zero-gradient boundary conditions (BCs).

7.2.1 Grease ice strength parameter

The sensitivity of the constant grease ice strength parameter, P_g^*, on ice floe displacement is studied by ranging P_g^* values between 0.02Nm^{-2} and 2Nm^{-2}.

In Fig. 7.7 displacements are shown in both the x- and y-direction for different values of P_g^*. In all three simulations a part of ice floe C moved out of the domain before $t = 60$s was reached. A significant increase in the constant grease ice strength parameter of two orders of magnitude, does not affect the ice floe displacement in the x- and y-directions. Therefore, $P_g^* = 0.02\text{Nm}^{-2}$, closest to realistic grease ice viscosity values used in literature [134, 142, 205, 206], is used for the calibration in Sec. 7.3.

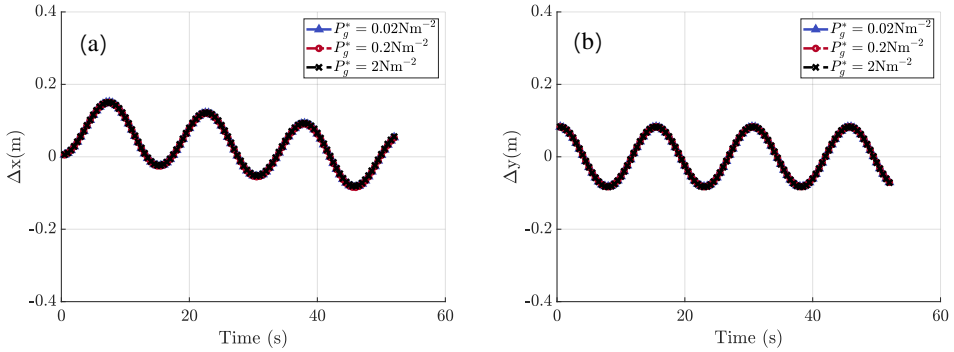

Figure 7.7: Displacement curves [m], obtained for ice floe C, are shown for three different values of P_g^*, illustrating motion in the **(a)** x-direction and **(b)** y-direction.

7.2.2 Air drag coefficient

The sensitivity of the air drag coefficient, C_a, on ice floe displacement is studied by ranging three values of the air drag multiplication factor, C_{a_λ}, between 0.5 and 1.5. As mentioned previously in Sec. 3.4.1, a

multiplication factor multiplies the wave dependent air drag coefficient in the entire domain with an arbitrary factor. A value equal to one corresponds to air drag coefficient values found in literature [8, 214].

In Fig. 7.8 ice floe displacements are shown in both the x- and y-direction for different C_{a_λ} values, $C_{a_\lambda} = 0.5, 1,$ and 1.5, each corresponding to a domain-averaged air drag coefficient equal to $\overline{C_a} = 0.0013, 0.0026$ and 0.0038.

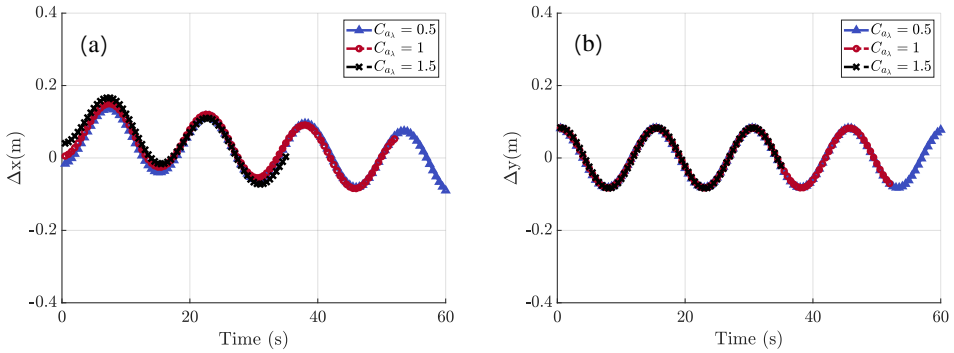

Figure 7.8: Displacement curves [m], obtained for ice floe C, are shown for three different values of C_{a_λ}, in the **(a)** x-direction and **(b)** y-direction.

All simulations start with a non-zero initial sea ice velocity, corresponding to a velocity that has reached equilibrium conditions after only applying a wind forcing first. This is done to ensure that the wind forcing is fully developed in the short time windows. The initial sea ice velocity increases for increasing air drag coefficient, resulting in higher initial ice floe displacements for larger C_a values.

Additionally, an increasing wave-dependent air drag coefficient results in an increasing wind forcing, which in turn, results in a shift of the displacement curve away from the equilibrium of zero displacements. Note that curves with larger multiplication factors finish earlier because tracking of ice floe C stopped after it has moved out of the domain due to an increased wind forcing. Displacement data points from the imaging analysis, shown in Figs. 7.5 and 7.6 mainly oscillate around zero, implying that a multiplication factor $C_{a_\lambda} = 0.5$ is most suitable for the calibration in Sec. 7.3.

7.2.3 Water drag coefficients

The sensitivity of water drag coefficients on the displacement of ice floe C is studied by ranging values of water drag coefficient values for ice floes, C_{w_f}, from 0.02 - 0.10 considering increments of 0.01, and corresponding water drag coefficient values for grease ice, C_{w_g}, from 0.008 - 0.040. The reason for different coefficient values between ice floes and grease ice is derived from the density difference, resulting in a negligibly small bulk velocity between the two ice constituents. As previously mentioned in Sec. 5.3.2, the water drag coefficient ratio of ice floe to grease ice was obtained as 2.5 : 1.

Displacements of ice floe C are shown in Fig. 7.9 for three different C_{w_f} values with corresponding C_{w_g} values. All curves end before $t = 60$s, as a part of ice floe C has moved out of the domain. Note, however, that the curves of $C_{w_f} = 0.02$, with corresponding $C_{w_g} = 0.008$, end earliest, because the contribution of the wind is more pronounced for smaller water drag coefficient values.

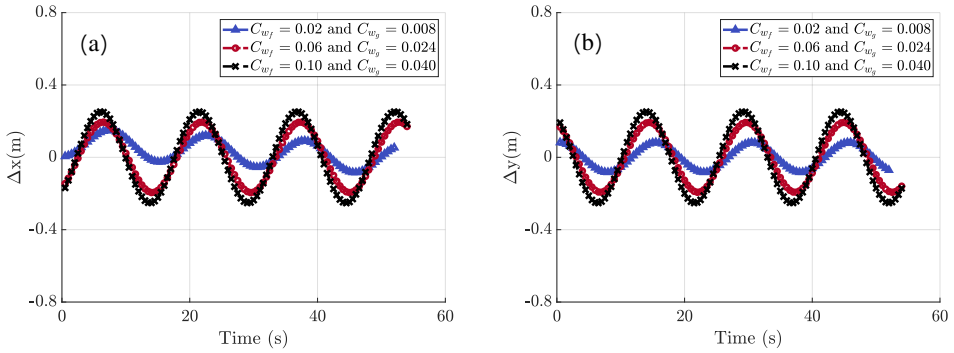

Figure 7.9: Displacement curves [m], obtained for ice floe C, are shown for three different combinations of C_{w_f} and C_{w_g}, in the **(a)** x-direction and **(b)** y-direction.

In Tab. 7.2 all combinations of the water drag coefficient values are shown, complemented with resulting absolute wave amplitude values in both the x- and y-direction. The wave amplitude is shown because a simplified sinusoidal harmonic propagating wave can be described by just the wave amplitude, the already known wave period, $T = 15.06$s and the wave direction angle. The default value of the wave direction angle is set to $\theta_{wa} = 45°$, resulting in wave amplitude values equal in the x- and y-direction.

Table 7.2: All combinations of water drag coefficients, C_{w_f} and C_{w_g}, with corresponding absolute wave amplitude values in the x- and y-direction for ice floe C. a_x and a_y represent the amplitude in the x- and y-direction.

P_g^* (Nm^{-2})	C_{a_λ} (-)	θ_{wa} (°)	C_{w_f} (-)	C_{w_g} (-)	a_x (m)	a_y (m)
0.02	1	45	0.02	0.008	|0.08|	|0.08|
0.02	1	45	0.03	0.012	|0.12|	|0.12|
0.02	1	45	0.04	0.016	|0.15|	|0.15|
0.02	1	45	0.05	0.020	|0.17|	|0.17|
0.02	1	45	0.06	0.024	|0.19|	|0.19|
0.02	1	45	0.07	0.028	|0.21|	|0.21|
0.02	1	45	0.08	0.032	|0.23|	|0.23|
0.02	1	45	0.09	0.036	|0.24|	|0.24|
0.02	1	45	0.10	0.040	|0.25|	|0.25|

7.2.4 Wave direction angle

The sensitivity of the wave direction angle, θ_{wa}, on ice floe displacement is studied by running simulations for θ_{wa} ranging from 25 - 45°, considering increments of 5°. Three different wave direction angles are shown in Fig. 7.10.

Wave direction angles of 0° and 90° correspond to waves propagating only in the x- and y-direction, respectively. Note that the displacement curves finish earlier for smaller wave direction angles, as a part of ice floe C has moved out of the domain. The reason for this is that a smaller wave direction angle results in a larger displacement in the x-direction and a smaller displacement in the y-direction. All wave direction angle variations for ice floe C are shown in Tab. 7.3.

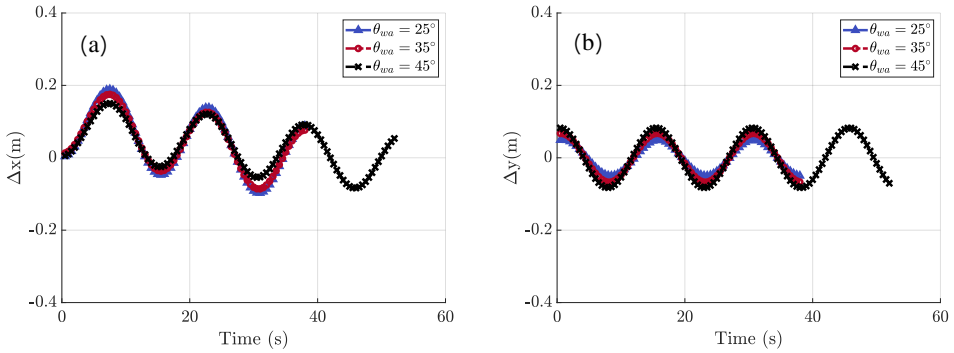

Figure 7.10: Displacement curves [m], obtained for ice floe C, are shown for three different values of θ_{wa}, in the **(a)** x-direction and **(b)** y-direction.

Table 7.3: All combinations of the wave direction angle, θ_{wa}, with corresponding absolute wave amplitude values in the x- and y-direction for ice floe C.

P_g^* (Nm^{-2})	C_{a_λ} (-)	θ_{wa} (°)	C_{w_f} (-)	C_{w_g} (-)	a_x (m)	a_y (m)
0.02	1	25	0.02	0.008	|0.10|	|0.05|
0.02	1	30	0.02	0.008	|0.09|	|0.06|
0.02	1	35	0.02	0.008	|0.08|	|0.07|
0.02	1	40	0.02	0.008	|0.08|	|0.07|
0.02	1	45	0.02	0.008	|0.08|	|0.08|

7.3 Final parameter calibration and model verification

A smooth fit of the motion data obtained from the imaging analyses, with time periods ranging between $10 - 25$s, are compared to modelled results from OpenFOAM, such that a most accurate interval is found within the 60s simulation time window.

The calibration and model verification is expressed in terms of the $RMSE$. In both the x- and y-direction the $RMSE$ is calculated as

$$RMSE = \sqrt{\frac{\sum_{i=1}^{N_i}(l_i - \hat{l}_i)^2}{N_i}}, \tag{7.1}$$

where l_i and $\hat{l}_i$ represent the ice floe displacement values in both the x- and y-direction of a smooth fit of the motion data obtained from the imaging analysis and the simulated fitting curve from OpenFOAM, respectively.

The ice floe motion of four ice floes in the sea ice domain is calibrated, namely for ice floes B, C, L, and z. The small-scale model is considered successfully calibrated when floe displacements obtained from the imaging analysis correspond to simulation results, which is when $RMSE$ values are close to zero. The $RMSE$ is calculated and indicated for the four ice floes in Tabs. 7.4-7.8. The drag coefficients for ice floes, C_{w_f}, range from 0.06 - 0.10, considering increments of 0.01. The corresponding water drag coefficient values for grease ice, C_{w_g}, range from 0.024 - 0.040. The constant grease ice strength parameter and the air drag multiplication factor are set to $P_g^* = 0.02\text{Nm}^{-2}$ and $C_{a_\lambda} = 0.5$ in all the calibration results.

Table 7.4: Calibration results of ice floes B, C, L and z for $C_{w_f} = 0.06$ and $C_{w_g} = 0.024$.

Ice floe	θ_{wa} [°]	$C_{w,i}$ [-]	$C_{w,g}$ [-]	a_x [m]	a_y [m]	$RMSE_x$ [m]	$RMSE_y$ [m]	$\sum RMSE_x$ [m]	$\sum RMSE_y$ [m]
B	25	0.06	0.024	|0.25|	|0.12|	0.0662	0.0986	0.1759	0.4515
C	25	0.06	0.024	|0.25|	|0.12|	0.0416	0.1096		
L	25	0.06	0.024	|0.25|	|0.12|	0.0353	0.1752		
z	25	0.06	0.024	|0.25|	|0.11|	0.0328	0.0681		
B	30	0.06	0.024	|0.24|	|0.14|	0.0737	0.1002	0.1924	0.4801
C	30	0.06	0.024	|0.24|	|0.14|	0.0454	0.1186		
L	30	0.06	0.024	|0.24|	|0.14|	0.0418	0.1823		
z	30	0.06	0.024	|0.24|	|0.14|	0.0315	0.0790		
B	35	0.06	0.024	|0.22|	|0.16|	0.0830	0.1041	0.2155	0.5148
C	35	0.06	0.024	|0.22|	|0.16|	0.0514	0.1285		
L	35	0.06	0.024	|0.23|	|0.16|	0.0485	0.1908		
z	35	0.06	0.024	|0.22|	|0.16|	0.0326	0.0914		
B	40	0.06	0.024	|0.21|	|0.18|	0.0944	0.1093	0.2471	0.5512
C	40	0.06	0.024	|0.21|	|0.18|	0.0579	0.1385		
L	40	0.06	0.024	|0.21|	|0.18|	0.0577	0.1996		
z	40	0.06	0.024	|0.21|	|0.18|	0.0371	0.1038		
B	45	0.06	0.024	|0.19|	|0.19|	0.1054	0.1152	0.2859	0.5879
C	45	0.06	0.024	|0.19|	|0.19|	0.0679	0.1487		
L	45	0.06	0.024	|0.19|	|0.19|	0.0676	0.2070		
z	45	0.06	0.024	|0.19|	|0.19|	0.0450	0.1170		

Table 7.5: Calibration results of ice floes B, C, L and z for $C_{w_f} = 0.07$ and $C_{w_g} = 0.028$.

Ice floe	θ_{wa} [°]	$C_{w,i}$ [-]	$C_{w,g}$ [-]	a_x [m]	a_y [m]	$RMSE_x$ [m]	$RMSE_y$ [m]	$\sum RMSE_x$ [m]	$\sum RMSE_y$ [m]
B	25	0.07	0.028	|0.27|	|0.13|	0.0463	0.0986	0.1318	0.4686
C	25	0.07	0.028	|0.27|	|0.13|	0.0265	0.1156		
L	25	0.07	0.028	|0.27|	|0.13|	0.0181	0.1793		
z	25	0.07	0.028	|0.27|	|0.13|	0.0409	0.0751		
B	30	0.07	0.028	|0.26|	|0.15|	0.0551	0.1021	0.1454	0.5062
C	30	0.07	0.028	|0.26|	|0.15|	0.0304	0.1267		
L	30	0.07	0.028	|0.26|	|0.15|	0.0243	0.1880		
z	30	0.07	0.028	|0.26|	|0.15|	0.0356	0.0894		
B	35	0.07	0.028	|0.25|	|0.17|	0.0654	0.1078	0.1652	0.5461
C	35	0.07	0.028	|0.24|	|0.17|	0.0361	0.1377		
L	35	0.07	0.028	|0.25|	|0.17|	0.0317	0.1973		
z	35	0.07	0.028	|0.25|	|0.17|	0.0320	0.1033		
B	40	0.07	0.028	|0.23|	|0.19|	0.0767	0.1150	0.2471	0.5512
C	40	0.07	0.028	|0.23|	|0.19|	0.0439	0.1493		
L	40	0.07	0.028	|0.23|	|0.19|	0.0411	0.2068		
z	40	0.07	0.028	|0.23|	|0.19|	0.0318	0.1173		
B	45	0.07	0.028	|0.21|	|0.21|	0.0903	0.1232	0.2327	0.6325
C	45	0.07	0.028	|0.21|	|0.21|	0.0536	0.1612		
L	45	0.07	0.028	|0.21|	|0.21|	0.0524	0.2171		
z	45	0.07	0.028	|0.21|	|0.21|	0.0364	0.1310		

Table 7.6: Calibration results of ice floes B, C, L and z for $C_{w_f} = 0.08$ and $C_{w_g} = 0.032$.

Ice floe	θ_{wa} [°]	$C_{w,i}$ [-]	$C_{w,g}$ [-]	a_x [m]	a_y [m]	$RMSE_x$ [m]	$RMSE_y$ [m]	$\sum RMSE_x$ [m]	$\sum RMSE_y$ [m]
B	25	0.08	0.032	|0.29|	|0.14|	0.0287	0.0995	0.1099	0.4825
C	25	0.08	0.032	|0.29|	|0.14|	0.0160	0.1198		
L	25	0.08	0.032	|0.29|	|0.14|	0.0124	0.1825		
z	25	0.08	0.032	|0.29|	|0.13|	0.0528	0.0807		
B	30	0.08	0.032	|0.28|	|0.16|	0.0385	0.1046	0.1154	0.5272
C	30	0.08	0.032	|0.28|	|0.16|	0.0197	0.1335		
L	30	0.08	0.032	|0.28|	|0.16|	0.0112	0.1932		
z	30	0.08	0.032	|0.28|	|0.16|	0.0460	0.0959		
B	35	0.08	0.032	|0.26|	|0.19|	0.0505	0.1123	0.1311	0.5740
C	35	0.08	0.032	|0.26|	|0.18|	0.0246	0.1462		
L	35	0.08	0.032	|0.27|	|0.18|	0.0171	0.2030		
z	35	0.08	0.032	|0.26|	|0.18|	0.0389	0.1125		
B	40	0.08	0.032	|0.25|	|0.21|	0.0630	0.1213	0.1574	0.6243
C	40	0.08	0.032	|0.25|	|0.21|	0.0323	0.1597		
L	40	0.08	0.032	|0.25|	|0.21|	0.0278	0.2150		
z	40	0.08	0.032	|0.25|	|0.21|	0.0343	0.1283		
B	45	0.08	0.032	|0.23|	|0.23|	0.0758	0.1308	0.1938	0.6723
C	45	0.08	0.032	|0.23|	|0.23|	0.0429	0.1725		
L	45	0.08	0.032	|0.23|	|0.23|	0.0412	0.2251		
z	45	0.08	0.032	|0.23|	|0.23|	0.0339	0.1439		

Table 7.7: Calibration results of ice floes B, C, L and z for $C_{w_f} = 0.09$ and $C_{w_g} = 0.036$.

Ice floe	θ_{wa} [°]	$C_{w,i}$ [-]	$C_{w,g}$ [-]	a_x [m]	a_y [m]	$RMSE_x$ [m]	$RMSE_y$ [m]	$\sum RMSE_x$ [m]	$\sum RMSE_y$ [m]
B	25	0.09	0.036	|0.31|	|0.14|	0.0144	0.1007	0.1210	0.4994
C	25	0.09	0.036	|0.30|	|0.14|	0.0187	0.1250		
L	25	0.09	0.036	|0.31|	|0.14|	0.0224	0.1859		
z	25	0.09	0.036	|0.31|	|0.14|	0.0655	0.0878		
B	30	0.09	0.036	|0.30|	|0.17|	0.0248	0.1076	0.1153	0.5488
C	30	0.09	0.036	|0.29|	|0.17|	0.0191	0.1398		
L	30	0.09	0.036	|0.30|	|0.17|	0.0142	0.1974		
z	30	0.09	0.036	|0.29|	|0.17|	0.0572	0.1040		
B	35	0.09	0.036	|0.28|	|0.20|	0.0377	0.1170	0.1168	0.6016
C	35	0.09	0.036	|0.28|	|0.20|	0.0195	0.1539		
L	35	0.09	0.036	|0.28|	|0.20|	0.0107	0.2090		
z	35	0.09	0.036	|0.28|	|0.20|	0.0489	0.1217		
B	40	0.09	0.036	|0.26|	|0.22|	0.0504	0.1271	0.1345	0.6544
C	40	0.09	0.036	|0.26|	|0.22|	0.0248	0.1685		
L	40	0.09	0.036	|0.26|	|0.22|	0.0183	0.2207		
z	40	0.09	0.036	|0.26|	|0.22|	0.0410	0.1381		
B	45	0.09	0.036	|0.24|	|0.24|	0.0654	0.1385	0.1693	0.7086
C	45	0.09	0.036	|0.24|	|0.24|	0.0351	0.1822		
L	45	0.09	0.036	|0.24|	|0.24|	0.0323	0.2331		
z	45	0.09	0.036	|0.24|	|0.24|	0.0365	0.1548		

Table 7.8: Calibration results of ice floes B, C, L and z for $C_{w_f} = 0.10$ and $C_{w_g} = 0.040$.

Ice floe	θ_{wa} [°]	$C_{w,i}$ [-]	$C_{w,g}$ [-]	a_x [m]	a_y [m]	$RMSE_x$ [m]	$RMSE_y$ [m]	$\sum RMSE_x$ [m]	$\sum RMSE_y$ [m]
B	25	0.10	0.040	|0.32|	|0.15|	0.0060	0.1026	NaN	NaN
C	25	0.10	0.040	|0.32|	|0.15|	NaN	NaN		
L	25	0.10	0.040	|0.33|	|0.15|	0.0345	0.1891		
z	25	0.10	0.040	|0.32|	|0.15|	0.0782	0.0931		
B	30	0.10	0.040	|0.31|	|0.18|	0.0129	0.1108	0.1278	0.5674
C	30	0.10	0.040	|0.31|	|0.18|	0.0204	0.1442		
L	30	0.10	0.040	|0.31|	|0.18|	0.0254	0.2014		
z	30	0.10	0.040	|0.31|	|0.18|	0.0691	0.1110		
B	35	0.10	0.040	|0.29|	|0.21|	0.0253	0.1211	0.1229	0.6249
C	35	0.10	0.040	|0.29|	|0.21|	0.0205	0.1609		
L	35	0.10	0.040	|0.30|	|0.21|	0.0179	0.2137		
z	35	0.10	0.040	|0.29|	|0.21|	0.0592	0.1292		
B	40	0.10	0.040	|0.27|	|0.23|	0.0405	0.1336	0.1276	0.6829
C	40	0.10	0.040	|0.27|	|0.23|	0.0220	0.1758		
L	40	0.10	0.040	|0.28|	|0.23|	0.0158	0.2265		
z	40	0.10	0.040	|0.27|	|0.23|	0.0493	0.1470		
B	45	0.06	0.040	|0.25|	|0.25|	0.0563	0.1455	0.1544	0.7403
C	45	0.06	0.040	|0.25|	|0.25|	0.0305	0.1913		
L	45	0.06	0.040	|0.26|	|0.26|	0.0255	0.2394		
z	45	0.06	0.040	|0.25|	|0.25|	0.0421	0.1641		

Note that Tab. 7.8 shows NaN, which means 'not a number', for a wave direction angle of 25°. This is because ice floe C moved out of the domain. Accordingly, $RMSE$ values could not be calculated. The best fit in the calibration results, shown in the Tabs. 7.4-7.8, can be visualised by plotting the ice floe displacement curves in the x- and y-direction.

As previously mentioned in Sec. 7.1, displacements obtained from the imaging analysis are indicated by blue triangular data points. Albeit the photo sampling rate is 2Hz, which is equal to $\Delta t = 0.5$s, the actual time step between two consecutive data points can be larger than 0.5s due to the previously mentioned quality control of images during post-processing and the reliability requirement used in the imaging analysis. The blue curve represents a smooth fit of the motion data obtained from the imaging analysis used as calibration target. The simulated fitting curve from OpenFOAM, indicated in red, has the same time increment, which allows for comparing the idealised fitting curve to the simulated fitting curve.

Displacement curves in the x-direction are illustrated in Fig. 7.11, showing $RMSE_x$ values close to zero. One set of parameters is obtained, which is applicable to all four ice floes in the entire domain. The best fit is obtained with $\theta_{wa} = 25°$, $C_{w,f} = 0.08$ and $C_{w,g} = 0.032$, resulting in $\sum RMSE_x = 0.1099$m. This set of parameters generates successfully calibrated ice floe displacements in the x-direction. Ice floe z, however, shows an $RMSE_x$ value, which is significantly higher than the remaining ice floes. This is due to the wave period of ice floe z, obtained from the imaging analysis, which is slightly smaller than the wave amplitude value as given by the WIIOS. These calibrated parameters of all four ice floes together, represent the parameter values of the entire domain.

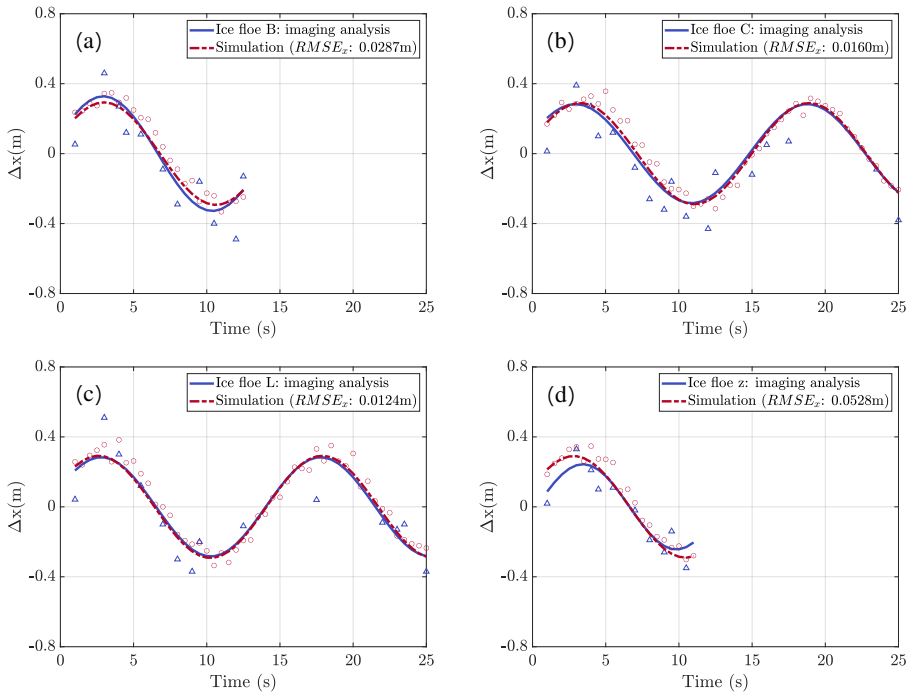

Figure 7.11: Calibration results with displacement curves in the x-direction [m], showing for **(a)** ice floe B with $RMSE_x = 0.0287$m, **(b)** ice floe C with $RMSE_x = 0.0160$m, **(c)** ice floe L with $RMSE_x = 0.0124$m and **(d)** ice floe z with $RMSE_x = 0.0528$m.

On the other hand, the displacement curves in the y-direction are extremely poor. Fig. 7.12 shows the displacement curves in the y-direction which are paired with the best fit in the x-direction, depicted in Fig. 7.11. $\sum RMSE_y = 0.4825$m, is almost five times larger than $\sum RMSE_x = 0.1099$m. This can be explained by two reasons. Firstly, the data is obtained during an intense storm on the 4^{th} of July 2017, which complicates the calibration. Both the quality control of images during post-processing and the reliability requirement used in the imaging analysis are significantly affected. Secondly, WIIOS generated values representing the main wave period and corresponding wave amplitude propagating through the sea ice domain, averaged over a period of 12 minutes. These main wave properties are used as input in the OpenFOAM simulations, resulting in only an accurate solution in the main direction. In real life, however, especially during a storm, an infinite number of wave periods and wave amplitudes are propagating through a domain in an infinite number of wave directions [72], resulting in more chaotic ice floe motion. This motion is captured in the photos of the imaging analysis, resulting in more complex displacement curves in the y-direction.

The wave forcing implemented in OpenFOAM is described by one sine function only. Therefore, when comparing idealised simulation results to chaotic motion of ice floes captured in images, it is currently not yet possible to simulate the motion of ice floes sufficiently in both the x- and y-direction with just one value for the wave period and the wave amplitude. However, the drag coefficient values and wave direction are chosen such, that the wave amplitude of the simulated results in the y-direction are relatively close to the results from the imaging analysis, as can be seen in Fig. 7.12, yet, the wave period is far off.

The calibration results found in both the x- and y-direction are not a unique solution, but rather ill-posed. More than one set of parameters could generate the same ice floe displacement results, as the wind forcing could have a more pronounced effect on the interplay between the wind and the wave forcing. For this reason,

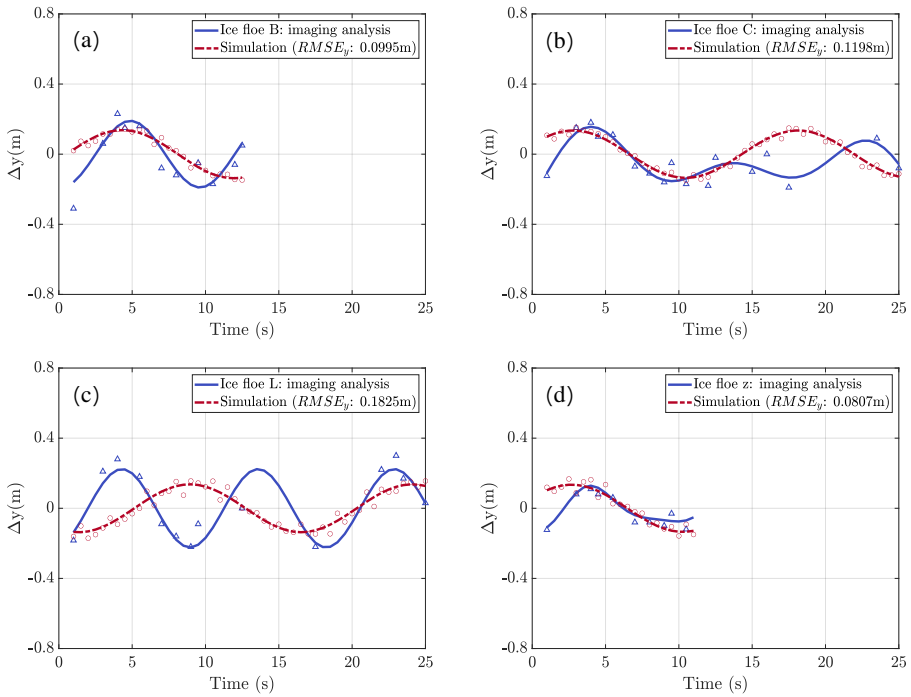

Figure 7.12: Calibration results with displacement curves in the y-direction [m], showing for **(a)** ice floe B with $RMSE_x = 0.0995$m, **(b)** ice floe C with $RMSE_x = 0.1198$m, **(c)** ice floe L with $RMSE_x = 0.1825$m and **(d)** ice floe z with $RMSE_x = 0.0807$m.

the air drag multiplication factor is roughly chosen, as opposed to the more thoroughly obtained water drag coefficients. In this calibration analysis only one set of parameters is presented.

Chapter 8

Conclusion

The global climate strongly depends on sea ice in the polar regions [167]. A substantial part of the Southern Ocean (SO), in winter equivalent to 4% of the Earth's surface [136, 160], is covered by highly dynamic sea ice in the Antarctic marginal ice zone (MIZ), which due to a wide variety of dynamic and thermodynamic processes form the basis of an extremely complex system. The impact of waves on sea ice is one of these dynamic processes on small-scale, which is a fundamental aspect in the formation of sea ice [163], causing a highly non-uniform strain rate distribution due to the heterogeneous ice composition and the interaction between colliding ice floes [163, 178].

To date, mainly large-scale models have been developed [34, 69], where these models consider a smeared model approach with effective sea ice properties [168, 179]. The well-established viscous-plastic (VP) rheology by Hibler III [69] describes the large-scale drift of sea ice, however, only with a certain level of accuracy. The actual properties of sea ice and the scale dependency are linked to distinct sea ice materials [38, 150], which is only sufficiently included in small-scale models [168]. Modelling the detailed interaction between the atmosphere, the sea ice ocean surface and the underlying ocean, is crucial to improve the understanding of the dynamic sea ice cover, which ultimately contributes to more accurate predictions on the larger-scale.

Discrete non-continuum models are often believed to be more suitable to deal with the strong spatial variations in the mechanical properties on small scale [37]. However, they suffer from simplifying assumptions related to the collision dynamics [65]. Existing small-scale continuum models, summarised in Chap. 2, do not explicitly describe an assembly of ice floes surrounded by a VP fluid, such as grease ice. This work, on the other hand, demonstrated that a continuum small-scale approach is able to capture the mechanical response on small-scale and provide new insights with regards to the detailed distributions of stress and strain rate including areas of highly localised behaviour. The newly-developed continuum small-scale model in this study considers a detailed heterogeneous sea ice layout with irregularly-shaped ice floes embedded in grease ice. Both ice constituents are governed by their own sea ice rheology, in which ice floes are described by a solid-like flow rule, controlled by floe collisions. Grease ice is represented by a VP material law, derived from the well-known VP rheology by Hibler III [69]. The interaction between waves and sea ice is investigated, considering skin drag, form drag and the Froude-Krylov force. Additionally, the interaction between ice floes and grease ice is implicitly accounted for. All aspects mentioned above, combined in one numerical framework, have not been studied before.

The main research question in this study reads as follows:

> *How do oceanic and atmospheric conditions affect the dynamics of sea ice in the Antarctic MIZ on a small scale?*

The answer to the main research question is found, by studying different main aspects of sea ice dynamics, focusing on the implementation of the sea ice rheology in Chaps. 4 and 5, the heterogeneous sea ice composition subjected to wind and wave forcing, ice floe collision dynamics and the interaction between ice floes and grease ice in Chap. 6, including the ice floe motion and displacements in Chap. 7. The response of the material behaviour of ice floes and grease ice is expressed in terms of stress, strain rate, velocity and viscosity. The most important findings and corresponding conclusions of the main aspects of sea ice dynamics studied in this work, are discussed below.

The small-scale model, developed in the computational fluid dynamics (CFD) software OpenFOAM, is formulated in terms of velocity rather than displacements. Consequently, the ice floe rheology is implemented as a Hookean-like flow rule for solid regions. This is because chequerboard oscillations were encountered, originating from the implementation of the ice floe stress. The stress state from the previous time step is entirely decoupled from the velocity, and thus in essence a constant, which in the current set of equations cannot be updated, as explained in Sec. 4.2. This is a limitation of the solver, as OpenFOAM strictly works with a collocated grid approach. It is important to note that the current implementation, consisting of the partially implemented stress state as studied in Sec. 5.3.4, avoids numerical complications due to chequerboard oscillations. However, it does not account for elastic unloading, because the total stress state cannot be accurately tracked and updated over time within a purely Eulerian approach. This implies that a portion of the elastic stored strain energy is continuously dissipated. The introduced error, however, is effectively limited as this study considers regions deeper into the MIZ, where ice floes move more gently in surrounding grease ice, causing gentle floe collisions. Therefore, the kinetic energy of colliding ice floes can be assumed to largely dissipate due to inelastic deformation of the soft outer floe rims. In this sense, there is effectively no elastic collision restitution taking place and colliding ice floes detach from each other due to the action of grease ice form drag and the Froude-Krylov force.

On the other hand, the grease ice rheology only depends on variables from the current time step. However, the grease ice rheology suffers from a singularity, resulting in locally very high viscosity values, when strain rate values approach zero. As a result, viscosity values not affected by the singularity in the inner domain are underestimated. Consequently, the difference between the three considered kinematic viscosity values is also to some degree underestimated. Additionally, the singularity results in a stress discontinuity in grease ice, which ideally should be more gradual.

The current implementation of the sea ice rheology is able to clearly distinguish between easily deformable regions, grease ice, and stiff regions, ice floes, with a continuous approximation of the velocity field distribution over the domain. The interaction of colliding ice floes, which resist collisional forces, are accounted for in the small-scale model via the elastic stress and strain rate response. Form drag acts on the circumference of ice floes due to velocity differences between ice floes and grease ice. Both are implicitly included, due to the continuity requirement of the velocity field throughout the domain, which is modelled as a continuum, and separated using a VoF approach. The importance of detailed small-scale modelling on the sub-kilometre scale is demonstrated, resolving the mechanical response of a heterogeneous sea ice cover due to the complex interaction of waves, floes, and grease ice. In particular, the floe shape and diameter variations as well as the

different wave-ice interaction mechanisms are accounted for.

The heterogeneous sea ice composition is studied in Sec. 6.1, by comparing three realistic sea ice layouts, extracted from in situ images of the Antarctic MIZ, and one idealised sea ice layout. It was found that the mechanical sea ice response depends on the detailed distribution of ice floes. Additionally, the robustness of the implemented frame work was demonstrated. In the case of homogeneous sea ice conditions with similar ice concentrations and median floe caliper diameters, discrepancies expressed in terms of the root mean square error ($RMSE$), of ice floe stress and grease ice strain rate curves, seem to increase for increasing wave period due to an increase in sea ice velocity. However, discrepancies in the grease ice viscosity curves decrease for increasing wave period, as strain rate and viscosity are inversely related. An increasing ratio of ice floe diameter to wave length results in a reduced stress and strain rate response in the considered realistic sea ice layouts. Observations of significantly larger differences in ice floe stress between layouts, compared to that of grease ice, are explained by the Froude-Krylov force. It is the main source for those observations, considering that it solely acts on the ice floe circumference. As such, the dependency on the ratio of floe diameter to wave length becomes significant. Additionally, both the number of ice floes in the domain and the position of the ice floes relative to each other have a significant impact on the behaviour of the stress, strain rate, and viscosity variables. The influence of floe shape and diameter variations was shown to be significant by comparing results from a randomly distributed idealised sea ice layout with disk-shaped floes with identical ice concentration and average area per ice floe. The largest discrepancy between the realistic and idealised layouts was shown for the grease ice viscosity and strain rate magnitude.

Ice floe collision dynamics was investigated in Sec. 6.2, by conducting a numerical analysis of the rheology variables. Stress due to the Froude-Krylov force, acting at the circumference of ice floes, results in ice floe stress which is several orders of magnitude greater than stress acting in grease ice. The wind and ocean current velocities were set to zero, resulting in a near negligible net ice floe movement in horizontal direction, due to the orbital wave velocity. The relative motion between the sea ice cover and the ocean layer underneath is affected by the sea ice layout and the wave forcing [171]. As a result, a phase shift due to inertia can be observed between the sea ice velocity and the orbital wave velocity in the x-direction, which is constant over time and increases for increasing wave period. This phase shift leads to a less straight-forward interplay between the sea ice velocity, wave elevation and collision stress intensity. Smaller wave periods, with $T < 16$s, result in little ice floe collisions, with mainly the same ice floes colliding over time and an oscillating collision stress intensity. A larger variety of ice floes collide for larger wave periods, with $T \geq 16$s, due to a higher kinetic wave energy in the system. Therefore, the number of ice floe collisions and the collision stress intensity gradually increase for increasing wave periods.

The effects of floe inertia and form drag within the surrounding grease ice were demonstrated with respect to velocity and strain rate distributions in Sec. 6.2.2. Both exhibited high localised gradients at the floe-grease ice interface. The number of interface cells, represented by extreme strain rate magnitude values due to form drag, shows a similar correlation as previously found for the collision pattern. The smaller wave periods, with $T < 16$s, show a higher number of interface cells, whereas the number of interface cells is smaller for the larger wave periods, with $T \geq 16$s. Therefore, for smaller wave periods, form drag of solitary floes is more pronounced, as indicated by a higher number of extreme strain rate magnitude values. This, however, does not affect the mean strain rate magnitude at the interface, as the results show higher values for increasing wave period. Both, grease ice away from the interface, and grease ice at the interface, show higher strain rate values for larger wave periods, due to a higher sea ice velocity magnitudes.

It was shown in Secs. 6.2.1 and 6.2.2 that increasing grease ice viscosity barely affects the sea ice stress and strain rate response. This is mainly due to the considered range of viscosity values which reflect in situ conditions but are relatively small. The resulting mechanical response exhibits negligibly small differences. Additionally, an imposed harmonic wave is considered whereas a freely propagating wave in sea ice would dissipate energy, affecting both the stress and strain rate response. However, this affect can be disregarded, due to the small size of the considered sea ice domain.

Ice floe displacements were studied in Sec. 7.3, considering in situ ice floe motions. Final parameter values for calibration and model verification were obtained. The inverse analysis was performed using four ice floes, obtained from image analysis of actual sea ice layouts, which showed the highest number of uninterrupted time steps in the imaging analysis and satisfy the reliability requirement. The modelled results, using the calibrated parameters, produced closely correlated dominant displacements in the x-direction, but less accurately the small motion component in the y-direction. It should be noted, however, that the calibrated parameters are not unique, since the nature of the problem is an ill-posed one. This implies that the interrelation between the wind and wave forcing parameters may be varied producing the same results. For this reason the air drag multiplication factor was studied to a lesser extent, in comparison to the water drag coefficients, which were investigated more rigorously. While multiple sets of parameters could lead to the same results in Sec. 7.3 only one set was presented.

The newly-developed model, presented in this thesis, serves as pioneering work of small-scale sea ice modelling in a continuum framework. This project demonstrated the general applicability of this computational approach in a detailed fashion, to describe the collision dynamics of ice floes in grease ice. The small-scale model is distinctively different from the existing continuum small-scale models which describe wave-ice interaction, as outlined in Chap. 2. The obtained results of interacting ice floes in grease ice show a higher resolution of the mechanical behaviour of sea ice on the meter-scale, as discussed in Chaps. 6 and 7. The model provides insights regarding the ongoing research to data of small-scale atmosphere-ocean physical processes, which is still limited [188]. Additionally, the newly-developed model can be used for parametrisation of large-scale models, which contribute to global climate modelling.

Chapter 9

Recommendations and future work

To further improve the general applicability of the newly-developed small-scale model, a couple of recommendations are listed below.

In the current formulation of the rheologies in OpenFOAM, both grease ice and ice floes were described by using velocity as the primary variable to be solved for. This resulted in chequerboard oscillations. One possible solution to this would be to split the formulation of both ice constituents into two separate formulations, which are independently implemented. This implies that grease ice would have velocity as primary unknown, whereas for ice floes this would be displacement. This may resolve the currently encountered issue regarding chequerboard oscillations and corresponding permanent ice floe deformations. Two numerical approaches, which can be implemented in the software OpenFOAM, allow splitting of the formulation of both ice constituents: the fluid-structure interaction (FSI) method [80, 135] or the reference mapping method [90].

The model can be extended by considering water as a third component, besides the two existing ice components, ice floes and grease ice. This would allow for the modelling of a sea ice region closer to the edge of the marginal ice zone (MIZ), where the interplay between sea ice and open water is more prominent, compared to sea ice regions found deeper into the MIZ. Additionally, the influence of ice floe-grease ice-open water area ratios should be studied in terms of collision frequency and violence, with differences in phase shift, temporary and permanent fusing and separation of floes at collision. Furthermore, ice drag coefficients influence the grease ice viscosity, which in turn affects the collision dynamics. To what extent though, is still unknown, and therefore requires further investigation.

The viscosity suffers from a singularity with locally very high viscosity values in the sea ice domain. This is because of the strain rate values, which approach zero. The existing VP rheology should be reformulated to avoid the singularity. This would affect the stress and strain rate results, which are related to a varying viscosity. The viscosity values, which are not affected by the singularity in the inner domain, would then not be underestimated. Consequently, wave dissipation effects due to an increase in viscosity would be more pronounced.

The current framework considers an imposed wave, affecting the stress and strain rate response to a still uncertain extent. A more in-depth study, considering the effects of wave dissipation, is necessary to understand the influence of the imposed wave on stress, strain rate and viscosity results. Additionally, the thickness

of both ice floes and grease ice is implemented as a parameter, which is constant both spatially and temporally. The reason for not including thickness variations was because the change of sea ice thickness is negligibly small compared to the size of the domain in the lateral direction. This assumption, however, may affect the interaction between ice floes and grease ice. Due to the applied wave forcing ice floes move back-and-forth, following the orbital wave motion. As a result, the thickness of grease ice in between ice floes can increase or decrease, which may influence the ice floe collision dynamics. In future versions of the model, both the thickness of ice floes and grease ice should be implemented as a variable, allowing sea ice thickness variations.

Lastly, the currently implemented wave forcing only allows for an accurate calibration in the main direction, as the calibration of the small-scale model in the y-direction is inadequate. More advanced data from the Antarctic MIZ in winter, coupled with a wave dynamics model which considers multiple wave directions and spectra, is essential to calibrate the model in both the primary and secondary direction.

Chapter 10

Appendix

10.1 Implementation details of the small-scale sea ice model in the Finite Volume Method

The normalised momentum equation, shown in Eq. (4.100), is spatially discretised, utilizing the FVM. The volume of cell P is integrated in a two-dimensional uniform grid, as shown in Fig. 10.1. Five cell centres are illustrated by P, N, E, S, W. The cell faces of central cell P are indicated by n, e, s, w.

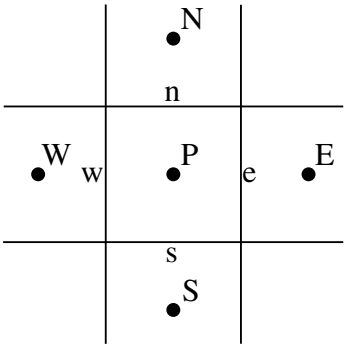

Figure 10.1: Two-dimensional collocated uniform grid [35].

.

The time-dependent term in Eq. (4.97) is constant over the cell volume. Therefore, this term is not included in the spatial discretisation scheme explained below. Additionally, the stress term, $\nabla \cdot \boldsymbol{\sigma}_f'^b$, pressure term, $\boldsymbol{\nabla} p_g'$, and source term, $\boldsymbol{S}'$, are not part of the discretisation, as the focus is on the convective terms and the extensive diffusive terms.

The normalised convective and diffusive terms of the momentum equation in the x-direction are given as

$$\begin{aligned} hU\frac{\partial U}{\partial x} + hV\frac{\partial U}{\partial y} =& \alpha_1\left(\frac{\partial}{\partial x}\left(\Delta t\mu'\frac{\partial U}{\partial x}\right) + \frac{\partial}{\partial y}\left(\Delta t\mu'\frac{\partial U}{\partial y}\right) + \frac{\partial}{\partial x}\left(\Delta t\mu'\frac{\partial U}{\partial x}\right) + \frac{\partial}{\partial y}\left(\Delta t\mu'\frac{\partial V}{\partial x}\right)\right) \\ &+\alpha_1\left(\frac{\partial}{\partial x}\left(\Delta t\lambda'\frac{\partial U}{\partial x}\right) + \frac{\partial}{\partial x}\left(\Delta t\lambda'\frac{\partial V}{\partial y}\right) + \frac{\partial}{\partial y}\left(\Delta t\lambda'\frac{\partial U}{\partial x}\right) + \frac{\partial}{\partial y}\left(\Delta t\lambda'\frac{\partial V}{\partial y}\right)\right) \\ &+\alpha_2\left(\frac{\partial}{\partial x}(\eta'+\zeta')\frac{\partial U}{\partial x} + \frac{\partial}{\partial y}(\eta'+\zeta')\frac{\partial U}{\partial y} + \frac{\partial}{\partial x}\left(\eta'\frac{\partial U}{\partial x}\right) + \frac{\partial}{\partial y}\left(\eta'\frac{\partial V}{\partial x}\right) + \frac{\partial}{\partial x}(\zeta'-\eta')\frac{\partial U}{\partial x}\right) \\ &+\alpha_2\left(\frac{\partial}{\partial x}(\zeta'-\eta')\frac{\partial V}{\partial y} + \frac{\partial}{\partial y}(\zeta'-\eta')\frac{\partial U}{\partial x} + \frac{\partial}{\partial y}(\zeta'-\eta')\frac{\partial V}{\partial y} - \frac{\partial}{\partial x}\left(\zeta'\frac{\partial U}{\partial x}\right) - \frac{\partial}{\partial y}\left(\zeta'\frac{\partial U}{\partial y}\right)\right), \end{aligned} \tag{10.1}$$

where U and V represent the velocity in the x- and y-direction, respectively. Eq. (10.1) can be rewritten as

$$\begin{aligned} &hU\frac{\partial U}{\partial x} + hV\frac{\partial U}{\partial y} = 2\alpha_1\left(\frac{\partial}{\partial x}\left(\Delta t\mu'\frac{\partial U}{\partial x}\right)\right) + \alpha_1\left(\frac{\partial}{\partial y}\left(\Delta t\mu'\frac{\partial U}{\partial y}\right)\right) + \alpha_1\left(\frac{\partial}{\partial y}\left(\Delta t\mu'\frac{\partial V}{\partial x}\right)\right) \\ &+\alpha_1\left(\frac{\partial}{\partial x}\left(\Delta t\lambda'\frac{\partial U}{\partial x}\right)\right) + \alpha_1\left(\frac{\partial}{\partial x}\left(\Delta t\lambda'\frac{\partial V}{\partial y}\right)\right) + \alpha_1\left(\frac{\partial}{\partial y}\left(\Delta t\lambda'\frac{\partial U}{\partial x}\right)\right) + \alpha_1\left(\frac{\partial}{\partial y}\left(\Delta t\lambda'\frac{\partial V}{\partial y}\right)\right) \\ &+\alpha_2\left(\frac{\partial}{\partial x}\left(\eta'\frac{\partial U}{\partial x}\right)\right) + \alpha_2\left(\frac{\partial}{\partial x}\left(\zeta'\frac{\partial U}{\partial x}\right)\right) + \alpha_2\left(\frac{\partial}{\partial y}\left(\eta'\frac{\partial U}{\partial y}\right)\right) + \alpha_2\left(\frac{\partial}{\partial y}\left(\eta'\frac{\partial V}{\partial x}\right)\right) + \alpha_2\left(\frac{\partial}{\partial x}\left(\zeta'\frac{\partial V}{\partial y}\right)\right) \\ &-\alpha_2\left(\frac{\partial}{\partial x}\left(\eta'\frac{\partial V}{\partial y}\right)\right) + \alpha_2\left(\frac{\partial}{\partial y}\left(\zeta'\frac{\partial U}{\partial x}\right)\right) - \alpha_2\left(\frac{\partial}{\partial y}\left(\eta'\frac{\partial U}{\partial x}\right)\right) + \alpha_2\left(\frac{\partial}{\partial y}\left(\zeta'\frac{\partial V}{\partial y}\right)\right) - \alpha_2\left(\frac{\partial}{\partial y}\left(\eta'\frac{\partial V}{\partial y}\right)\right). \end{aligned} \tag{10.2}$$

The FVM discretisation is applied to the normalised convective and diffusive terms of the momentum equation in the x-direction. The integration over the volume of cell P can be written, after rearrangement, as

$$\begin{aligned} &\int_{V_P}\left(hU\frac{\partial U}{\partial x} + hV\frac{\partial U}{\partial y}\right)dV = 2\alpha_1\int_{V_P}\frac{\partial}{\partial x}\left(\Delta t\mu'\frac{\partial U}{\partial x}\right)dV + \alpha_1\int_{V_P}\frac{\partial}{\partial y}\left(\Delta t\mu'\frac{\partial U}{\partial y}\right)dV \\ &+\alpha_1\int_{V_P}\frac{\partial}{\partial y}\left(\Delta t\mu'\frac{\partial V}{\partial x}\right)dV + \alpha_1\int_{V_P}\frac{\partial}{\partial x}\left(\Delta t\lambda'\frac{\partial U}{\partial x}\right)dV + \alpha_1\int_{V_P}\frac{\partial}{\partial x}\left(\Delta t\lambda'\frac{\partial V}{\partial y}\right)dV \\ &+\alpha_1\int_{V_P}\frac{\partial}{\partial y}\left(\Delta t\lambda'\frac{\partial U}{\partial x}\right)dV + \alpha_1\int_{V_P}\frac{\partial}{\partial y}\left(\Delta t\lambda'\frac{\partial V}{\partial y}\right)dV + \alpha_2\int_{V_P}\frac{\partial}{\partial x}\left(\eta'\frac{\partial U}{\partial x}\right)dV + \alpha_2\int_{V_P}\frac{\partial}{\partial x}\left(\zeta'\frac{\partial U}{\partial x}\right)dV \\ &+\alpha_2\int_{V_P}\frac{\partial}{\partial y}\left(\eta'\frac{\partial U}{\partial y}\right)dV + \alpha_2\int_{V_P}\frac{\partial}{\partial y}\left(\eta'\frac{\partial V}{\partial x}\right)dV + \alpha_2\int_{V_P}\frac{\partial}{\partial x}\left(\zeta'\frac{\partial V}{\partial y}\right)dV - \alpha_2\int_{V_P}\frac{\partial}{\partial x}\left(\eta'\frac{\partial V}{\partial y}\right)dV \\ &+\alpha_2\int_{V_P}\frac{\partial}{\partial y}\left(\zeta'\frac{\partial U}{\partial x}\right)dV - \alpha_2\int_{V_P}\frac{\partial}{\partial y}\left(\eta'\frac{\partial U}{\partial x}\right)dV + \alpha_2\int_{V_P}\frac{\partial}{\partial y}\left(\zeta'\frac{\partial V}{\partial y}\right)dV - \alpha_2\int_{V_P}\frac{\partial}{\partial y}\left(\eta'\frac{\partial V}{\partial y}\right)dV, \end{aligned} \tag{10.3}$$

Subsequently, the divergence theorem is applied to Eq. (10.3). After rearrangement, this can be written as

$$\begin{aligned} &\int_{\partial V_P}(hUU + hVU)\cdot\boldsymbol{n}dS = 2\alpha_1\int_{\partial V_P}\left(\Delta t\mu'\frac{\partial U}{\partial x}\right)\cdot\boldsymbol{n}dS + \alpha_1\int_{\partial V_P}\left(\Delta t\mu'\frac{\partial U}{\partial y}\right)\cdot\boldsymbol{n}dS \\ &+\alpha_1\int_{\partial V_P}\left(\Delta t\mu'\frac{\partial V}{\partial x}\right)\cdot\boldsymbol{n}dS + 2\alpha_1\int_{\partial V_P}\left(\Delta t\lambda'\frac{\partial U}{\partial x}\right)\cdot\boldsymbol{n}dS + 2\alpha_1\int_{\partial V_P}\left(\Delta t\lambda'\frac{\partial V}{\partial y}\right)\cdot\boldsymbol{n}dS \\ &+2\alpha_2\int_{\partial V_P}\left(\zeta'\frac{\partial U}{\partial x}\right)\cdot\boldsymbol{n}dS + \alpha_2\int_{\partial V_P}\left(\eta'\frac{\partial U}{\partial y}\right)\cdot\boldsymbol{n}dS + \alpha_2\int_{\partial V_P}\left(\eta'\frac{\partial V}{\partial x}\right)\cdot\boldsymbol{n}dS \\ &+2\alpha_2\int_{\partial V_P}\left(\zeta'\frac{\partial V}{\partial y}\right)\cdot\boldsymbol{n}dS - 2\alpha_2\int_{\partial V_P}\left(\eta'\frac{\partial V}{\partial y}\right)\cdot\boldsymbol{n}dS. \end{aligned} \tag{10.4}$$

The components in the x- and y-direction are separated, and written in discretised form. For the x-direction, this results in

$$\sum_k \left(hUU - 2\alpha_1 \Delta t \mu' \frac{\partial U}{\partial x} - \alpha_1 \Delta t \mu' \frac{\partial V}{\partial x} - 2\alpha_1 \Delta t \lambda' \frac{\partial U}{\partial x} - 2\alpha_2 \zeta' \frac{\partial U}{\partial x} - \alpha_2 \eta' \frac{\partial V}{\partial x} \right)_k \cdot (\boldsymbol{n} \Delta y)_k, \tag{10.5}$$

with $k = e, w$. In y-direction, the discretised form is given as

$$\sum_k \left(hVU - \alpha_1 \Delta t \mu' \frac{\partial U}{\partial y} - 2\alpha_1 \Delta t \lambda' \frac{\partial V}{\partial y} - \alpha_2 \eta' \frac{\partial U}{\partial y} - 2\alpha_2 \zeta' \frac{\partial V}{\partial y} + 2\alpha_2 \eta' \frac{\partial V}{\partial y} \right)_k \cdot (\boldsymbol{n} \Delta x)_k, \tag{10.6}$$

with $k = n, s$. Substitution of cell faces $k = e, w$ into Eq. (10.5) results in the discretised convective and diffusive terms in the x-direction. Substitution of cell faces $k = n, s$ into Eq. (10.6) results in the discretised convective and diffusive terms in the y-direction.

Collecting the discretised convective flux terms in both Eqs. (10.5) and (10.6), results in

$$(hUU)_e (\Delta y)_e - (hUU)_w (\Delta y)_w + (hVU)_n (\Delta x)_n - (hVU)_s (\Delta x)_s. \tag{10.7}$$

Eq. (10.7) can be rewritten as

$$C_{xe} U_e - C_{xw} U_w + C_{yn} U_n - C_{ys} U_s, \tag{10.8}$$

where $C_{xe} = h(U\Delta y)_e$, $C_{xw} = h(U\Delta y)_w$, $C_{yn} = h(V\Delta x)_n$ and $C_{ys} = h(V\Delta x)_s$. These coefficients represent the max flux through the relevant faces. Considering the First Order Upwind Scheme, the convective terms can be rewritten as

$$-a_e^c U_E - a_w^c U_W - a_n^c U_N - a_s^c U_S + a_P^c U_P, \tag{10.9}$$

where $a_e^c = \max(-C_{xe}, 0)$, $a_w^c = \max(C_{xw}, 0)$, $a_n^c = \max(-C_{yn}, 0)$, $a_s^c = \max(-C_{ys}, 0)$ and $a_P^c = a_e^c + a_w^c + a_n^c + a_s^c + (C_{xe} - C_{xw} + C_{yn} - C_{ys})$, resulting in positive a_i^c coefficients, with $i = e, w, n, s$. As the net mass flux in cell P needs to be equal to zero, one could simply write $a_P^c = a_e^c + a_w^c + a_n^c + a_s^c$.

Collecting the discretised diffusive flux terms in both Eqs. (10.5) and (10.6), results in

$$\begin{aligned}
&\left(-2\alpha_1 \Delta t \mu' \frac{\partial U}{\partial x} - \alpha_1 \Delta t \mu' \frac{\partial V}{\partial x} - 2\alpha_1 \Delta t \lambda' \frac{\partial U}{\partial x} - 2\alpha_2 \zeta' \frac{\partial U}{\partial x} - \alpha_2 \eta' \frac{\partial V}{\partial x} \right)_e (\Delta y)_e \\
&\left(+2\alpha_1 \Delta t \mu' \frac{\partial U}{\partial x} + \alpha_1 \Delta t \mu' \frac{\partial V}{\partial x} + 2\alpha_1 \Delta t \lambda' \frac{\partial U}{\partial x} + 2\alpha_2 \zeta' \frac{\partial U}{\partial x} + \alpha_2 \eta' \frac{\partial V}{\partial x} \right)_w (\Delta y)_w \\
&\left(-\alpha_1 \Delta t \mu' \frac{\partial U}{\partial y} - 2\alpha_1 \Delta t \lambda' \frac{\partial V}{\partial y} - \alpha_2 \mu' \frac{\partial U}{\partial y} - 2\alpha_2 \zeta' \frac{\partial V}{\partial y} + 2\alpha_2 \eta' \frac{\partial V}{\partial y} \right)_n (\Delta x)_n \\
&\left(+\alpha_1 \Delta t \mu' \frac{\partial U}{\partial y} + 2\alpha_1 \Delta t \lambda' \frac{\partial V}{\partial y} + \alpha_2 \mu' \frac{\partial U}{\partial y} + 2\alpha_2 \zeta' \frac{\partial V}{\partial y} - 2\alpha_2 \eta' \frac{\partial V}{\partial y} \right)_s (\Delta x)_s,
\end{aligned} \tag{10.10}$$

where $\partial U/\partial x$, $\partial U/\partial y$, $\partial V/\partial x$, and $\partial V/\partial y$, represent the gradients at the cell faces. These gradients can be

found by utilizing the central difference scheme, resulting in diffusive flux terms, given as

$$
\begin{aligned}
&-2\alpha_1\Delta t\mu'(\Delta y)_e\frac{U_E-U_P}{\Delta x}-\alpha_1\Delta t\mu'(\Delta y)_e\frac{V_E-V_P}{\Delta x}-2\alpha_1\Delta t\lambda'(\Delta y)_e\frac{U_E-U_P}{\Delta x}-2\alpha_2\zeta'(\Delta y)_e\frac{U_E-U_P}{\Delta x}\\
&-\alpha_2\eta'(\Delta y)_e\frac{V_E-V_P}{\Delta x}+2\alpha_1\Delta t\mu'(\Delta y)_w\frac{U_P-U_W}{\Delta x}+\alpha_1\Delta t\mu'(\Delta y)_w\frac{V_P-V_W}{\Delta x}+2\alpha_1\Delta t\lambda'(\Delta y)_w\frac{U_P-U_W}{\Delta x}\\
&+2\alpha_2\zeta'(\Delta y)_w\frac{U_P-U_W}{\Delta x}+\alpha_2\eta'(\Delta y)_w\frac{V_P-V_W}{\Delta x}-\alpha_1\Delta t\mu'(\Delta x)_n\frac{U_N-U_P}{\Delta y}-2\alpha_1\Delta t\lambda'(\Delta x)_n\frac{V_N-V_P}{\Delta y}\\
&-\alpha_2\eta'(\Delta x)_n\frac{U_N-U_P}{\Delta y}-2\alpha_2\zeta'(\Delta x)_n\frac{V_N-V_P}{\Delta y}+2\alpha_2\eta'(\Delta x)_n\frac{V_N-V_P}{\Delta y}+\alpha_1\Delta t\mu'(\Delta x)_s\frac{U_P-U_S}{\Delta y}\\
&+2\alpha_1\Delta t\lambda'(\Delta x)_s\frac{V_P-V_S}{\Delta y}+\alpha_2\eta'(\Delta x)_s\frac{U_P-U_S}{\Delta y}+2\alpha_2\zeta'(\Delta x)_s\frac{V_P-V_S}{\Delta y}-2\alpha_2\eta'(\Delta x)_s\frac{V_P-V_S}{\Delta y}. \qquad (10.11)
\end{aligned}
$$

Eq. (10.11) can be rewritten as

$$
\begin{aligned}
&\left(-2a_e^{d_1}(\mu'+\lambda')-2\zeta'a_e^{d_2}\right)U_E+\left(-2a_w^{d_1}(\mu'+\lambda')-2\zeta'a_w^{d_2}\right)U_W+\left(-a_n^{d_1}(\mu'+\eta')\right)U_N \qquad (10.12)\\
&+\left(-a_s^{d_1}(\mu'+\lambda')\right)U_S-\left(-2a_e^{d_1}(\mu'+\lambda')-2\zeta'a_e^{d_2}\right)U_P-\left(-2a_w^{d_1}(\mu'+\lambda')-2\zeta'a_w^{d_2}\right)U_P\\
&-\left(-a_n^{d_1}(\mu'+\eta')\right)U_P-\left(-a_s^{d_1}(\mu'+\eta')\right)U_P+\left(a_e^{d_1}\mu'-a_e^{d_2}\eta'\right)V_E+\left(-a_w^{d_1}-a_w^{d_2}\eta'\right)V_W\\
&+\left(-2a_n^{d_1}\lambda'-2a_n^{d_2}(\zeta'-\eta')\right)V_N+\left(-2a_s^{d_1}\lambda'-2a_s^{d_2}(\zeta'-\eta')\right)V_S-\left(-a_e^{d_1}\mu'-a_e^{d_2}\eta'\right)V_P\\
&-\left(-a_w^{d_1}\mu'-a_w^{d_2}\eta'\right)V_P-\left(-2a_n^{d_1}\lambda'-2a_n^{d_2}(\zeta'-\eta')\right)V_P-\left(-2a_s^{d_1}\lambda'-2a_s^{d_2}(\zeta'-\eta')\right)V_P,
\end{aligned}
$$

where the terms which include α_1 can be written as $a_k^{d_1}=\alpha_1\Delta t(\Delta y/\Delta x)_k$ for $k=e,w$ and $a_k^{d_1}=\alpha_1\Delta t(\Delta x/\Delta y)_k$ for $k=n,s$. The same principle can be applied to the terms which include α_2, where $a_k^{d_2}=\alpha_2(\Delta y/\Delta x)_k$ for $k=e,w$ and $a_k^{d_2}=\alpha_2(\Delta x/\Delta y)_k$ for $k=n,s$.

Eq. (10.12) can be simplified as

$$
\begin{aligned}
&a_e^UU_E+a_w^UU_W+a_n^UU_N+a_s^UU_S-a_e^UU_P-a_w^UU_P-a_n^UU_P-a_s^UU_P \qquad (10.13)\\
&+a_e^VV_E+a_w^VV_W+a_n^VV_N+a_s^VV_S-a_e^VV_P-a_w^VV_P-a_n^VV_P-a_s^VV_P,
\end{aligned}
$$

where $a_e^U=-2a_e^{d_1}(\mu'+\lambda')-2\zeta'a_e^{d_2}$, $a_w^U=-2a_w^{d_1}(\mu'+\lambda')-2\zeta'a_w^{d_2}$, $a_n^U=-a_n^{d_1}(\mu'+\eta')$, $a_s^U=-a_s^{d_1}(\mu'+\lambda')$, and $a_e^V=a_e^{d_1}\mu'-a_e^{d_2}\eta'$, $a_w^V=-a_w^{d_1}-a_w^{d_2}\eta'$, $a_n^V=-2a_n^{d_1}\lambda'-2a_n^{d_2}(\zeta'-\eta')$, $a_s^V=-2a_s^{d_1}\lambda'-2a_s^{d_2}(\zeta'-\eta')$.

Eq. (10.13) can be rewritten as

$$
a_e^UU_E+a_w^UU_W+a_n^UU_N+a_s^UU_S-a_P^UU_P+a_e^VV_E+a_w^VV_W+a_n^VV_N+a_s^VV_S-a_P^VV_P, \qquad (10.14)
$$

where $a_P^U=a_e^U+a_w^U+a_n^U+a_s^U$, and $a_P^V=a_e^V+a_w^V+a_n^V+a_s^V$.

The generalised expression can be found by collecting the discretised convective and diffusive terms. This results in the discretised equations of the form

$$
a_PU_P+a_P^VV_P=a_eU_E+a_wU_W+a_nU_N+a_sU_S+a_e^VV_E+a_w^VV_W+a_n^VV_N+a_s^VV_S, \qquad (10.15)
$$

where $a_e=a_e^U-a_e^c$, $a_w=a_w^U-a_w^c$, $a_n=a_n^U-a_n^c$, $a_s=a_s^U-a_s^c$ and $a_P=a_e+a_w+a_n+a_s$.

As a result, a relation has been obtained which links the velocity at the centre of cell P, U_P, to neighbouring

cell-centred velocity values. Eq. (10.15) can be rewritten as

$$a_P^U U_P + a_P^V V_P = \sum a_i U_i + \sum a_i^V V_i + S'_{U_P} + S'_U, \tag{10.16}$$

which includes S'_{U_P} and S'_U, representing the pressure term and the source terms after volume integration. a_i and a_i^V indicate the sum of convective and diffusive coefficients at the neighbouring cell faces and U_i and V_i denote the velocity components of the adjacent cell centres.

Bibliography

[1] E. A. Afolabi and J. Lee. An eulerian-eulerian cfd simulation of air-water flow in a pipe separator. *The Journal of Computational Multiphase Flows*, 6(2):133–149, 2014.

[2] A. Alberello, F. Nelli, A. Dolatshah, L. G. Bennetts, M. Onorato, and A. Toffoli. An experimental model of wave attenuation in pancake ice. In *The 29th International Ocean and Polar Engineering Conference*. International Society of Offshore and Polar Engineers, 2019.

[3] A. Alberello, M. Onorato, L. Bennetts, M. Vichi, C. Eayrs, K. MacHutchon, and A. Toffoli. Brief communication: Pancake ice floe size distribution during the winter expansion of the antarctic marginal ice zone. *The Cryosphere*, 13(1):41–48, 2019.

[4] A. Alberello, L. Bennetts, P. Heil, C. Eayrs, M. Vichi, K. MacHutchon, M. Onorato, and A. Toffoli. Drift of pancake ice floes in the winter antarctic marginal ice zone during polar cyclones. *Journal of Geophysical Research: Oceans*, 125(3):e2019JC015418, 2020.

[5] A. Alberello, F. Nelli, A. Dolatshah, L. G. Bennetts, M. Onorato, and A. Toffoli. A physical model of wave attenuation in pancake ice. *International Journal of Offshore and Polar Engineering*, 31(03): 263–269, 2021.

[6] R. Alkama, E. N. Koffi, S. J. Vavrus, T. Diehl, J. A. Francis, J. Stroeve, G. Forzieri, T. Vihma, and A. Cescatti. Wind amplifies the polar sea ice retreat. *Environmental Research Letters*, 15(12):124022, 2020.

[7] I. Allison, R. E. Brandt, and S. G. Warren. East antarctic sea ice: Albedo, thickness distribution, and snow cover. *Journal of Geophysical Research: Oceans*, 98(C7):12417–12429, 1993.

[8] C. Amory, H. Gallée, F. Naaim-Bouvet, V. Favier, E. Vignon, G. Picard, A. Trouvilliez, L. Piard, C. Genthon, and H. Bellot. Seasonal variations in drag coefficient over a sastrugi-covered snowfield in coastal east antarctica. *Boundary-Layer Meteorology*, 164(1):107–133, 2017.

[9] J. D. Anderson. *Governing equations of fluid dynamics*, pages 15–51. Springer Berlin Heidelberg, 1992.

[10] E. L. Andreas. A theory for the scalar roughness and the scalar transfer coefficients over snow and sea ice. *Boundary-Layer Meteorology*, 38(1):159–184, 1987.

[11] F. Ardhuin, G. Boutin, J. Stopa, F. Girard-Ardhuin, C. Melsheimer, J. Thomson, A. Kohout, M. Doble, and P. Wadhams. Wave attenuation through an arctic marginal ice zone on 12 october 2015: 2. numerical modeling of waves and associated ice breakup. *Journal of Geophysical Research: Oceans*, 123(8):5652–5668, 2018.

[12] A. V. Babanin, J. McConochie, and D. Chalikov. Winds near the surface of waves: Observations and modeling. *Journal of Physical Oceanography*, 48(5):1079–1088, 2018.

[13] A. V. Babanin, W. E. Rogers, R. De Camargo, M. Doble, T. Durrant, K. Filchuk, K. Ewans, M. Hemer, T. Janssen, B. Kelly-Gerreyn, et al. Waves and swells in high wind and extreme fetches, measurements in the southern ocean. *Frontiers in Marine Science*, 6:361, 2019.

[14] W. Bai, T. Zhang, and D. J. McGovern. Response of small sea ice floes in regular waves: A comparison of numerical and experimental results. *Ocean Engineering*, 129:495–506, 2017.

[15] N. Balmforth and R. Craster. Ocean waves and ice sheets. *Journal of Fluid Mechanics*, 395:89–124, 1999.

[16] P. Bartholomew, F. Denner, M. H. Abdol-Azis, A. Marquis, and B. G. van Wachem. Unified formulation of the momentum-weighted interpolation for collocated variable arrangements. *Journal of Computational Physics*, 375:177–208, 2018.

[17] G. K. Batchelor. *Kinematics of the Flow Field*, pages 71–130. Cambridge Mathematical Library. Cambridge University Press, 2000.

[18] L. Bennetts and T. Williams. Water wave transmission by an array of floating discs. *Proceedings of the Royal Society A: Mathematical, Physical and Engineering Sciences*, 471(2173):20140698, 2015.

[19] L. Bennetts, S. O'Farrell, and P. Uotila. Brief communication: Impacts of ocean-wave-induced breakup of antarctic sea ice via thermodynamics in a stand-alone version of the cice sea-ice model. *The Cryosphere*, 11(3):1035–1040, 2017.

[20] L. G. Bennetts and V. A. Squire. On the calculation of an attenuation coefficient for transects of ice-covered ocean. *Proceedings of the Royal Society A: Mathematical, Physical and Engineering Sciences*, 468(2137):136–162, 2012.

[21] L. Biddle and S. Swart. The observed seasonal cycle of submesoscale processes in the antarctic marginal ice zone. *Journal of Geophysical Research: Oceans*, 125(6):e2019JC015587, 2020.

[22] R. B. Bird. Transport phenomena. *Applied Mechanics Reviews*, 55(1):R1–R4, 2002.

[23] E. Blockley, M. Vancoppenolle, E. Hunke, C. Bitz, D. Feltham, J.-F. Lemieux, M. Losch, E. Maisonnave, D. Notz, P. Rampal, et al. The future of sea ice modeling: where do we go from here? *Bulletin of the American Meteorological Society*, 101(8):E1304–E1311, 2020.

[24] A. Bouchat, N. Hutter, J. Chanut, F. Dupont, D. Dukhovskoy, G. Garric, Y. J. Lee, J.-F. Lemieux, C. Lique, M. Losch, W. Maslowski, P. G. Myers, E. Olason, P. Rampal, T. Rasmussen, C. Talandier, B. Tremblay, and Q. Wang. Sea ice rheology experiment (sirex): 1. scaling and statistical properties of sea-ice deformation fields. *Journal of Geophysical Research: Oceans*, 127(4):e2021JC017667, 2022.

[25] G. Boutin, F. Ardhuin, D. Dumont, C. Sévigny, F. Girard-Ardhuin, and M. Accensi. Floe size effect on wave-ice interactions: Possible effects, implementation in wave model, and evaluation. *Journal of Geophysical Research: Oceans*, 123(7):4779–4805, 2018.

[26] I. Bratchie. Rheology of an ice-floe field. *Annals of Glaciology*, 5:23–28, 1984.

[27] C. E. Brennen and C. E. Brennen. *Fundamentals of multiphase flow*. Cambridge university press, 2005.

[28] M. P. Buckley and F. Veron. Structure of the airflow above surface waves. *Journal of Physical Oceanography*, 46(5):1377–1397, 2016.

[29] M. P. Buckley and F. Veron. The turbulent airflow over wind generated surface waves. *European Journal of Mechanics-B/Fluids*, 73:132–143, 2019.

[30] L. Chen and B. Basu. Wave-current interaction effects on structural responses of floating offshore wind turbines. *Wind Energy*, 22(2):327–339, 2019.

[31] S. Chen, F. Qiao, C. J. Huang, and B. Zhao. Deviation of wind stress from wind direction under low wind conditions. *Journal of Geophysical Research: Oceans*, 123(12):9357–9368, 2018.

[32] S. T. Cole, J. M. Toole, R. Lele, M.-L. Timmermans, S. G. Gallaher, T. P. Stanton, W. J. Shaw, B. Hwang, T. Maksym, J. P. Wilkinson, et al. Ice and ocean velocity in the arctic marginal ice zone: Ice roughness and momentum transfer. *Elementa: Science of the Anthropocene*, 5, 2017.

[33] M. Coon. A review of aidjex modeling. *Sea ice processes and models*, 12:25, 1980.

[34] M. D. Coon, G. A. Maykut, R. S. Pritchard, D. A. Rothrock, and A. S. Thorndike. Modeling the pack ice as an elastic-plastic material. *AIDJEX Bulletin*, 24:1–106, 1974.

[35] T. Craft, H. Iacovides, and M. Yates. Application of the finite-volume method to fluid-structure interaction analysis. In *European Fluid Mechanics Conference*, 2008.

[36] C. T. Crowe. *Multiphase flow handbook*. CRC press, 2005.

[37] A. Damsgaard, A. Adcroft, and O. Sergienko. Application of discrete element methods to approximate sea ice dynamics. *Journal of Advances in Modeling Earth Systems*, 10(9):2228–2244, 2018.

[38] V. Dansereau, J. Weiss, P. Saramito, and P. Lattes. A maxwell elasto-brittle rheology for sea ice modelling. *Cryosphere*, 10(3):1339–1359, 2016.

[39] M. Darwish and F. Moukalled. *The Finite Volume Method in Computational Fluid Dynamics: An Advanced Introduction with OpenFOAM® and Matlab®*. Springer, 2021.

[40] R. G. Dean. Stream function representation of nonlinear ocean waves. *Journal of Geophysical Research*, 70(18):4561–4572, 1965.

[41] M. H. Derkani. *Waves in the Southern Ocean and Antarctic Marginal Ice Zone: Observations and Modelling*. PhD thesis, The University of Melbourne, 2021.

[42] S. S. Deshpande, L. Anumolu, and M. F. Trujillo. Evaluating the performance of the two-phase flow solver interfoam. *Computational science & discovery*, 5(1):014016, 2012.

[43] G. Deskos, J. C. Lee, C. Draxl, and M. A. Sprague. Review of wind-wave coupling models for large-eddy simulation of the marine atmospheric boundary layer. *Journal of the Atmospheric Sciences*, 78 (10):3025–3045, 2021.

[44] M. J. Doble, M. D. Coon, and P. Wadhams. Pancake ice formation in the weddell sea. *Journal of Geophysical Research: Oceans*, 108(C7), 2003.

[45] A. Dolatshah, F. Nelli, L. Bennetts, A. Alberello, M. Meylan, J. Monty, and A. Toffoli. Letter: Hydroelastic interactions between water waves and floating freshwater ice. *Physics of Fluids*, 30(9):091702, 2018.

[46] X. Dong, Y. Wang, S. Hou, M. Ding, B. Yin, and Y. Zhang. Robustness of the recent global atmospheric reanalyses for antarctic near-surface wind speed climatology. *Journal of Climate*, 33(10):4027–4043, 2020.

[47] N. Ebuchi, Y. Toba, and H. Kawamura. Statistical study on the local equilibrium between wind and wind waves by using data from ocean data buoy stations. *Journal of Oceanography*, 48(1):77–92, 1992.

[48] A. Eghbalzadeh and M. Javan. Comparison of mixture and vof models for numerical simulation of air-entrainment in skimming flow over stepped spillways. *Procedia engineering*, 28:657–660, 2012.

[49] D. L. Feltham. Granular flow in the marginal ice zone. *Philosophical Transactions of the Royal Society A: Mathematical, Physical and Engineering Sciences*, 363(1832):1677–1700, 2005.

[50] D. L. Feltham. Sea ice rheology. *Annual Review of Fluid Mechanics*, 40(1):91–112, 2008.

[51] J. H. Ferziger, M. Perić, and R. L. Street. *Computational methods for fluid dynamics*, volume 3. Springer, 2002.

[52] J. Fish and T. Belytschko. *Strong and Weak Forms for One-Dimensional Problems*, chapter 3, pages 41–76. John Wiley and Sons, Ltd, 2007.

[53] C. Fox and V. A. Squire. Reflection and transmission characteristics at the edge of shore fast sea ice. *Journal of Geophysical Research: Oceans*, 95(C7):11629–11639, 1990.

[54] J. Garratt. Review of drag coefficients over oceans and continents. *Monthly weather review*, 105(7): 915–929, 1977.

[55] D. Gerlach, G. Tomar, G. Biswas, and F. Durst. Comparison of volume-of-fluid methods for surface tension-dominant two-phase flows. *International Journal of Heat and Mass Transfer*, 49(3-4):740–754, 2006.

[56] L. Girard, S. Bouillon, J. Weiss, D. Amitrano, T. Fichefet, and V. Legat. A new modeling framework for sea-ice mechanics based on elasto-brittle rheology. *Annals of Glaciology*, 52(57):123–132, 2011.

[57] C. Greenshields. *OpenFOAM v9 User Guide*. The OpenFOAM Foundation, 2021.

[58] C. Grossmann, H.-G. Roos, and M. Stynes. *Finite Difference Methods*, pages 23–124. Springer Berlin Heidelberg, 2007.

[59] X. Hao and L. Shen. Wind-wave coupling study using les of wind and phase-resolved simulation of nonlinear waves. *Journal of Fluid Mechanics*, 874:391–425, 2019.

[60] P. Heil and I. Allison. The pattern and variability of antarctic sea-ice drift in the indian ocean and western pacific sectors. *Journal of Geophysical Research: Oceans*, 104(C7):15789–15802, 1999.

[61] H. Heorton, D. L. Feltham, and M. Tsamados. Stress and deformation characteristics of sea ice in a high-resolution, anisotropic sea ice model. *Philosophical Transactions of the Royal Society A: Mathematical, Physical and Engineering Sciences*, 376(2129):20170349, 2018.

[62] A. Herman. Influence of ice concentration and floe-size distribution on cluster formation in sea-ice floes. *Central European Journal of Physics*, 10(3):715–722, 2012.

[63] A. Herman. Numerical modeling of force and contact networks in fragmented sea ice. *Annals of Glaciology*, 54(62):114–120, 2013.

[64] A. Herman. Numerical modeling of force and contact networks in fragmented sea ice. *Annals of glaciology*, 54(62):114–120, 2013.

[65] A. Herman. Discrete-element bonded-particle sea ice model design, version 1.3a - model description and implementation. *Geoscientific Model Development*, 9(3):1219–1241, 2016.

[66] A. Herman. Wave-induced surge motion and collisions of sea ice floes: Finite-floe-size effects. *Journal of Geophysical Research: Oceans*, 123(10):7472–7494, 2018.

[67] A. Herman, S. Cheng, and H. H. Shen. Wave energy attenuation in fields of colliding ice floes–part 2: A laboratory case study. *The Cryosphere*, 13(11):2901–2914, 2019.

[68] W. D. Hibler. A viscous sea ice law as a stochastic average of plasticity. *Journal of Geophysical Research*, 82(27):3932–3938, 1977.

[69] W. Hibler III. A dynamic thermodynamic sea ice model. *Journal of physical oceanography*, 9(4):815–846, 1979.

[70] G. Hidy. A view of recent air-sea interaction research. *Bulletin of the American Meteorological Society*, 53(11):1083–1102, 1972.

[71] W. R. Hobbs, R. Massom, S. Stammerjohn, P. Reid, G. Williams, and W. Meier. A review of recent changes in southern ocean sea ice, their drivers and forcings. *Global and Planetary Change*, 143:228–250, 2016.

[72] L. H. Holthuijsen. *Waves in oceanic and coastal waters*. Cambridge university press, 2010.

[73] M. Hopkins. A discrete element lagrangian sea ice model. *Engineering Computations*, 21:409–421, 2004.

[74] M. Hopkins and W. Hibler. Numerical simulations of a compact convergent system of ice floes. *Annals of Glaciology*, 15:26–30, 1991.

[75] M. A. Hopkins. On the mesoscale interaction of lead ice and floes. *Journal of Geophysical Research: Oceans*, 101(C8):18315–18326, 1996.

[76] M. A. Hopkins and H. H. Shen. Simulation of pancake-ice dynamics in a wave field. *Annals of Glaciology*, 33:355–360, 2001.

[77] M. A. Hopkins and A. S. Thorndike. Floe formation in arctic sea ice. *Journal of Geophysical Research: Oceans*, 111(C11), 2006.

[78] M. A. Hopkins, W. Hibler III, and G. Flato. On the numerical simulation of the sea ice ridging process. *Journal of Geophysical Research: Oceans*, 96(C3):4809–4820, 1991.

[79] T. Hristov, S. Miller, and C. Friehe. Dynamical coupling of wind and ocean waves through wave-induced air flow. *Nature*, 422(6927):55–58, 2003.

[80] L. Huang, K. Ren, M. Li, Z. Tuković, P. Cardiff, and G. Thomas. Fluid-structure interaction of a large ice sheet in waves. *Ocean Engineering*, 182:102–111, 2019.

[81] E. C. Hunke and J. K. Dukowicz. An elastic-viscous-plastic model for sea ice dynamics. *J. Phys. Oceanogr*, 27(9):1849–1867, 1997.

[82] J. K. Hutchings. *On modelling the mass of Arctic sea ice*. University of London, University College London (United Kingdom), 2000.

[83] J. K. Hutchings, H. Jasak, and S. W. Laxon. A strength implicit correction scheme for the viscous-plastic sea ice model. *Ocean Modelling*, 7(1):111–133, 2004.

[84] R. I. Issa, A. Gosman, and A. Watkins. The computation of compressible and incompressible recirculating flows by a non-iterative implicit scheme. *Journal of Computational Physics*, 62(1):66–82, 1986.

[85] P. Janssen and P. A. Janssen. *The interaction of ocean waves and wind*. Cambridge University Press, 2004.

[86] P. A. E. M. Janssen. Wave-induced stress and the drag of air flow over sea waves. *Journal of Physical Oceanography*, 19(6):745–754, 1989.

[87] H. Jasak. *Error analysis and estimation for the finite volume method with applications to fluid flows.* PhD thesis, Imperial College London (University of London), 1996.

[88] C. S. Jog and R. B. Haber. Stability of finite element models for distributed-parameter optimization and topology design. *Computer methods in applied mechanics and engineering*, 130(3-4):203–226, 1996.

[89] K. L. Johnson. *Normal contact of elastic solids – Hertz theory*, page 84–106. Cambridge University Press, 1985.

[90] K. Kamrin, C. H. Rycroft, and J.-C. Nave. Reference map technique for finite-strain elasticity and fluid–solid interaction. *Journal of the Mechanics and Physics of Solids*, 60(11):1952–1969, 2012.

[91] A. Kang, B. Zhu, P. Lin, J. Ju, J. Zhang, and D. Zhang. Experimental and numerical study of wave-current interactions with a dumbbell-shaped bridge cofferdam. *Ocean Engineering*, 210:107433, 2020.

[92] J. B. Keller. Gravity waves on ice-covered water. *Journal of Geophysical Research: Oceans*, 103(C4): 7663–7669, 1998.

[93] M. Ketabdari, H. Saghi, and H. Rezaei. Comparison of staggered and collocated grids for solving navier-stokes equations. In *5th National Congress on Civil Engineering*, 2010.

[94] S.-Y. Kim, K.-M. Kim, J.-C. Park, G.-M. Jeon, and H.-H. Chun. Numerical simulation of wave and current interaction with a fixed offshore substructure. *International Journal of naval Architecture and ocean engineering*, 8(2):188–197, 2016.

[95] T.-W. Kim, H. K. Ha, A. Wåhlin, S. Lee, C.-S. Kim, J. H. Lee, and Y.-K. Cho. Is ekman pumping responsible for the seasonal variation of warm circumpolar deep water in the amundsen sea? *Continental Shelf Research*, 132:38–48, 2017.

[96] A. Kohout, M. Williams, S. Dean, and M. Meylan. Storm-induced sea-ice breakup and the implications for ice extent. *Nature*, 509(7502):604–607, 2014.

[97] A. L. Kohout, M. H. Meylan, and D. R. Plew. Wave attenuation in a marginal ice zone due to the bottom roughness of ice floes. *Annals of Glaciology*, 52(57):118–122, 2011.

[98] A. L. Kohout, B. Penrose, S. Penrose, and M. J. Williams. A device for measuring wave-induced motion of ice floes in the antarctic marginal ice zone. *Annals of Glaciology*, 56(69):415–424, 2015.

[99] E. Konstantinidis. Added mass of a circular cylinder oscillating in a free stream. *Proceedings of the Royal Society A: Mathematical, Physical and Engineering Sciences*, 469(2156):20130135, 2013.

[100] D. Kordeweg and G. de Vries. On the change of form of long waves advancing in a rectangular channel, and a new type of long stationary wave. *The London, Edinburgh, and Dublin Philosophical Magazine and Journal of Science*, 39(240):422–443, 1895.

[101] U. Küttler and W. A. Wall. Fixed-point fluid–structure interaction solvers with dynamic relaxation. *Computational mechanics*, 43(1):61–72, 2008.

[102] J. Lee and J. Monty. On the interaction between wind stress and waves: Wave growth and statistical properties of large waves. *Journal of Physical Oceanography*, 50(2):383–397, 2020.

[103] M. Leppäranta. *The drift of sea ice*. Springer Science & Business Media, 2011.

[104] M. Leppäranta and W. D. Hibler. The role of plastic ice interaction in marginal ice zone dynamics. *Journal of Geophysical Research: Oceans*, 90(C6):11899–11909, 1985.

[105] M. Lepparanta, M. Lensu, and Q.-M. Lu. Shear flow of sea ice in the marginal ice zone with collision rheology. *Geophysica*, 25(1-2):57–74, 1990.

[106] B. Li, H. Li, Y. Liu, A. Wang, and S. Ji. A modified discrete element model for sea ice dynamics. *Acta oceanologica sinica*, 33(1):56–63, 2014.

[107] T. Li and L. Shen. The principal stage in wind-wave generation. *Journal of Fluid Mechanics*, 934:A41, 2022.

[108] A. K. Liu, B. Holt, and P. W. Vachon. Wave propagation in the marginal ice zone: Model predictions and comparisons with buoy and synthetic aperture radar data. *Journal of Geophysical Research: Oceans*, 96(C3):4605–4621, 1991.

[109] D. Logan. *A First Course in the Finite Element Method*. Thomson, 2007.

[110] S. Loset, K. N. Shkhinek, O. T. Gudmestad, and K. V. Hoyland. *Actions from ice on Arctic offshore and coastal structures*. Lan St. Petersburg, Russia, 2006.

[111] Q.-m. Lu, J. Larsen, and P. Tryde. On the role of ice interaction due to floe collisions in marginal ice zone dynamics. *Journal of Geophysical Research: Oceans*, 94(C10):14525–14537, 1989.

[112] L. Mahrt, D. Vickers, P. Frederickson, K. Davidson, and A.-S. Smedman. Sea-surface aerodynamic roughness. *Journal of Geophysical Research: Oceans*, 108(C6), 2003.

[113] T. Marić, D. B. Kothe, and D. Bothe. Unstructured un-split geometrical volume-of-fluid methods - a review. *Journal of Computational Physics*, 420:109695, 2020.

[114] R. A. Massom and S. E. Stammerjohn. Antarctic sea ice change and variability - Physical and ecological implications. *Polar Science*, 4(2):149–186, 2010.

[115] R. J. Matear, T. J. O'Kane, J. S. Risbey, and M. Chamberlain. Sources of heterogeneous variability and trends in antarctic sea-ice. *Nature communications*, 6(1):1–9, 2015.

[116] S. Maus and S. De La Rosa. Salinity and solid fraction of frazil and grease ice. *Journal of Glaciology*, 58(209):594–612, 2012.

[117] J. J. McCarthy, O. F. Canziani, N. A. Leary, D. J. Dokken, K. S. White, et al. *Climate change 2001: impacts, adaptation, and vulnerability: contribution of Working Group II to the third assessment report of the Intergovernmental Panel on Climate Change*, volume 2. Cambridge University Press, 2001.

[118] D. J. McGovern and W. Bai. Experimental study of wave-driven impact of sea ice floes on a circular cylinder. *Cold regions science and technology*, 108:36–48, 2014.

[119] D. J. McGovern and W. Bai. Experimental study on kinematics of sea ice floes in regular waves. *Cold regions science and technology*, 103:15–30, 2014.

[120] C. Mehlmann and T. Richter. A finite element multigrid-framework to solve the sea ice momentum equation. *Journal of Computational Physics*, 348:847–861, 2017.

[121] C. Mehlmann and T. Richter. A modified global newton solver for viscous-plastic sea ice models. *Ocean Modelling*, 116:96–107, 2017.

[122] D. Mendes and T. C. Oliveira. Deep-water spectral wave steepness offshore mainland portugal. *Ocean Engineering*, 236:109548, 2021.

[123] M. Meylan, L. Bennetts, C. Cavaliere, A. Alberello, and A. Toffoli. Experimental and theoretical models of wave-induced flexure of a sea ice floe. *Physics of Fluids*, 27(4):041704, 2015.

[124] M. H. Meylan, L. G. Bennetts, and A. L. Kohout. In situ measurements and analysis of ocean waves in the antarctic marginal ice zone. *Geophysical Research Letters*, 41(14):5046–5051, 2014.

[125] J. W. Miles. On the generation of surface waves by shear flows. *Journal of Fluid Mechanics*, 3(2): 185–204, 1957.

[126] P. Montalvo, R. Kraenkel, M. Manna, and C. Kharif. Wind-wave amplification mechanisms: possible models for steep wave events in finite depth. *Natural Hazards and Earth System Sciences*, 13(11): 2805–2813, 2013.

[127] F. Montiel, V. Squire, and L. Bennetts. Attenuation and directional spreading of ocean wave spectra in the marginal ice zone. *Journal of Fluid Mechanics*, 790:492–522, 2016.

[128] F. Montiel, V. Squire, M. Doble, J. Thomson, and P. Wadhams. Attenuation and directional spreading of ocean waves during a storm event in the autumn beaufort sea marginal ice zone. *Journal of Geophysical Research: Oceans*, 123(8):5912–5932, 2018.

[129] F. A. Morrison et al. *Understanding rheology*, volume 1. Oxford university press New York, 2001.

[130] J. E. M. Mosig. *Contemporary wave–ice interaction models*. PhD thesis, University of Otago, 2018.

[131] J. Nagy and G. Steinbichler. Fluid dynamic and thermal modeling of the injection molding process in openfoam. In *OpenFOAM®*, pages 183–196. Springer, 2019.

[132] J. N. Newman. *Marine hydrodynamics*. The MIT press, 2018.

[133] K. Newyear and S. Martin. A comparison of theory and laboratory measurements of wave propagation and attenuation in grease ice. *Journal of Geophysical Research: Oceans*, 102(C11):25091–25099, 1997.

[134] K. Newyear and S. Martin. Comparison of laboratory data with a viscous two-layer model of wave propagation in grease ice. *Journal of Geophysical Research: Oceans*, 104(C4):7837–7840, 1999.

[135] B.-y. Ni, D.-f. Han, S.-c. Di, and Y.-z. Xue. On the development of ice-water-structure interaction. *Journal of Hydrodynamics*, 32(4):629–652, 2020.

[136] S. M. NOAA. Understanding climate: Antarctic sea ice extent, 2020. URL https://www.climate.gov/news-features/understanding-climate/understanding-climate-antarctic-sea-ice-extent.

[137] E. Olason, G. Boutin, A. Korosov, P. Rampal, T. Williams, M. Kimmritz, V. Dansereau, and A. Samaké. A new brittle rheology and numerical framework for large-scale sea-ice models. *Journal of Advances in Modeling Earth Systems*, 14(8):e2021MS002685, 2022.

[138] J. Pan, D. W. Wang, and P. A. Hwang. A study of wave effects on wind stress over the ocean in a fetch-limited case. *Journal of Geophysical Research: Oceans*, 110(C2), 2005.

[139] R. Parmerter and M. Coon. Mechanical models of ridging in the arctic sea ice cover. *AIDJEX Bulletin*, 19:59–112, 1973.

[140] U. Passow and C. A. Carlson. The biological pump in a high co2 world. *Marine Ecology Progress Series*, 470:249–271, 2012.

[141] S. V. Patankar. *Numerical heat transfer and fluid flow*. CRC press, 2018.

[142] F. Paul, T. Mielke, C. Schwarz, J. Schröder, T. Rampai, S. Skatulla, R. R. Audh, E. Hepworth, M. Vichi, and D. C. Lupascu. Frazil ice in the antarctic marginal ice zone. *Journal of Marine Science and Engineering*, 9(6):647, 2021.

[143] C. A. Paulson, E. Leavitt, and R. Fleagle. Air-sea transfer of momentum, heat and water determined from profile measurements during bomex. *Journal of Physical Oceanography*, 2(4):487–497, 1972.

[144] J. Peiró and S. Sherwin. *Finite Difference, Finite Element and Finite Volume Methods for Partial Differential Equations*, pages 2415–2446. Springer Netherlands, 2005.

[145] J. Peiró and S. Sherwin. Finite difference, finite element and finite volume methods for partial differential equations. In *Handbook of materials modeling*, pages 2415–2446. Springer, 2005.

[146] A. S. Peters. The effect of a floating mat on water waves. *Communications on Pure and Applied Mathematics*, 3(4):319–354, 1950.

[147] O. M. Phillips. On the generation of waves by turbulent wind. *Journal of fluid mechanics*, 2(5):417–445, 1957.

[148] M. Rabatel, S. Labbé, and J. Weiss. Dynamics of an assembly of rigid ice floes. *Journal of Geophysical Research: Oceans*, 120(9):5887–5909, 2015.

[149] N. V. Radia. *Frazil ice formation in the polar oceans*. PhD thesis, UCL (University College London), 2014.

[150] P. Rampal, J. Weiss, D. Marsan, R. Lindsay, and H. Stern. Scaling properties of sea ice deformation from buoy dispersion analysis. *Journal of Geophysical Research: Oceans*, 113(C3), 2008.

[151] C. M. Rhie and W.-L. Chow. Numerical study of the turbulent flow past an airfoil with trailing edge separation. *AIAA journal*, 21(11):1525–1532, 1983.

[152] L. A. Roach, C. Horvat, S. M. Dean, and C. M. Bitz. An emergent sea ice floe size distribution in a global coupled ocean-sea ice model. *Journal of Geophysical Research: Oceans*, 123(6):4322–4337, 2018.

[153] J. Roenby, H. Bredmose, and H. Jasak. A computational method for sharp interface advection. *Royal Society open science*, 3(11):160405, 2016.

[154] J. Roenby, B. E. Larsen, H. Bredmose, and H. Jasak. A new volume-of-fluid method in openfoam. In *MARINE VI: Proceedings of the VI International Conference on Computational Methods in Marine Engineering*, pages 266–277. CIMNE, 2017.

[155] J. Roenby, H. Bredmose, and H. Jasak. *IsoAdvector: Geometric VOF on general meshes*, pages 281–296. Springer, 2019.

[156] D. A. Rothrock. The energetics of the plastic deformation of pack ice by ridging. *Journal of Geophysical Research*, 80(33):4514–4519, 1975.

[157] S. Sajjadi, J. Hunt, and F. Drullion. Asymptotic multi-layer analysis of wind over unsteady monochromatic surface waves. *Journal of Engineering Mathematics*, 84(1):73–85, 2014.

[158] F. Saucier, S. Senneville, S. Prinsenberg, F. Roy, G. Smith, P. Gachon, D. Caya, and R. Laprise. Modelling the sea ice-ocean seasonal cycle in hudson bay, foxe basin and hudson strait, canada. *Climate Dynamics*, 23(3-4):303–326, 2004.

[159] H. Scheufler and J. Roenby. Accurate and efficient surface reconstruction from volume fraction data on general meshes. *Journal of Computational Physics*, 383:1–23, 2019.

[160] M. Scott. Antarctica is colder than the arctic, but it's still losing ice, 2019. URL https://www.climate.gov/news-features/features/antarctica-colder-arctic-it%E2%80%99s-still-losing-ice.

[161] L. H. Shapiro, J. B. Johnson, M. Sturm, and G. L. Blaisdell. Snow mechanics: review of the state of knowledge and applications. Technical report, Cold Regions Research and Engineering Laboratory, Hanover, New Hampshire 03755-1290, 1997.

[162] H. Shen, W. Hibler, and M. Leppäranta. On applying granular flow theory to a deforming broken ice field. *Acta Mechanica*, 63(1):143–160, 1986.

[163] H. Shen, W. Perrie, Y. Hu, and Y. He. Remote sensing of waves propagating in the marginal ice zone by sar. *Journal of Geophysical Research: Oceans*, 123(1):189–200, 2018.

[164] H. H. Shen, W. D. Hibler III, and M. Leppäranta. The role of floe collisions in sea ice rheology. *Journal of Geophysical Research: Oceans*, 92(C7):7085–7096, 1987.

[165] O. Sigmund and J. Petersson. Numerical instabilities in topology optimization: a survey on procedures dealing with checkerboards, mesh-dependencies and local minima. *Structural optimization*, 16(1):68–75, 1998.

[166] M. Silva, M. Vitola, P. Esperanca, S. Sphaier, and C. Levi. Numerical simulations of wave–current flow in an ocean basin. *Applied Ocean Research*, 61:32–41, 2016.

[167] I. Simmonds. Comparing and contrasting the behaviour of arctic and antarctic sea ice over the 35 year period 1979-2013. *Annals of Glaciology*, 56(69):18–28, 2015.

[168] S. Skatulla, R. R. Audh, A. Cook, E. Hepworth, S. Johnson, D. C. Lupascu, K. MacHutchon, R. Marquart, T. Mielke, E. Omatuku, et al. Physical and mechanical properties of winter first-year ice in the antarctic marginal ice zone along the good hope line. *The Cryosphere*, 16(7):2899–2925, 2022.

[169] L. H. Smedsrud and R. Skogseth. Field measurements of arctic grease ice properties and processes. *Cold regions science and technology*, 44(3):171–183, 2006.

[170] M. Smith and J. Thomson. Ocean surface turbulence in newly formed marginal ice zones. *Journal of Geophysical Research: Oceans*, 124(3):1382–1398, 2019.

[171] M. Smith and J. Thomson. Pancake sea ice kinematics and dynamics using shipboard stereo video. *Annals of Glaciology*, 61(82):1–11, 2020.

[172] S. D. Smith. Wind stress and turbulence over a flat ice floe. *Journal of Geophysical Research*, 77(21): 3886–3901, 1972.

[173] S. D. Smith. Wind stress and heat flux over the ocean in gale force winds. *Journal of Physical Oceanography*, 10(5):709–726, 1980.

[174] H. Solomon. A study of ice dynamics relevant to aidjex. *AIDJEX Bull*, 2(33-50), 1970.

[175] M. Sommerfeld. Numerical methods for dispersed multiphase flows. In *Particles in flows*, pages 327–396. Springer, 2017.

[176] V. Squire and C. Fox. On ice coupled waves: a comparison of data and theory. In *Advances in ice technology: Proc. 3rd Int. Conf. on Ice Technology*, pages 269–280. Computational Mechanics Publications Cambridge, MA, 1992.

[177] V. A. Squire. A theoretical, laboratory, and field study of ice-coupled waves. *Journal of Geophysical Research: Oceans*, 89(C5):8069–8079, 1984.

[178] V. A. Squire. Of ocean waves and sea-ice revisited. *Cold Regions Science and Technology*, 49(2):110–133, 2007.

[179] V. A. Squire. A fresh look at how ocean waves and sea ice interact. *Philosophical Transactions of the Royal Society A: Mathematical, Physical and Engineering Sciences*, 376(2129):20170342, 2018.

[180] V. A. Squire and A. Allan. *Propagation of flexural gravity waves in sea ice*. Centre for Cold Ocean Resources Engineering, Memorial University of Newfoundland, 1977.

[181] V. A. Squire, J. P. Dugan, P. Wadhams, P. J. Rottier, and A. K. Liu. Of ocean waves and sea ice. *Annual Review of Fluid Mechanics*, 27(1):115–168, 1995.

[182] N. Steiner. Introduction of variable drag coefficients into sea-ice models. *Annals of Glaciology*, 33: 181–186, 2001.

[183] G. G. Stokes. On the theory of oscillatory waves. *Trans. Camb. Phil. Soc.*, 8:411–455, 1847.

[184] G. G. Stokes. *On the Effect of the Internal Friction of Fluids on the Motion of Pendulums*, volume 3 of *Cambridge Library Collection - Mathematics*, page 1–10. Cambridge University Press, 2009.

[185] J. E. Stopa, P. Sutherland, and F. Ardhuin. Strong and highly variable push of ocean waves on southern ocean sea ice. *Proceedings of the National Academy of Sciences*, 115(23):5861–5865, 2018.

[186] G. Sutherland, J. Rabault, K. H. Christensen, and A. Jensen. A two layer model for wave dissipation in sea ice. *Applied Ocean Research*, 88:111–118, 2019.

[187] P. Sutherland, J. Brozena, W. E. Rogers, M. Doble, and P. Wadhams. Airborne remote sensing of wave propagation in the marginal ice zone. *Journal of Geophysical Research: Oceans*, 123(6):4132–4152, 2018.

[188] S. Swart, M. D. du Plessis, A. F. Thompson, L. C. Biddle, I. Giddy, T. Linders, M. Mohrmann, and S.-A. Nicholson. Submesoscale fronts in the antarctic marginal ice zone and their response to wind forcing. *Geophysical Research Letters*, 47(6):e2019GL086649, 2020.

[189] A. Syrakos, S. Varchanis, Y. Dimakopoulos, A. Goulas, and J. Tsamopoulos. A critical analysis of some popular methods for the discretisation of the gradient operator in finite volume methods. *Physics of Fluids*, 29(12):127103, 2017.

[190] H. Tamura, W. M. Drennan, C. O. Collins, and H. C. Graber. Turbulent airflow and wave-induced stress over the ocean. *Boundary-layer meteorology*, 169(1):47–66, 2018.

[191] A. S. Thorndike, D. A. Rothrock, G. A. Maykut, and R. Colony. The thickness distribution of sea ice. *Journal of Geophysical Research*, 80(33):4501–4513, 1975.

[192] A. S. Thorndike, D. A. Rothrock, G. A. Maykut, and R. Colony. The thickness distribution of sea ice. *Journal of Geophysical Research*, 80(33):4501–4513, 1975.

[193] N. S. Tinnaluri and J. K. Devanuri. A collocated grid based finite volume approach for the visualization of heat transport in 2d complex geometries. *Procedia Engineering*, 127:79–86, 2015.

[194] T. Toyota, A. Kohout, and A. D. Fraser. Formation processes of sea ice floe size distribution in the interior pack and its relationship to the marginal ice zone off east antarctica. *Deep Sea Research Part II: Topical Studies in Oceanography*, 131:28–40, 2016.

[195] A. Trujillo and H. Thurman. *Essentials of Oceanography*. Number bk. 1 in Books a la Carte. Prentice Hall, 2011.

[196] A. K. Turner. A new discrete element sea-ice model for earth system modeling. Technical report, Los Alamos National Lab.(LANL), Los Alamos, NM (United States), 2017.

[197] J. Ukita and R. E. Moritz. Yield curves and flow rules of pack ice. *Journal of Geophysical Research: Oceans*, 100(C3):4545–4557, 1995.

[198] H. K. Versteeg and W. Malalasekera. *An introduction to computational fluid dynamics: the finite volume method*. Pearson education, 2007.

[199] M. Vichi. Cruise report and track data of the SA Agulhas II Winter 2017 expedition (voyage 25), Sept. 2018. URL https://doi.org/10.5281/zenodo.7038073.

[200] M. Vichi, C. Eayrs, A. Alberello, A. Bekker, L. Bennetts, D. Holland, E. de Jong, W. Joubert, K. MacHutchon, G. Messori, J. F. Mojica, M. Onorato, C. Saunders, S. Skatulla, and A. Toffoli. Effects of an explosive polar cyclone crossing the antarctic marginal ice zone. *Geophysical Research Letters*, 46 (11):5948–5958, 2019.

[201] T. Wacławczyk and T. Koronowicz. Modeling of the flow in systems of immiscible fluids using volume of fluid method with cicsam scheme. *Turbulence*, 8:267–276, 2005.

[202] T. Wacławczyk and T. Koronowicz. Comparison of cicsam and hric high-resolution schemes for interface capturing. *Journal of theoretical and applied mechanics*, 46:325–345, 2008.

[203] P. Wadhams. Attenuation of swell by sea ice. *Journal of Geophysical Research*, 78(18):3552–3563, 1973.

[204] P. Wadhams, F. Parmiggiani, G. De Carolis, D. Desiderio, and M. Doble. Sar imaging of wave dispersion in antarctic pancake ice and its use in measuring ice thickness. *Geophysical Research Letters*, 31(15), 2004.

[205] P. Wadhams, F. Parmiggiani, and G. de Carolis. Wave dispersion by antarctic pancake ice from sar images: A method for measuring ice thickness. *Advances in SAR Oceanography from Envisat and ERS Missions*, 613:36, 2006.

[206] R. Wang and H. H. Shen. Experimental study on surface wave propagating through a grease - pancake ice mixture. *Cold Regions Science and Technology*, 61(2-3):90–96, 2010.

[207] R. Wang and H. H. Shen. Gravity waves propagating into an ice-covered ocean: A viscoelastic model. *Journal of Geophysical Research: Oceans*, 115(C6), 2010.

[208] J. E. Weber. Wave attenuation and wave drift in the marginal ice zone. *Journal of physical oceanography*, 17(12):2351–2361, 1987.

[209] J. Weiss, E. M. Schulson, and H. L. Stern. Sea ice rheology from in-situ, satellite and laboratory observations: Fracture and friction. *Earth and Planetary Science Letters*, 255(1):1–8, 2007.

[210] M. Weitz and J. B. Keller. Reflection of water waves from floating ice in water of finite depth. *Communications on Pure and Applied Mathematics*, 3(3):305–318, 1950.

[211] P. Wesseling. *Principles of computational fluid dynamics*, volume 29. Springer Science & Business Media, 2009.

[212] H.-C. Wu. *Continuum mechanics and plasticity*. Chapman and Hall/CRC, 2004.

[213] J. Wu. Wind-stress coefficients over sea surface near neutral conditions - a revisit. *Journal of Physical Oceanography*, 10(5):727–740, 1980.

[214] L. Wu, A. Rutgersson, E. Sahlée, and X. Guo Larsén. Swell impact on wind stress and atmospheric mixing in a regional coupled atmosphere-wave model. *Journal of Geophysical Research: Oceans*, 121 (7):4633–4648, 2016.

[215] L. Wu, T. Hristov, and A. Rutgersson. Vertical profiles of wave-coherent momentum flux and velocity variances in the marine atmospheric boundary layer. *Journal of Physical Oceanography*, 48(3):625–641, 2018.

[216] W. Ye, Y. Pan, L. He, B. Chen, J. Liu, J. Gao, Y. Wang, and Y. Yang. Chapter 3 - design with modeling techniques. In H. D. Goodfellow and Y. Wang, editors, *Industrial Ventilation Design Guidebook*, pages 109–183. Academic Press, second edition edition, 2021.

[217] S. Zhang, X. Zhao, and S. Bayyuk. Generalized formulations for the rhie–chow interpolation. *Journal of Computational Physics*, 258:880–914, 2014.

[218] X. Zhao and H. H. Shen. Cold regions science and technology wave propagation in frazil / pancake , pancake , and fragmented ice covers. *Cold Regions Science and Technology*, 113:71–80, 2015.

[219] X. Zhao and H. H. Shen. Three-layer viscoelastic model with eddy viscosity effect for flexural-gravity wave propagation through ice cover. *Ocean Modelling*, 131:15–23, 2018.